

May 2023

Utilizing Fluorescent Nanoscale Particles to Create a Map of the Electric Double Layer

Quintus Owen
University of Wisconsin-Milwaukee

Follow this and additional works at: <https://dc.uwm.edu/etd>



Part of the [Nanoscience and Nanotechnology Commons](#), and the [Physical Chemistry Commons](#)

Recommended Citation

Owen, Quintus, "Utilizing Fluorescent Nanoscale Particles to Create a Map of the Electric Double Layer" (2023). *Theses and Dissertations*. 3201.
<https://dc.uwm.edu/etd/3201>

This Dissertation is brought to you for free and open access by UWM Digital Commons. It has been accepted for inclusion in Theses and Dissertations by an authorized administrator of UWM Digital Commons. For more information, please contact scholarlycommunicationteam-group@uwm.edu.

UTILIZING FLUORESCENT NANOSCALE PARTICLES
TO CREATE A MAP OF THE ELECTRIC DOUBLE LAYER

by

Quintus S. Owen

A Dissertation Submitted in
Partial Fulfillment of the
Requirements for the Degree of

Doctor of Philosophy
in Chemistry

at

The University of Wisconsin-Milwaukee

May 2023

ABSTRACT

UTILIZING FLUORESCENT NANOSCALE PARTICLES TO CREATE A MAP OF THE ELECTRIC DOUBLE LAYER

by

Quintus S. Owen

The University of Wisconsin-Milwaukee 2023
Under the Supervision of Professor Jörg C. Woehl

The interactions between charged particles in solution and an applied electric field follow several models, most notably the Gouy-Chapman-Stern model, for the establishment of an electric double layer along the electrode, but these models make several assumptions of ionic concentrations and an infinite bulk solution. As more scientific progress is made for the finite and single molecule reactions inside microfluidic cells, the limitations of the models become more extreme. Thus, creating an accurate map of the precise response of charged nanoparticles in an electric field becomes increasingly vital. Another compounding factor is Brownian motion's inverse relationship with size: large easily observable particles have relatively small Brownian movements, while nanoscale particles are simultaneously more difficult to be observed directly and have much larger magnitude Brownian movements. The research presented here tackles both cases simultaneously using fluorescently tagged, negatively charged, 20 nm diameter polystyrene nanoparticles. By utilizing parallel plate electrodes within a specially constructed microfluidic device that limits the z-direction, the nanoparticle movements become restricted to two dimensions. By using one axis to measure purely Brownian motion, while the other axis has both Brownian motion and ballistic movement from the applied electric

field, the ballistic component can be disentangled and isolated. Using this terminal velocity to calculate the direct effect of the field on a single nanoparticle, as opposed to the reaction of the bulk solution, several curious phenomena were observed: the trajectory of the nanoparticle suggests that the charge time of the electrode is several magnitudes larger than the theoretical value, lasting for over a minute instead of tens of milliseconds. Additionally, the effective electric field does not reduce to below the Brownian limit, but instead has a continued influence for far longer than the model suggests. Finally, when the electrode was toggled off, a repeatable response was observed where the nanoparticle would immediately alter course in the opposite direction of the previously established field, rebounding with a high degree of force for several seconds after the potential had been cut before settling to a neutral and stochastic Brownian motion. While some initial hypotheses are presented in this dissertation as possible explanations, these findings indicate the need for additional experiments to find the root cause of these unexpected results and observations.

©Copyright by Quintus S. Owen, 2023
All Rights Reserved

TABLE OF CONTENTS

LIST OF FIGURES	viii
LIST OF TABLES	xii
LIST OF ABBREVIATIONS	xiii
LIST OF SYMBOLS	xiv
ACKNOWLEDGEMENTS	xvi
Chapter 1. Introduction and the Einstein-Smoluchowski Equation	1
1.1 A Personal Anecdote	2
1.2 Dissertation Organization	3
1.3 Chapter 1 Overview	6
1.4 Robert Brown and Brownian Motion	7
1.5 Einstein's Other Paper	9
1.5.1 Osmotic Pressure Equations	11
1.5.2 Diffusion Equations	13
1.6 Einstein-Smoluchowski Equation	14
1.7 Some Enquirer: Jean Baptiste Perrin	16
1.8 Dimensionality and Additive Factors	20
Chapter 2. Electric Potential Theory and the Debye Length	24
2.1 Chapter Overview	25
2.2 Electrical Field of a Single Particle	25
2.2.1 Electrical Field of Two Particles	29
2.2.2 Electrical Field of a Charged Surface	31
2.2.3 Electrical Field of Two Parallel Plates	32
2.2.4 A Particle Between Two Plates	33
2.3 Electrical Field Theory	34
2.4 Gauss's Law and Poisson Equation	36
2.5 Parallel Plate Capacitor	39
2.6 Poisson-Boltzmann Equation	40
2.7 Debye-Hückel Theory	42
2.8 Dielectrophoretic Forces	43
Chapter 3. Gouy-Chapman-Stern Model of the Electric Double Layer	48
3.1 Chapter Overview	49
3.2 Helmholtz Model	49
3.3 Gouy-Chapman Model	50
3.4 Stern Model	53
3.5 Additional EDL Theories	55
3.5.1 Specifically Adsorbed Ions	56
3.5.2 Solvation Layer	57
3.5.3 Pseudocapacitance	59

Chapter 4.	Nanoscale Microscopy and Fluorescence	64
4.1	Chapter Overview	65
4.2	Telescopes to Microscopes	65
4.3	Resolution Limits and the Airy Disk	70
4.4	Fluorescence Microscopy	74
4.5	Particle Tracking	79
Chapter 5.	Contemporary Inspiring Research	85
5.1	Chapter Overview	86
5.2	The ABEL Trap by Cohen and Moerner	87
5.3	Electrostatic Corral Trap by Woehl, Carlson, and Udad	88
5.4	Undamped Brownian using LC(S)TEM by Welling et al.	89
5.5	Brownian Tracking with Motion Blur by Mortensen et al.	90
5.6	EDL Pressure Gradient-Induced Dispersion by McCallum and Pennathur	91
		92
5.7	Surface Potential at Electrolyte Interfaces by Brown et al.	93
5.8	Electrode Capacitance in Aqueous Solutions by Khademi and Barz	94
5.9	Rapid Particle Tracking by Radial Symmetry by Parthasarathy	95
5.10	General Defocusing Particle Tracking by Barnko et al.	
Chapter 6.	Methods and Materials	98
6.1	Chapter Overview	99
6.2	Glass Cleaning Procedures	99
6.2.1	Slide Drying	101
6.2.2	Preliminary HMDS Layer	102
6.3	Application of Positive Photoresist	103
6.3.1	Patterning via UV Exposure	106
6.4	Metal Deposition Chamber	108
6.4.1	Removal of Patterned Photoresist	113
6.5	Attachment of Top Coverslip	113
6.6	Fluorescent Nanoparticle Solution Preparation	115
6.7	Microfluidic Device Set-up	118
6.8	Excitation Laser Intensity and Stabilization	120
6.9	Brightfield and Fluorescent Microscopy	124
Chapter 7.	Troubleshooting and Initial Results	127
7.1	Chapter Overview	128
7.2	The Penumbra Problem	128
7.3	EDL Estimates via COMSOL Calculation	131
7.4	Simulated Brownian and Data Bootstrapping with Lag Times	138
7.5	Hardware and Software Calibration for Particle Viewing	142
7.6	Solution Refinement and Edge Sealing	144
7.7	Z-Direction: Solution Height Importance	148
7.8	Voltage Assessment and Electrode Issues	150

Chapter 8.	Potential Reduction and EDL Establishment Results	155
8.1	Chapter Overview	156
8.2	Brownian Motion and Calculated Diffusion Coefficient	156
8.2.1	Simulated Ballistic Component Extraction	159
8.2.2	X-and-Y Axis Similarity	163
8.3	Single-Direction Ballistic Component	166
8.4	Multi-Particle Analysis	173
8.5	Effective Voltage Calculations	175
8.6	Supplemental Examples	179
Chapter 9.	The Rebound Effect and Future Goals	184
9.1	Chapter Overview	185
9.2	EDL Establishment Time	185
9.3	Rebound Effect	194
9.4	The Effects of Increasing Viscosity	201
9.5	Hypotheses and Future Goals	207
9.6	Conclusions	216
Curriculum Vitae		218

LIST OF FIGURES

Fig.		pg.
1.1	A Van der Graaf generator diagram	1
1.2	Portrait of Robert Brown	7
1.3	<i>Clarkia pulchella</i> pollen grains	8
1.4	Photograph of Albert Einstein	10
1.5	Portrait of Jean Baptiste Perrin	11
1.6	Perrin's hand-drawn paths	18
1.7	Displacement of a silica sphere in water	21
2.1	COMSOL plots of the position, electrostatic potential, field lines, and equipotential lines of a circular source.	26
2.2	COMSOL plot combining equipotential lines, electric potential, and electrostatic field lines.	28
2.3	COMSOL plot of two negatively charged particles	29
2.4	COMSOL plot of oppositely charged particles	30
2.5	COMSOL plot of a negatively charged particle attracted towards a positively charged plate.	31
2.6	COMSOL plot of a negatively charged particle repelled by a negatively charged plate.	32
2.7	COMSOL plot showing oppositely charged electrode plates.	33
2.8	Two curves highlighting the difference in flux	37
2.9	Two electrodes with an overlapping area and charges.	39
2.10	Diagram of DEP forces for uniform and non-uniform fields.	43
2.11	COMSOL plots of the dielectrophoretic potential of two electrode setups	45
3.1	A positively charged metal electrode with counter-ions	50
3.2	The Helmholtz Model	51
3.3	The Gouy-Chapman Model	53
3.4	The Stern Model	54
3.5	The Inner and Outer Helmholtz Planes according to Grahame	57
3.6	Molecular representation according to Bockris/Devanathan/Mueller.	58
3.7	Characteristic depictions of capacitors, pseudocapacitors, and Faradic batteries	60
4.1	17 th Century telescopes and a tripod microscope	66
4.2	The difference between reflected and refracted light	67
4.3	Convex Lenses and Concave Lenses	68
4.4	Compound Microscope diagram	68
4.5	NASA's image of galaxy cluster SMACS 0723 using the James Webb Space Telescope	69
4.6	Depiction of the Airy Disk and the resolution limit of a point-source of light	70
4.7	Depiction of several Airy disks either resolved, at the Rayleigh resolution limit, or unresolvable	71
4.8	Illustrations of a microscope objective and the diffraction limit	72
4.9	A logarithmic scale bar showing the location of the diffraction limit	73
4.10	Fluorescence and elastic scattering	75
4.11	Airy disk placements and their resulting pixelated camera image	76
4.12	Airy disk point spread functions of a fluorophore	77

4.13	Simplified mechanism of STORM	78
4.14	Exposure and Mobility differences for a single moving fluorophore	80
4.15	Depiction of a particle undergoing Brownian motion	80
5.1	Banner for the One Molecule Group	86
5.2	The ABEL Trap diagrams	87
5.3	Electrostatic Corral Trap diagrams	88
5.4	Undamped 3D Brownian using LC(S)TEM diagrams	89
5.5	Confined Brownian tracking with motion blur diagrams	90
5.6	EDL and pressure gradient-induced dispersion for microfluidic current monitoring diagrams	91
5.7	Surface potential, hydration, and XPS results of nanoparticles	92
5.8	EDL capacitance vs log scale concentration of NaCl and large molecules, TDAPS and SDS.	93
5.9	Rapid particle tracking using radial symmetry diagrams	94
5.10	General defocusing particle tracking diagrams	95
6.1	Slide holder diagram	100
6.2	Nitrogen gas purging solution from the coverslip diagram	101
6.3	HMDS vapor chamber	102
6.4	Depiction of photolithography procedures	104
6.5	Spin speed vs photoresist thickness for S1813 Photoresist	105
6.6	Real image of the photoresist mask	107
6.7	Solidworks schematic and real image of the custom slide holder.	108
6.8	Metal evaporation at three different time points	109
6.9	Metal lithography diagram	109
6.10	Real image and schematic of the metal evaporation system with attached pumps	110
6.11	Schematic of the Woehl Group metal evaporation inner chamber	112
6.12	Top coverslip attachment steps	114
6.13	Assembled microfluidic devices	115
6.14	Logarithmic scale of size, with indicators for the two sizes of nanoparticles	116
6.15	Real image and schematic of non-conductive sample-holder and microfluidic device	118
6.16	Absorbance and emission bands for the 20 nm fluorescent nanoparticles	120
6.17	Real image and Schematic of the laser table	122
6.18	Schematic of the inside of the microscope.	123
6.19	Real image of the microscope table	124
6.20	Brightfield and FL camera images of two different corral traps	125
7.1	Diagram of the cause of the penumbra	129
7.2	Schematic of the penumbra	130
7.3	Electrostatic potential between two parallel plates, previously shown in Chapter 2	131
7.4	Real image of a microfluidic cell	132
7.5	2D COMSOL simulation of the electrostatic potential for a microfluidic cell	132
7.6	Enhanced view of Figure 7.5	133
7.7	1D plot of the electric potential shown in Figure 7.5	133
7.8	COMSOL image of the cross-section of the microfluidic cell	134
7.9	2D COMSOL simulation of the cross section of the microfluidic cell	135

7.10	1D plot of the electric potential, using Figures 7.7 and 7.9	135
7.11	1D plot of the electric potential according to conventional EDL theory	137
7.12	Four simulated 1D particles undergoing Brownian motion	139
7.13	The ideal result of the Einstein-Smoluchowski equation	139
7.14	Different methods of analysis: individual steps, cumulative steps, and lag frames	140
7.15	Comparison of the Einstein-Smoluchowski Equation and the RMS values of Simulated Brownian motion.	141
7.16	Newport LBP HR program window showing the symmetry and Gaussian fit of the 514 nm laser	143
7.17	Viewing window of a micrometer ruler used for calibration at 40x magnification	144
7.18	Importance of low concentration of fluorescent particles	145
7.19	Immobilized nanoparticles on glass and particles undergoing Brownian motion.	146
7.20	Directional flow of a nanoparticle.	147
7.21	Brownian particle trajectories at two different times	148
7.22	Fluorescent nanoparticle in different parts of the focal plane	149
7.23	Time-lapse FL nanoparticle moving into focus	149
7.24	Simplified side-view depiction of the particle's trajectory in Figure 7.23.	149
7.25	Two frames of a 20 nm fluorescent particle travelling at high speed.	151
7.26	Nanoparticles diffusing off an electrode after voltage has been turned off	152
7.27	Nanoparticles aggregating along an electrode after the application of a high potential	153
8.1	RMS deviation vs increasing lag time for a FL particle undergoing Brownian motion.	156
8.2	Linear MSD plot of the experiment seen in Figure 8.1.	157
8.3	Two MSD plots of additional experiments for comparison to Figure 8.2	158
8.4	Simulated trajectory of a Brownian particle after an added perturbation.	160
8.5	Mean-Square Displacement vs Lag-time.	161
8.6	The calculated ballistic component found by subtracting the values previous Figures.	162
8.7	Trajectories of three 20 nm FL particles undergoing pure Brownian motion.	164
8.8	The X-axis and Y-axis mean square displacements of the three freely diffusing particles	165
8.9	The difference between Brownian and Ballistic motion.	167
8.10	The X-axis movements of the particle shown in Figure 8.9, and the isolated ballistic component	168
8.11	Two different particle trajectories of negatively charged 20 nm FL particles.	169
8.12	Plots of X-axis movement vs time and RMS displacement vs lag time of a particle	170
8.13	Plots of X-axis movement vs time and RMS displacement vs lag time of a different particle	171
8.14	Trajectories of two negatively charged 20 nm FL particles over 25 seconds.	173
8.15	X-axis movements and ballistic values for the two particles shown in Figure 8.12.	174
8.16	Particle trajectories and calculated ballistic components of two 20 nm FL particles	177
8.17	Particle Tracking and ballistic component of a 20 nm FL particle.	180
8.18	Particle Tracking of two particles and their ballistic components	181
8.19	Particle Tracking and ballistic component of a 20 nm FL particle.	181
8.20	Particle Tracking of two particles and their ballistic components	181
8.21	Particle Tracking and ballistic component of a 20 nm FL particle.	182
8.22	Particle Tracking and ballistic component of another 20 nm FL particle.	182

8.23	Particle Tracking and ballistic component of a single FL particle, with electrodes 75 μm apart	183
9.1	Particle trajectories of 4 different particles in a 175 μm channel.	187
9.2	Particle velocities calculated via R-MSD subtraction from Figure 9.1.	188
9.3	Multiple camera positions of a particle travelling from the negative electrode, through the bulk, to the positive electrode over an extended period.	189
9.4	X-axis position vs time graph and ballistic components of the particle shown in Figure 9.3	190
9.5	100-frame average velocities of the nanoparticle shown in Figure 9.4.	192
9.6	Velocities from Figure 9.5 converted into percent reduction of the applied voltage	193
9.7	Two sets of a nanoparticle's trajectories as it rebounds after the potential is cut	195
9.8	The full x-axis movements of the nanoparticle shown in Figure 9.7	196
9.9	Ballistic components of the particle shown in Figure 9.8	197
9.10	X-axis movements of a nanoparticle after multiple applications of potential.	198
9.11	Highlighted sections from Figure 9.10 showing the rebound effect	199
9.12	Y-Axis Brownian movements and ballistic components of all attractive and repulsive potentials applied in Figure 9.10	200
9.13	X-Axis movements of a nanoparticle in a 10% glycerol solution.	202
9.14	A highlighted rebound section and ballistic components from Figure 9.13	203
9.15	Trajectories of two nanoparticles in a 25% glycerol solution, with rebounds.	204
9.16	The X-axis movements of a nanoparticle in 25% glycerol within a 75 μm channel	206
9.17	Hypothetical 1D graphs of the electric potential across a 175 μm channel, comparing the Stern Model, non-EDL model, and observed experimental hypothesis	208
9.18	Hypothetical 1D line graphs of the decay in electric potential over time.	208
9.19	Cross-section of an idealized microfluidic cell and the deprotonation of the glass surface.	209
9.20	Electroosmotic flow at five time points: electrode off, initial application, depletion of positive ions, cessation of electroosmotic flow, and field deactivation.	210
9.21	Hypothetical cyclic electrode charging mechanism	213
9.22	Hypothesis of the battery-like behavior observed at different time points	214

LIST OF TABLES

Table		pg.
8.1	Calculated average diffusion coefficients from Figure 8.5	166
8.2	Summary of the terminal velocities, effective electric fields, and %Reduction from examples presented throughout Chapter 8.	178
8.3	Summary of the terminal velocities, effective electric fields, and %Reduction from the Supplemental Figures of Chapter 8	179
9.1	Summation of the terminal velocities, effective potentials, and %Reduction from Figure 9.2.	188
9.2	Summation of the terminal velocities, effective potentials, and %Reduction from Figure 9.4.	191

LIST OF ABBREVIATIONS

UWM	University of Wisconsin-Milwaukee
3D/2D/1D	3-Dimensional / 2-Dimensional / 1-Dimensional
EDL	Electric Double Layer
RMS	Root-Mean-Square
DEP	Dielectrophoresis
PB	Poisson-Boltzmann
OHP	Outer Helmholtz Plane
IHP	Inner Helmholtz Plane
GCS	Gouy-Chapman-Stern
SEM	Scanning Electron Microscope
TEM	Transmission Electron Microscope
FL	Fluorescent/Fluorescence
PALM	Photoactivated Localization Microscopy
fPALM	Fluorescence PALM
FSM	Fluorescence Speckle Microscopy
STORM	Stochastic Optical Reconstruction Microscopy
ABEL	Anti-Brownian Electrophoretic
AC	Alternating Current
DC	Direct Current
LC(S)TEM	Liquid-Cell (Scanning) Transmission Electron Microscopy
MSD	Mean Square Displacement
XPS	X-Ray Photoelectron Spectroscopy
GDPT	General Defocusing Particle Tracking
AMII	Acetone-Methanol-Isopropanol-Isopropanol
HMDS	Hexamethyldisilazane
UV	Ultraviolet
RPM	Rotations Per Minute
EMCCD	Electron-Multiplying Charge Coupling Device
SUMSQ	Sum Squared
R-MSD subtraction	Root of the mean-square displacement subtraction

LIST OF SYMBOLS

Π	Osmotic pressure	W	An arbitrary constant
V_t	Volume	κ	Debye screening vector
V^*	Partitioned Volume	λ_D	Debye length
n_p	Number of suspended particles	c	Concentration of an ion
R	Ideal Gas constant	$CM(f)$	Clausius-Mossotti factor
T	Temperature	ϵ_m^*	Complex permittivity of the medium
N_A	Avogadro's number	ϵ_p^*	Complex permittivity of the particle
E_F	Free Energy	σ_m	Electrical conductivity of the medium
E_S	Energy of the system	σ_p	Electrical conductivity of the particle
S	Entropy of the system	f_E	Frequency of the electric field
K	Force applied from Diffusion	i	Imaginary constant, equal to $\sqrt{-1}$
v	Number of suspended particles in a set volume	F_{DEP}	Dielectrophoretic Force
x_D	Finite displacement	$Re[CM]$	Real component of the Clausius-Mossotti factor
D	Diffusion coefficient	∇E_{RMS}^2	Root mean squared value of the electric field
η	Viscosity of a liquid medium	$\varphi_{initial}$	Initial applied potential energy
a	Radius of a particle	x_a	Distance from an electrode
t	Time	φ_{drop}	Drop in potential across the Stern layer
f	Randomized displacements	d_{Stern}	Stern layer thickness
λ_x	X-axis Displacement	ζ_{pot}	Potential energy at the Stern plane
N	Number of steps	$\varphi_{Diffuse}$	Potential at a point within the Diffuse layer
λ_f	Mean free path length	θ	Fraction of occupied active sites
x_+	Steps in a positive direction	L	Rate of incidence
x_-	Steps in negative direction	P_A	Probability of adsorption
x_{step}	Value of all steps	L_D	Rate of desorption
P_x	Probability distance	K_{eq}	Equilibrium constant

$\overline{x^2}$	Mean square distance 1D	M_A	Concentration of the ion
$\overline{r^2}$	Mean square displacement 3D	F	Faraday constant
x, y, z	The 3 axial dimensions	C_ϕ	Pseudocapacitance
n	Number of dimensions	q_C	Charge coverage
$V(t)$	Ballistic motion as a function of time	NA	Numerical Aperture
q	Source charge	n_m	Refractive index of a medium
Q	Test charge	θ_A	Aperture angle
d	Charge separation distance	d_{Abbe}	Abbe resolution limit
ϵ	General permittivity	λ_L	Wavelength of light
E	Electric Field	$d_{Rayleigh}$	Rayleigh resolution limit
F	Force of attraction	L	Length of confinement
U_{pot}	Potential Energy	Δt	Image capture time
ϕ	Electrostatic potential energy	p	Initial position
∇	The del operator	g	Gravity
da	Vector normal to the surface of an enclosed surface	d_f	Distance fallen
q_{encl}	Enclosed charge	α	Brownian power factor
ρ	Charge density	$\langle \Delta x_{Perturbed}^2(t) \rangle$	MSD of the Ballistic + Brownian component
$d\tau$	Infinitesimal volume element	$\langle \Delta x_{Brown}^2(t) \rangle$	MSD of only Brownian component
ϵ_0	Permittivity of free space	$V_{RMS}(t)$	RMS value of only the Ballistic component
ϵ_r	Permittivity of the medium	x_{axis}	Position perpendicular to the electrode, the X-axis
C	Capacitance	y_{axis}	Position parallel to the electrode, the Y-axis
A	Area of electrode overlap	R^2	Coefficient of determination
V_q	Applied voltage	F_D	Drag Force
σ	Surface charge	v_t	Terminal velocity
n_i	Number of ions	F_A	Force of attraction
n_0	Total number of ions	V_{eff}	Effective potential voltage
z_i	Charge number	E_{eff}	Effective electric field
ϕ_i	Charge acting on ions	$\%Reduct$	Percent reduction of the electric field or potential
e_0	Elementary unit charge	V_0	Initially applied potential
k_B	Boltzmann constant	E_0	Initially applied electric field

ACKNOWLEDGEMENTS

Thank you so much to Dr. Woehl for guiding me along this path. Your input, insight, and intelligence made this work possible, and I will always be grateful for everything you have done for me. You have always spoken to me with genuine care and patience, and you have allowed me to grow far more than I thought possible. I can never thank you enough.

To all my colleagues over the years in the One Molecule Group, Xavier Udad, Nazmul Hassan, Brad Moran, and Alaknanda Patel, I cannot understate my appreciation for everything you've done to help me over the years. Thank you for the multiple idea sessions, the mutual commiserating about difficult experiments, and the ecstatically frantic discussions about our new discoveries. Whenever I was down, you were there to pick me up, and I hope I did the same for you. Our camaraderie is something I will carry with me for the rest of my life.

To my numerous undergrad research assistants throughout the years, I wanted to thank you all. Working with you and seeing your own excitement at our work always brought a smile to my face. I wanted to give special thanks to Erika Johansen for her never-ending willingness to dive into new ideas, as they led to some of our greatest discoveries.

Finally, thank you to my wonderful committee: Dr. Carlson, Dr. Chang, Dr. Frick, Dr. Owen, and Dr. Tysoe. You pushed me to be the best scientist I could be. Your encouragement and edifying challenges were the source of so much inspiration. I hope I make you proud.

This dissertation is dedicated to all the important people in my life.

To my loving spouse, thank you for being my refuge in the storm. You are the joy of my life and

I love you more every day. May our adventures never cease.

To my daughter, you are my world and my everything. I can't wait to see who you become.

I hope someday you'll read this and know that I wrote it all for you. Never stop learning.

To my parents and brothers, thank you for instilling in me the insatiable thirst for knowledge and the tools to seek it out. Without your constant push to inquire, challenge, and discover the

truths of the world, I would not be who I am today.

To my friends, thank you for helping me become the best version of myself.

“If I have seen further, it is by standing on the shoulders of giants.”

-Isaac Newton

Chapter 1

Introduction and the Einstein-Smoluchowski Equation

1.1 A Personal Anecdote

Some scientists can pinpoint the moment when their unending thirst for knowledge began. For me, it started with a rather simple experiment when I was 8 years old during the classical Parent Career Day. My father, a middle school science teacher, brought a Van de Graaf generator and asked for five volunteers. Due to obvious tongue-in-cheek parental nepotism for this small demonstration, I was part of the small group chosen.

The experiment was as follows: five children all stood in a line on their chairs, holding hands. Due to the rubber soles on our shoes, as well as the plastic seats, we were arguably insulated from the ground. At one end was my father with the Van de Graaf generator and on the other was a girl in my class with 3-foot-long hair. The student at the start of the chain touched the generator, we were all charged with static electricity, and then the entire class all gasped in bewildered excitement as the girl's hair ballooned into a massive sphere as her long hair carried the charge and repelled each other.

Staring at my classmate's hair standing on end brought an incredible number of questions to our minds. Speaking to a class of 2nd graders, my father naturally simplified the explanation as a facet of electricity, to which most of my class nodded and accepted that answer as reasoning enough. Yet it is difficult to explain how disappointed I was with that explanation. If one were to inquire about what makes cars drive, there is a spectrum of answers ranging from "cars run on gasoline" to "a detailed diagram of the internal combustion engine." My father provided the former, I wanted the latter. (To his credit, he did later provide me a detailed diagram of a Van de Graaf generator and dutifully answered all my nagging questions, but this just added more to my curiosity.)

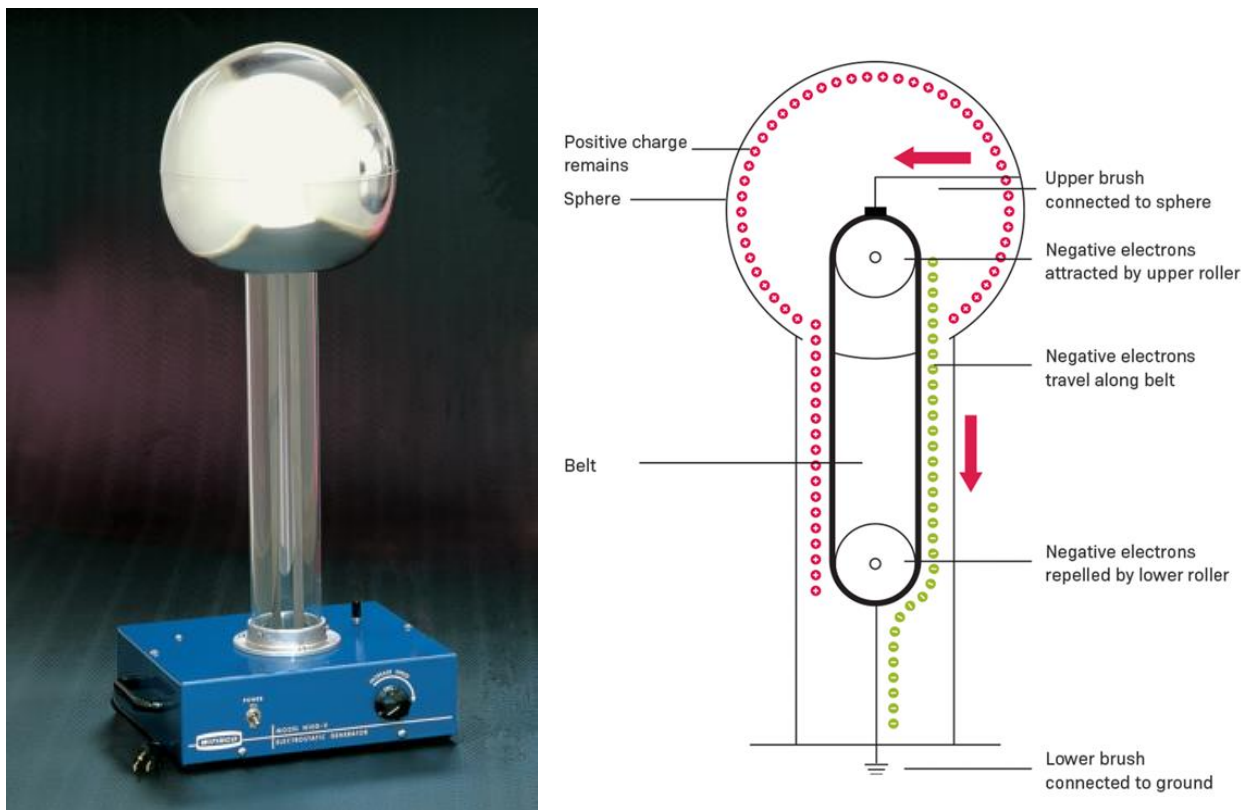


Figure 1.1: (left) Actual image of a Van der Graaf generator sold by Pasco¹, and (right) a depiction of how a Van der Graaf generator gathers and stores electrical charge on a metal sphere by Diyode².

1.2 Dissertation Organization

It is the ultimate goal of this dissertation to leave every reader, regardless of scientific background, with a satisfying understanding of the various details contained within. Walking the fine line between the previously discussed spectrum between “oversimplified” and “pedantic tedium,” it is my honest hope that this dissertation will provide a concise yet detailed account that is applicable to both my fellow scientists as well as the wider public audience. As such, this dissertation largely consists of discussing three core concepts:

1. Creating microfluidic cells for the categorization of specific particle interactions with both nanoscale Brownian motion and the Electric Double Layer (EDL), as inspired by

previous similar work done in the pursuit of slowing or preventing Brownian motion.

2. Theoretical models to determine how an electrolytic solution interacts with a charged surface, both along the surface and throughout the
3. Computational analysis of experimental results; namely fluorescent images of ionic particles interacting with charged surfaces, ideally matching the theoretical models presented.

This dissertation's main focus is on the electric double layer (EDL) theory, which has been very well-developed and theoretically established for over a century but remains relatively poorly understood and relatively unobserved for real-world experiments on nanoscopic ionic particles. The research presented here thus aims to observe the formation and establishment of the EDL in a simple and well-defined system - two plane-parallel metal electrodes with a very dilute electrolyte solution filling the space between them. The electric field was probed by tracking the movement of nanometer-sized and fluorescent spherical particles, which exhibited both Brownian motion and a directed motion in the electric field direction if a field was applied. According to EDL theory, once the double layer has been established, the electric field in the bulk region becomes effectively zero. The results of the research presented in this dissertation show that the electric field did not drop to zero during the expected timeframe of EDL formation, but instead, the directed motion continued for as long as the nanobeads were tracked, in some cases taking several magnitudes longer than any expected value. This finding contradicts current EDL theory, indicating the need for further experimental investigation. Our research also found other unexpected behaviors, such as an apparent rebound effect, which

similarly requires closer investigation in the future to properly isolate and framework the force that causes this occurrence. These results highlight the need for accurate maps of the precise response of charged nanoparticles in an electric field, especially as more scientific progress is made for finite and single-molecule reactions inside microfluidic cells. The use of fluorescent nanoparticles, restricted to two dimensions using a specially constructed microfluidic device, offers a promising method to investigate these curious phenomena.

It is thus necessary to describe the nanoscale realm in which we find ourselves. As such, the rest of Chapter 1 will be dedicated to giving an overview of the history and work behind Brownian motion. Chapter 2 is dedicated to exploring the necessary information regarding electric fields, potential, and charged particles. Chapter 3 will cover the historical models, as well as the current working models, of the electric double layer. Chapter 4 consists of the methods used in exploring the history of microscopes, specifically both the advantages and the severe limitations in analyzing anything below microscopic scales, subpixel localization, as well as the particle-to-pixel discrepancy, particle tracking, and super-resolution microscopy. Considering that our EDL story spans a minimum of two-hundred years, Chapter 5 is dedicated to contemporary research to give us a more modern perspective on how others have used these methods in their research.

Getting to the bulk of my own research, Chapter 6 consist of the methods, materials, and instrumentation used in the experiments, while Chapter 7 will be the initial results and errors that had to be accounted for in the methods, as well as ways in which to overcome the limitations of the microfluidic cell. Chapter 8 is the core of the thesis, with in-depth analysis on the Brownian movements of nanoparticles, extrapolating ballistic components from particle

tracked images, and the resulting implications of the nature of the EDL. Chapter 9 will be the final chapter, dedicated to presenting and understanding the anomalous results and unexpected outcomes, as well as probing the future and presenting possible ideas on where additional research will be needed to complete the detailed map of the EDL.

1.3 Chapter 1 Overview

The rest of this chapter focuses largely on the historical aspects of the study of nanoscale objects and microfluidic solutions, and I include it in my introduction specifically to act as a rough facsimile of the themes of this dissertation: validating observation and theory with precise particle tracking. We will begin with a historical account of Brownian motion: Robert Brown's observations in 1827, Albert Einstein's theoretical model in 1905, and Jean Baptiste Perrin's experimental results in 1908. From there, we will discuss expanding Brownian motion dimensionally, and how ballistic factors have a variable effect on Brownian motion depending on their magnitude.

Before we begin, however, I must make an important declaration: most of the work presented in this thesis comes from a global community of scientists. As such, most of these works are in a foreign language: Brown presented his research in Latin, Einstein's original papers and observations were all in his native German, and Perrin wrote in his native French. While some of you reading this might possibly be able to read and understand English, German, Latin, and French, I've made the executive decision to only use translated titles and texts from here forward for the sake of simplicity and readability.

1.4 Robert Brown and Brownian Motion

Robert Brown, a Scottish botanist and paleobotanist, was not the first pioneer of the microscopic world, but he certainly had a remarkable effect on the totality of biology. While other biologists were interested in large-scale categorization of newer species, Brown was instead interested in the more minute details of already well-known plants^{4,5}. Equipped with his much-admired double-convex single-lens microscope⁶ (“with focal length of about 1/32nd of an inch,” which was the only microscope he used “to give greater consistency to [his] statements,”⁶) he often studied the reproductive traits of living plants or attempted to observe the small structures in fossilized plant-life. Over the course of his multi-decade career as a scientist, he was instrumental in identifying the seed distinctions between cone-bearing plants (gymnosperms) and flowering plants (angiosperms).^{7,8} For his multitude of years of scientific discovery, he was awarded the Copley Medal in 1839.



Figure 1.2: Portrait of Robert Brown by Henry William Pickersgill³

Eventually, he wanted to see if he could make further separations and categorizations of these plants by observing pollen grains suspended on the surface of water. It was his hope to observe the precise mechanism in which male pollen grains and female ovule interact in plant reproduction. It was while observing the *Clarkia pulchella* pollen grains that he made a startling observation: there were small particles within the pollen grains that moved, despite no obvious biological motor⁶. After frequent and repeated observations, he was quite satisfied to declare to himself that these motions were not due to microcurrents in the water or from evaporation, but instead believed that it might possibly be some factor inherent to the pollen itself: Life.

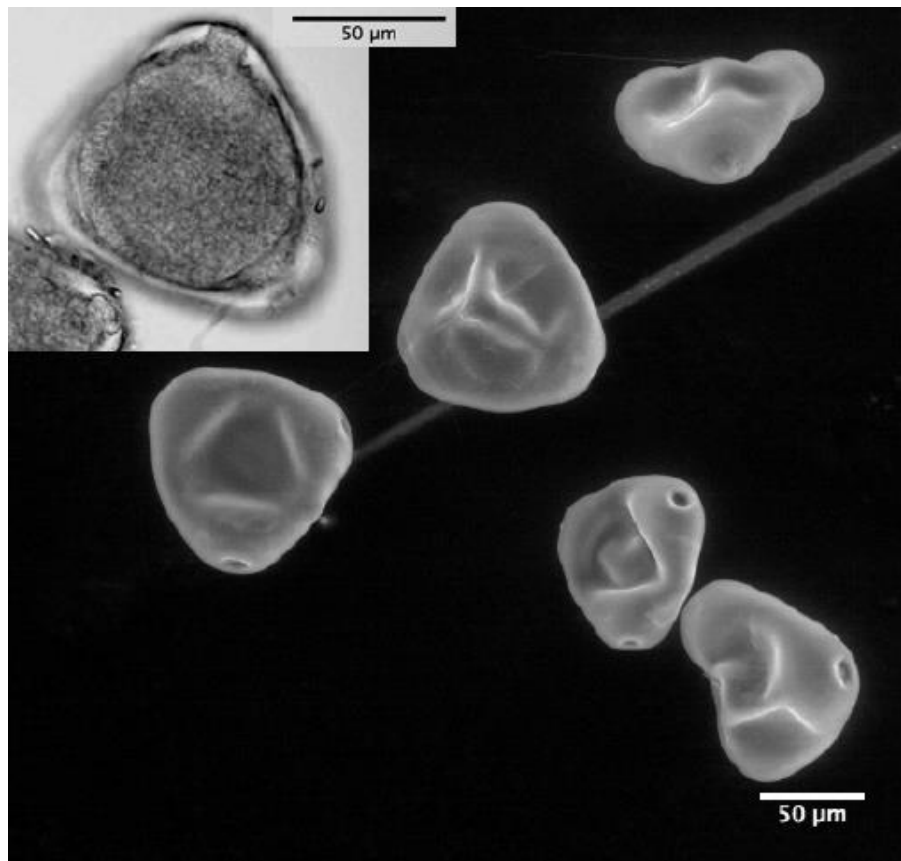


Figure 1.3: *Clarkia pulchella* pollen grains under electron microscope and traditional light microscope (top left)⁹

Being a critical scientist, he worked to verify this as a function of life, dubbed “vitality”⁶. In

his report, *A Brief Account of Microscopical Observations Made in the Months of June, July, and August 1827*, he performed a series of experiments that all sought to establish a root cause of the motion. He took long-dead pollen grains from the genus *Equisteum*, aged and dried for over 100 years, and repeated the experiment. Stunningly, he observed the exact same motions at the exact same magnitude. Thinking that perhaps it was some function of the pollen, he ground up coal and wood fragments to be the roughly the same size as the pollen, but he got the exact same results. Believing that it might be a function of organic matter, he ground up volcanic ash, obsidian, and pumice. Still the motion persisted. At one point, he even used metal powders (as inorganic as one could possibly get) and he still observed the exact same motions. As he presented his findings and investigations, Brown vehemently stated that he had no explanation for the motion; he had exhausted every possible reasoning.

This motion, later named “Brownian motion,” was characterized by the particles moving, rotating, changing direction rapidly, and even bending themselves while under observation, with rapidly changing magnitudes of movement in all directions. There is no immediately apparent rhyme or reason to the movements, and they are almost completely unpredictable as to how they will move, outside of obvious dimensional limitations. This movement is also often referred to as “random walk” motion or even tongue-in-cheek as “drunken sailor” motion.

1.5 Einstein’s Other Paper

In 1905, Albert Einstein wrote several landmark and stunning papers, dubbed the “Annus mirabilis” papers or “The Miracle Year” papers.¹⁰ His first paper, *Concerning an Heuristic Point of View toward the Emission and Transformation of Light*¹¹ delves into Max Planck’s critical

conjecture of the black-body radiation problem and proposes the idea that energy must be emitted in specified and discrete amounts, or quanta. For this paper, he was awarded the Nobel Prize in 1921. Another paper, *On the Electrodynamics of Moving Bodies*¹², delves into the theory of special relativity and that the speed of light must be a constant in all frames of reference. As such, time itself must therefore be referential for the speed of light to remain constant. For this, as well as his first paper, he was awarded the Copley Medal in 1925. In yet another paper, *Does the Inertia of a Body Depend Upon Its Energy Content?*¹³, Einstein systematically and mathematically deduces the relation between energy and mass, $E = mc^2$, which is the foundation for nuclear reaction physics and the equation for which he is most well-known.

As exciting as they are, however, we will not be discussing *any* of those papers.

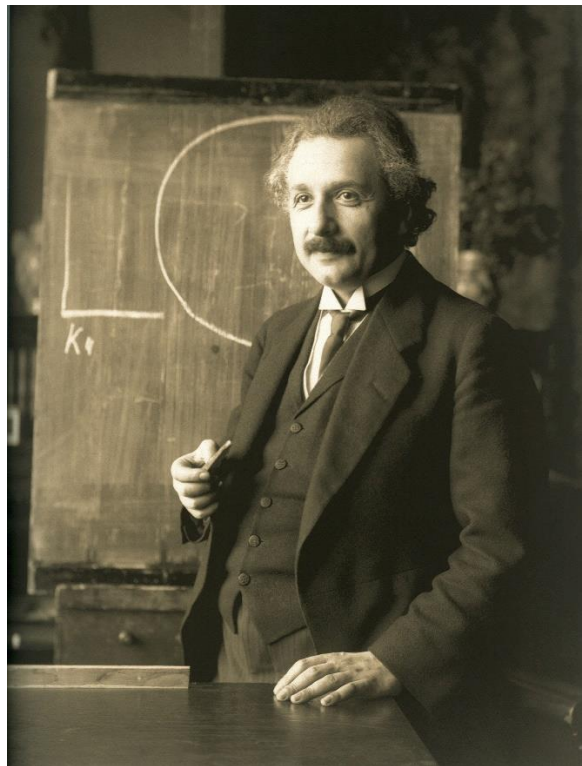


Figure 1.4: Photograph of Albert Einstein in Vienna, 1921, by Ferdinand Schmutzer¹⁴

Instead, we will be focused on the least publicly-known paper: *On the Motion of Small Particles Suspended in a Stationary Liquid, as Required by the Molecular Kinetic Theory of Heat*¹⁵. Before getting into the specifics of this paper, the general premise is quite direct: by taking the kinetic theory of gases and applying the same concepts to the diffusion of small particles in water via osmotic pressure forces, one can sufficiently measure the transfer of kinetic energy as a randomized motion, “identical to so-called Brownian molecular motion.”

In our current scientific climate, it is easy to take for granted how atomic theory is remarkably well-accepted by the public, but just at the start of the 20th century it was an incredibly hotly debated topic among very prominent physical chemists, with notable detractors including Lord Kelvin, Wilhelm Ostwald, Josiah Gibbs, and Max Planck.^{16,17} Atomic theory was useful for estimations, but there had been no tangible proof presented to validate it, so it was little more than well-wishing to many scientists. So, by mathematically tying atomic theory to Brownian motion, Einstein created an avenue for validation. His thought process was remarkably direct: suspended particles in a liquid medium should follow the same physical laws as ideal gas particles, which were well-established at this time. If this were true, then both liquids and gases are formed of similar components: atoms.

1.5.1 Osmotic Pressure Equations

Einstein started with the natural diffusion of dissolved electrolytes in a liquid medium via osmotic pressure, where the osmotic pressure Π of an electrolyte against a semi-permeable membrane is dependent on the partitioned volume V^* , the number of suspended particles n_p , Avogadro’s number N_A , temperature T , and a constant factor of R :

$$\Pi = \frac{RT}{N_A} \left(\frac{n_p}{V^*} \right) \quad (1.1)$$

If you instead suspend large, visible particles, however, there should be no osmotic pressure according to classical thermodynamics, and as the forces of gravity are essentially negligible on the microscopic scale, we can ignore the force of gravity acting upon the liquid. It is here that Einstein makes his first postulate: according to the molecular-kinetic theory of heat, a dissolved non-ionic electrolyte molecule and a suspended uncharged particle are functionally the same and are only differentiated by size.

From this point, we can connect the kinetic theory of heat to the diffusion of small particles. By starting with the amount of free energy in the system E_F , the energy of the system E_S , and the entropy of the system S , we can relate it to an equilibrium position (note the similarity to enthalpy, which wasn't coined until five years later, and Gibbs free energy, which was not widely used until after 1922):

$$\delta E_F = \delta E_S - T \delta S = 0 \quad (1.2)$$

From here, we can relate the free energy of the system to the force acting on a particle K , the number of suspended particles in a certain volume v (equal to n_p/V^* from Equation 1.1), and a finite displacement of the particle x_D .

$$\delta E_S = - \int_0^1 K v x_D dx \quad (1.3)$$

$$\delta S = \int_0^1 \frac{Rv}{N_A} \frac{\partial x_D}{\partial x} dx = - \frac{R}{N_A} \int_0^1 \frac{\partial v}{\partial x} x_D dx \quad (1.4)$$

Solving the integral for x_D and recombining Equations 1.3 and 1.4 back into Equation 1.2 leads to the following equation relating to the force:

$$-Kv + \frac{RT}{N_A} \frac{dv}{dx} = 0 \quad (1.5)$$

1.5.2 Diffusion Equations

If the suspended particles are spheres (or at least rough estimations of spheres), we can directly relate the rate of diffusion of a particle D , the radius of the particle a , the viscosity of the liquid η , the number of particles passing through an area, and the velocity of these particles:

$$\frac{Kv}{6\pi\eta a} = D \frac{\partial v}{\partial x} \quad (1.6)$$

By rearranging this equation, we substitute in the Kv term from Equation 1.5 and solve for diffusion coefficient. This does a massive simplification, removing several complicated variables, showing diffusion is a function of just temperature, particle radius, and viscosity:

$$D = \frac{Kv}{6\pi\eta a} * \frac{\partial x}{\partial v} = \left(\frac{RT}{N_A} \frac{\partial v}{\partial x} \right) \frac{1}{6\pi\eta a} * \frac{\partial x}{\partial v} \quad (1.7)$$

$$D = \frac{RT}{N_A} \frac{1}{6\pi\eta a} \quad (1.8)$$

Taking this a step further, we can relate diffusion to a probability distribution of randomized displacements f over time t :

$$\frac{df}{dt} = D \frac{d^2f}{dx^2} \quad (1.9)$$

$$f(x, t) = \frac{n}{\sqrt{4\pi D}} \frac{e^{-\frac{x^2}{4Dt}}}{\sqrt{t}} \quad (1.10)$$

By solving for a 1-dimensional displacement along the x-axis λ_x , we can then solve for the square root of the arithmetic mean of the square of the displacements:

$$\lambda_x = \sqrt{\langle x^2 \rangle} = \sqrt{2D * t} \quad (1.11)$$

Using the diffusion coefficient term solved earlier, the root-mean-squared (RMS) displacement is dependent on several constant values: particle diameter and viscosity are roughly unchanging values and temperature can easily be held constant in an experiment. This shows that RMS displacement increases with the square root of time:

$$\lambda_x = \sqrt{t} * \sqrt{\frac{RT}{N_A} \frac{1}{3\pi\eta a}} \quad (1.12)$$

1.6 Einstein-Smoluchowski Equation

As Einstein released his paper in 1905, Polish scientist Marian Smoluchowski had been working diligently on his own derivation of Brownian motion. Smoluchowski had been waiting for verifiable results before presenting his article, but became pressured once Einstein broke ground on the subject¹⁸. His submittals are dated just a few months later in 1906, and while they are similar in subject matter and even in conclusion, they greatly vary when it comes to the method.

Whereas Einstein relied on kinetic-molecular theory of gases, Smoluchowski's article, *On the Kinetic Theory of the Brownian Molecular Motion and of Suspensions*¹⁹, instead focused on changes in momentum. Electrolytes move through a medium via random chaotic impacts with the solvent particles, and because both are on the same magnitude of size, these transfers of momentum are large. As such, the particle will move quite dramatically over a set period. For a larger suspended particle, however, the same solvent particles will still impart their momentum, but the large difference in mass between solvent and suspended particle causes

the magnitudes to be far smaller.

It is a common, yet erroneous, assumption that if a particle is being constantly bombarded by solvent molecules, that the sum of these collisions would be null. The error is that randomization will inexorably lead to a non-zero value in individual interactions; the randomized values on one side of the particle will almost certainly either be slightly greater than or slightly less than the other, while the chances of a perfect net zero²¹ will not be true in a more limited timeframe. Or, as Smoluchowski wrote: “This is the same error in reasoning as if a gambler were to believe that he can never lose an amount of money that is greater than the stake of a single throw.”²⁰

Using the analysis as done by Islam²², we can characterize Smoluchowski’s method as follows: the particle in a given timestep should take N steps of a mean free path length of λ_f , of which there are some steps in the positive direction x_+ , and some steps in the negative direction x_- . Unless $x_+ = x_-$ (statistically unlikely for many steps) there will be a dominating factor x_{step} , which determines the distance from the origin x_D .

$$N = x_+ + x_- \quad (1.13)$$

$$x_{dist} = x_{step} \lambda_f = (x_+ - x_-) \lambda_f \quad (1.14)$$

There is thus a probability P_x , that characterizes how far the particle has travelled:

$$P_x = \left(\frac{2}{\pi N} \right)^{\frac{1}{2}} e^{-\frac{x_{step}^2}{2N}} \quad (1.15)$$

By adding in the coefficient of diffusion, we can approach a more uniform equation:

$$D = \frac{N\lambda_f^2}{2t} \quad (1.16)$$

$$P_x = \left(\frac{\lambda_f^2}{\pi Dt} \right)^{\frac{1}{2}} e^{-\frac{x_D^2}{4Dt}} \quad (1.17)$$

Assuming that the value of the mean free path is a constant, this equation can then be integrated to find a mean square distance $\overline{x^2}$ that looks remarkably familiar:

$$dP = \frac{1}{2} \left(\frac{1}{\pi Dt} \right)^{\frac{1}{2}} e^{-\frac{x_D^2}{4Dt}} dx \quad (1.18)$$

$$\overline{x^2} = \frac{\int_0^\infty x_D^2 dP}{\int_0^\infty dP} = 2Dt \quad (1.19)$$

Having derived the exact same equation as Einstein, but via calculations determined by momentum, it further added legitimacy to the model. In fact, Einstein even praised Smoluchowski's method for its "basis on mechanics."²³ This equation, now known as the Einstein-Smoluchowski equation, is the very basis on which we will later expand upon our work.

1.7 Some Enquirer: Jean Baptiste Perrin

As a final point in his paper, Einstein calculated a possible displacement value as a suggested matter of validation. Using water at 17 °C and a particle of diameter of 1 μm, he found that after 1 min the displacement should be about 0.8 μm. In addition, he also suggested that knowing the displacement could also be used to calculate the value of N_A as another method of validating atomic theory. He then finished his paper with a request for help: "It is hoped that some enquirer may succeed shortly in solving the problem suggested here."¹⁵

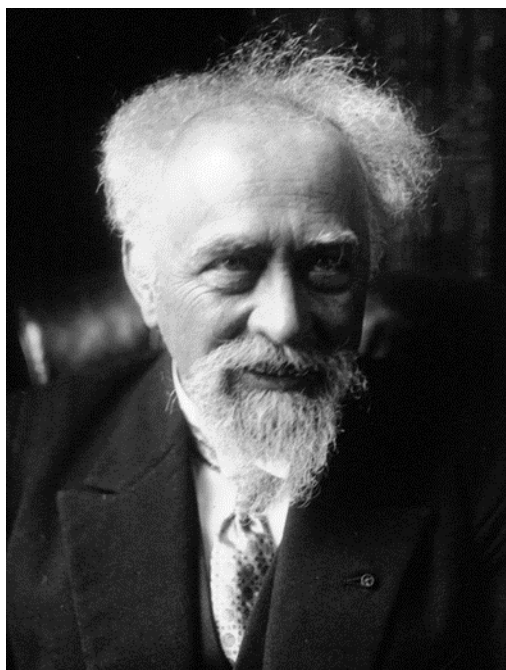


Figure 1.5: Portrait of Jean Baptiste Perrin from 1926²⁴

Four short years later a French physicist, Jean Baptiste Perrin, sought to authenticate this proposed theory suggested by Einstein. Perrin had already established himself as a notable physicist by discovering that cathode rays were negatively charged particles in 1895²⁵, two full years before J. J. Thomson discovered the electron in 1897²⁶. (Note: the reason as to why Thomson is given the credit of the electron instead of Perrin is a technicality. Perrin identified that cathode rays were negative particles, Thomson identified that the rays were negative particles and found their charge-to-mass ratio. It is this writer's opinion that Perrin deserves more credit.)

In Perrin's landmark paper, *Brownian Movement and Molecular Reality*²⁷, he sought to confirm atomic theory via rigorous measurement and direct observations, something that atomic theory was severely lacking at that time: "In brief, the examination of Brownian

movement alone suffices to suggest that every fluid is formed of elastic molecules.”²⁷ His method for doing so was to repeatedly calculate Avogadro’s number, an accreditation that Perrin coined. By connecting a vast myriad of well-accepted scientific theories to the same constant, and then experimentally finding that constant via Brownian motion observations, it provides hard proof that the kinetic molecular theory of heat can be applied to liquids, and thus atomic theory itself is given a vast network of additional proof. To do so, he diligently recorded the precise locations of a colloidal particle as it moved vertically in suspension, and he repeated this methodology over two hundred times with different particles of varying sizes. In addition, using the values he calculated, he was able to follow through with Einstein’s proposal on using a suspended colloidal particle to calculate Avogadro’s number, at the time considered solely a gas constant.

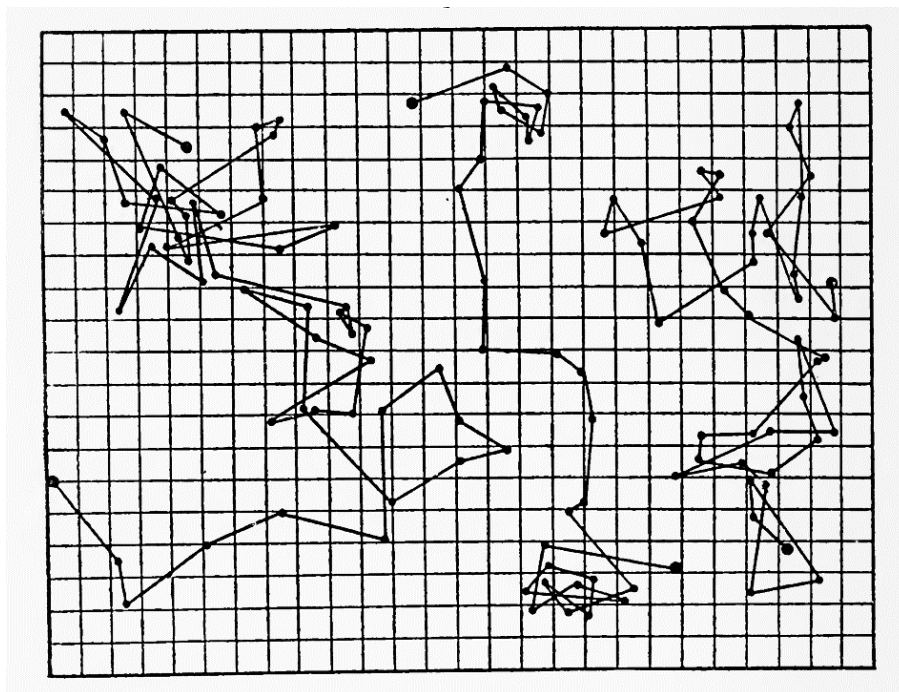


Figure 1.6: Perrin’s hand-drawn paths of three granules of mastic, roughly 1 μm diameter, at 30 second intervals.²⁷

Perrin outright refers to both Einstein's and Smoluchowski's work and does a very detailed breakdown of their parameters for his experiments: Einstein's equation for a specific particle only refers to the size of particle and the mean displacement over time. He verifies that it is independent of mass by using different substances with different densities: granules of gamboge (a pigment obtained from evergreen trees) and mastic (a plant resin obtained from *Pistacia lenticus*). Despite this, consistent with Einstein's estimations, Perrin obtained nearly identical mean displacements. He even repeated the experiments with much larger particles, measuring nearly 50 μm , a fifty-fold increase. This increase in size would naturally produce a smaller Brownian mean displacement, and Perrin found that these results are yet again consistent: an estimated mean displacement of 2.50 μm rather nicely matched his measured displacement of 2.35 μm , even before accounting for various expected errors and difficulties in obtaining ideal solution criteria.

What he found is unsurprising to us now, but at the time was incredible. His results matched Einstein's estimations and his estimate for Avogadro's number was practically a match: between all his experimental calculations, independent of the "mass, density, or nature" of the particle, he found values for N_A between $5.0\text{-}8.0 \times 10^{23}$, with a final estimation of 6.8×10^{23} . At the time, the commonly accepted value was 6.0×10^{23} , as determined by the van der Waals equation.

To say that this paper was influential is an understatement. This paper, as well as Perrin's book *Les Atomes* have been credited by even the most die-hard detractors of atomic theory as the evidence that finally convinced them of its validity, most notably Wilhelm Ostwald^{17,28}. For Perrin's tireless work, he was awarded the Nobel Prize in 1926.²⁵

1.8 Dimensionality and Additive Factors

To finish off this chapter, and to expand briefly upon the Einstein-Smoluchowski equation, we can adapt the Einstein-Smoluchowski equation into more than one dimension²⁹. Thankfully, it does not create an undue burden. If we consider a mean square displacement in three dimensions r^2 , as a function of x - y - z dimensions, and assuming that the diffusion coefficient is isotropic (meaning consistent in all directions) we can come to a general equation where n is the number of dimensions³⁰:

$$r^2 = x^2 + y^2 + z^2 \quad (1.20)$$

$$\langle \Delta r^2(t) \rangle = 2D_x t + 2D_y t + 2D_z t = 2nDt \quad (1.21)$$

This equation can then be further adapted using additional systemic drift factors coming from any number of multiple sources, including but not limited to: temperature gradients creating convection currents, electrical fields inducing electromagnetic forces, organic cellular locomotion, and counteractive frictional forces³¹. By considering the force on an object as the combination of the vectors of all forces, we can create a more general all-encapsulating term for this ballistic motion $V(t)$, that describes these forces as a function of time.

$$\langle \Delta r^2(t) \rangle = 2nDt + \langle V(t)^2 \rangle \quad (1.22)$$

Figure 1.7 shows that there are a few distinctive regions for an isolated particle undergoing some form of ballistic motion. The first region is characterized by the second half of the equation, which dominates over the Brownian factor to such a degree that it is functionally irrelevant. The second region is the diffusion, which follows Einstein's equation of $2Dt$ for a 1-dimensional particle. Finally, the third region, characterizes that if a particle is limited in the

distance it is allowed to travel (eg: an electrostatically trapped or a physically obstructed particle), then there is an upper limit on the particle's long-form displacement.

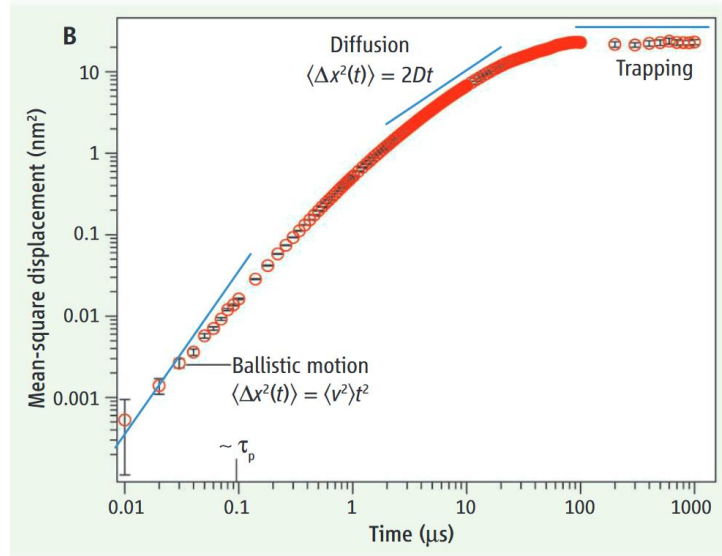


Figure 1.7: Mean square displacement of a 1.0 μm diameter silica sphere in water as it transitioned from ballistic motion to Brownian motion due to confinement factors, measured by Huang et al, with addendums by Pusey.^{32,33}

Specifically, this dissertation seeks to probe the area of ambiguity between the first and second region by using data of a diffusing particle: what if the diffuse and ballistic components are of similar magnitude? Following the full equation, a combination of diffusion and drift will be the basis of much of the work presented later in this dissertation. We will calculate $\langle \Delta r^2(t) \rangle$ and $2nDt$ experimentally to find the sum of ballistic effects, $V(x)$, on a particle and see if they match the theoretical values.

- (1) *Van de Graaff Generator, High Voltage • SE-8691*. PASCO scientific. Reprinted with permission. <https://www.pasco.com/products/lab-apparatus/electricity-and-magnetism/electrostatics-and-electric-fields/se-8691> (accessed 2022-05-31).
- (2) *Super Size Me: Van De Graaf Generator*. Reprinted with permission. https://diyodemag.com/projects/super_size_me_van_de_graaf_generator (accessed 2022-05-31).
- (3) Robert Brown (Botanist, Born 1773). *Wikipedia*; 2022.
- (4) Encyclopaedia Britannica. *Robert Brown | Scottish botanist*. Encyclopedia Britannica. <https://www.britannica.com/biography/Robert-Brown-Scottish-botanist> (accessed 2020-06-23).
- (5) Mabberley, D. J. *Jupiter Botanicus: Robert Brown of the British Museum*; Oxford University Press, 2009.
- (6) Brown, R. XXVII. a Brief Account of Microscopical Observations Made in the Months of June, July and August 1827, on the Particles Contained in the Pollen of Plants; and on the General Existence of Active Molecules in Organic and Inorganic Bodies. *Philos. Mag.* **1828**, 4 (21), 161–173. <https://doi.org/10.1080/14786442808674769>.
- (7) Brown, R. XII. On Some Remarkable Deviations from the Usual Structure of Seeds and Fruits. *Trans. Linn. Soc. Lond.* **1818**, 12, 143–151. <https://doi.org/10.1111/j.1095-8339.1817.tb00224.x>.
- (8) Brown, R. *Prodromus Florae Novae Hollandiae et Insulae Van-Diemen, Exhibens Characteres Plantarum*; Typis R Taylor, veneunt apud J. Johnson: Londini; Vol. 1, pp 1–464.
- (9) Pearle, P.; Bart, K.; Bilderback, D.; Collett, B.; Newman, D.; Samuels, D. S. What Brown Saw and You Can Too. *American Journal of Physics* **2010**, 78. Reprinted with permission (#5532260854885) <https://doi.org/10.1119/1.3475685>.
- (10) Flood, R. Einstein’s Annus Mirabilis, 1905, 2015.
- (11) Einstein, A. Concerning an Heuristic Point of View Toward the Emission and Transformation of Light. *Am. J. Phys.* **1905**, 33 (5).
- (12) Einstein, A. On the Electrodynamics of Moving Bodies. **1905**.
- (13) Einstein, A. Does the Inertia of a Body Depend upon Its Energy-Content?
- (14) Albert Einstein. *Wikipedia*; 2023.
- (15) Einstein, A. Investigations on the Theory of the Brownian Movement. 11.
- (16) Fleck, G. M. Atomism in Late Nineteenth-Century Physical Chemistry. *J. Hist. Ideas* **1963**, 24 (1), 106–114. <https://doi.org/10.2307/2707861>.
- (17) Broda, E. *The Interaction of Boltzmann with Mach, Ostwald and Planck, and His Influence on Nernst and Einstein*. https://inis.iaea.org/collection/NCLCollectionStore/_Public/48/103/48103564.pdf (accessed 2020-06-24).
- (18) Genthon, A. The Concept of Velocity in the History of Brownian Motion -- from Physics to Mathematics and Back. *Eur. Phys. J. H* **2020**, 45 (1), 49–105. <https://doi.org/10.1140/epjh/e2020-10009-8>.

- (19) Smoluchowski, M. von. Zur Kinetischen Theorie Der Brownschen Molekularbewegung Und Der Suspensionen. **1906**, 756–780.
- (20) Smoluchowski, M. On the Kinetic Theory of the Brownian Molecular Motion and of Suspensions. 5.
- (21) Piasecki, J. Centenary of Marian Smoluchowski’s Theory of Brownian Motion. 7.
- (22) Islam, M. A. Einstein–Smoluchowski Diffusion Equation: A Discussion. *Phys. Scr.* **2004**, *70* (2–3), 120–125. <https://doi.org/10.1088/0031-8949/70/2-3/008>.
- (23) *Volume 2: The Swiss Years: Writings, 1900-1909 page 216.*
<https://einsteinpapers.press.princeton.edu/vol2-doc/252> (accessed 2022-06-07).
- (24) Jean Baptiste Perrin. *Wikipedia*; 2022.
- (25) NobelPrize.org. *The Nobel Prize in Physics 1926*. NobelPrize.org.
<https://www.nobelprize.org/prizes/physics/1926/perrin/biographical/> (accessed 2020-06-24).
- (26) Thomson, J. J. *Nobel Lecture: Carriers of Negative Electricity.*
<https://web.lemoyne.edu/~giunta/EA/THOMSONann.HTML> (accessed 2020-06-24).
- (27) Perrin, J. *Brownian Movement and Molecular Reality*. Reprinted with permission (#5532321167494) http://web.mit.edu/swangroup/footer/perrin_bm.pdf (accessed 2020-06-24).
- (28) Schubert, F. E. Perrin’s Experiment Handed Ostwald “Avogadro’s Constant”: He Lauded the Results but Did Not Move to Associate the Number with the Mole Definition. *J. Chem. Educ.* **2020**, *97* (8), 2370–2371. <https://doi.org/10.1021/acs.jchemed.0c00421>.
- (29) Makris, N. Impulse Response Function for Brownian Motion. *Soft Matter* **2021**, *17* (21), 5410–5426. <https://doi.org/10.1039/d1sm00380a>.
- (30) Berg, H. C. Chapter 1. Diffusion: Microscopic Theory. In *Chapter 1. Diffusion: Microscopic Theory*; Princeton University Press, 2018; pp 5–16.
<https://doi.org/10.1515/9781400820023-004>.
- (31) Qian, H.; Sheetz, M. P.; Elson, E. L. Single Particle Tracking. Analysis of Diffusion and Flow in Two-Dimensional Systems. *Biophys. J.* **1991**, *60* (4), 910–921.
[https://doi.org/10.1016/S0006-3495\(91\)82125-7](https://doi.org/10.1016/S0006-3495(91)82125-7).
- (32) Huang, R.; Lukic, B.; Jeney, S.; Florin, E.-L. Direct Observation of Ballistic Brownian Motion on a Single Particle. 23.
- (33) Pusey, P. N. Brownian Motion Goes Ballistic. *Science* **2011**, *332* (6031), 802–803.
<https://doi.org/10.1126/science.1192222>.

Chapter 2

Electric Potential Theory and the Debye Length

2.1. Chapter Overview

This chapter gives a complete overview of the electrical concepts that will be used later in the dissertation. This chapter is specifically presented out of order, with the visualizations presented first, followed by the mathematical formulae that describe these visualizations presented second.

2.2. Electrical Field of a Single Particle

When confronting large, complicated, and multi-faceted systems, it is often best to start at a more basic concept and then build complexity. As such, the simplest geometry for calculating an electric field is a solitary perfectly circular source, with some arbitrary electrical charge. For our purposes, to be consistent with later examples, we will assume that our circular source is negatively charged. This source is arbitrarily set at a radius of 1 nm and a potential of -0.5 V.

To best depict this, we will use the COMSOL¹ Multiphysics program, version 5.5. COMSOL can render any user-created structure and calculate a myriad of properties, including electrostatic fields, fluid flow, heat transfer, structural integrity, acoustics, liquid and gas interactions, and even chemical reactions such as battery discharge, metal deposition, and corrosion. For our purposes, we will only be using the electrostatics module. Each model was user-generated, and the values were indicated on each model. Insofar as accuracy is concerned, these models also match readily available analytical solutions.

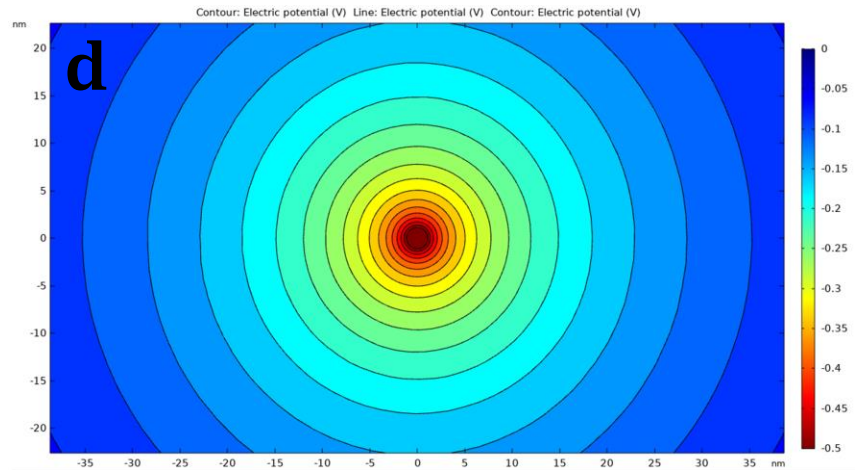
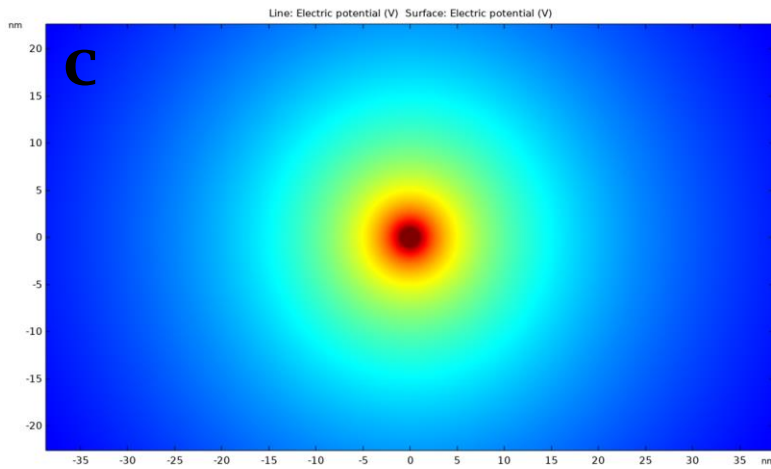
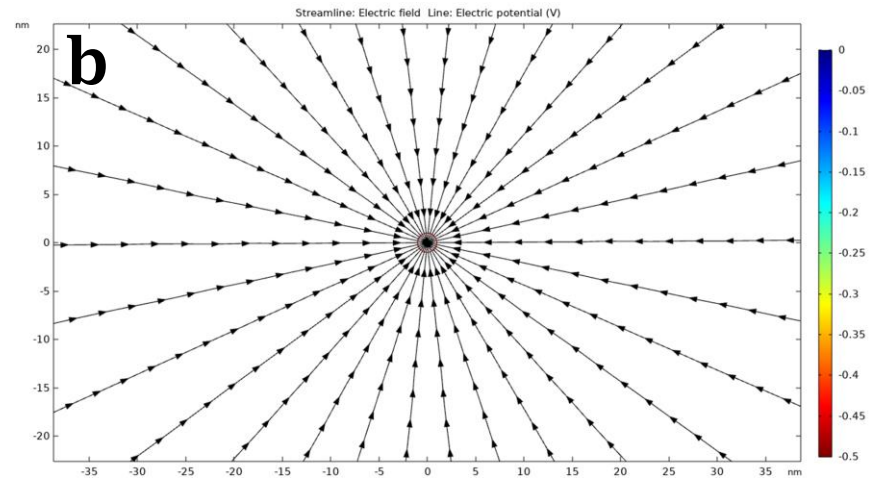
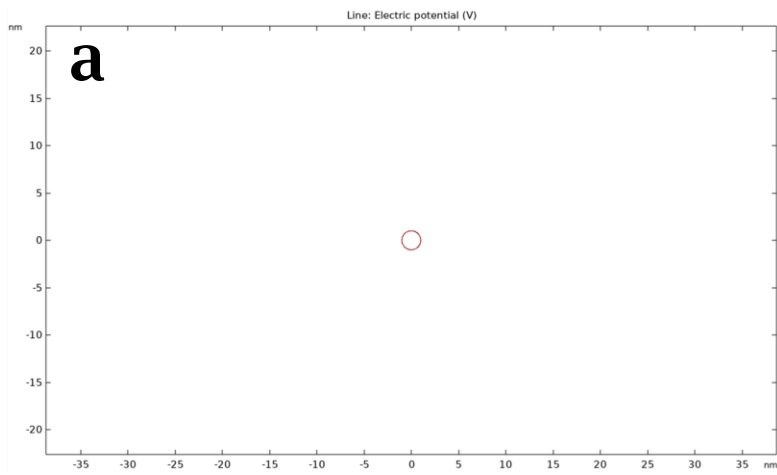


Figure 2.1: COMSOL plots showing: **(a)** the dimension and position of a single circular source at -0.5 V. **(b)** The electrostatic potential shown by their field lines, with arrows along those lines pointing towards negative potential. **(c)** The continuous electric potential generated by the source. **(d)** The same electric field, now segmented into single-color regions, with grey equipotential lines delineating the regions.

Here we can observe three of the different functions that will be relevant to understanding any future models: electrical field lines (Figure 2.1.b), electric potential (Figure 2.1.c), and equipotential lines (Figure 2.1.d). Firstly, the field lines, shown as small black arrowed lines, are defined as the directional force on a positive charge; the arrows always point from-positive-to-negative potential. For our hypothetical negatively charged source, that means that all arrows will point *towards* the negative surface.

The electric potential, emanating from the electrical charge present on the source, radiates outwards from the source: the farther away from the source, the less the electrical field will have influence. This decreasing effect is represented by the colorful spectrum, where red is indicative of negative potential and blue is indicative of relatively positive charge potential. As the distance from the charge source increases, the felt potential decreases according to the spectrum-scale on the right.

Finally, equipotential lines (“equivalent potential”), shown as small grey lines between the different colors, are drawn at the distance from the source where the potential is a constant value. This is a useful method of viewing an electrical field, as it more easily shows whether a change in the field is constant or exponential by seeing whether the equipotential lines are spaced evenly or not. An important note is that these lines are perpendicular to the electric field lines shown in Figure 2.1.b. Secondly, similar to how the electric field arrows are clustered tightly around the source, the equipotential lines are also quite dense near the source, but quickly become farther apart as the distance increases. For example, the equipotential line of -0.45 V (shown as red) is a source very close to the source, while the -0.15 V equipotential line (shown as light blue) is much farther away and much larger. This shows that there is a rapid

decrease in the potential close to the circular source but decreases more slowly in further out areas.

By combining these different concepts, we can form a singular image that imparts all the relevant information. It is important, though, to see how each of these different variables are just a function of the singular electrical field. With just a single solitary circular source, these lines are perfectly symmetrical and extend outwards towards infinity (or an arbitrary zero distance). With the combined image, we can also see how the field lines and the equipotential lines are truly perpendicular to each other. As everything is symmetrical, this means that all field lines are equal in strength and density.

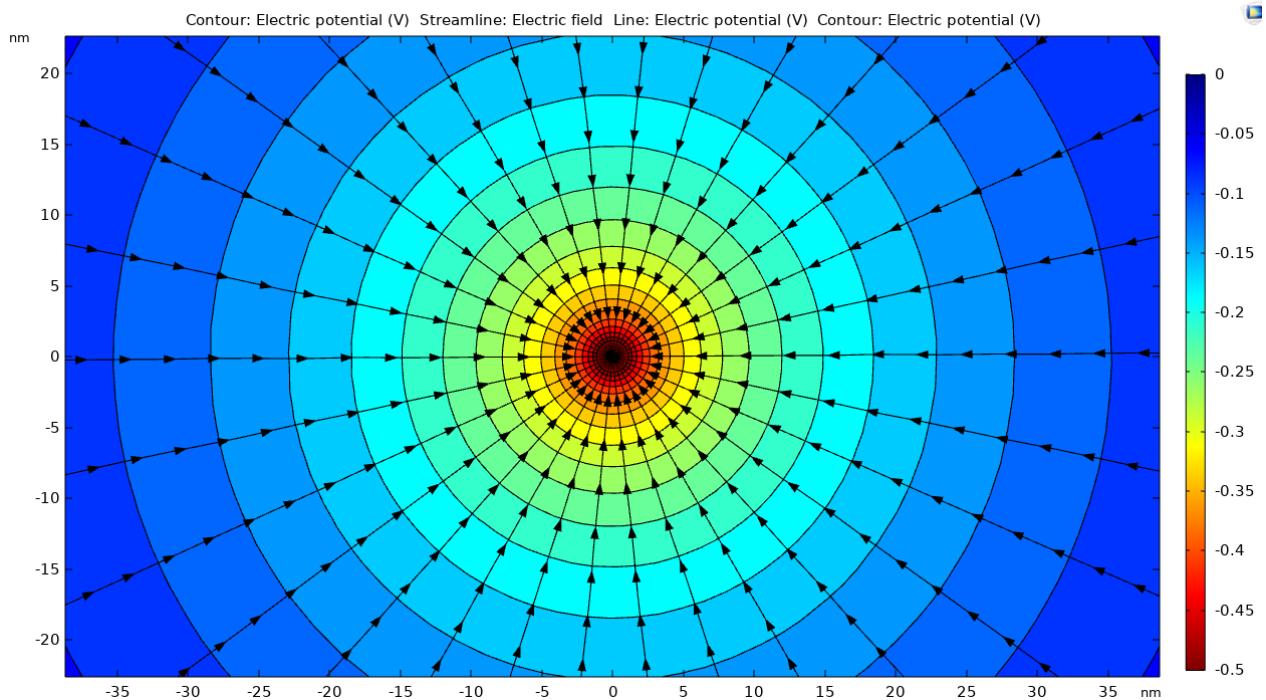


Figure 2.2: COMSOL plot combining equipotential lines, electric potential, and electrostatic field lines.

2.2.1. Electrical Field of a Two Particles

The more interesting phenomenon, of course, is the relation between two objects and their relative charges. For our case, we will now consider our object as a floating particle, the first particle is already set as negatively charged; the other particle can be either positively or negatively charged. Which leaves us with two unique cases we will have to explore: similarly charged or oppositely charged.

For the first case, with similarly charged particles, we can see a departure from the previous case: the field lines no longer radiate outwards evenly in all directions. All the field lines pointed at the other particle curve dramatically away at sharp angles as it progresses. We can partially consider these field lines as the potential direction of movement of the particles: all lines point away from the other particle. Thus, these two particles will repel each other.

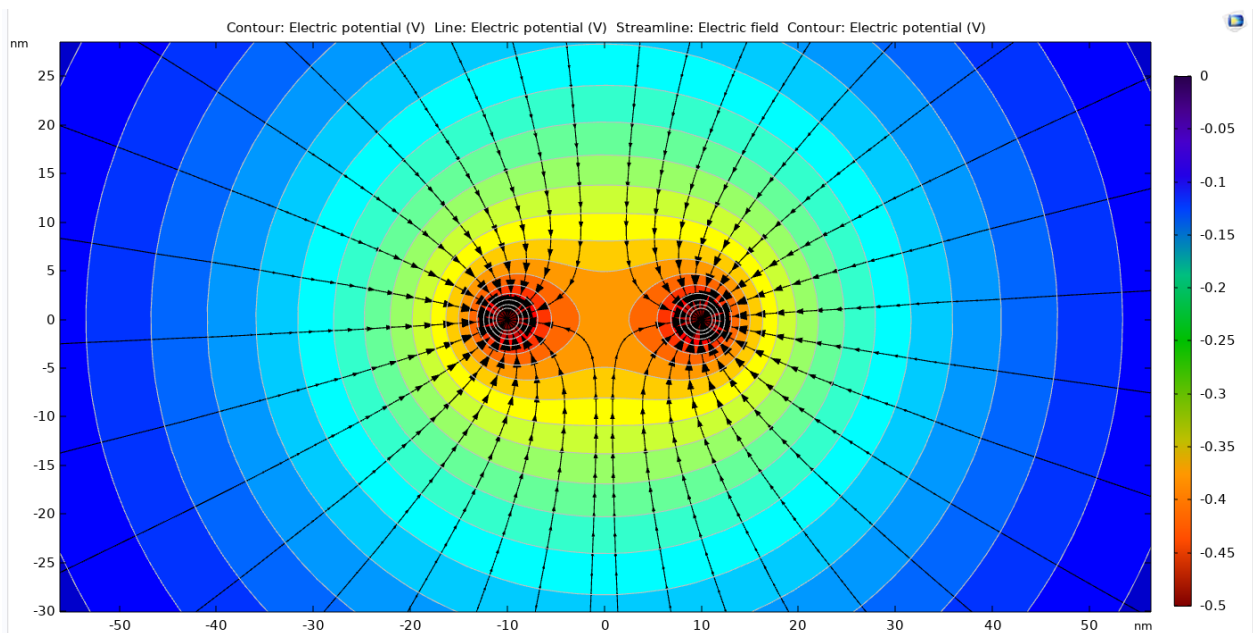


Figure 2.3: COMSOL plot of two negatively charged particles, shown as black circles. Divergent lines show that the particles will repel each other.

The second case, oppositely charged particles, is quite dramatically different. Instead of having the field lines point away from the other particle, now all the field lines must connect to the opposite charge. As seen below, the field lines cluster very tightly in the space between the two particles. If these two particles were allowed to move freely, they would immediately be attracted to each other.

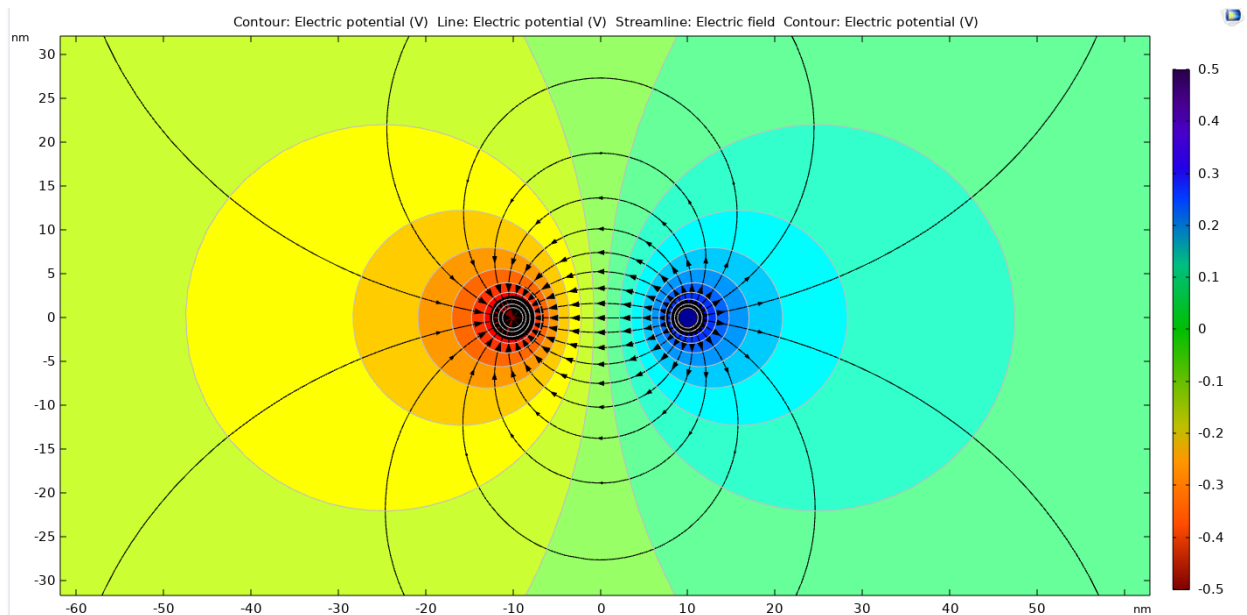


Figure 2.4: COMSOL plot of oppositely charged particles, shown as black circles. Lines connecting the two particles show that the particles will be attracted to each other.

It is from these two examples that we can begin to better our understanding of how particles interact with other charged bodies. In areas of high electrostatic potential change, such as between the two particles, we expect to see a large density of electromagnetic field lines, which in turn implies a stronger attractive force. Similarly, the size of the arrowheads is representative of their relative strength, with the strength of the field rapidly decreasing as the distance to the particles increases.

2.2.2. Electrical Field of a Charged Surface

It is important now that we move away from arbitrarily small, charged particles and begin to transition towards our eventual destination: the field lines of two parallel plates. For the sake of consistency, we will adapt our previous examples one at a time to see how the system changes with each step.

Our first case is replacing our secondary positively charged particle with a positively charged surface, where we can see how the particle is attracted to the surface, with all its field lines bending dramatically towards the surface. Even the field lines that extend from the far-side of the particle all bend towards the conductive surface. Thus, if allowed to move freely, we would expect our negatively charged particle to approach the surface very quickly.

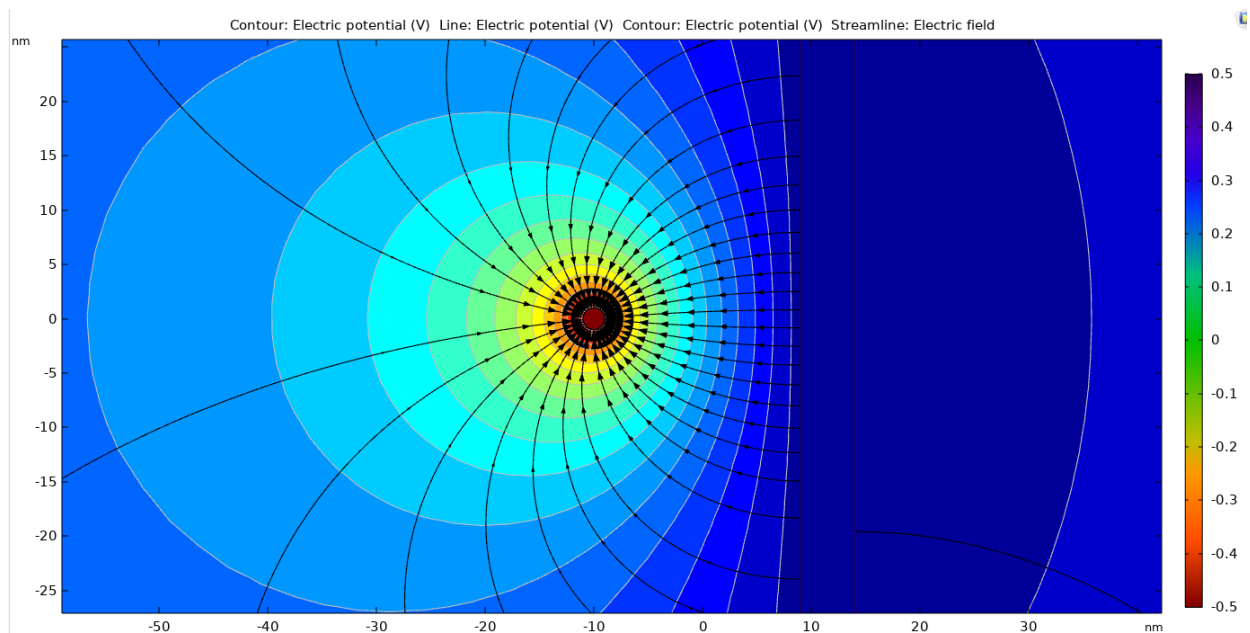


Figure 2.5: COMSOL plot of a negatively charged particle being attracted towards a positively charged plate. The highest density of lines, and the largest arrows, are directly between the particle and the plate.

Otherwise, if the surface is similarly charged as the particle, now the field lines are very much clustered in the opposite direction. This particle will very rapidly be repelled by the surface.

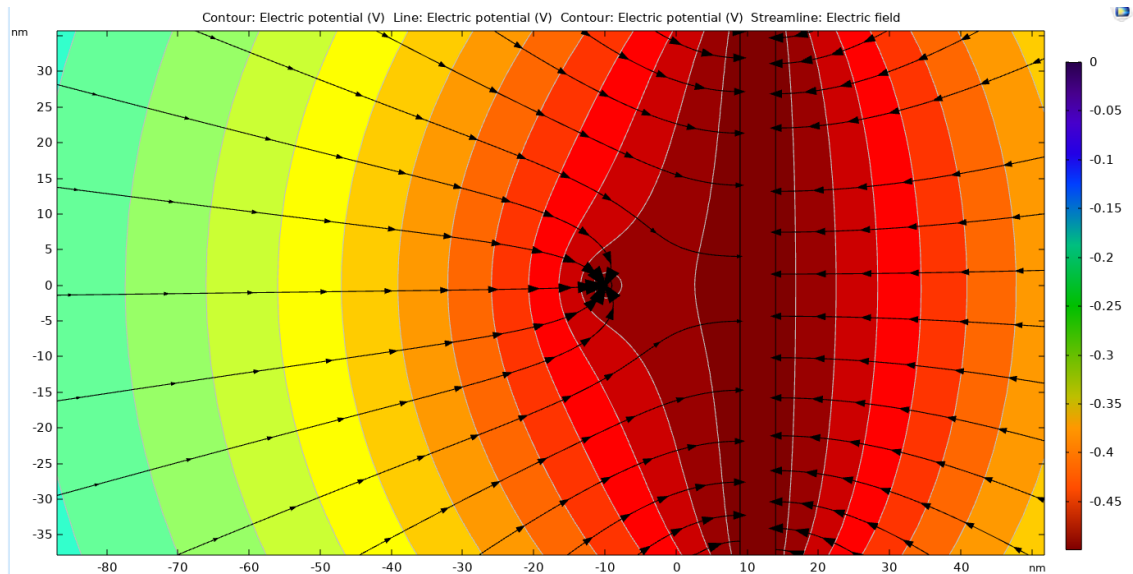


Figure 2.6: COMSOL plot of a negatively charged particle being repelled by a negatively charged plate. None of the lines from the particle ever approach the plate, and instead all move directly away from it.

2.2.3. Electrical Field of Two Parallel Plates

The final theoretical simulation we will be discussing in this section is also the one that will be most vital for our understanding of the experimental results. Namely, two parallel plates at some distance. Whereas before we observed that the radial field lines highlight an exponential increase or decrease in potential, shown by diverging and converging field lines, two parallel conductive plates provide us with a unique situation: a uniform field with a constant rate of change for the potential. Between these two plates, we can observe that the equipotential lines and the field lines are both perfectly straight, forming an even transition. Of course, once we start approaching the top and bottom edges, the field lines begin to bulge outwards similarly to

the two-particle system, and the equipotential lines begin to diverge, and the strength of the field arrows decrease. For an experiment, however, if we limited ourselves to staying within these two plates and didn't approach the edges too much, we could work within the uniform area of the field.

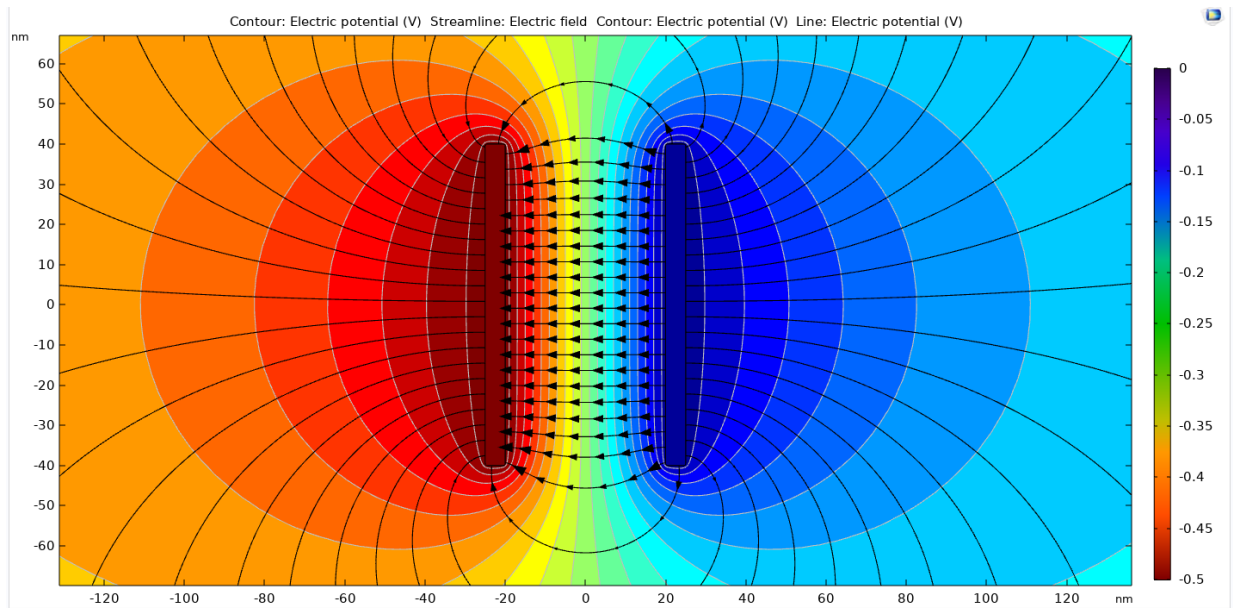


Figure 2.7: COMSOL plot of oppositely charged plates. The electrostatic potential lines between the two plates are parallel and with even strength, the lines near the edges begin to bend and lose strength, and the field lines not between the two plates are very weak.

2.2.4. A Particle Between Two Plates

It is here that we must momentarily depart from these COMSOL simulations, as charting particle trajectories between these two plates becomes more theoretical and less visually interesting: a single suspended particle will have no noticeable effect on the field between the two rigid plates, as they hold several orders of magnitude more charge, and the mobile particle will now move in the direction of the field. Similarly, as soon as there are a sizable number of mobile particles then the calculation of the potential moves quickly into a mathematical time-

based function, as well as becoming dramatically more difficult to chart effectively: the particles will repel each other in addition to being driven by the electric field; summarizing these effects as an electric potential plot is impractical.

As we dig further into the theorems of Helmholtz, Gouy-Chapman, and Stern for Electric Double Layers, it is difficult to present their research as they were originally presented. Due to the subtle changes in mathematical nomenclature over the past 150 years (Helmholtz in particular uses archaic and outdated terminology), we will be using the modern understanding of these classical systems to keep things concise.

2.3. Electrical Field Theory

Before we begin, the following material is considered a fundamental base of electrochemistry, mathematics, and physics, and all of it can be found in various textbooks and papers. For the purposes of this dissertation, and to give proper credit where it is due, we will be loosely following the approach as presented by Dr. John Quine², a professor of Mathematics at Florida State University.

Our starting point in electrostatic equations is also the most fundamental; Coulomb's Law describes the interaction and attraction between a source charge q , and a test charge Q , separated by a particular distance d as a vector directed away from the origin. The force of this interaction \mathbf{F} is given by a vector:

$$\mathbf{F} = \frac{1}{4\pi\epsilon} \frac{qQ}{d^2} \hat{\mathbf{d}} \quad (2.1)$$

The factor of $1/4\pi\epsilon$ is a conversion factor for our modernized standardized units, with ϵ as the permittivity for the medium (in this case, a vacuum). To describe this in practical terms, we can

envison this as the two-particle system described earlier where if the charges are oppositely charged, they'll be attracted, but if they're the same charge then they'll be repelled. If we increase the distance between these two particles dramatically, the force of the attraction decreases not linearly, but with the square of the distance between them.

By defining the electric field \mathbf{E} as being a function of the source charge, we can then simplify the force of attraction as the electric field acting on the unit charge:

$$\mathbf{E} = \frac{1}{4\pi\epsilon} \frac{q}{d^2} \hat{\mathbf{d}} \quad (2.2)$$

$$\mathbf{F} = Q\mathbf{E} \quad (2.3)$$

Similarly, we can derive the potential energy of the system U_{pot} , as a function of the electrostatic potential energy φ :

$$U_{pot} = \frac{1}{4\pi\epsilon} \frac{qQ}{d} \quad (2.4)$$

$$\varphi = \frac{1}{4\pi\epsilon} \frac{q}{d} \quad (2.5)$$

$$U_{pot} = Q\varphi \quad (2.6)$$

While Equation 2.2 and 2.4 might look similar, there is not a distance term in the denominator. In fact, the electrostatic force is the negative vector derivative of the potential energy:

$$\mathbf{F} = -\nabla U_{pot} \quad (2.7)$$

Where ∇ is the del operator, the derivative function in three dimensions and often known as the gradient of a field. This allows us to directly relate the electric field as the gradient of the electrostatic potential energy:

$$\mathbf{F} = Q\mathbf{E} = -\nabla U_{pot} = -Q\nabla\phi \quad (2.8)$$

$$\mathbf{E} = -\nabla\phi \quad (2.9)$$

In simpler terms, this means we have effectively removed the charge Q of our target particle from our calculation, and thus can instead simply concern ourselves with the electronic potential applied to our system. This will be useful for our system of two parallel metal plates with some applied potential, leading to a uniform electrostatic field between the two plates. However, we still have more to do before we can apply values to this system.

2.4. Gauss's Law and Poisson Equation

To evaluate the characteristics of this electrostatic potential and field, it is going to be impractical to count the vast number of charges aligned along the metal surface. The calculations work for a few single particles, but definitely not for the quintillion particles in our system. So, having removed the test charge, we must now endeavor to remove the surface charge q .

Our way forward is using Gauss's Law, which measures the flux of an electrostatic field. Flux is the net amount of electrostatic field that emanates from some specific volume occupied by a closed surface. We can visualize this as one of two possibilities: the field's source is inside or outside the closed surface. In our case, let us use the electric field lines emanating from a single particle, as discussed earlier in this chapter. We will consider two shapes: a red surface that does not contain the source and a blue surface that does. For every field line entering the surface, there is an equivalent line leaving the surface. Therefore, the overall net flux is zero. But for the blue surface, every single field line enters the surface, with none exiting the surface.

Thus, the overall net flux is determined exactly by the field.

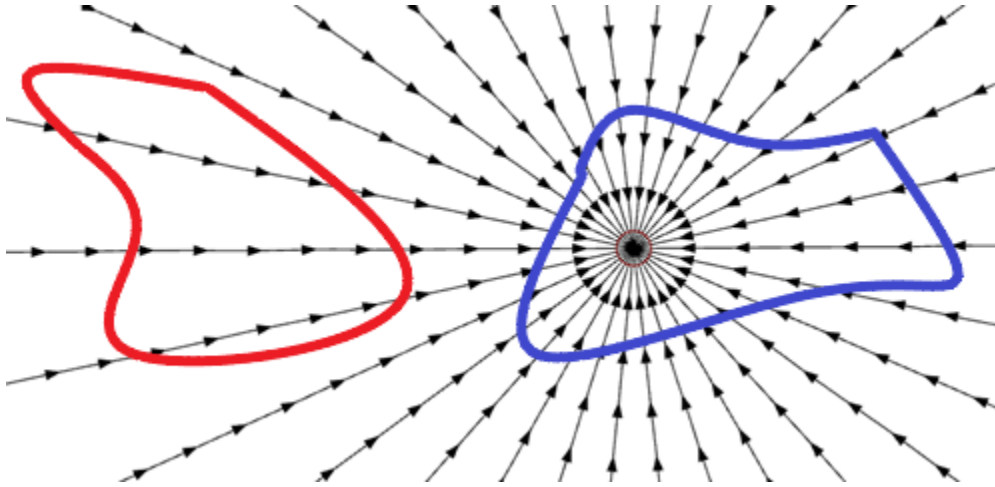


Figure 2.8: Two curves highlighting the difference in flux. The electrostatic field lines (black arrows) radiate from the particle. The blue surface encapsulates the particle, while the red surface does not.

We can describe this mathematically, converting briefly from Cartesian distance d to spherical coordinate distance r , as:

$$\oint_S \mathbf{E} * \mathbf{d}\mathbf{a} = \oint_S \frac{1}{4\pi\epsilon} \frac{q}{r^2} \hat{\mathbf{r}} \mathbf{d}\mathbf{a} \quad (2.10)$$

$$\mathbf{d}\mathbf{a} = r^2 \sin \theta \, d\theta \, d\varphi \hat{\mathbf{r}} \quad (2.11)$$

$$\oint_S \mathbf{E} * \mathbf{d}\mathbf{a} = \frac{q_{encl}}{4\pi\epsilon} \oint_S \sin \theta \, d\theta \, d\varphi = \frac{q_{encl}}{4\pi\epsilon} \int_0^\pi \sin \theta \, d\theta \int_0^{2\pi} d\varphi \quad (2.12)$$

The integral uses $\mathbf{d}\mathbf{a}$, a vector factor normal to the surface of our enclosed surface and directed outwards, and the enclosed charge q_{encl} , which can be a single charge or a multitude of charges in a specific volume. By converting both E and $d\mathbf{a}$ to a spherical coordinate system, we can simplify the integral considerably: the integrals of $\sin \theta \, d\theta$ and $d\varphi$ can be solved mathematically as 2 and 2π respectively, which results in an elegant formula:

$$\oint_S \mathbf{E} * d\mathbf{a} = \frac{q_{encl}}{\epsilon} \quad (2.13)$$

For sufficiently large quantities, we can characterize this as a function of volume V_t , an infinitesimal volume element $d\tau$, and most crucially the charge density ρ .

$$q_{encl} = \int_{V_t} \rho d\tau \quad (2.14)$$

By then combining this with the previous equation with the divergence theorem, we obtain our final goal:

$$\oint_S \mathbf{E} * d\mathbf{a} = \int_V (\nabla \cdot \mathbf{E}) d\tau \quad (2.15)$$

$$\oint_S \mathbf{E} * d\mathbf{a} = \int_V \frac{\rho}{\epsilon} d\tau \quad (2.16)$$

$$\nabla \cdot \mathbf{E} = \frac{\rho}{\epsilon} \quad (2.17)$$

In summation, the gradient of the electric field is proportional to the charge density of the system. By combining this with our understanding of the electrostatic potential and substituting in the permittivity of free space ϵ_0 and the permittivity of the medium ϵ_r for permittivity, we can now relate our electrostatic potential to a quantity that does not rely on a specific number of charges. This results in the Poisson Equation³:

$$\epsilon = \epsilon_r \epsilon_0 \quad (2.18)$$

$$-\frac{\rho}{\epsilon_r \epsilon_0} = -\nabla \cdot \mathbf{E} = \nabla^2 \phi \quad (2.19)$$

2.5. Parallel Plate Capacitor

With our nanoscale understanding established, let us momentarily consider the macro level. Specifically, a parallel plate capacitor can be imagined initially as two metal plates separated by some distance and with an overlapping area of effect A :

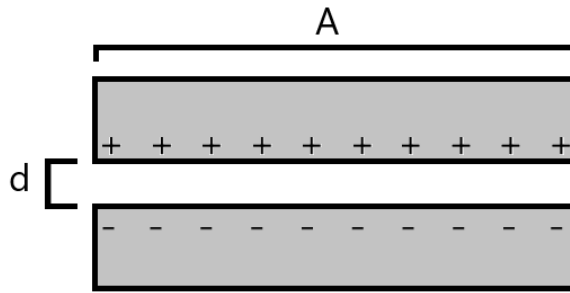


Figure 2.9: Two electrodes (grey) set apart at a particular distance, d , with an overlapping area, A . Charges can be seen along the surface of each electrode, denoted by (+/-) signs.

For this capacitor, with the capacitance of the plate C , the permittivity of the medium (i.e. water) between the two plates, and the permittivity of free space:

$$C = \left(\frac{\epsilon_r \epsilon_0}{d} \right) * A \quad (2.20)$$

From here, with the capacitance also equal to the charge per applied voltage V_q , which can then be related to the surface charge density of the surface σ as being a charge per unit area:

$$C = \frac{q}{V_q} \quad \sigma = \frac{q}{A} \quad (2.21)$$

$$\frac{C}{A} = \frac{q}{V_q A} = \frac{\sigma}{V_q} = \frac{\epsilon_r \epsilon_0}{d} \quad (2.22)$$

With a rearrangement of Equation 2.22, we can obtain a relation between the surface charge density as a function of the voltage per unit distance:

$$\frac{V_q}{d} = \frac{\sigma}{\epsilon_r \epsilon_0} \quad (2.23)$$

In other words, as the distance between the two plates increases, the charge density of the surface will decrease.

2.6. Poisson-Boltzmann Equation

Another model we will be using in Chapter 3 depicts exponential decrease in charge density of a suspension of point charges. We can characterize⁴ the relative concentrations of these charges by their distance from the electrode as a Boltzmann-Maxwell^{5,6} distribution. We can start with considering a specific ion species which has a number of ions in a particular space n_i , which can be described as a function of the total number of ions in the bulk solution n_0 , the charge number z_i , the potential acting on those ions φ_i , the elementary unit charge e_0 , the Boltzmann constant k_B , and temperature:

$$n_i = n_0 e^{-\frac{z_i e_0 \varphi_i}{k_B T}} \quad (2.24)$$

This can then be further refined by considering the total free charge density to be a collection of all ions:

$$\rho(x) = \sum_i z_i e_0 (n_i) = \sum_i z_i e_0 \left(n_0 e^{-\frac{z_i e_0 \varphi_i}{k_B T}} \right) \quad (2.25)$$

This can then be simplified further by first using a property of derivatives, where W is an arbitrary constant:

$$\frac{d}{dx} \left[\left(\frac{d\varphi}{dx} \right)^2 + W \right] = 2 \frac{d\varphi}{dx} \left(\frac{d^2\varphi}{dx^2} \right) \quad (2.26)$$

$$\frac{d^2\varphi}{dx^2} = \frac{1}{2} \frac{d}{d\varphi} \left[\left(\frac{d\varphi}{dx} \right)^2 + W \right] \quad (2.27)$$

By then combining a one-dimensional version of Equation 2.19 with 2.25, and inserting it into

Equation 2.27, we can reduce this down to a first-order differential equation:

$$\frac{d^2\varphi}{dx^2} = -\frac{1}{\varepsilon_r \varepsilon_0} \rho(x) = -\frac{1}{\varepsilon_r \varepsilon_0} \sum_i z_i e_0 \left(n_0 e^{-\frac{z_i e_0 \varphi_i}{k_B T}} \right) \quad (2.28)$$

$$d \left[\left(\frac{d\varphi}{dx} \right)^2 + W \right] = -2 \frac{e_0}{\varepsilon_r \varepsilon_0} \sum_i z_i \left(n_0 e^{-\frac{z_i e_0 \varphi_i}{k_B T}} \right) d\varphi \quad (2.29)$$

By integrating Equation 2.29, selecting the specific bounds in 1-dimension, where at x , $\varphi_i =$

φ , $(d\varphi_i/dx) = (d\varphi/dx)$ and when at ∞ , $\varphi_i = 0$, and $(d\varphi_i/dx) = 0$

$$\int_x^\infty d \left[\left(\frac{d\varphi}{dx} \right)^2 + W \right] = \int_x^\infty -2 \frac{e_0}{\varepsilon_r \varepsilon_0} \sum_i z_i \left(n_0 e^{-\frac{z_i e_0 \varphi_i}{k_B T}} \right) d\varphi \quad (2.30)$$

$$\left(\frac{d\varphi}{dx} \right)^2 = \frac{2k_B T}{\varepsilon_r \varepsilon_0} \sum_i n_0 \left(e^{-\frac{z_i e_0 \varphi_i}{k_B T}} - 1 \right) \quad (2.31)$$

$$\frac{d\varphi}{dx} = \left(\frac{2k_B T n_0}{\varepsilon_r \varepsilon_0} \right)^{\frac{1}{2}} \left(e^{\frac{z_i e_0 \varphi_i}{2k_B T}} - e^{-\frac{z_i e_0 \varphi_i}{2k_B T}} \right) \quad (2.32)$$

We can also use the hyperbolic sine function definition to finally obtain a differential equation

that will help us make estimates for our systems:

$$\sinh(x) \equiv \frac{1}{2} (e^x - e^{-x}) \quad (2.33)$$

$$\frac{d\varphi}{dx} = \left(\frac{8k_B T n_0}{\varepsilon_r \varepsilon_0} \right)^{\frac{1}{2}} \sinh \left(\frac{z e_0 \varphi_i}{2k_B T} \right) \quad (2.34)$$

2.7. Debye-Hückel Theory

While the previous equation might seem complicated, it is effectively a whole series of constants multiplied by a *sinh* function. If we can estimate this the function, we will have a very direct and solvable value. Our estimation is going to be that if the electrostatic energy is much smaller than thermal energy, then $\sinh(x)$ can be approximated as x . By setting all our constants equal to a singular constant, the Debye screening vector κ , this means that we can find that the gradient of the potential is equal to a series of constants multiplied by that field:

$$\text{estimate: } \frac{d\varphi}{dx} = \left(\frac{2n_0 z_i^2 e_0^2}{k_B T \epsilon_r \epsilon_0} \right)^{\frac{1}{2}} \varphi_i \quad (2.35)$$

$$\kappa = \left(\frac{2n_0 z_i^2 e_0^2}{k_B T \epsilon_r \epsilon_0} \right)^{\frac{1}{2}} \quad (2.36)$$

$$\frac{d\varphi}{dx} = \kappa \varphi \quad (2.37)$$

This constant is most often seen inverted and referred to as the Debye Length λ_D

$$\lambda_D = \kappa^{-1} = \left(\frac{k_B T \epsilon_r \epsilon_0}{2n_0 z_i^2 e_0^2} \right)^{\frac{1}{2}} \quad (2.38)$$

By inputting a series of constants, we can finally have a single set value for this distance⁷.

Noting that the number of ions is a function of the concentration c , that $n_0 = c * N_A$, we can find that if we use a 10^{-4} M aqueous solution of a 1:1 electrolyte at 20 °C, and assuming the dielectric constant of the solution is roughly equal to water, 80.1, we obtain a Debye length of 30.5 nm. As we will discuss in the next chapter, this length is a characteristic of the exponential decrease, and is essential to our understanding of how the electric potential decreases over distance; after every Debye length^{8,9}, the potential has decreased by a factor of $1/e$, or 36.8%.

After 5 Debye lengths, it would be $1/e^5$ or 0.67% of the original potential, which is roughly where the field is considered to have dissipated and the bulk of the solution where the concentration is back to the rough average.

2.8. Dielectrophoretic Forces

Having completed the brief summation of forces relevant towards understanding the EDL, it is here that we make a small departure into non-uniform electric fields. While not necessary for later chapters, dielectrophoresis (DEP) is a force-effect that can have strong effects on a suspended particle, and it is thus vital to understand and limit DEP as much as possible.

Dielectrophoresis is a resultant force that occurs in non-uniform electrostatic fields, where there is an observed motion either towards (positive) or away from (negative) that area with a larger change in potential, easily recognized by a higher concentration of field lines.

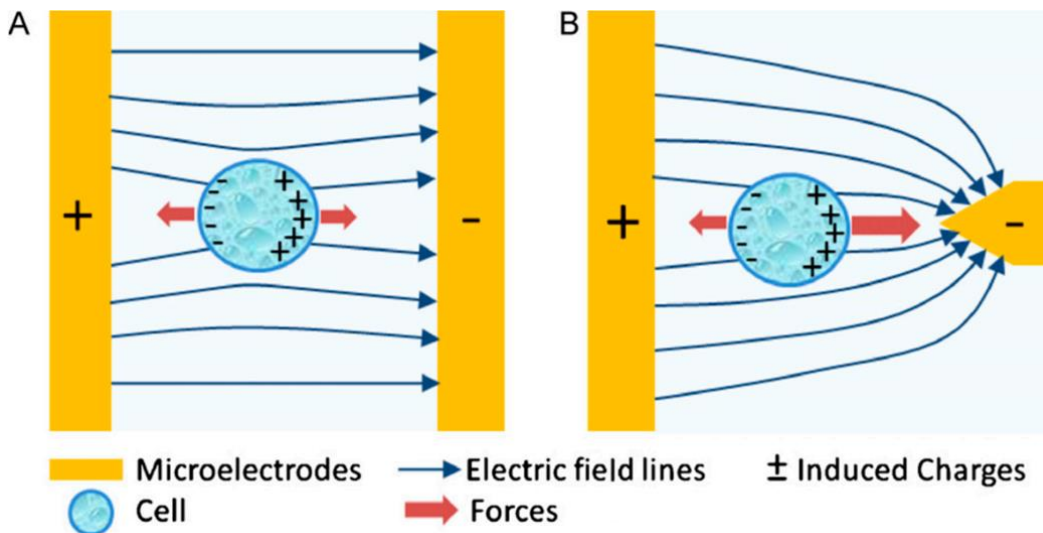


Figure 2.10: Diagram of positive-DEP by Khoshmanesh et al.^{10,11} of an electric field acting on a neutral, but polarizable, cell. **A)** Uniform symmetrical fields induce equivalent DEP-forces, thus having a net zero effect. **B)** Non-uniform fields have non-equivalent forces. For positive-DEP, this means moving towards the maximum field.

The largest determining factor for DEP is the relational permittivity between the particle and the medium, also known as the Clausius-Mossotti factor¹¹, $CM(f)$, shown here where ϵ_m^* is the complex permittivity of the medium and ϵ_p^* is the complex permittivity of the particle, σ_p and σ_m are the electrical conductivities, f_E is the frequency of the electric field, and i is the imaginary constant equal to $\sqrt{-1}$. The complex permittivity, as opposed to relative permittivity, includes an additional factor for heat loss through dissipation.

$$\epsilon_p^* = \epsilon_0 \epsilon_p + i \frac{\sigma_p}{\pi f_E} \qquad \epsilon_m^* = \epsilon_0 \epsilon_m + i \frac{\sigma_m}{\pi f_E} \qquad (2.39)$$

$$CM(f) = \frac{\epsilon_p^* - \epsilon_m^*}{\epsilon_p^* + 2\epsilon_m^*} \qquad (2.40)$$

The Clausius-Mossotti factor is a way of describing if the particle or the medium is more polarizable: if the particle has a higher polarizability, then it will be more strongly affected by the non-uniformity of the field and will thus move towards the maximum electric field. If the particle and the medium are equal, this factor equals zero, and thus the DEP force trends towards zero. The strangest case is negative dielectrophoresis: if the medium is more polarizable than the particle, then the particle will shift away from higher field density. We typically only observe the movement of the particle, and it is often difficult to directly observe the medium's response, but essentially it is the medium itself that is pushing the particle further away.

To put this in more layperson terms, a visual example helps to clarify: imagine for a moment a single particle floating in water. If an electric potential is applied to a distant asymmetrical electrode, both the water and the particle are attracted to it. In the simplest case, positive DEP, if the particle is more polarizable by the field, it will have a greater attraction to the electrode

and will push past the solvent. If the water is more polarizable, however, then the opposite occurs: the water pushes past the particle as it is more attracted to the electrode. As the water continually pushes in front of the particle, the particle is effectively “repelled” from the electrode, despite not being repulsed from it. Thus, dielectrophoretic forces are not directly an attractive/repulsive effect, but instead the difference between two attractive values.

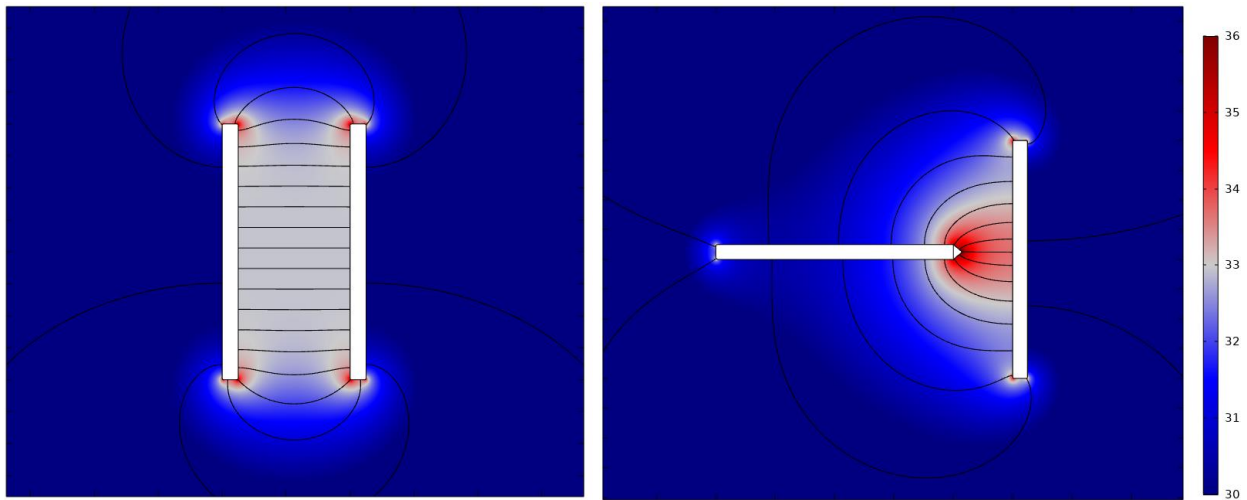


Figure 2.11: COMSOL plots of the dielectrophoretic potential of two electrode setups, **(left)** uniform field between two electrode plates and **(right)** non-uniform field. In both cases, the red region signifies high dielectrophoretic potential, while the lines show the electrostatic potential.

To return to the COMSOL calculations from earlier in the chapter, as seen in Figures 2.1 to 2.7, the classification of the electrostatic potential as uniform or non-uniform has a dramatic effect on the dielectrophoretic potential. Dielectrophoresis occurs when there is a notable gradient, with positive dielectrophoresis pushing particles towards red sections, and negative dielectrophoresis pushing particles towards blue. However, when the field is uniform the gradient effect is negligible and thus DEP has almost zero effect, as seen by the constant grey region between the plates. In non-uniform fields there are no large stable zones of a constant

DEP potential^{12,13}.

With the understanding of how the Clausius-Mossotti factor functions, we can then take this one step further to find the magnitude of this force effect¹⁴, \mathbf{F}_{DEP} . We can take the real part of the complex Clausius-Mossotti factor, $Re[CM(f)]$, and the three-dimensional derivative of the square of the root-mean-squared value of the applied electric field, $\nabla \mathbf{E}_{RMS}^2$, we can come to the following equation for spherical dielectric particles:

$$\mathbf{F}_{DEP} = 2\pi\epsilon_m\epsilon_0r^3 \cdot Re[CM(f)] \cdot \nabla \mathbf{E}_{RMS}^2 \quad (2.41)$$

As our goal is to eliminate dielectrophoresis, there are three methods that this can be reduced as much as possible: modifying the radius, relative permittivity, and the electric field. If the volume is minimized, then the polarity of the particle becomes less and less of a factor: a small particle will have a smaller separation of its similarly reduced charge. If the complex permittivities of the medium and the particle are the same, then the CM factor trends to zero as $(\epsilon_p^* - \epsilon_m^*)$ effectively becomes zero. And finally, if the electrical field is uniform and parallel, then the derivative of this linear function becomes zero. As controlling the permittivity of a particle is difficult, the research presented later in this dissertation will focus on the other two factors: small particle volume and ensuring a uniform electric field.

- (1) COMSOL Multiphysics® Software - Understand, Predict, and Optimize. COMSOL. <https://www.comsol.com/comsol-multiphysics> (accessed 2022-06-14).
- (2) Quine, J. *Poisson-Boltzmann Summary*. <https://www.math.fsu.edu/~quine/biotopics07/PB.pdf> (accessed 2021-10-27).
- (3) Poisson, S. D. *Mémoire sur la théorie du magnétisme en mouvement; par M. Poisson. Lu à l'Académie des Sciences, le 10 juillet 1826; 1826.*
- (4) Woehl, J. C. A Guide to Electrostatic Potential Calculations in Dielectrics and Electrolyte Solutions.
- (5) Uffink, J. Boltzmann's Work in Statistical Physics. In *The Stanford Encyclopedia of Philosophy*; Zalta, E. N., Ed.; Metaphysics Research Lab, Stanford University, 2022.
- (6) Pham, P.; Howorth, M.; Planat-Chrétien, A.; Tardu, S. Numerical Simulation of the Electrical Double Layer Based on the Poisson-Boltzmann Models for AC Electroosmosis Flows. **2007**, 10.
- (7) Butt, H.-J.; Graf, K.; Kappl, M. *Physics and Chemistry of Interfaces*. 376.
- (8) Debye, P.; Huckel, E. *Zur Theorie Der Elektrolyte. I. Gefrierpunktserniedrigung Und Verwandte Erscheinungen; 1923; Vol. 24.*
- (9) Braus, M. The Theory of Electrolytes. I. Freezing Point Depression and Related Phenomena (Translation). *Zur Theorie der Elektrolyte. I. Gefrierpunktserniedrigung und verwandte Erscheinungen* **2019**.
- (10) Koslover, E.; Chan, C.; Theriot, J. *Disentangling Random Motion and Flow in a Complex Medium | Elsevier Enhanced Reader*. <https://doi.org/10.1016/j.bpj.2015.11.008>.
- (11) Zhang, H.; Chang, H.; Neuzil, P. DEP-on-a-Chip: Dielectrophoresis Applied to Microfluidic Platforms. *Micromachines* **2019**, 10 (6), 423. Reprinted with permission (5532330841866). <https://doi.org/10.3390/mi10060423>.
- (12) Kwak, T. J.; Lee, H.; Lee, S. W.; Woehl, J. C.; Chang, W.-J. Size-Selective Particle Trapping in Dielectrophoretic Corral Traps. *J. Phys. Chem. C* **2021**, 125 (11), 6278–6286. <https://doi.org/10.1021/acs.jpcc.0c10592>.
- (13) Udad, X. S. Controlling and Manipulating Microscopic Particles in Solution By Using Various Electric Field Geometries, 2019.
- (14) Khoshmanesh, K.; Nahavandi, S.; Baratchi, S.; Mitchell, A.; Kalantar-zadeh, K. Dielectrophoretic Platforms for Bio-Microfluidic Systems. *Biosensors and Bioelectronics* **2011**, 26 (5), 1800–1814. <https://doi.org/10.1016/j.bios.2010.09.022>.

Chapter 3

Gouy-Chapman-Stern Model of the Electric Double Layer

3.1 Chapter Overview

This chapter's overall goal is to describe the many different current theories regarding the electric double layer. While I cannot resist the temptation to imply that there are many *layers* to these theories, it is nevertheless true: each hypothesis builds upon the previous hypothesis's concepts and adds new informational modeling and details that were previously unknown, assumed to be minimal, or outright ignored. Thus, each progression builds upon the idea instead of completely overwriting it. We will begin with the three "core" theories by Helmholtz, Gouy-Chapman, and Stern to get a broad idea, followed by some additional theories that introduce smaller changes.

This chapter will refer heavily to Chapter 2. The theories presented here are going to be made without constantly re-stating the equations and variables already described to keep this chapter as succinct as possible.

3.2 Helmholtz Model

In 1879, Herman von Helmholtz released his paper, *Studies on Electric Boundary-Layers*¹, in which he describes the interactions of charged ions upon two parallel plates of copper and zinc, with the copper plate being negative and the zinc plate being positive in potential. He describes it as "a finite quantity of electricity spread out in an infinitely thin layer," and then proceeds to propose a mathematical formula for its calculation. As a reminder, atomic theory wasn't fully established yet², and so his proposal of infinitely thin layers of charge wasn't seen as an impossibility. As an example, Helmholtz proposes a variety of ideas, such as separating two metal plates by 0.03 nm with an insulating barrier between them. Considering that the width of

a hydrogen atom is around 0.11 nm, there is no possible way for a molecular insulating barrier to exist at such a distance.

More importantly, he proposed a system in which the ionic charges suspended in solution would migrate towards the electrodes of the opposite charge³. In his hypothesis, he proposed that the charges in solution would form a uniformly thick layer along the entire electrode surface. This uniform thickness of charge would perfectly match the electric charge present on the metal surface, and thus it be a perfectly linear decrease of potential until it reached a net zero potential, after which the solution would return to homogeneity. This thickness, oddly enough, accounted for atomic size and charge density despite not being known at the time⁴. His approach compared it to a classical form of a parallel plate capacitor for storing charge, with parallel plates of exactly opposite potential depending on the capacitance per unit area, which lead to the term of a “double layer” along the metal surface.

By slightly adapting the parallel plate capacitor example presented in Chapter 2.9, we can create a system that matches Helmholtz’s hypothesis by lining one of the electrodes with a line of rigid ions⁵. For our example, we will assume that there is a monolayer, but the same theory applies for multiple stacked layers:

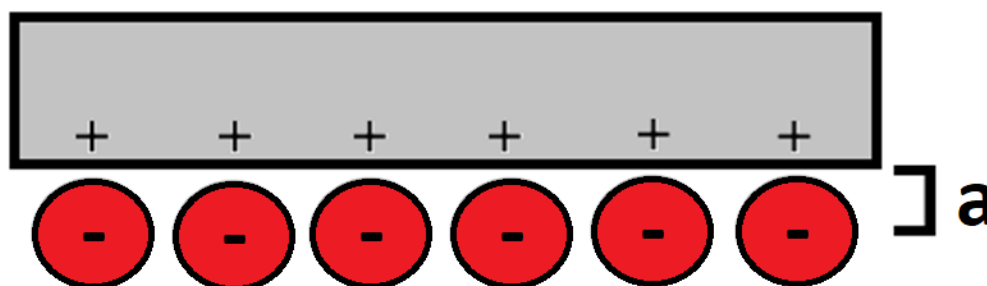


Figure 3.1: A positively charged metal electrode (grey) with counter-ions (red) in close proximity.

For the monolayer, instead of taking the distance as being the entire diameter of the ion, we are instead going to consider the “center” of the ion as the location of the overall charge, which means we will instead use the radius of the ion r , as shown on the right. This can then be related back to the Poisson Equation’s use of charge density in Equation 2.19:

$$\nabla^2 \varphi = -\frac{\rho(x)}{\varepsilon_r \varepsilon_0} \quad (2.19)$$

The Poisson Equation itself has many solutions, depending on the specific geometry of the system⁶. For the EDL, we can derive a concise analytical solution by relating it to the 1-dimensional distance to the electrode. We can summarize this as a very simple linear equation, starting at our initial applied potential, φ_{initial} , that drops to 0 as the distance from the surface x_r goes from 0 to a :

$$\varphi = \varphi_{\text{initial}}(a - x_a) \quad (3.1)$$

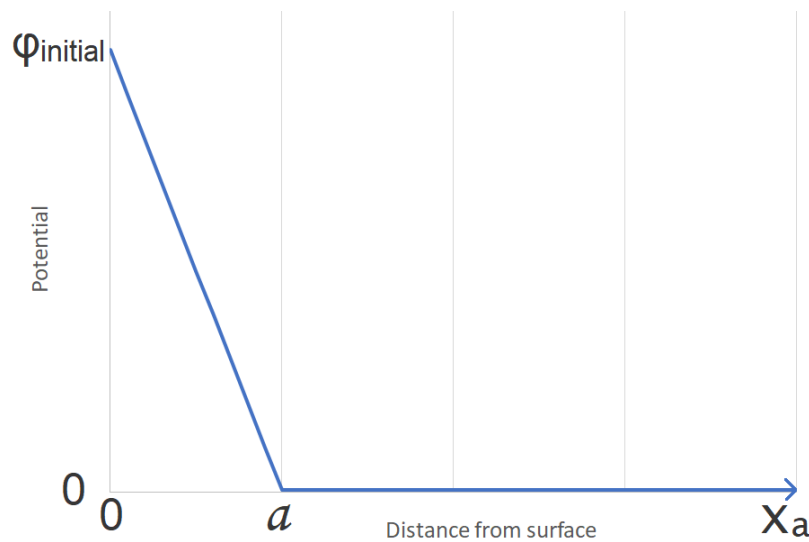


Figure 3.2: The Helmholtz Model: a linear decrease in potential across the radius of a particle. At a characteristic distance of the electrode, the potential has reached zero.

This approach was not necessarily flawed given the knowledge at the time but is nonetheless devastating: it does not match experimental data. Namely, the applied potential on the electrode is not immediately cancelled, and instead there is a diffuse layer that is not compensated for in his mathematical formulations⁷. We now know that, according to molecular theory, ions that form along the electrode are only partially rigidly held: as the potential drops, the repulsion between ions becomes a significant factor⁴.

3.3 Gouy-Chapman Model

In the early 1910s, Louis Gouy⁸ and David Chapman⁹ simultaneously and independently proposed a similar approach to finding a mathematical system of explaining experimental results of the EDL. Going beyond Helmholtz's proposed rigid layer, they each proposed a system that accounted for the thermal vibration and movement of ions near the surface. Their system had no rigid layer, but instead a fully diffuse medium of ions and counterions that were attracted to and repelled by the surface¹⁰.

Instead of starting with the charge density of the surface, they both used the Poisson-Boltzmann (PB) distribution equation to create an exponential curve, using Equation 2.28:

$$\nabla^2 \varphi = -\frac{e_0}{\varepsilon_r \varepsilon_0} \sum_i z_i n_0 \left(e^{-\frac{z_i e_0 \varphi_i}{k_B T}} \right) \quad (2.28)$$

As we discussed in Chapter 2.11, this can be mathematically solved to show the initial potential will drop consistently over each Debye Length by a factor of 1/e, or about 36.7%. Simplifying as a generalized exponential decrease allows us to create the following graph, using the relation shown in Equation 2.37 (where $\kappa = \frac{1}{\lambda_D}$) and x is the distance from the electrode:

$$\varphi = \varphi_{\text{initial}} e^{-\kappa x} \quad (3.2)$$

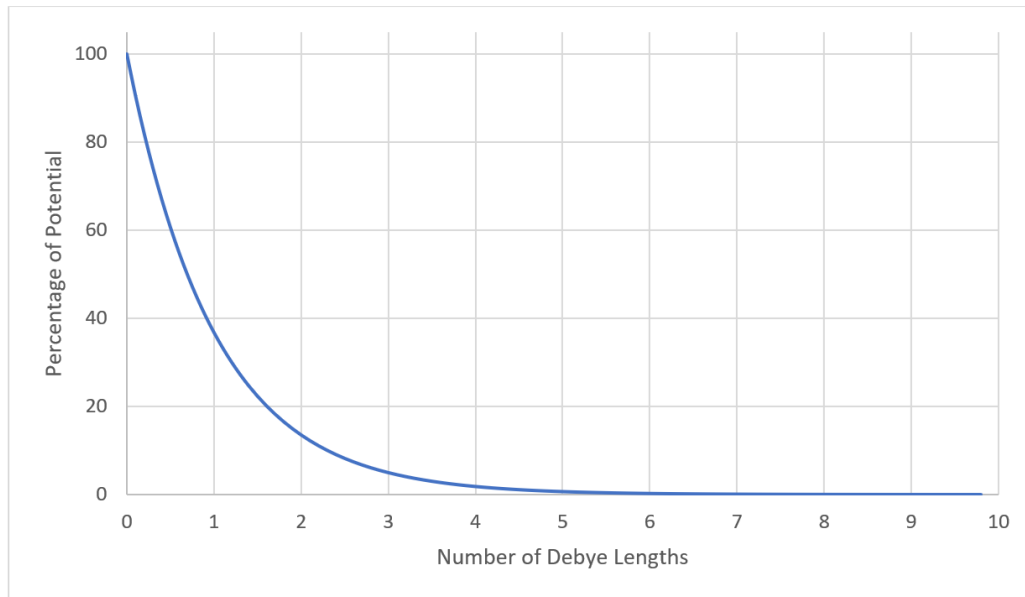


Figure 3.3: The Gouy-Chapman Model: the percentage decrease in potential as a function of Debye lengths.

Gouy-Chapman theory, however, made several assumptions to fit their mathematical solution to the EDL model, the most glaring issue being that the ions had to be assumed to be infinitesimal point-charges that ignored atomic size and ion density in order to fit the PB equation¹¹, which leads to impossibly high concentrations along the electrode's surface⁶. They had swung too far in the opposite direction from Helmholtz's model; they created a model that characterized the diffuse layer but failed at the surface.

3.4 Stern Model

If the Helmholtz Model's capacitor-like rigid layer worked along the surface, and the Gouy-Chapman Model matched the diffuse layer, why not simply combine the two together? Otto Stern¹², clearly, had the same idea in 1924.

The Gouy-Chapman-Stern (GCS) model he proposed breaks the interface into two major regions: an immobile layer along the electrode (later named the Outer Helmholtz Plane, or OHP) and the mobile region where the potential decays exponentially (later named the diffuse Layer). The boundary between these two regions is also now called the Stern Plane¹⁰. This combination solves the issues present in both of the previous hypotheses: the OHP properly accounts for atomic size along the surface and the potential will decrease linearly as it passes through the rigid lattice of oppositely charged ions. After the Stern Plane, the diffuse layer allows for ion mobility, following the more accurate Gouy-Chapman's model, as they are no longer adhered to a solid-like structure.

Mathematically, it is simply a repetition of the previous two subchapters, but with an added addendum for the location of the Stern Plane.

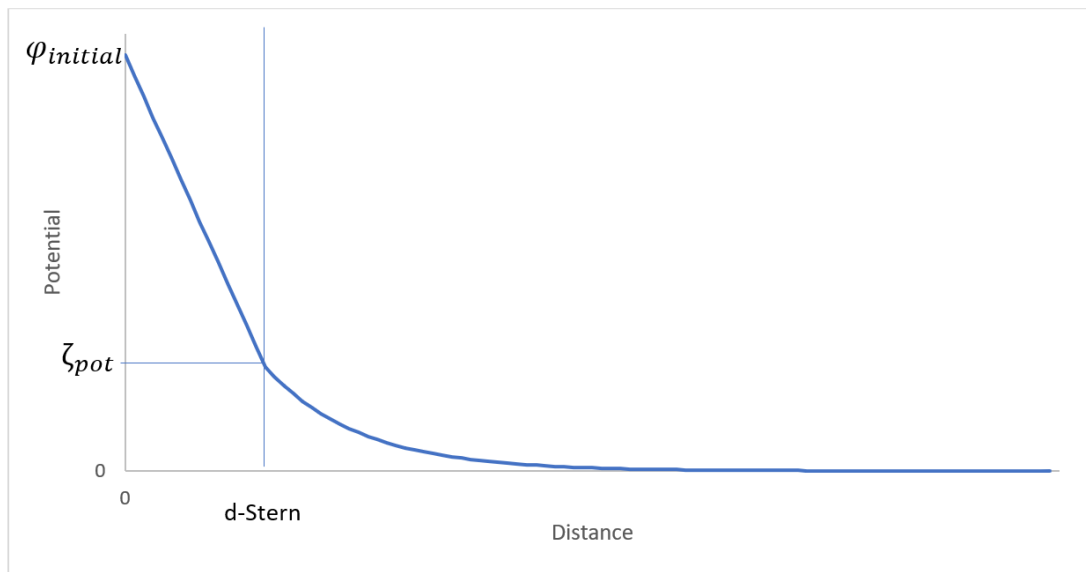


Figure 3.4: Decrease in potential across a certain distance according to the GCS model. Up to the Stern Plane $d-Stern$, the potential decreases linearly according to the Helmholtz Model. The model then decreases according to the Gouy-Chapman Model using the reduced potential at the Stern Plane, the zeta potential.

The equations of the characteristics of this model are simply a combination of the previous two hypotheses¹³:

$$\varphi_{\text{initial}} = \varphi_{\text{drop}} + \zeta_{\text{pot}} \quad (3.3)$$

$$\varphi_{\text{drop}} = \left(\frac{\sigma}{\varepsilon_0 \varepsilon_r} \right) d_{\text{Stern}} \quad (3.4)$$

$$\varphi_{\text{Diffuse}} = \zeta_{\text{pot}} e^{-\kappa x} \quad (3.5)$$

The overall potential drops (φ_{drop}) linearly as a function of distance and the charge density of the surface. This distance reaches its termination at the Stern plane distance d_{Stern} , which corresponds to the zeta potential ζ_{pot} , which is where the Stern layer ends and the diffuse layer begins. This is where the model then shifts into the Guoy-Chapman model using Debye lengths based on this new set of coordinates.

3.5 Additional EDL Theories

At this point, we have now covered a large portion of what will directly influence our results and calculations used later in this paper. There are, however, multiple additional theories that change and adapt our understanding of the EDL. These will focus upon the very thin Stern layer, while leaving the calculation of the bulk solution region relatively untouched. For the sake of completeness, these are presented below because understanding the interactions on the electrode surface is important to get a complete picture, but not necessarily vital for the conclusions of this paper.

3.5.1 Specifically Adsorbed Ions

In 1947, David Grahame discusses various aspects of the EDL, but he adds in a new concept: specifically adsorbed ions¹⁴. Grahame believed that while the oppositely charged ions are most often held in place by the Coulombic attraction, sometimes the ion will undergo a redox reaction to become covalently linked to the surface (although we will soon discuss in a later chapter how this is not quite accurate). These specifically adsorbed ions thus create a slightly-higher-than-expected concentration of counter-ions along the surface, and more crucially, these ions become attached to the electrode. Thus, the Stern layer will be slightly changed as the electrode surface is no longer a hypothetical uniform flat surface and will instead have small protrusions into the solution via the adsorbed ions. These ions can undergo another redox reaction to return to the solution, but otherwise the ions cannot be simply diluted like the other ions in solution because they are either covalently or coordinately bound to the surface¹⁵.

In addition to this concept, Grahame¹⁴ also expanded upon the delineation of the Stern Layer. Instead of a uniformly dense layer of ions that neutralizes the charge across the boundary, he proposed that there are two layers inside the Stern layer: the Inner Helmholtz Plane (IHP) and the Outer Helmholtz Plane (OHP). The Outer Helmholtz Plane is the Stern Layer: a semi-rigid layer of immobile ions packed together and causing a linear decrease in potential, attracted to and bound to the surface via electrostatic attraction, except that these ions are now conceived as still being fully surrounded by a solvation layer. The Inner Helmholtz Plane, however, is the previous addendum to the model: there are a small amount of specifically adsorbed ions studded along the surface. For both Planes, the line is drawn directly through the center of the rigid layer of ions.

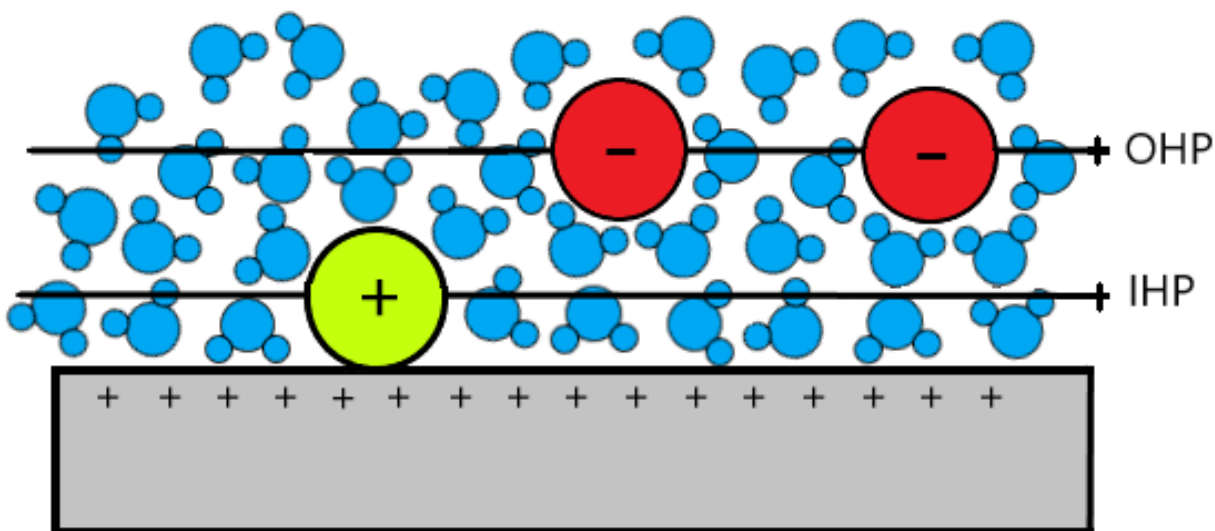


Figure 3.5: Molecular representation of the Inner and Outer Helmholtz Planes according to Grahame. Negative ions (red), a specifically adsorbed ion (yellow), and water molecules (light blue) partially oriented with the ions

In Figure 3.5, we can see a rough schematic of Grahame's theory, with the lines drawn through the center of our solvated ions. The specifically adsorbed ion functions as part of the electrode, while the non-bonded ions retain their negative charge. The water molecules solvate the ions but are otherwise randomly distributed. It is important to note, however, that each of the red ions and the yellow ion shown in Figure 3.5 are the same ion, but with differing charges. The specifically adsorbed ion has undergone a redox reaction to bond with the electrode, and thus aids the electrode in its capacitance.

3.5.2 Solvation Layer

To further expand upon the Inner Helmholtz Plane, in 1963 Bockris, Devanathan, and Mueller postulated that in addition to orienting the water molecules geometrically with respect

to the charge on the ions, there should also be a very thin layer of solvent molecules that have oriented themselves along the surface of the electrode and act as a barrier between the ions and the electrode¹⁶. These more rigidly bound and oriented water molecules are effectively acting as a massive solvation layer for the electrode, and it is only when one of the solution's ions can fully pierce through the Inner Helmholtz Plane that it would be able to undergo a redox reaction to become a specifically adsorbed ion.

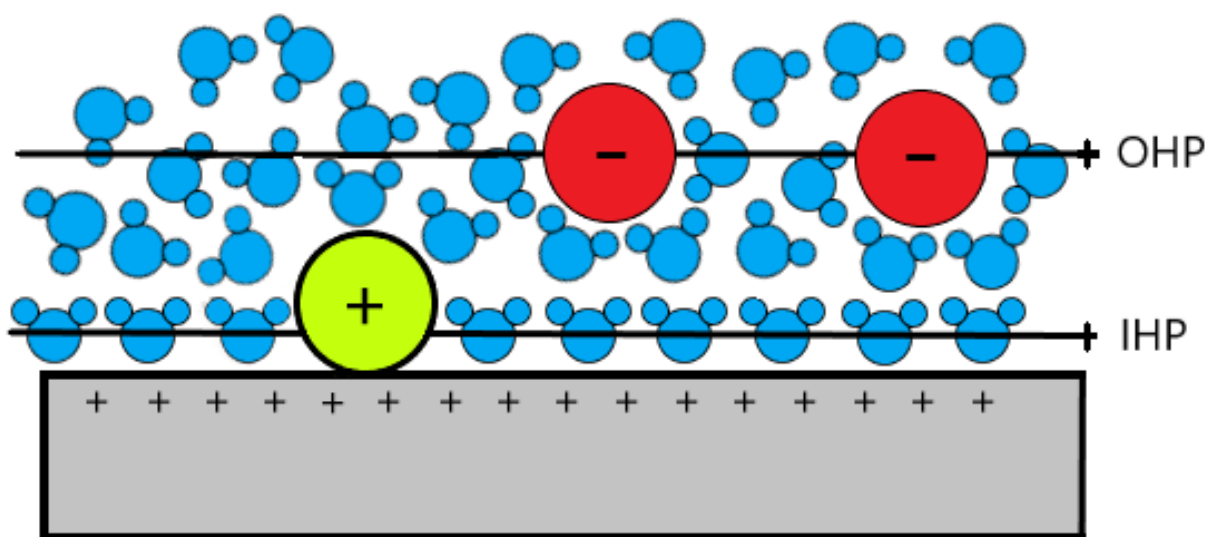


Figure 3.6: Molecular representation according to Bockris/Devanathan/Mueller. The only changes from Figure 3.5 are that the water molecules are now rigidly oriented along the electrode surface, and the IHP line has been moved to cut through the center of these reorientated solvent molecules.

Figure 3.6 is similar to Figure 3.5, but with the Inner Helmholtz Plane now being made up of solvent molecules oriented with the electric field created by the electrode surface, as well as the specifically adsorbed ion that has attached itself to the electrode. The Outer Helmholtz Plane remains unchanged.

3.5.3 Pseudocapacitance

In a departure from the previously understood theory of Grahame, the exact nature of specifically adsorbed ions changed due to another crucial addition to EDL theory: pseudocapacitance¹⁷. Essentially, between the two extremes of a simple capacitor, where all applied charge builds on an electrode but doesn't transfer across, and a simple battery, where all applied charge fuels a chemical redox reaction that either depletes or deposits the electrode material, is a region of ambiguity. Between the two extremes, there is a spectrum of pseudocapacitance where there is both charge build-up and depletion, as well as a weaker form of ionic deposition¹⁸.

In a simplified standard battery, both the electrodes and the solution between them contain the same specific elements, either in solid or ionic form. As the electron transfer occurs, the ions undergo an irreversible chemical redox reaction that either creates or breaks covalent/ionic bonds. This is then a semi-permanent structure, or at least until another charge transfer occurs in the opposite direction, another irreversible change. Up until now, it was generally understood that this same effect must be occurring to the specifically adsorbed ions, but this is slightly incorrect: while there may be a charge transfer between the electrode and the ion, a bond is not formed. Instead, the ion can become highly polarized and restructured via an internal charge transfer, a reversible change¹⁷. This gives the effect of becoming attached to the electrode and functioning as part of it, but as soon as the potential on the electrode is removed, the ions can gradually return to the solution by reversing the internal polarization. Thus, depletion of the electrode can occur without inducing an opposite applied charge, as in the case of a battery.

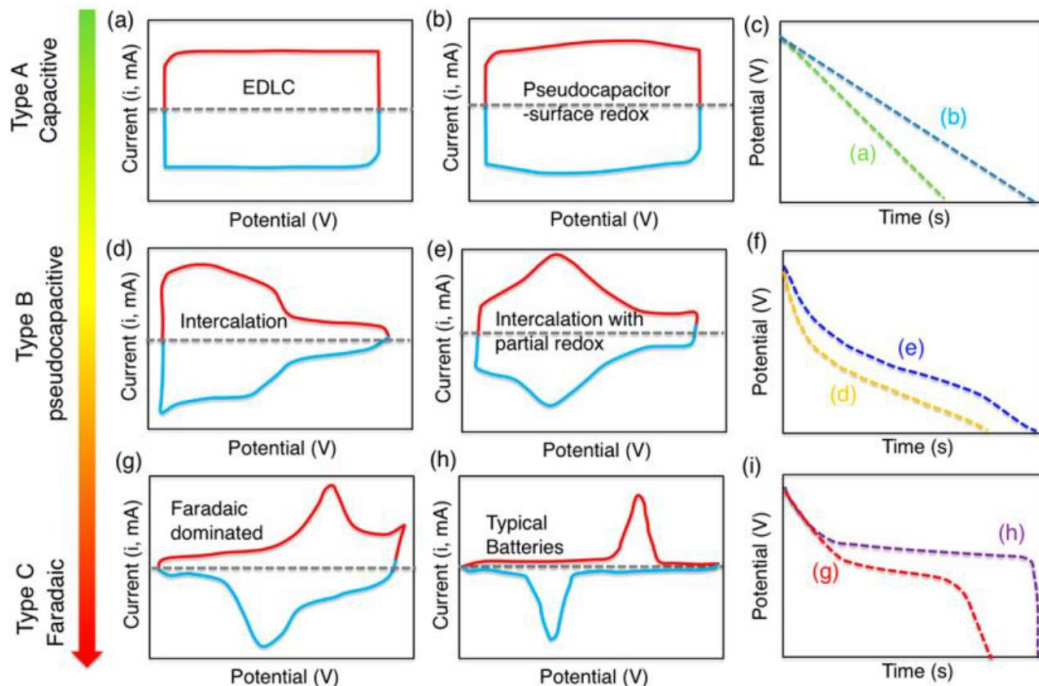


Figure 3.7: Characteristic depictions of capacitors, pseudocapacitors, and Faradic batteries by Gogotsi et al.¹⁸

(a, b, d, e, g, h): cyclic voltammograms and their (c, f, i) corresponding galvanostatic discharge curves.

Voltammograms of electrode material and ionic mediums will have characteristics that is some combination of these graphs. Note the lateral symmetry of capacitors and pseudocapacitors.

This was first observed for transition metals in the oxides of ruthenium in 1971 by Trasatti and Buzzanca when they noted that there was an incredibly symmetrical voltammogram¹⁹. Batteries, by comparison, depict very non-symmetrical voltammograms due to the irreversibility of the redox reactions involved. By using hydrous ruthenium oxide nanoparticles, instead of ruthenium ions, this allowed for the internal polarizability without causing ionic charge transfers.

Work by Conway and Gileadi sought to further refine the concept of pseudocapacitance²⁰, with an increased emphasis on the highly reversible electrochemical charge transfer reactions observed, using the Langmuir model. This model crucially makes several assumptions which are

extremely optimistic: the surface contains a limited number of adsorption sites, these sites do not interfere with each other, the adsorption is local and immobile, the surface is ideal and smooth, and only a single monolayer of adsorbed material is formed²¹. Clearly, most of these assumptions start to fail when considering real-world experiments of the EDL, but it at least provided a solid starting point.

If θ is the fraction of occupied active sites at equilibrium, Langmuir's equation is given by the following²², with L as the rate of incidence, P_A as the probability of *adsorption*, and L_D as the rate of *desorption* at full saturation:

$$\theta = \frac{LP_A}{L_D} \quad (3.6)$$

Taking this framework, it can be expanded into the Langmuir adsorption isotherm equation, where M_A is the concentration of the ion, K_{eq} is the equilibrium constant, F is the faraday constant, V_q is the applied electrode potential, and T is the temperature in Kelvin:

$$\frac{\theta}{1 - \theta} = K_{eq} M_A e^{\frac{V_q F}{RT}} \quad (3.7)$$

This can then in turn be adapted by a bit of rearrangement¹⁷ and taking the derivative with respect to potential to find the pseudocapacitance C_ϕ , with a required charge of coverage, q_c :

$$C_\phi = q_c \frac{d\theta}{dV} = \frac{q_c F}{RT} \theta (1 - \theta) \quad (3.8)$$

Thus, the pseudocapacitance for a such a process is a function of both the applied potential and the surface coverage of adsorbed material, which again highlights the theoretical understanding of the position of pseudocapacitance existing between a standard capacitor and a simplified battery²³.

- (1) Helmholtz, H. Studien Über Electriche Grenzschichten. *Ann. Phys. Chem.* **1879**, 243 (7), 337–382. <https://doi.org/10.1002/andp.18792430702>.
- (2) Fleck, G. M. Atomism in Late Nineteenth-Century Physical Chemistry. *Journal of the History of Ideas* **1963**, 24 (1), 106–114. <https://doi.org/10.2307/2707861>.
- (3) Helmholtz, H. *Physical Memoirs: Studies on Electric Boundary-Layers*; Taylor & Francis, 1888.
- (4) Bohinc, K.; Kralj-Iglič, V.; Iglič, A. Thickness of Electrical Double Layer. Effect of Ion Size. *Electrochimica Acta* **2001**, 46 (19), 3033–3040. [https://doi.org/10.1016/S0013-4686\(01\)00525-4](https://doi.org/10.1016/S0013-4686(01)00525-4).
- (5) COMSOL. Diffuse Double Layer.
- (6) Butt, H.-J.; Graf, K.; Kappl, M. Physics and Chemistry of Interfaces. 376.
- (7) Roudgar, A. Lecture: Electric Double Layer.
- (8) Gouy, M. Sur La Constitution de La Charge Électrique à La Surface d'un Électrolyte. *J. Phys. Theor. Appl.* **1910**, 9 (1), 457–468. <https://doi.org/10.1051/jphysap:019100090045700>.
- (9) Chapman, D. L. A Contribution to the Theory of Electrocapillarity. *The London, Edinburgh, and Dublin Philosophical Magazine and Journal of Science* **1913**, 25 (148), 475–481. <https://doi.org/10.1080/14786440408634187>.
- (10) Oldham, K. B. A Gouy–Chapman–Stern Model of the Double Layer at a (Metal)/(Ionic Liquid) Interface. *Journal of Electroanalytical Chemistry* **2008**, 613 (2), 131–138. <https://doi.org/10.1016/j.jelechem.2007.10.017>.
- (11) Bhuiyan, L. B.; Outhwaite, C. W. Comparison of Exclusion Volume Corrections to the Poisson–Boltzmann Equation for Inhomogeneous Electrolytes. *Journal of Colloid and Interface Science* **2009**, 331 (2), 543–547. <https://doi.org/10.1016/j.jcis.2008.11.059>.
- (12) Stern, O. Zur Theorie Der Elektrolytischen Doppelschicht. *Zeitschrift fur Elektrochemie* **1924**, 30.
- (13) Brown, M. A.; Bossa, G. V.; May, S. Emergence of a Stern Layer from the Incorporation of Hydration Interactions into the Gouy–Chapman Model of the Electrical Double Layer. *Langmuir* **2015**, 31 (42), 11477–11483. <https://doi.org/10.1021/acs.langmuir.5b02389>.
- (14) Grahame, D. C. The Electrical Double Layer and the Theory of Electrocapillarity. *Chem. Rev.* **1947**, 41 (3), 441–501. <https://doi.org/10.1021/cr60130a002>.
- (15) Wakatsuki, T.; Furukawa, H.; Kawaguchi, K. Specific and Non-Specific Adsorption of Inorganic Ions I. Evaluation of Specific Adsorbability by Means of Minimum Concentration for Specific Adsorption. *Soil Science and Plant Nutrition* **1974**, 20 (4), 353–362. <https://doi.org/10.1080/00380768.1974.10432606>.
- (16) Bockris, J. O.; Devanathan, M. A. V.; Mueller, K. *On the Structure of Charged Interfaces*. <https://royalsocietypublishing.org/doi/epdf/10.1098/rspa.1963.0114> (accessed 2022-04-28). <https://doi.org/10.1098/rspa.1963.0114>.
- (17) Fleischmann, S.; Mitchell, J. B.; Wang, R.; Zhan, C.; Jiang, D.; Presser, V.; Augustyn, V. Pseudocapacitance: From Fundamental Understanding to High Power Energy Storage Materials. *Chem. Rev.* **2020**, 120 (14), 6738–6782. <https://doi.org/10.1021/acs.chemrev.0c00170>.
- (18) Gogotsi, Y.; Penner, R. M. Energy Storage in Nanomaterials – Capacitive, Pseudocapacitive, or Battery-Like? *ACS Nano* **2018**, 12 (3), 2081–2083. Reprinted with

- permission. <https://doi.org/10.1021/acsnano.8b01914>.
- (19) Trasatti, S.; Buzzanca, G. Ruthenium Dioxide: A New Interesting Electrode Material. Solid State Structure and Electrochemical Behaviour. *Journal of Electroanalytical Chemistry and Interfacial Electrochemistry* **1971**, *29* (2), A1–A5. [https://doi.org/10.1016/S0022-0728\(71\)80111-0](https://doi.org/10.1016/S0022-0728(71)80111-0).
- (20) Conway, B. E.; Gileadi, E. Kinetic Theory of Pseudo-Capacitance and Electrode Reactions at Appreciable Surface Coverage. *Trans. Faraday Soc.* **1962**, *58* (0), 2493–2509. <https://doi.org/10.1039/TF9625802493>.
- (21) Bauer, A. The Langmuir Adsorption Model. *Materials Characterization Lab*, 2021.
- (22) Conway, B. E.; Angerstein-Kozłowska, H. *The electrochemical study of multiple-state adsorption in monolayers*. ACS Publications. <https://pubs.acs.org/doi/pdf/10.1021/ar00062a004> (accessed 2022-07-29). <https://doi.org/10.1021/ar00062a004>.
- (23) Conway, B. E. Transition from “Supercapacitor” to “Battery” Behavior in Electrochemical Energy Storage. *J. Electrochem. Soc.* **1991**, *138* (6), 1539. <https://doi.org/10.1149/1.2085829>.

Chapter 4

Nanoscale Microscopy and Fluorescence

4.1. Chapter Overview

This chapter describes the laser-based and digital components of the research presented here. While it is important to understand the physics and chemistry that is occurring in the experiments, it is just as important to understand that the exact nature of the nanoscale world cannot be directly observed with brightfield microscopy; nanoscale particles are too small to be resolved by the limitations of light's photon size and wave characteristics.

First, we will discuss the different functions of the various glass components used in our microscope, as well as their limitations when using light in the visible range. Then we will discuss the workaround for these limitations: fluorescence signals captured through a photosensitive camera. While this is a vast improvement upon simple light scattering, this brings its own set of complications which must be accounted for: signal-to-pixel discrepancies and frame effects. By using subpixel localizations and particle tracking, we can pull out the vital information that we will use in Chapters 6 to 9 of this thesis.

4.2. Telescopes to Microscopes

Writings on the refractive and reflective properties of glass and water exist throughout history, but the first time that lenses were finely detailed, hypothesized, and experimented on were by Ibn al-Haytham in the 11th Century, who is considered by many historians to be the first true scientist¹ and the father of modern optics². Ibn al-Haytham's work was limited to single optics, like magnifying an image with a convex lens, but his extensive writings on the nature of light and lenses greatly influenced and inspired scientists centuries later in Europe.



Figure 4.1: 17th Century telescopes³ (left) and tripod microscope⁴ (right). Both use lenses to magnify images.

The first constructed instrument that utilizes *compound* optics (the use of multiple lenses in succession) occurred just 400 years ago in the Netherlands⁵, and improved upon just a year later by Galileo⁶. By using a series of eight lenses, in what we now would call a telescope, Galileo was able to magnify the incoming light from space to make human-eye observations of extraterrestrial bodies, noting the revolution of Jupiter’s moons and the phases of Venus³, which completely upended the core philosophies of astronomy at that time. 250 years later, as previously discussed, Robert Brown was able to use a compound microscope to magnify images of pollen grains⁷. Because optical microscopy is at the core of all observations made in our research, I will briefly discuss these principles.

The geometrical laws of reflection and refraction are the foundation on which light-based microscopes are based. Reflection occurs on mirrored surfaces, where an incoming beam of light will “bounce” in a manner that maintains the angle of incidence. Refraction, in contrast,

occurs when a beam of light passes from one medium to the next, often from air to glass or vice-versa, which bends the light rays in a reliable manner. This process occurs because light travels at different speeds through air and glass, which leads to a change in the direction at the interface that is dependent on the relative speeds of light travelling through glass and air. This is then reversed as the light ray leaves the glass on the other side, returning the light ray to the original travel direction, but now displaced by a small distance. This, however, only works if the glass surfaces are both flat and parallel; if one of the surfaces is curved, like in convex or concave lenses, it instead causes the light to have a different angle of refraction upon leaving the glass, thus causing the light to be either convergent or divergent.

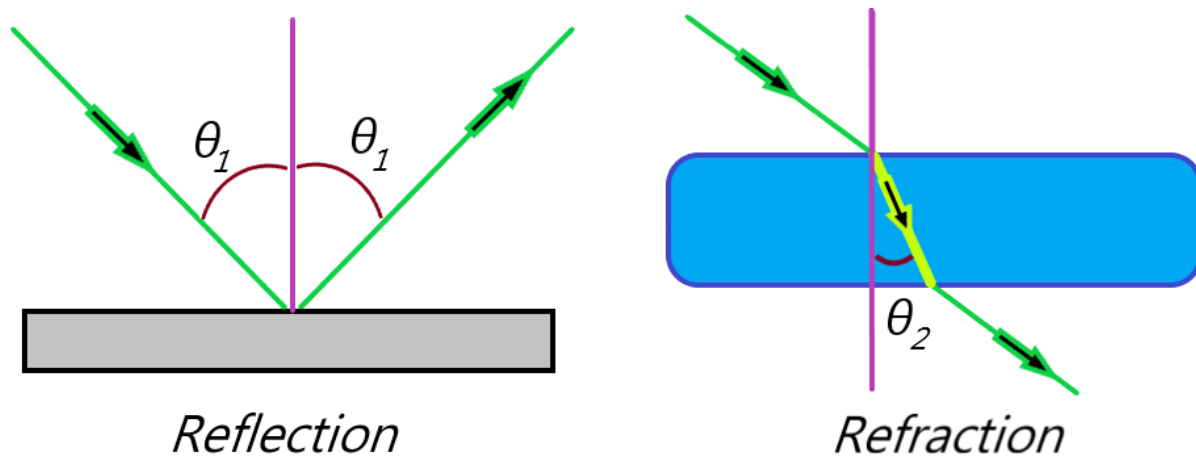


Figure 4.2: The difference between reflected (**left**) and refracted (**right**) light. The incoming light (green) interacts with a surface at a specific point (purple line), and then either reflects off of a surface (grey) or passes through the material (blue). The angle of reflection θ_1 or refraction θ_2 determines the outgoing light. For refraction, if the light then leaves a parallel surface, the angle of refraction restores the original propagation direction.

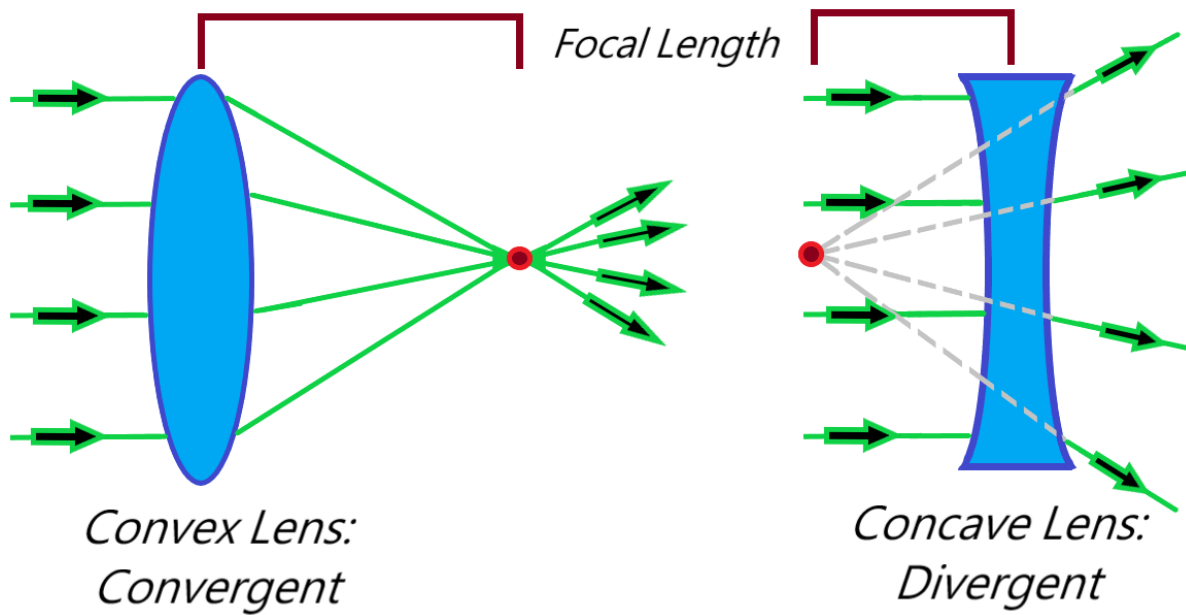


Figure 4.3: Convex Lenses and Concave Lenses. An incoming set of parallel light rays (green) when passing through a convex lens will converge onto the focal point (red) at a specific distance known as the focal length.

Similarly Parallel light rays passing through a concave lens will diverge from a common focal point.

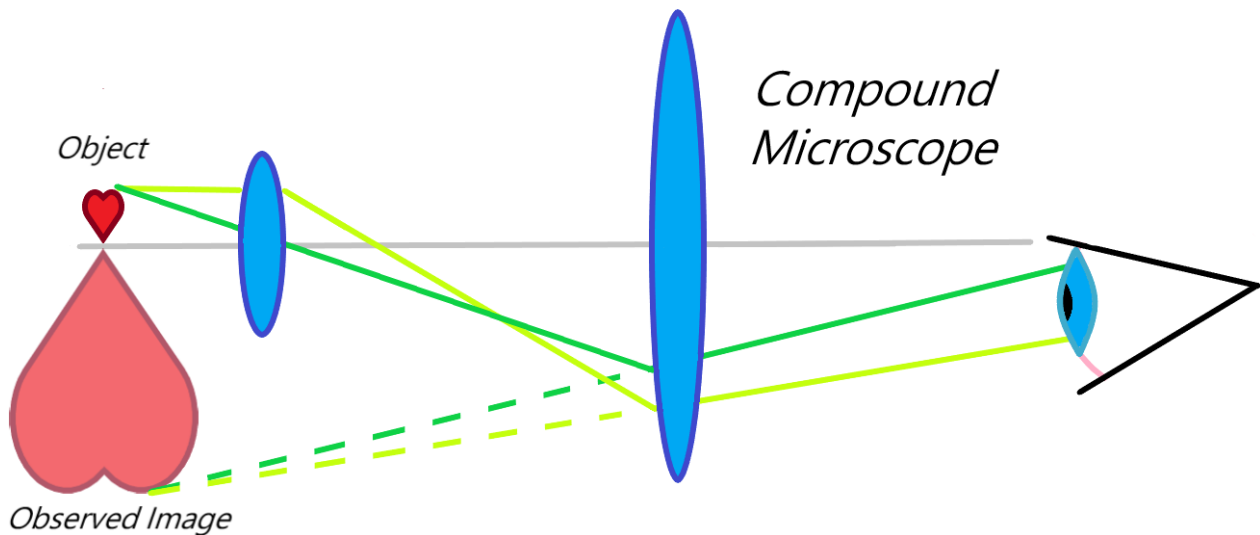


Figure 4.4: Compound Microscope diagram. An object (left, dark red) has its image refracted through two convex lenses (blue) which creates a magnified observed image (left, red) for an observer (right, eye). The two shades of green lines represent light coming off of the object.

By using a series of lenses, an image can be magnified by “capturing” the diverging light with a lens at the right distance, as seen in Figure 4.4 with the 2nd lens. This allows very small objects to appear far larger, or for wide beams of collimated light to be focused into a tighter collimated beam. This simple idea allowed Galileo to see the moons of Jupiter because the Sun’s light reflected off their surface, travelled to Earth, and could then be magnified to a degree that the human eye could differentiate. More modern telescopes, such as the Hubble and Webb Telescopes, can now resolve objects billions of light-years away (10^{25} meters)^{8,9}.

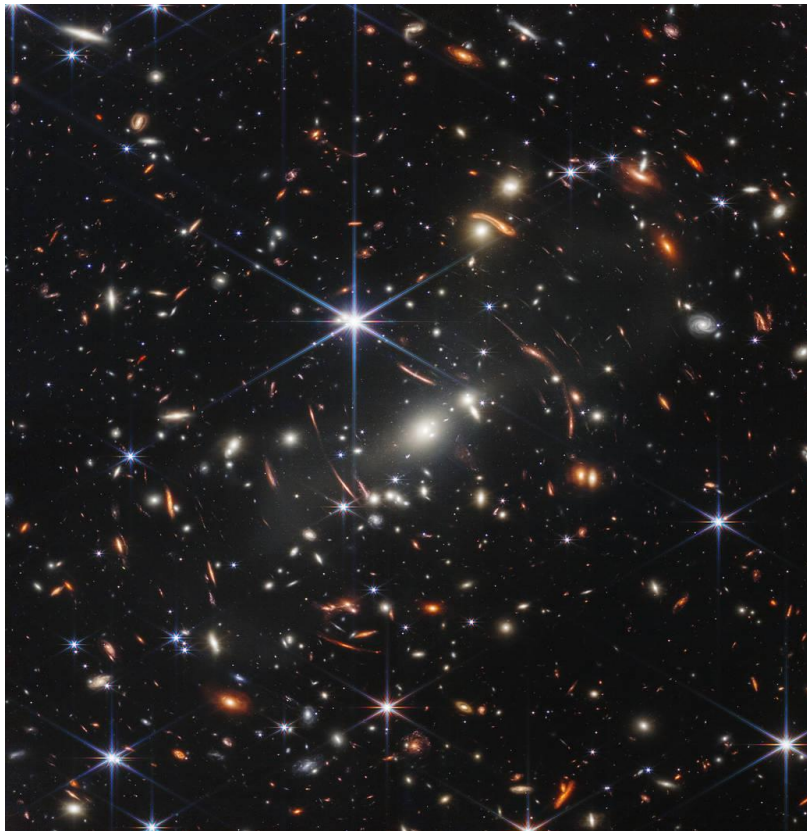


Figure 4.5: NASA’s image of galaxy cluster SMACS 0723 using the James Webb Space Telescope⁹. The dots with the prominent hexagonal diffraction spikes are stars¹⁰, while all the circular and ovular objects in this image are distant nebulae and galaxies billions of light-years away from Earth.

4.3. Resolution Limits and the Airy Disk

When observing the moons of Jupiter, Galileo was relying on sunlight reflecting off the massive celestial bodies, but after travelling a great distance towards Earth, the light's signal has become very weak, making it undetectable to the naked eye; only by magnifying the signal were they detectable. In a similar fashion, incredibly small objects under a microscope scatter and reflect light, but their small size means that reflection becomes less and less feasible, resulting in a weak signal and we rapidly approach the limit to which the wave of light is larger than the molecule.

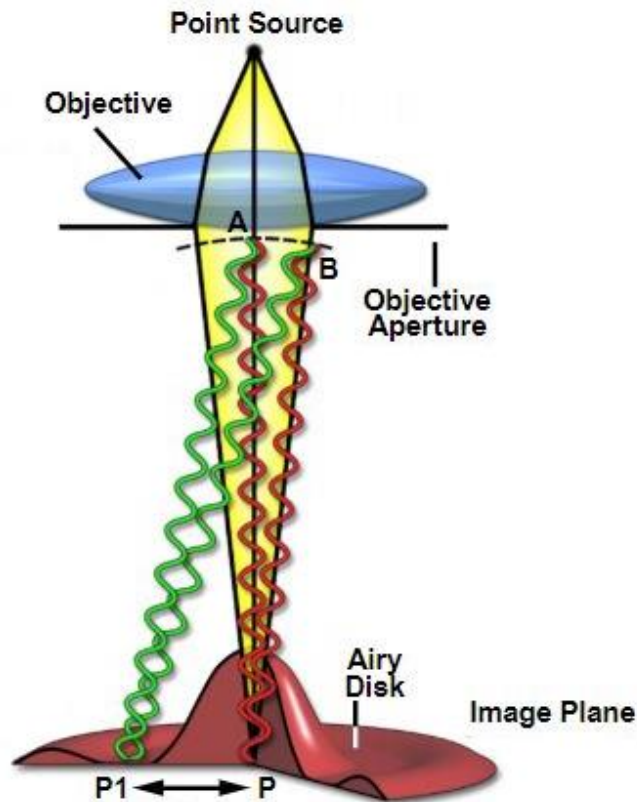


Figure 4.6: Depiction of the resolution limit of a point-source of light. As light passes through a glass objective, the objective aperture blocks all but a subset of the incoming light. These light waves pass through the aperture interfere with each other, constructively (red) and destructively (green). Location P is the central maximum, while P1 is the first minimum ring. Original image created by Silfies, Schwartz, and Davidson for Nikon MicroscopyU¹⁵

While large objects scatter light in all directions (constructively and destructively interfering with each other to produce a rough uniform continuum of light), small object or very distant objects¹¹ behaving like functional point-sources, such as stars¹², will instead have their captured light result in interference patterns, which in the ideal case results in a pattern known as an Airy disk¹³⁻¹⁵, named after Sir George Airy for his contributions in research in these diffraction patterns¹⁶, as seen in Figures 4.6 and 4.7.

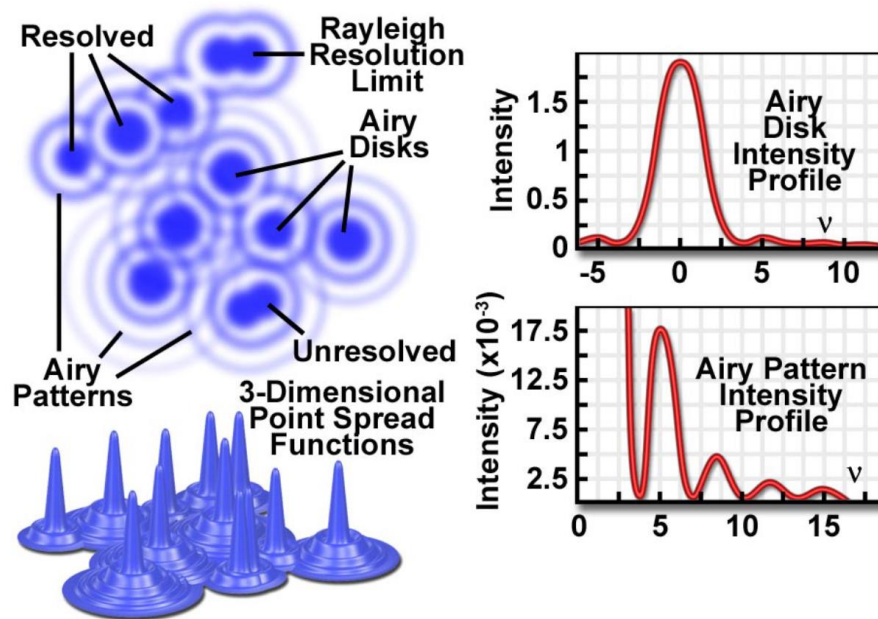


Figure 4.7: (left) Depiction of several Airy disks either resolved, at the Rayleigh resolution limit, or unresolvable. (right) Intensity profiles of Airy disks, with the majority of signal (84%¹⁴) in the central primary peak, decreasing after every subsequent diffraction ring. Image created by M. Ulrich in *Confocal Laser Scanning Microscopy*¹¹

These Airy disks are many magnitudes larger than the source signal, which can result in multiple Airy disks of an extended object made up of multiple point emitters to overlap and mask each other. In 1873, Ernst Abbe¹⁷ proposed that to separate two particle signals as

sufficiently distinct, the particles must be separated by a distance d_{Abbe} that is some function of the wavelength of light λ_L and the numerical aperture of the objective NA , which is itself a function of the refractive index of the medium n_m (1.00 for air) and the aperture angle θ_A . He estimated it, somewhat arbitrarily and without much explanation¹⁸, as:

$$d_{Abbe} = \frac{1}{2} \frac{\lambda_L}{NA} \quad (4.1)$$

$$NA = n_m * \sin(\theta_A) \quad (4.2)$$

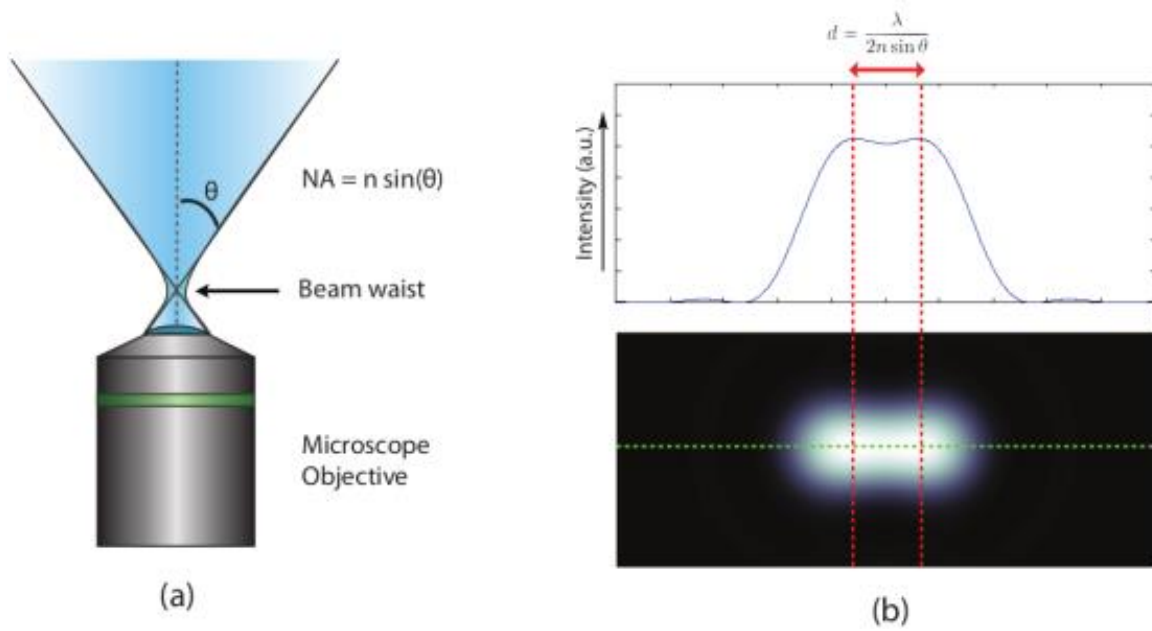


Figure 4.8: illustrations of a microscope objective and the diffraction limit by R. Dijkstra¹⁹

(a): illustration of a microscope objective, including the aperture angle. The beam waist is the minimum beam radius, which is a function of the physical optics and the incoming beam quality²⁰. **(b):** two illuminated points, blurred by diffraction, at the diffraction limit.

In contrast to the Abbe limit's seemingly arbitrary restriction with a $\frac{1}{2}$ factor included, Baron John William Strutt, more commonly known as Lord Rayleigh, instead proposed that the resolution limit is instead determined by ensuring that the primary peaks do not overlap. He

suggested that the minimum distance, d_{Rayleigh} , at which two particles can still be resolved is obtained when the intensity center of the Airy disk of the first particle coincides with the first dark ring of the Airy ring of the second particle; any closer, and the central peaks will merge and will become unresolved. This distance leads to a multiplication factor of approximately 1.22 onto the Abbe Resolution^{21,22}:

$$d_{\text{Rayleigh}} = 1.22 * d_{\text{Abbe}} = 0.61 \frac{\lambda_L}{NA} \quad (4.3)$$

As a brief calculation, the numerical aperture for the 40x objective used in our experiments is given from the manufacturer as 0.75 and our emission wavelength is roughly 500 nm. This means that the Rayleigh resolution for this is 407 nm. If we instead use the 100x objective, which has a numerical aperture of 1.3, the Rayleigh limit is approximately 235 nm.

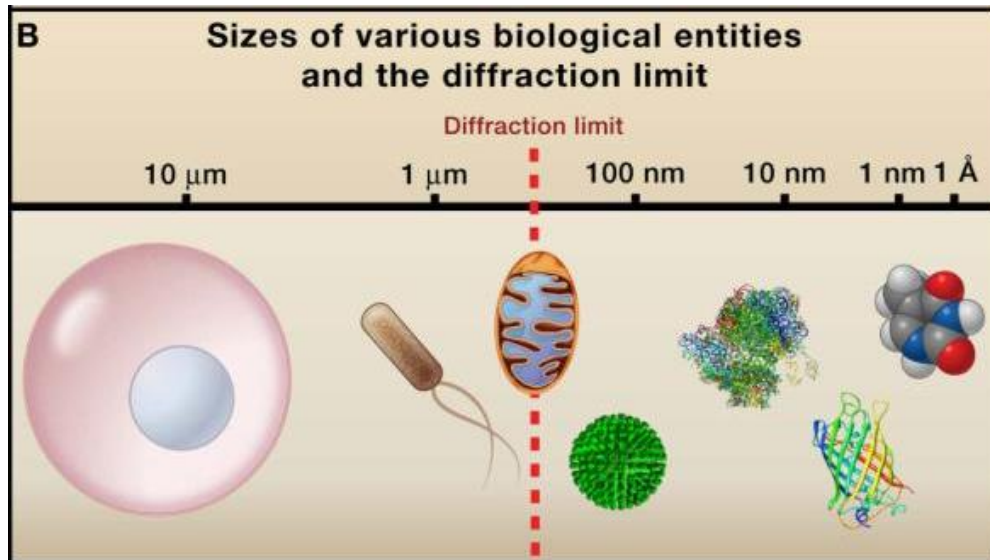


Figure 4.9: A logarithmic scale bar showing the location of the diffraction limit created by Huang, Babcock, and Zhuang in *Breaking the Diffraction Barrier: Super-Resolution Imaging of Cells*²³. Above the diffraction limit (left) is a mammalian cell and bacteria, at the diffraction limit is mitochondria, and below the diffraction limit are viruses, ribosomes, proteins, and molecules.

A common approximation for the resolution limit is set as roughly one-half the wavelength of light²⁴, and considering that all the wavelengths of visible light are tightly clustered in the 400-700nm range²⁵, it suggests that two small particles less than 200 nm apart cannot properly be resolved by standard light-based microscopy without resorting to the dangerous and extreme short wavelengths of x-ray and gamma. While the quick estimate of one-half the wavelength isn't scientifically meticulous, it still gives an approximate value that is efficient in its simplicity: a quick estimation of $500/2 \approx 250$ nm, as compared to the previously calculated 407 and 235 nm. The most important thing to remember is that reflected or refracted light will consistently fail to overcome the Abbe and Rayleigh limits because diffraction is an inherent and immutable aspect of light-waves.

4.4. Fluorescence Microscopy

The largest issue when attempting to view the nanoscale world is that of size: smaller objects become difficult or impossible to view because the scattering of light causes small objects to blur to such a degree that it becomes functionally impossible to view anything smaller than ~ 250 - 500 nm²³. One solution is to move away from light entirely, utilizing techniques that rely on the more particle-like nature of electrons in Scanning Electron Microscopy (SEM) and Transmission Electron Microscopy (TEM)²⁶. These systems, however, rely on high vacuum conditions and are therefore unsuitable for our aqueous-based experiments.

Taking a step back, we can reflect upon the origins of microscopy: astronomy. Stars do not *reflect* light but are instead *sources* of light; instead of relying on light to *bounce off* of a nanoparticle we can instead have it be *emitted* by the nanoparticle.

For many nanoparticles, the absorption of energy causes an electron to be excited to a virtual state, or one in which there is no stable energy level for the nanoparticle's electron to occupy. This then near-instantly returns the absorbed energy as an emission of the same wavelength in a random direction, known as elastic scattering²⁷. If instead this absorbed light reaches a real excited singlet energy state, it can undergo an internal relaxation before emitting a lower wavelength of light, a process known as fluorescence (FL)^{28,29}. Using a monochromatic excitation light, these particles become the sole source of these lower energy wavelengths, which can then be selectively isolated from the incoming excitation wavelength of light using a color-selective filter. Due to the necessity of lens apertures for the capture process, the light still results in an Airy disk, which results in a digitized signal when captured by a camera, with each pixel representing the sum of captured photons from a given object area.

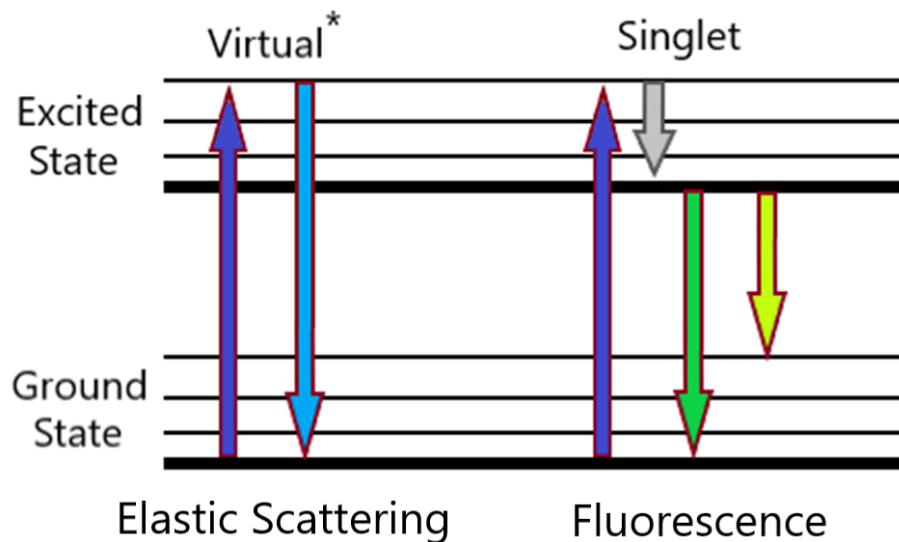


Figure 4.10: Incoming light (dark blue) excites an electron to a higher energy state (black lines). For elastic scattering, the emission is unchanged in wavelength (light blue). For fluorescence, the electron undergoes an internal non-emissive relaxation (grey, $\sim 10^{-9}$ seconds) before the emission of lower energy light (green and yellow).

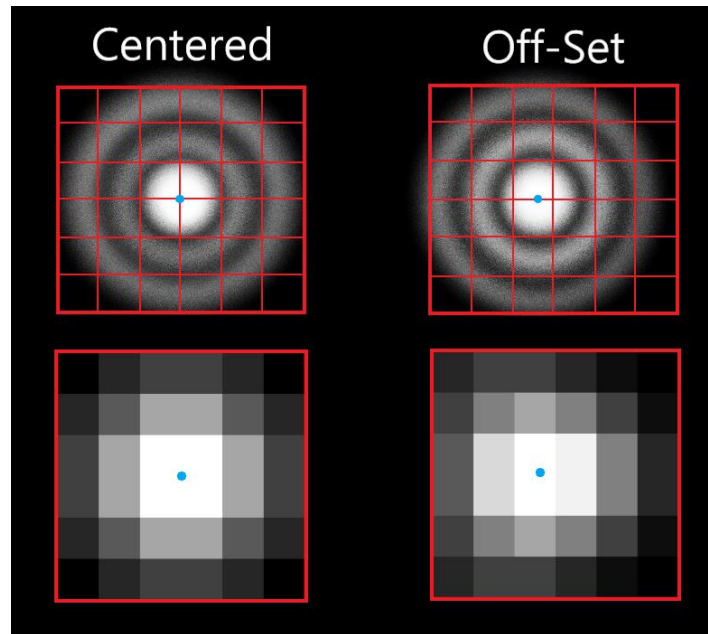


Figure 4.11: Airy disks (top) and resulting pixelated camera image (bottom) of a fluorescing particle (blue dot). Each pixel corresponds to the amount of photon signals in each area of the Airy disk. The Centered particle (left) is at an axis point, corresponding with a symmetrical pixel image. The Off-Set particle (right) has been displaced by a small amount, resulting in a non-symmetrical pixel image.

Due to the Airy disk being much larger than the FL nanoparticle source, the pixel signal falsely implies that the particle is much larger than it truly is, as in Figure 4.11. The fastest method of locating the particle's true position is to assume that it will be somewhere within the brightest pixel. However, because an off-set particle creates an asymmetric pattern in the surrounding pixels, the particle can be localized with sub-pixel accuracy by using the uniquely characteristic point spread function of the entire data set, as seen in Figure 4.12. There are several possible fitting methods for these algorithms, based on how the surrounding pixels have varying intensity according to the fitting models, such as Gaussian or Airy³¹, but these analytical tools are still restricted by the Abbe and Rayleigh diffraction limits.

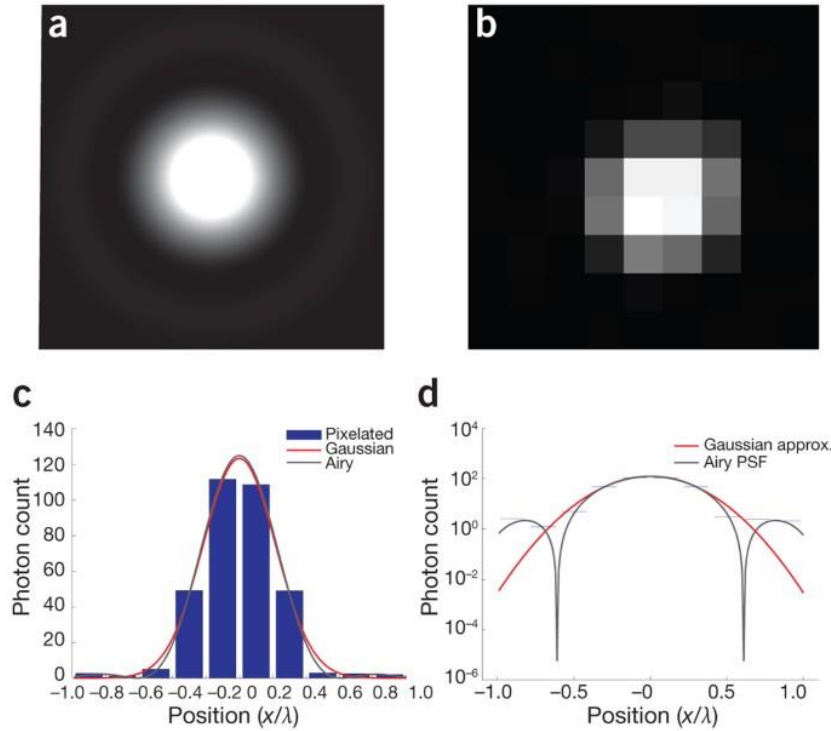


Figure 4.12: Point spread functions created by Small and Stahlheber in *Fluorophore Localization Algorithms for Super-Resolution Microscopy*³⁰. **(a)** Airy disk of a fluorophore, two wavelengths across, and **(b)** its corresponding pixelated image as it would be captured by a camera, with each pixel representing an area of $1/5^{\text{th}}$ of the wavelength. **(c)** The cross section of the pixels in (b) with an overlaid approximation for the Airy and Gaussian models. **(d)** The logarithmic scale of (c) to highlight the discrepancy in the tails between Airy and Gaussian models.

Crucially, FL microscopy allows for a unique solution that was not present with simple light scattering: the near absence of background signal and therefore a huge improvement in signal contrast. For brightfield imaging, the scattering of light of equal wavelength made particles difficult to distinguish. In contrast, even with very weak signals, fluorescence can be isolated from the excitation light, and then detected and distinguished from the background noise.

Additional resolution techniques that allow for a large number of FL signals to be resolved have been developed to accomplish the separation of multiple point sources that normally

make up an object, including Photoactivated Localization Microscopy (PALM)³², Fluorescence PALM (fPALM)³³, Fluorescence Speckle Microscopy (FSM)³⁴, and Stochastic Optical Reconstruction Microscopy (STORM)³⁵. Each utilizes a different mechanism to introduce multiple-frame analysis to overcome the resolution limit, but the premise is similar between all of them. Instead of capturing all possible FL signal from all particles at the same time, it is instead possible to collect single particle signals in distinct frames, which avoids any resolution overlap issues, and then reconstructing the final image from the total of all localized signals.

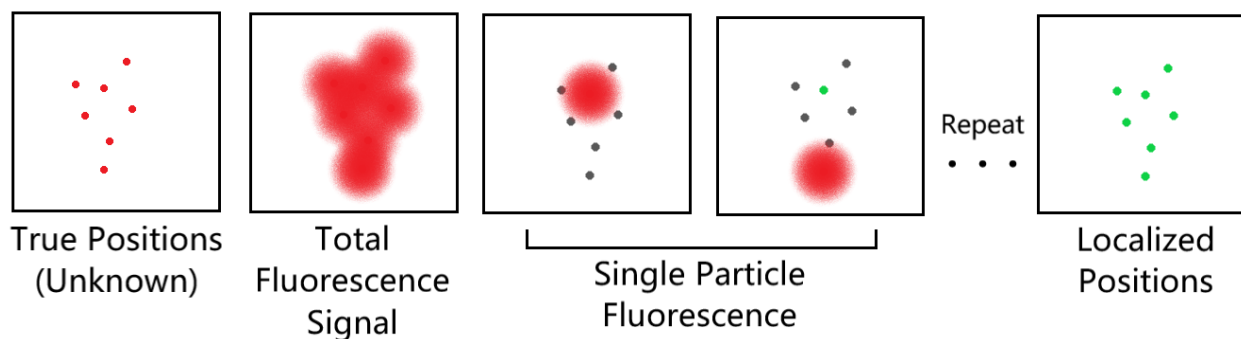


Figure 4.13: Simplified mechanism of STORM. Fluorescing particles (red) cannot be resolved with all particles fluorescing at the same time. By only allowing one particle to emit a signal while the other particles remain inert (grey), this allows for one particle to be localized (green) at a time. By repeating the process, eventually all particles can be localized, despite being at a distance below the Abbe resolution limit.

While the PALM and STORM methods are ground-breaking, the research presented later in this dissertation does not use the enhanced multi-particle resolution methods presented here for a very important reason: these techniques are not required for single emitters with large distances of separation and low incidence of overlap. In addition, the multiple-particle localization techniques mentioned above require relatively immobile and stable fluorophores, ideally as part of a much larger structure that does not migrate over time. Localizing multiple

fluorophores over an extended period of time only works if the particles can be assumed to continue existing in that location during their “dark” state. As previously discussed, Brownian motion and the force of an electric field are such large factors when it comes to small particles that a particle can be tens or hundreds of micrometers away after just a few seconds. Very quickly, our use of these localization techniques transitioned to tracking the particle over an extended period of time.

4.5. Particle Tracking

As a FL nanoparticle moves, it now becomes a function of two different time-based measurements: exposure time and frame capture rate³⁶. With longer exposure times, there is an increase in the amount of signal gained from the particle, enough to overcome the static noise present in cameras, but this simultaneously increases the uncertainty in the position of the particle³⁷. On the opposite end, knowing the absolute position of the particle for the entirety of its movement requires having multiple frames for multiple positions. With a low frame rate, there are large sections of time where the particle’s position is largely unknown, but an incredibly high frame rate results in a low exposure time, decreasing the number of detectable photons per frame³⁸. These two measures must be carefully balanced to achieve optimal data acquisition: enough exposure time to properly detect the fluorescent signal and enough frames to accurately measure the particle’s trajectory³⁹. The precise method of balancing these two competing measurements depends upon several factors, including the camera type, microscope setup, fluorescent particle parameters, excitation beam parameters, and microfluidic cell design⁴⁰.

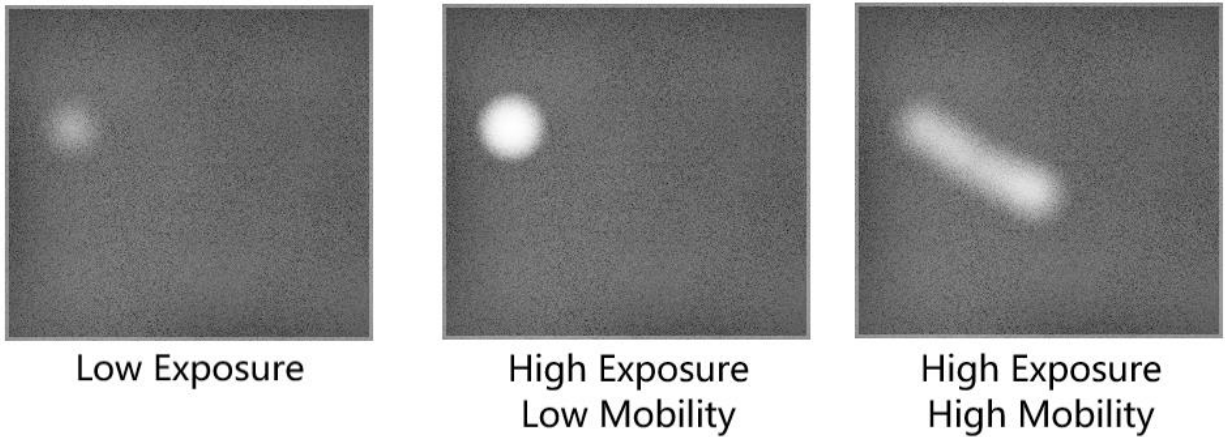


Figure 4.14: Exposure differences for a single moving fluorophore.

(Low Exposure): the weak signal is barely detectable above the static noise of the camera.

(High Exposure, Low Mobility): the ideal case for particle localization, but unrealistic for Brownian particle tracking.

(High Exposure, High Mobility): the worst-case scenario for an over-exposed particle as it moves, where the position of the particle is ambiguous and blurred.

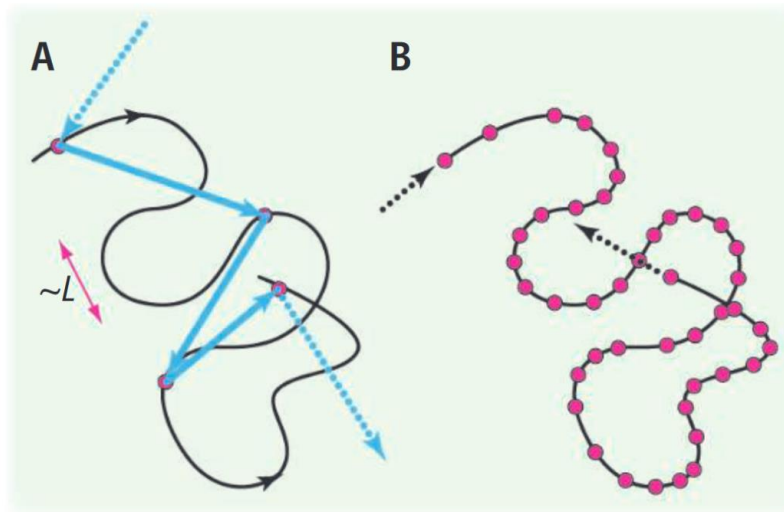


Figure 4.15: Depiction of a particle undergoing Brownian motion by P. Pusey in *Brownian Motion goes Ballistic*³⁸.

The particle follows a chaotic but smooth trajectory (black line), with measured positions of the particle (red dots)

with either **A**) low or **B**) high relative frame rates. For low frame rate, the particle's speed and direction (blue arrows) appear to change dramatically between measurements and with a large loss in its true position.

It is important to remember that no single set of frame rate and exposure time is universally applicable and that the two parameters are in direct conflict. For any given particle, enough exposure time must be achieved to properly locate and isolate a particle's signal without overexposing and blurring the position, with enough frames-per-second as to chart as much of the true path as is allowed by the exposure rate.

- (1) Al-Khalili, J. In Retrospect: Book of Optics. *Nature* **2015**, *518* (7538), 164–165. <https://doi.org/10.1038/518164a>.
- (2) Tbakhi, A.; Amr, S. S. Ibn Al-Haytham: Father of Modern Optics. *Ann Saudi Med* **2007**, *27* (6), 464–467. <https://doi.org/10.5144/0256-4947.2007.464>.
- (3) Zde. English: Galilei Telescopes.; 2022. https://commons.wikimedia.org/wiki/File:Galilei_telescopes,_Museo_Galileo,_Florence,_Inv._242,_2428,_224088.jpg (accessed 2023-05-15).
- (4) Zde. English: Galilean Compound Microscope. Inventor Galileo Galilei (1610-1625). Maker Giuseppe Campani (Attr.), Second Half 17th Century. Cardboard, Leather, Wood, Iron, Height 200 Mm, Diameter 55 Mm. Museo Galileo, Florence, Inv. 3429.; 2022. https://commons.wikimedia.org/wiki/File:Galilean_Compound_Microscop,_Museo_Galileo,_Florence,_Inv._3429,_224113.jpg (accessed 2023-05-15).
- (5) *Galileo and the Telescope | Modeling the Cosmos | Articles and Essays | Finding Our Place in the Cosmos: From Galileo to Sagan and Beyond | Digital Collections | Library of Congress*. Library of Congress, Washington, D.C. 20540 USA. <https://www.loc.gov/collections/finding-our-place-in-the-cosmos-with-carl-sagan/articles-and-essays/modeling-the-cosmos/galileo-and-the-telescope> (accessed 2023-04-04).
- (6) Haden, R. L. Galileo and the Compound Microscope. *Bulletin of the History of Medicine* **1942**, *12* (2), 242–247.
- (7) Brown, R. XXVII. a Brief Account of Microscopical Observations Made in the Months of June, July and August 1827, on the Particles Contained in the Pollen of Plants; and on the General Existence of Active Molecules in Organic and Inorganic Bodies. *The Philosophical Magazine* **1828**, *4* (21), 161–173. <https://doi.org/10.1080/14786442808674769>.
- (8) Belleville, M. *Discoveries - Hubble's Deep Fields*. NASA. <http://www.nasa.gov/content/discoveries-hubbles-deep-fields> (accessed 2022-08-26).
- (9) Garner, R. *NASA's Webb Delivers Deepest Infrared Image of Universe Yet*. NASA. <http://www.nasa.gov/image-feature/goddard/2022/nasa-s-webb-delivers-deepest-infrared-image-of-universe-yet> (accessed 2023-02-28).
- (10) Griggs, M. B. *Here's why the first images from JWST look riddled with "lens flare."* The Verge. <https://www.theverge.com/23220109/james-webb-space-telescope-stars-diffraction-spike> (accessed 2023-03-22).
- (11) Ulrich, M. Confocal Laser Scanning Microscopy. *Hautarzt* **2015**, *66* (7), 504–510. <https://doi.org/10.1007/s00105-015-3632-y>.
- (12) *RASC Calgary Centre - Star Sizes*. <https://calgary.rasc.ca/starsizes.htm> (accessed 2023-03-02).
- (13) *The Airy Disk and Diffraction Limit | Edmund Optics*. <https://www.edmundoptics.com/knowledge-center/application-notes/imaging/limitations-on-resolution-and-contrast-the-airy-disk/> (accessed 2023-03-02).
- (14) *ZEISS Microscopy Online Campus | Microscopy Basics | Numerical Aperture and Resolution*. <https://zeiss-campus.magnet.fsu.edu/articles/basics/resolution.html> (accessed 2023-03-02).
- (15) *The Diffraction Barrier in Optical Microscopy*. Nikon's MicroscopyU.

- <https://www.microscopyu.com/techniques/super-resolution/the-diffraction-barrier-in-optical-microscopy> (accessed 2023-03-02).
- (16) *Sir George Biddell Airy | British astronomer | Britannica*.
<https://www.britannica.com/biography/George-Biddell-Airy> (accessed 2023-03-03).
- (17) Abbe, E. Beiträge zur Theorie des Mikroskops und der mikroskopischen Wahrnehmung. *Archiv f. mikrosk. Anatomie* **1873**, 9 (1), 413–468. <https://doi.org/10.1007/BF02956173>.
- (18) Volkmann, H. Ernst Abbe and His Work. *Appl. Opt., AO* **1966**, 5 (11), 1720–1731. <https://doi.org/10.1364/AO.5.001720>.
- (19) Dijkstra, R. Brightness Characterization of Single Core and Core/Shell Yb³⁺, Er³⁺-Doped NaYF₄ Upconversion Nanoparticles, University of Twente, 2012.
http://essay.utwente.nl/65898/1/Master_Thesis_Remko_Dijkstra%20OVERSLAG%20IS%20NOG%201%20JAAR%20VERTROUWELIJK%21.pdf (accessed 2023-03-01).
- (20) Paschotta, D. R. *Beam Waist*. https://www.rp-photonics.com/beam_waist.html (accessed 2023-03-01).
- (21) Meilan, P. F.; Garavaglia, M. Rayleigh Resolution Criterion for Light Sources of Different Spectral Composition. *Brazilian Journal of Physics* **1997**, 27 (4).
- (22) Rayleigh. Investigations in Optics, with Special Reference to the Spectroscope. *The London, Edinburgh, and Dublin Philosophical Magazine and Journal of Science* **1879**, 8 (49), 261–274. <https://doi.org/10.1080/14786447908639684>.
- (23) Huang, B.; Babcock, H.; Zhuang, X. Breaking the Diffraction Barrier: Super-Resolution Imaging of Cells. *Cell* **2010**, 143 (7), 1047–1058. Reprinted with Permission (5533430745431) <https://doi.org/10.1016/j.cell.2010.12.002>.
- (24) Chen, K. R. Focusing of Light beyond the Diffraction Limit of Half the Wavelength. *Opt. Lett., OL* **2010**, 35 (22), 3763–3765. <https://doi.org/10.1364/OL.35.003763>.
- (25) *Visible Light | Science Mission Directorate*. https://science.nasa.gov/ems/09_visiblelight (accessed 2023-03-01).
- (26) *Electron Microscopy | TEM vs SEM - US*.
<https://www.thermofisher.com/us/en/home/materials-science/learning-center/applications/sem-tem-difference.html> (accessed 2023-03-08).
- (27) Sanjeeva Murthy, N. Scattering Techniques for Structural Analysis of Biomaterials. In *Characterization of Biomaterials*; Jaffe, M., Hammond, W., Tolias, P., Arinze, T., Eds.; Woodhead Publishing Series in Biomaterials; Woodhead Publishing, 2013; pp 34–72. <https://doi.org/10.1533/9780857093684.34>.
- (28) *Fluorescence Fundamentals | Thermo Fisher Scientific - US*.
<https://www.thermofisher.com/us/en/home/references/molecular-probes-the-handbook/introduction-to-fluorescence-techniques.html> (accessed 2023-03-08).
- (29) *FluoSpheres™ Carboxylate-Modified Microspheres*.
<https://www.thermofisher.com/order/catalog/product/F8787> (accessed 2022-10-20).
- (30) Small, A.; Stahlheber, S. Fluorophore Localization Algorithms for Super-Resolution Microscopy. *Nat Methods* **2014**, 11 (3), 267–279. Reprinted with permission (5533430907750) <https://doi.org/10.1038/nmeth.2844>.
- (31) Thompson, R. E.; Larson, D. R.; Webb, W. W. Precise Nanometer Localization Analysis for Individual Fluorescent Probes. *Biophysical Journal* **2002**, 82 (5), 2775–2783. [https://doi.org/10.1016/S0006-3495\(02\)75618-X](https://doi.org/10.1016/S0006-3495(02)75618-X).

- (32) Shroff, H.; White, H.; Betzig, E. Photoactivated Localization Microscopy (PALM) of Adhesion Complexes. *Curr Protoc Cell Biol* **2013**, CHAPTER 4, Unit4.21. <https://doi.org/10.1002/0471143030.cb0421s58>.
- (33) *Fluorescence PhotoActivation Localization Microscopy (FPALM) - Physics and Astronomy - University of Maine*. Physics and Astronomy. <https://physics.umaine.edu/research/biophysics-research-group/fpalmhome/fpalmoverview/> (accessed 2023-03-23).
- (34) Waterman-Storer, C. M.; Desai, A.; Chloe Bulinski, J.; Salmon, E. D. Fluorescent Speckle Microscopy, a Method to Visualize the Dynamics of Protein Assemblies in Living Cells. *Current Biology* **1998**, 8 (22), 1227-S1. [https://doi.org/10.1016/S0960-9822\(07\)00515-5](https://doi.org/10.1016/S0960-9822(07)00515-5).
- (35) Rust, M. J.; Bates, M.; Zhuang, X. Sub-Diffraction-Limit Imaging by Stochastic Optical Reconstruction Microscopy (STORM). *Nat Methods* **2006**, 3 (10), 793–796. <https://doi.org/10.1038/nmeth929>.
- (36) Jaqaman, K.; Loerke, D.; Mettlen, M.; Kuwata, H.; Grinstein, S.; Schmid, S. L.; Danuser, G. Robust Single-Particle Tracking in Live-Cell Time-Lapse Sequences. *Nat Methods* **2008**, 5 (8), 695–702. <https://doi.org/10.1038/nmeth.1237>.
- (37) Parthasarathy, R. Rapid, Accurate Particle Tracking by Calculation of Radial Symmetry Centers. *Nat Methods* **2012**, 9 (7), 724–726. <https://doi.org/10.1038/nmeth.2071>.
- (38) Pusey, P. N. Brownian Motion Goes Ballistic. *Science* **2011**, 332 (6031), 802–803. <https://doi.org/10.1126/science.1192222>.
- (39) Qian, H.; Sheetz, M. P.; Elson, E. L. Single Particle Tracking. Analysis of Diffusion and Flow in Two-Dimensional Systems. *Biophysical Journal* **1991**, 60 (4), 910–921. [https://doi.org/10.1016/S0006-3495\(91\)82125-7](https://doi.org/10.1016/S0006-3495(91)82125-7).
- (40) Barnkob, R.; Kähler, C. J.; Rossi, M. General Defocusing Particle Tracking. *Lab Chip* **2015**, 15 (17), 3556–3560. <https://doi.org/10.1039/C5LC00562K>.

Chapter 5

Contemporary Inspiring Research

5.1. Chapter Overview

This chapter is dedicated to highlighting more contemporary on-going research and the particularly inspiring research papers that have had direct influences towards our analysis of the Electric Double Layer. These include particle manipulation, particle tracking, microfluidic trap synthesis, solution-ion concentration analysis, non-Brownian movements, volumetric analysis, and directional fluid flow. Obviously, it would be impossible to discuss every single influential research topic, but the topics presented here are of such substantial impact and importance towards my own analysis chapters that I felt they warranted their own chapter. It is the goal of this chapter to be brief but tantalizing. I strongly encourage any reader to dig further on any of the papers presented here if they find themselves curious, as well as any other works created by other members of The One Molecule Group.

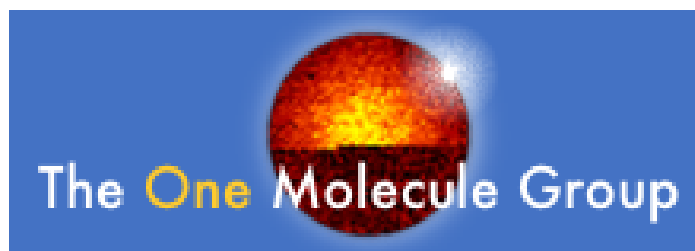


Figure 5.1: The official banner for Woehl Lab: The One Molecule Group

5.2. The Anti-Brownian Electrophoretic (ABEL) Trap by Cohen and Moerner (2006)¹⁻⁵

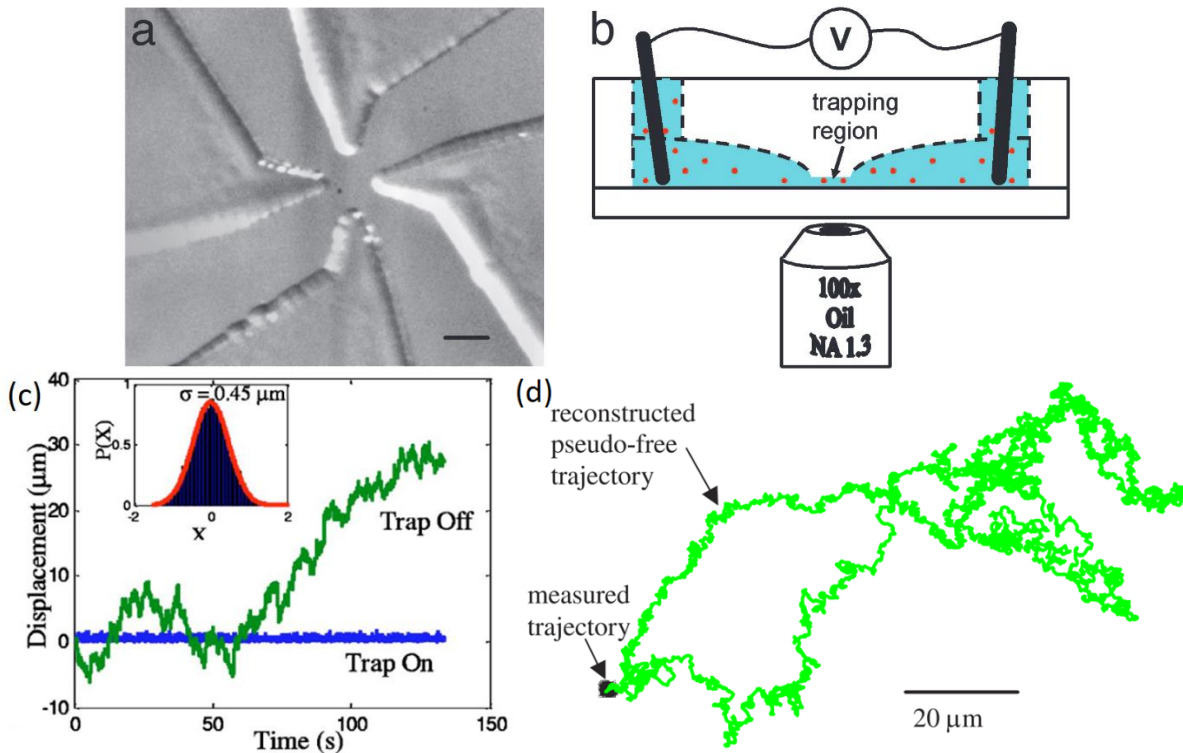


Figure 5.2: The ABEL Trap. **a)** The trapping region of four gold electrodes. **b)** Side view of the microfluidic device. **c)** 1-Dimensional displacement vs. time graph of a particle depending on whether the trap is on or off. **d)** A trapped particle analyzed over 45 seconds, with its real and reconstructed 2-Dimensional trajectory.

Seeking to simultaneously limit the movement and analyze the effects of Brownian motion on a particle, Cohen and Moerner created a unique trapping mechanism that uses a 2-axis electric field, where the two sets of gold electrodes can apply an electrokinetic force to a particle within the trap. By accurately measuring the particle's position, a brief feedback voltage can be applied to the electrodes to induce a counter-drift that returns the particle to the original position. While the corral trap is on the particle will be effectively stationary, the small displacements it would have undergone (but were countered) can be stitched together to create a hypothetical trajectory that it would have followed had it been free to do so.

5.3. Electrostatic Corral Trap by Woehl, Carlson, and Udad (2019)⁶⁻⁸

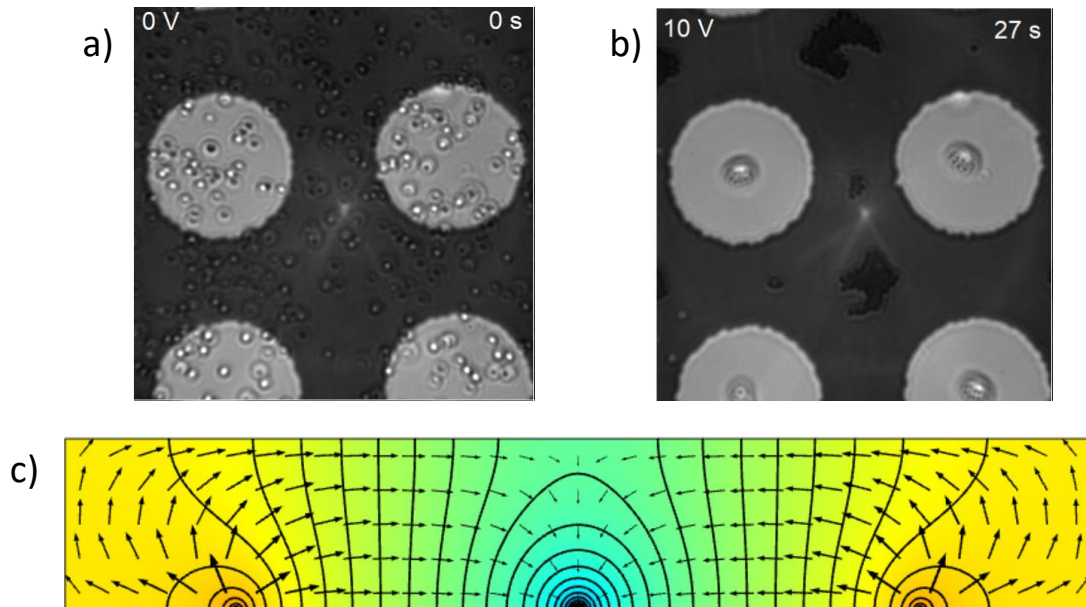


Figure 5.3: a) 40x magnification of 2 μm polystyrene beads in solution. b) The same sample after 27 seconds with 10V applied to the nickel chromium electrodes. c) COMSOL calculation of the dielectrophoretic potential as a logarithmic electric field, showing areas of high DEP potential (orange) and low (blue)

The Corral Trap can trap by applying either AC or DC potentials. With an AC field, dielectrophoretic forces guide the particles using non-uniform fields. By creating a unique set of trap geometries, particles can be attracted towards or repelled from specific areas. Switching between positive (towards increasing electric field) or negative (towards decreasing electric field) dielectrophoresis can be accomplished by tuning the frequency of the AC potential.

Trapping with a DC field, a main motivator for this dissertation, instead relies on static potentials on a single electrode: a negative potential on the electrode repels negatively charged particles. Inside non-conductive regions or voids in the metal, this will cause repulsion to push particles further into the non-conductive region until they reach a localized minimum, with the strength of the trap dependent on the applied voltage.

5.4. Undamped 3D Brownian Motion of Nanoparticles using Liquid-Cell (Scanning)

Transmission Electron Microscopy (LC(S)TEM) by Welling et al. (2020)⁹

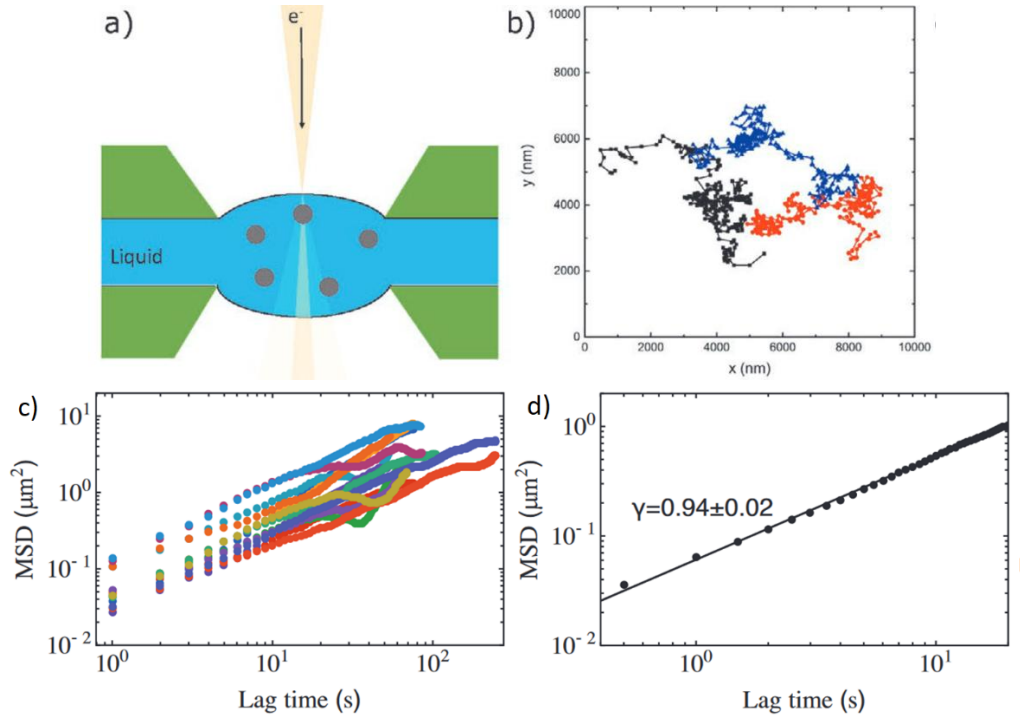


Figure 5.4: 350nm titanium oxide nanoparticles suspended in glycerol carbonate **a)** Liquid-cell diagram of the incident STEM focused electron beam and suspended particles. **b)** Particle trajectories over 100 seconds. **c)** MSD trajectories of 14 particles using a logarithmic scale. **d)** Averaged MSD showing subdiffuse motion.

During LC(S)TEM, a high energy electron beam is passed through a sample and the resulting scattering is analyzed. This high energy beam causes particles to have dramatically slower diffusion (up to 8 orders of magnitude away from theoretical values) as the particle is effectively held in place, much like optical tweezers. By utilizing a lower electron dosage rate ($0.6\text{-}2.4\text{ e}^- \text{ nm}^{-2} \text{ s}^{-1}$) on two specific sets of particles, 77nm neutral gold nanoparticles in glycerol and 350nm titanium oxide particles in glycerol carbonate, the perturbations were minimized. Finally, by analyzing the particle's pixel clarity and comparing it to a set of standardized images, rough estimations on the z-axis position in addition to x and y axes can be made.

5.5. Confined Brownian Tracking with Motion Blur by Mortensen et al. (2021)¹⁰

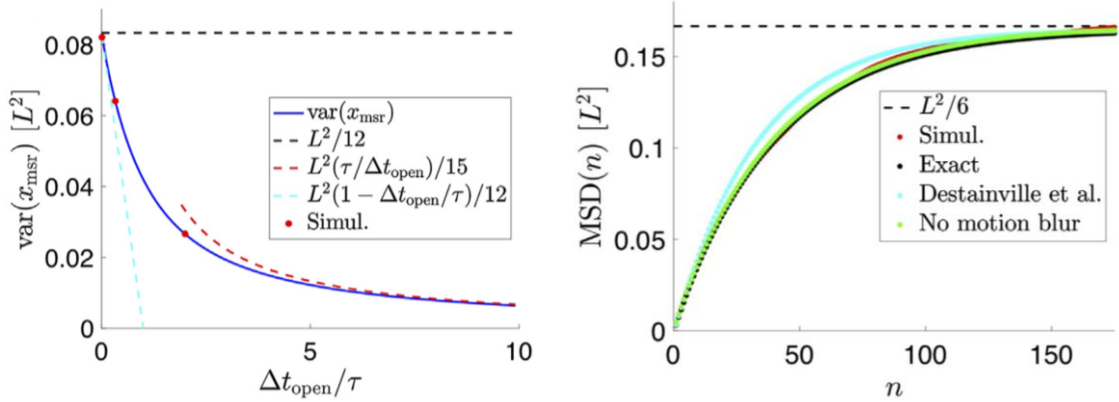


Figure 5.5: Variance (**left**) and mean-square-displacement (**right**) of a simulated particle undergoing Brownian motion in a 1D Box with a characteristic timescale of 0.01, comparing the limits, simulation, and exact values.

As measurements of particle positions are limited by image capture, motion blur causes the exact positions of a tracked particle to become inaccurate, favoring unrealistically low mobility. Mortensen thus derived exact expressions, accounting for this blurring effect, for the mean square displacement and variance of Brownian particles within finite spaces, such as a 1D Box:

$$\text{var}(x_{\text{msr}}) = \frac{L^2 \tau}{15 \Delta t} - L^2 \left(\frac{2}{\pi}\right)^8 \left(\frac{\tau}{\Delta t}\right)^2 \sum_{p=0}^{\infty} \frac{\left\{1 - \exp\left[-\left(\frac{(1+2p)\pi}{2}\right)^2 \frac{\Delta t}{\tau}\right]\right\}}{(1+2p)^8} \quad (5.1)$$

$$\text{MSD}(n) = 2\text{var}(x_{\text{msr}}) - L^2 \left(\frac{2}{\pi}\right)^8 \left(\frac{\tau}{\Delta t}\right)^2 \sum_{p=0}^{\infty} \frac{\left\{1 - \exp\left[-\left(\frac{(1+2p)\pi}{2}\right)^2 \frac{\Delta t}{\tau}\right]\right\}}{(1+2p)^8} \left(1 - e^{-\frac{[\frac{\pi}{2}(1+2p)]\Delta t}{\tau}}\right)^2 \quad (5.2)$$

Here, $\tau \equiv L^2/4D$, L is the length of the confinement, D is the diffusion coefficient, Δt is the image capture time, and p is the initial position. While lengthy, these equations are valid for all expression times, regardless of the size or geometric complexity of the confinement or the diffusion coefficient of the particle. These can also be simplified at high/low values of $\Delta t/\tau$ to provide the appropriate limits, although not presented here.

5.6. Accounting for Electric Double Layer and Pressure Gradient-Induced Dispersion Effects in Microfluidic Current Monitoring by McCallum and Pennathur (2016)¹¹

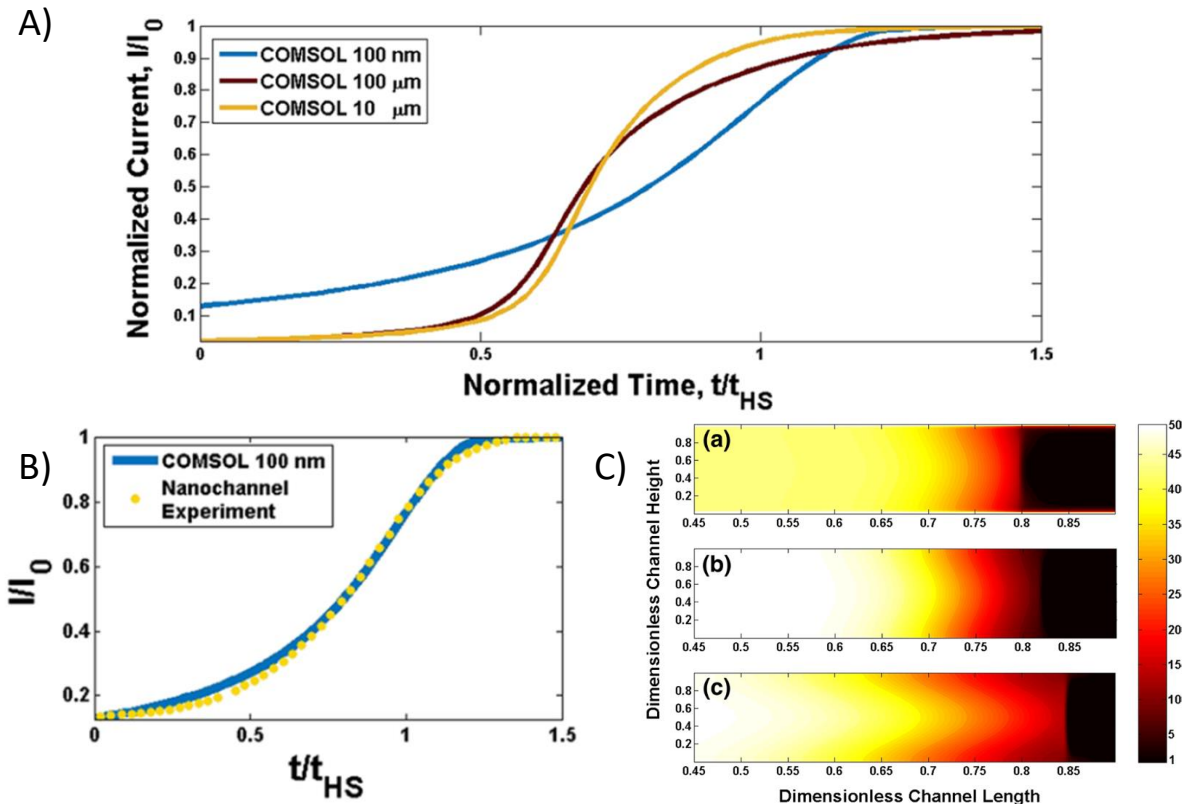


Figure 5.6: **A)** Normalized COMSOL simulations of 100 nm, 10 μm , and 100 μm separated electrodes when 50 mM KCl displaces 1 mM. **B)** Comparison of COMSOL simulation to experimental results. **C)** COMSOL color map of KCl ionic strength at a normalized timestep of 0.54 of (a) 100nm, (b) 10 μm , and (c) 100 μm

As a concentrated solution displaces another, the change in the zeta-potential of the EDL is a linear function determined by the flow rate as measured by current monitoring. Utilizing a 100nm electrode distance, a small increase in concentration results in a linear increase of current, while high concentration ratios (e.g. 50:1) result in non-linear increases in current.

If the Debye length constitutes a large percentage of the electrode distance, then the EDL no longer becomes negligible. With small distances, the concentration gradient is guided by convective dispersion, while with larger distances, advective diffusion becomes dominant.

5.7. Surface Potential at the Electrolyte-Nanoparticle Interface by Brown et al. (2016)^{12,13}

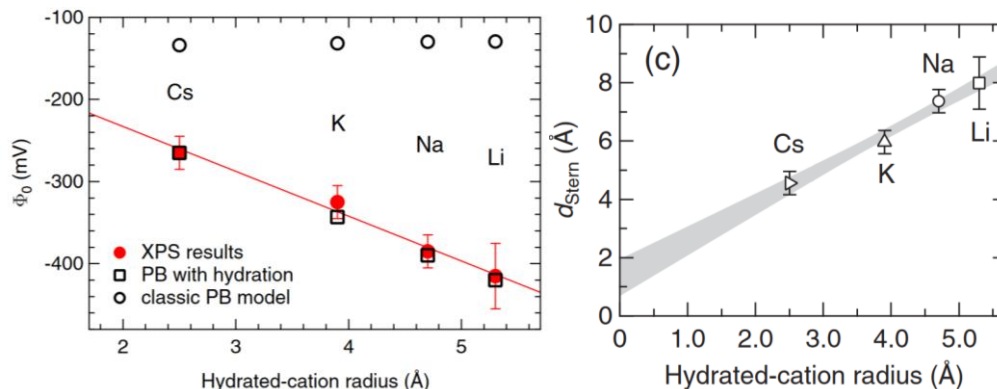


Figure 5.7: (left) Surface potential of the nanoparticles, showing the XPS results (red) are in line with the hydration model (squares) of the Poisson-Boltzmann theory. **(right)** Stern layer thickness as a function of cation radius.

While X-ray photoelectron spectroscopy (XPS) typically requires the sample be in vacuum, Brown et al. instead used a microjet of suspended silica nanoparticles to capture emitted photoelectrons, which can be analyzed to find the surface potential on the nanoparticles. The emitted photoelectrons are dependent upon the binding energy, which is either accelerated or decelerated depending on the surface potential.

The energy spectra's shifts were analyzed with several different cations in different pH ranges to impart differing surface-solution potentials to find the surface potential of the nanoparticles. They found that the experimental results greatly conflicted with the classical Poisson-Boltzmann model, but a modified model adding a hydration repulsion component removes this error. By then incorporating this into the GCS model, Brown et al. computed the structure and depth of the Stern layer: the radius of the ion plus a single monolayer of hydrating water molecules, consistent with other direct methods.

5.8. Structure of the Electrical Double Layer Revisited: Electrode Capacitance in Aqueous Solutions by Khademi & Barz (2020)¹⁴

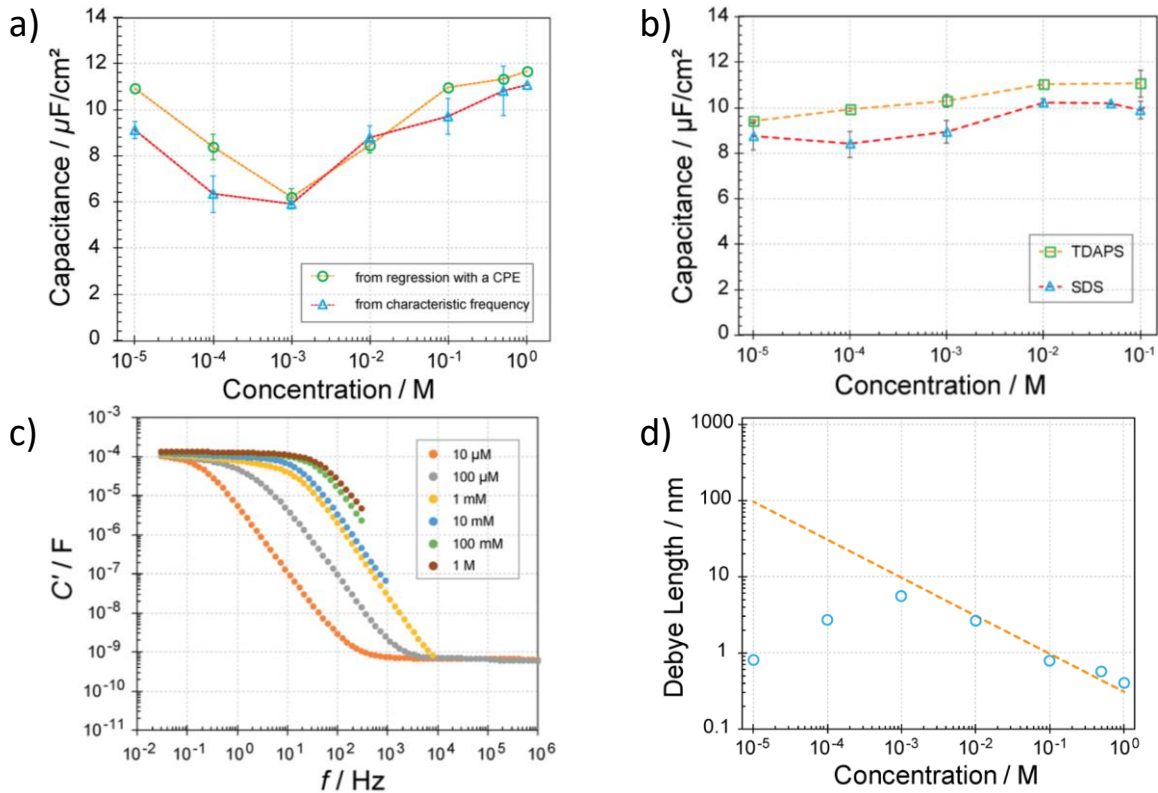


Figure 5.8: EDL capacitance vs log scale concentration of **a)** NaCl and **b)** large molecules, TDAPS and SDS.

c) Real factor of the complex capacitance vs frequency with varying concentrations of NaCl.

d) Experimental (dots) vs theoretical values (dashed line) of the Debye length vs concentration of NaCl

While the GCS model has capacitance determined by the diffuse layer, Khademi and Barz found the Stern Layer to be the dominant factor, which remains at a constant magnitude regardless of concentration. Utilizing sinusoidal AC voltage, they found that at either high or low frequencies, the capacitance plateaus to a constant value. As low frequency is DC-like, where the current has to pass all ohmic and charge transfer resistance, they were able to determine that the Debye length does not linearly change with varying concentration as the current theoretical model asserts, instead tapering off to a much lower value.

5.9. Rapid Particle Tracking by Calculation of Radial Symmetry by R. Parthasarathy (2012)¹⁵

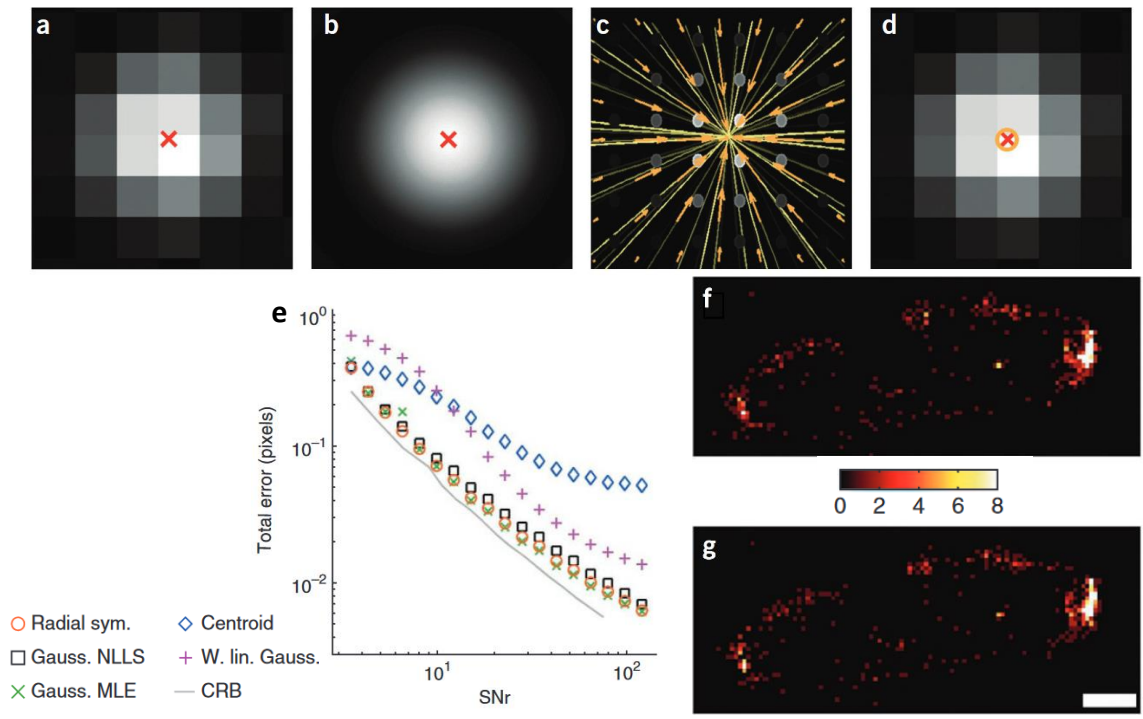


Figure 5.9: A simulated point-source, where X is the true center position. The pixelated image (a) is based on the noise-free simulated image (b). The orange intensity gradient lines (c) are calculated from each pixel’s shared borders, which give the estimation in (d) as the yellow circle. (e) The localization error from simulated particles over a range of signal-noise ratios, each point representing 1000 tests. (f) and (g) are localized microscopy images of *E. coli* bacterium, reconstructed from radial symmetry and Gaussian MLE, respectively. The scale bar is 500 nm.

As discussed in Chapter 4, typical sub-pixel localization uses two-dimensional least-squares Gaussian fitting. Parthasarathy proposes an approach using the intensity distribution of radial symmetry: any line drawn parallel to the gradient will intersect the particle’s center. With a simple matrix of points around the particle, an array of lines can quickly estimate the central position of any emission-symmetrical particle. It was found that radial symmetry is close to the Cramer-Rao Bound limit¹⁶, the theoretical limit on error, while also being roughly 100 times faster than other techniques.

5.10. General Defocusing Particle Tracking (GDPT) by Barnkob, Kahler, and Rossi (2015)¹⁷

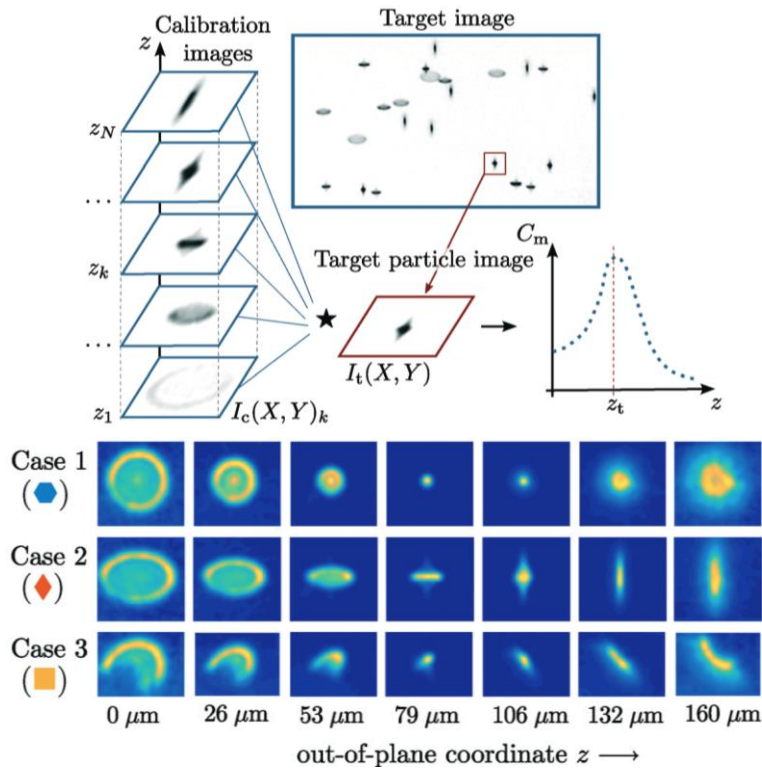


Figure 5.10: (top) A target particle image I_t is compared and correlated to a library of calibration images. The correlation function C_m is highest at the coordinate value z_t . **(bottom)** Images as a function of depth. Case 1 is a spherical particle, Case 2 has a 1-dimensional astigmatism, and Case 3 has a non-uniform astigmatism.

GDPT extracts additional data from the shape and size of a particle to form an approximation on the z -direction depth of a particle. By combining it with the standard x - y coordinates, particles can thus be tracked in 3-dimensions while using a single camera. This is done by creating a reference calibration library of particle images at varying depths, which can then be compared to a sample image. Using cross-correlation analysis, the image will be matched to a specific particle depth via its maximized correlated value. This analysis can be done on several particles within a single image, providing quick and efficient measurements with minimal error, if the particle profiles are uniform and roughly spherical.

- (1) Cohen, A. E. Control of Nanoparticles with Arbitrary Two-Dimensional Force Fields. *Phys. Rev. Lett.* **2005**, *94* (11), 118102. Reprinted with permission (RNP/23/APR/065395) <https://doi.org/10.1103/PhysRevLett.94.118102>.
- (2) Cohen, A. E.; Moerner, W. E. Method for Trapping and Manipulating Nanoscale Objects in Solution. *Appl. Phys. Lett.* **2005**, *86* (9), 093109. Reprinted with permission (5532730713746) <https://doi.org/10.1063/1.1872220>.
- (3) Cohen, A. E.; Moerner, W. E. Suppressing Brownian Motion of Individual Biomolecules in Solution. *Proc. Natl. Acad. Sci. U.S.A.* **2006**, *103* (12), 4362–4365. Copyright (2006) National Academy of Sciences, U.S.A <https://doi.org/10.1073/pnas.0509976103>.
- (4) Cohen, A. E.; Moerner, W. E. An All-Glass Microfluidic Cell for the ABEL Trap: Fabrication and Modeling; Dholakia, K., Spalding, G. C., Eds.; San Diego, California, USA, 2005; p 593005. <https://doi.org/10.1117/12.622418>.
- (5) Cohen, A. E.; Moerner, W. E. The Anti-Brownian Electrophoretic Trap (ABEL Trap): Fabrication and Software; Nicolau, D. V., Enderlein, J., Leif, R. C., Farkas, D. L., Raghavachari, R., Eds.; San Jose, CA, 2005; p 296. <https://doi.org/10.1117/12.598689>.
- (6) Udad, X. S. Controlling and Manipulating Microscopic Particles in Solution by Using Various Electric Field Geometries, 2019. Reprinted with Permission
- (7) Carlson, C. Development of the Electrostatic Corral for the Trapping of Single Molecules in Solution. **2010**.
- (8) Kwak, T. J.; Lee, H.; Lee, S. W.; Woehl, J. C.; Chang, W.-J. Size-Selective Particle Trapping in Dielectrophoretic Corral Traps. *J. Phys. Chem. C* **2021**, *125* (11), 6278–6286. <https://doi.org/10.1021/acs.jpcc.0c10592>.
- (9) Welling, T. A. J.; Sadighikia, S.; Watanabe, K.; Grau-Carbonell, A.; Bransen, M.; Nagao, D.; Blaaderen, A. van; Huis, M. A. van. Observation of Undamped 3D Brownian Motion of Nanoparticles Using Liquid-Cell Scanning Transmission Electron Microscopy. *Particle & Particle Systems Characterization* **2020**, *37* (6), 2000003. Reprinted with permission (5532830428738) <https://doi.org/10.1002/ppsc.202000003>.
- (10) Mortensen, K. I.; Flyvbjerg, H.; Pedersen, J. N. Confined Brownian Motion Tracked With Motion Blur: Estimating Diffusion Coefficient and Size of Confining Space. *Front. Phys.* **2021**, *0*. <https://doi.org/10.3389/fphy.2020.583202>.
- (11) McCallum, C.; Pennathur, S. Accounting for Electric Double Layer and Pressure Gradient-Induced Dispersion Effects in Microfluidic Current Monitoring. *Microfluid Nanofluid* **2016**, *20* (1), 13. Reprinted with permission (5532830882988) <https://doi.org/10.1007/s10404-015-1684-z>.
- (12) Brown, M. A.; Abbas, Z.; Kleibert, A.; Green, R. G.; Goel, A.; May, S.; Squires, T. M. Determination of Surface Potential and Electrical Double-Layer Structure at the Aqueous Electrolyte-Nanoparticle Interface. *Phys. Rev. X* **2016**, *6* (1), 011007. <https://doi.org/10.1103/PhysRevX.6.011007>.
- (13) Brown, M. A.; Bossa, G. V.; May, S. Emergence of a Stern Layer from the Incorporation of Hydration Interactions into the Gouy–Chapman Model of the Electrical Double Layer. *Langmuir* **2015**, *31* (42), 11477–11483. <https://doi.org/10.1021/acs.langmuir.5b02389>.
- (14) Khademi, M.; Barz, D. P. J. Structure of the Electrical Double Layer Revisited: Electrode Capacitance in Aqueous Solutions. *Langmuir* **2020**, *36* (16), 4250–4260. Reprinted with permission, American Chemical Society. <https://doi.org/10.1021/acs.langmuir.0c00024>.

- (15) Parthasarathy, R. Rapid, Accurate Particle Tracking by Calculation of Radial Symmetry Centers. *Nat Methods* **2012**, *9* (7), 724–726. Reprinted with Permission (5532831319636) <https://doi.org/10.1038/nmeth.2071>.
- (16) Abraham, A. V.; Ram, S.; Chao, J.; Ward, E. S.; Ober, R. J. Quantitative Study of Single Molecule Location Estimation Techniques. *Opt. Express* **2009**, *17* (26), 23352. <https://doi.org/10.1364/OE.17.023352>.
- (17) Barnkob, R.; Kähler, C. J.; Rossi, M. General Defocusing Particle Tracking. *Lab Chip* **2015**, *15* (17), 3556–3560. <https://doi.org/10.1039/C5LC00562K>.

Chapter 6

Methods and Materials

6.1 Chapter Overview

This chapter is dedicated to discussing the precise materials, amounts, and mechanics used for analyzing the EDL for the purpose of this dissertation. The chapter is outlined in the order of creation that I used when preparing the microfluidic devices used to analyze the various sections of the EDL. Whenever possible, I will include the manufacturer and part number for each piece the first time each part is referenced. If something was custom-made by UWM staff, there will be a brief schematic description included.

6.2 Glass Cleaning Procedures

Due to the specifications of our microscope stage and how the excitation light is collected, which will be discussed later in Section 6.12, the options for a sample microfluidic device are heavily restricted. Therefore, the cells were constructed on 25x25 mm glass coverslips (VWR micro cover glass, #48366-249) due to their sufficient thinness. To ensure an absolutely clean surface, small impurities or microscopic glass fragments present on the raw out-of-the-box slides were removed from the coverslip by placing into the slats of a custom-made Teflon slide holder, as shown in Figure 6.1, and subjected to a specific rinsing regiment.

Successive washes of acetone (Sigma-Aldrich, 99.5% purity), methanol (Sigma-Aldrich, 99.9% purity), and two sets of isopropanol (Sigma-Aldrich, 99.9% purity), from here forward referred to as an AMII wash, were completed as follows: with the slide holder in a standard 250 mL Pyrex glass beaker, a sufficient amount of the solvent was added to fully cover the slides. Depending on the slide size and orientation, the precise amount is variable, but care was made to ensure full submersion. The beaker was then placed within a sonicator (Branson Model 1510

Ultrasonic Cleaner) and sonicated for 10 min each and at a temperature of $\sim 30^{\circ}\text{C}$.

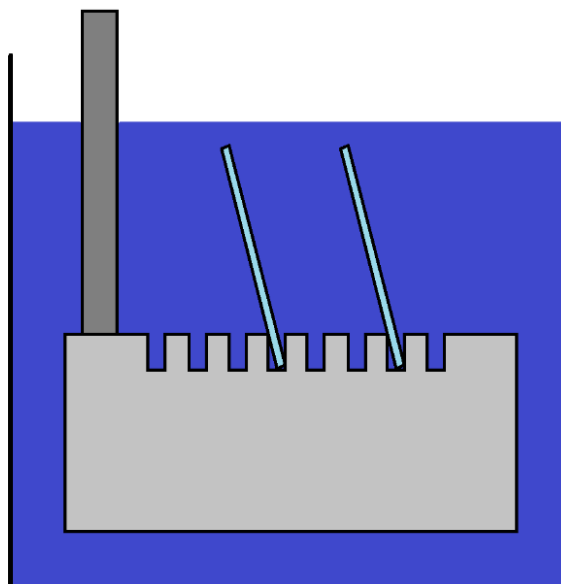


Figure 6.1 – Slide holder (grey) as viewed from the side inside a 250 mL beaker. Glass coverslips (light blue) are inserted into the slats to prevent overlap and to ensure solvent (dark blue) circulates properly.

After each sonication, the beaker was removed from the sonicator, and the slide holder was taken out of the solution via the attached handle. By slightly angling the slide holder, excess solvent would run-off back into the beaker to ensure minimal solvent mixing. The slide holder would then be placed into a fresh 250 mL beaker and filled with the next solvent. As an added precaution to possible solvent adhesion effects, the slide holder's handle also acted as a crude rotation-handle, allowing for a few quick rotations within the beaker to stir and mix the solvent to dilute the previous solvent that might be sticking to the slides and thus impeding proper cleaning. This process is repeated for each successive wash, with the extra isopropanol step at the end to ensure that it has been fully cleaned from any residual acetone or methanol from the previous steps. Each of the solvents targets a different set of impurities commonly found, while sonication helps dislodge any larger debris from the surface.

6.2.1 Slide Drying

After the final wash, the still-submerged slide holder is taken to a nitrogen tank (Airgas Nitrogen compressed, UN1066) where it will be air-purged. With a regulator (Concoa Inert Gas Regulator) and a nozzle through a filter (Millex-FA Filter, 1 μm) attached to the nitrogen tank, it allows for a controlled stream of nitrogen onto the slide surface, as shown in Figure 6.2.

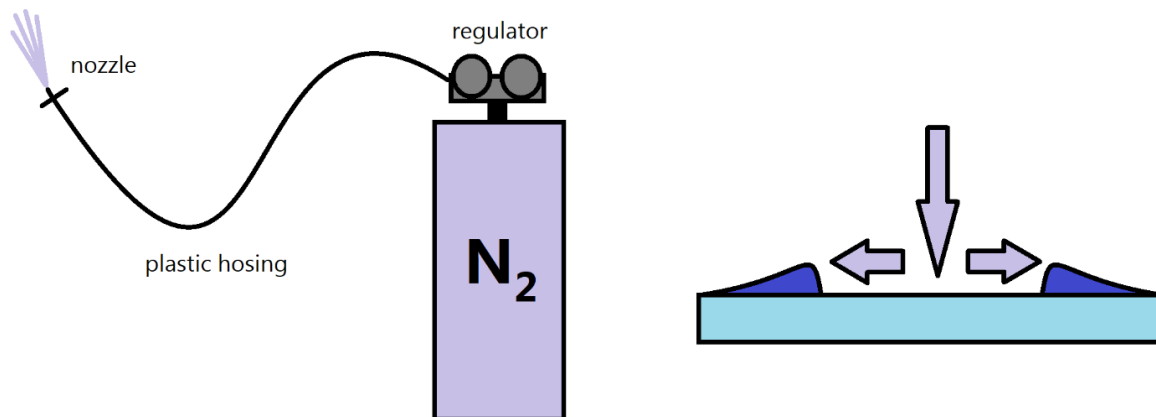


Figure 6.2 – (left) Nitrogen gas tank with attached hosing and nozzle. (right) As the gas pushes down onto the coverslip with sufficient force, it purges the solution (blue) from the surface.

If the slide were simply allowed to air-dry, it was found that even the smallest amount of impurities would concentrate as the solvent evaporated, eventually leaving behind an unnoticeable to the eye, but still detrimental, layer of impurities wherever the solvent evaporated last, akin to the “coffee-stain” effect¹. Instead, by air-purging, the controlled and sustained stream of nitrogen gas acts to create a shockwave like effect: the rapidly moving “wall” of solvent drags impurities to the edge of the slide, away from the center area in which the experiments take place. If there are impurities along the edge, it is sufficiently removed from the experimental area and thus completely negligible. The precise speed and timing of the nitrogen blast is variable depending on slide size, but it is easily repeatable if one ensures that

the solvent is being removed, and not simply dried. The rough amount of time used was a sustained stream of nitrogen for 3-5 seconds.

6.2.2 Preliminary Hexamethyldisilazane (HMDS) Layer

Ideally, the following several steps would be taken inside of a clean room. Lacking this, however, it is still possible to obtain satisfying synthesis if one moves quickly between each step. The longer the wait-time between steps, the higher the chance that a random flake of dust might interact with the surface. Considering that dust flakes are often hundreds of micrometers in diameter, far larger than our eventual goal for our channel height of <1 micrometer, it can be catastrophic for even a single piece of dust to land in our working-area of the slide. Speed and efficiency are essential.

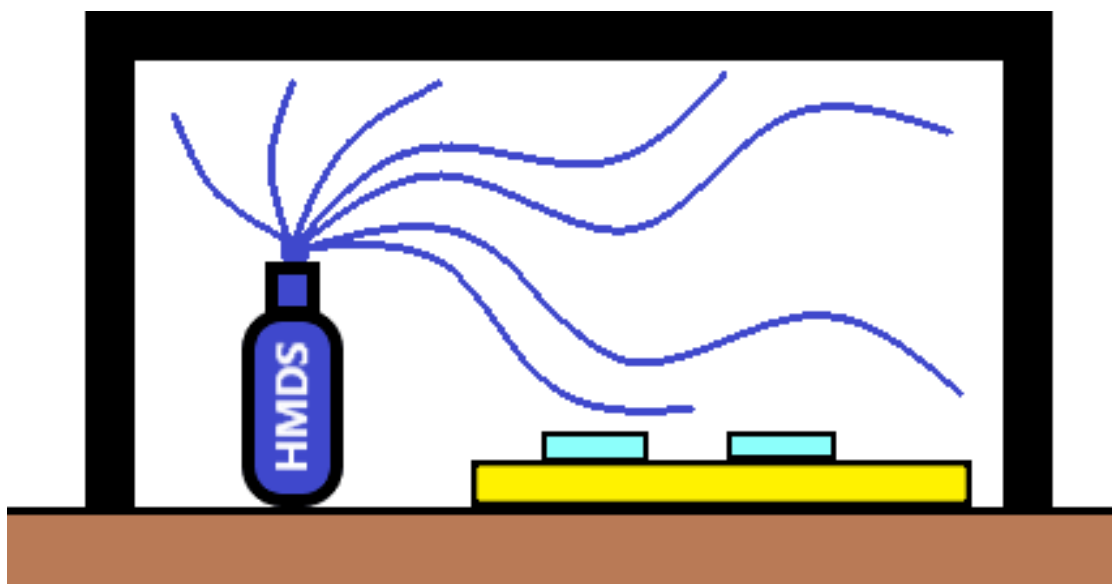


Figure 6.3 – Hexamethyldisilazane vapor (blue) allowed to permeate within a sealed chamber. Glass slides (light blue) are lightly coated with vapor atop a slide holder (yellow)

After all slides are cleaned, they are then placed onto a flat surface within a vapor-chamber where hexamethyldisilazane or HMDS (Sigma-Aldrich, 99.9% purity, #379213) is applied via simple evaporation from the bottle. The vapors within the bottle will spread throughout the chamber, creating a rough monolayer of HMDS on the slides. This layer is vital for the next step: without the HMDS proper adhesion of the polymer is not possible and would cause many of the nanostructures to be malformed or become unattached during the successive steps.

6.3 Application of Positive Photoresist

After the vapor-deposition of HMDS, a thin layer of positive photoresist, specially S1813 Photoresist (Microposit S1813 Positive Photoresist, Dow Chemical), was applied via a spin-coater system (Laurell Tech Model WS-400B-6NPP) to a thickness of 1.50 μm .

Firstly, a brief explanation of photolithography: it is a method of patterning intricate solid structures onto surfaces by utilizing either the breakdown or formation of chemical bonds upon exposure to ultraviolet (UV) light. Only very specific chemicals can achieve this and there are two major types: positive and negative. These two systems roughly follow the same setups (although the time and speed differ due to the differing chemical properties) and the key difference between these is dependent on their interaction with UV light.

Positive photoresist reacts upon UV-exposure: the high-energy light causes the long-chain polymers to completely break apart into shorter fragments which are at least partially soluble in water. Any region that isn't exposed is unaffected, leaving behind complete polymer chains. Negative photoresist, in contrast, works in almost the exact opposite pattern: upon UV-exposure, the high-energy light causes a mass of monomers to chaotically cross-link with the

surrounding chains, creating a tangled web of chemical bonds. For many negative photoresists, such as SU-8 (SU8 2000 Series by Microchem), these are permanent structures. This method is thus not typically recommended for metal deposition. While not used directly in this dissertation, it was used to great effect in many of Woehl Group's other projects.

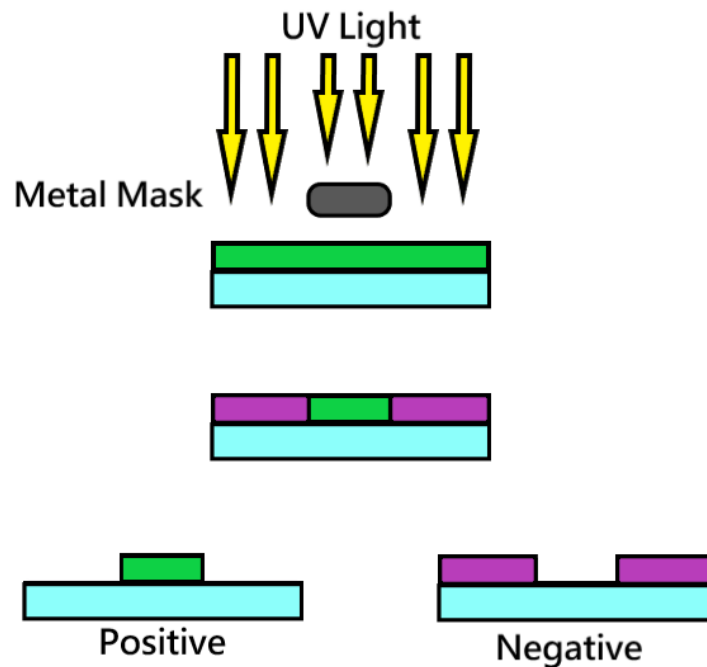


Figure 6.4 – Simplified depiction of photolithography. UV Light (yellow) is blocked by a metal mask (grey), creating an exposed region (purple) and an unexposed region (green). After development, a positive photoresist keeps unexposed substrate, while a negative photoresist keeps only the exposed regions.

Photoresists are typically coated onto a substrate surface via spin-coating, which is a process of high-speed rotation of a platform with an attached sample. In our case, this attachment was done via a vacuum pump built into the center of the platform. After solution is added to the surface at larger-than-desired amounts, the piston is then spun at high rotations per minute, RPM, (typically 1000-7000), which causes the bulk of the solution to be ejected off the surface via centripetal force effects. The solution that is in contact with the glass slide (and

aided by the previously applied HMDS) however will feel an opposed frictional force keeping it attached to the glass. Thus, the amount of polymer left on the slide is dependent on both the viscous nature of the solution used and the RPM. Higher RPM means a higher ejective force and thus less polymer.

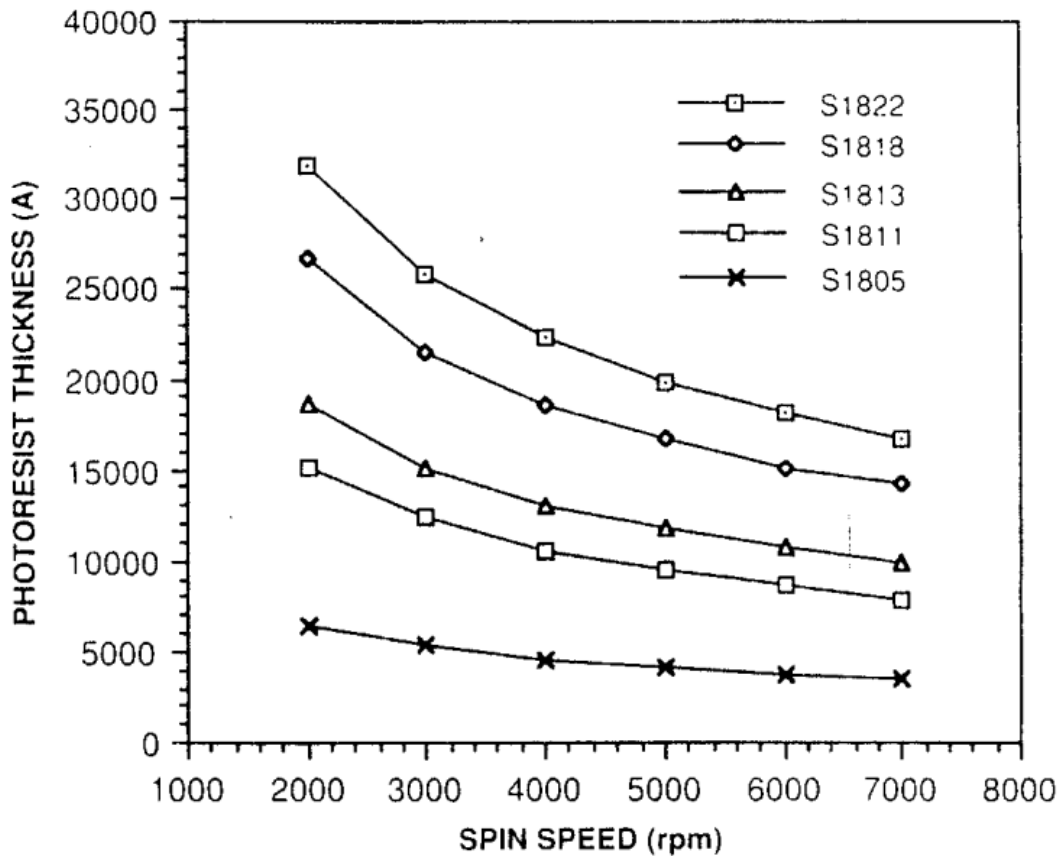


Figure 6.5 – Spin speed vs photoresist thickness for S1813 Photoresist, as provided by the manufacturer, Shipley².

The photoresist used in our experiments is S1813, designated as triangles.

The sequence used for spin-coating S1813 polymer were as follows:

1. Preliminary Spin: 500 RPM for 10 seconds. Ramp-speed: 500 RPM/s
2. Target Spin: 4000 RPM for 30 seconds. Ramp speed: 1000 RPM/s
3. Deceleration: 0 RPM for 0 seconds. Ramp speed: -500 RPM/s

By referencing the manufacturer's guidelines in Figure 6.4, this gave us the ideal photoresist thickness of 15000 Å, or 1.5 μm.

With photoresist at the appropriate thickness, the glass slides were then placed inside of a convection oven at 115 °C for 10 min to evaporate any solvent present within the polymer. After removal from the oven, the slides were allowed to cool down to room temperature.

It is important to note that the time-dependence of the slides is now temporarily paused: any dust that interacts with the slide will be effectively blocked by this polymer "shield" and will not have any meaningful effect on the device integrity, as long as they are held within opaque plastic boxes to block stray dust particles and ambient sunlight. As such, these now have a rather stable shelf-life with no noticeable detriments. Anecdotally, slides can be used a year later and perform exactly as well as freshly prepared slides.

6.3.1 Patterning via UV Exposure

Solidified with polymer, the slides can be masked and UV-exposed to create any desired pattern. For the best results, a custom-made professional mask can be made to exacting specifications, and our group's mask was purchased from and fabricated by Photo Sciences Inc (#116760). A thin sheet of lime-glass is patterned with chromium metal with incredibly high resolution down to the nanoscale.

The second important component of proper UV exposure is the UV-source. With crude sources, this then causes odd faults and flaws in the pattern if there is even the slightest variation in angle. While this is not a large issue for larger millimeter-scale patterns, it does cause dramatic issues where the mask's features are from micro-to-nanoscale, namely

penumbra effects (which will be discussed at length in the Metal Deposition section) and interference patterns.

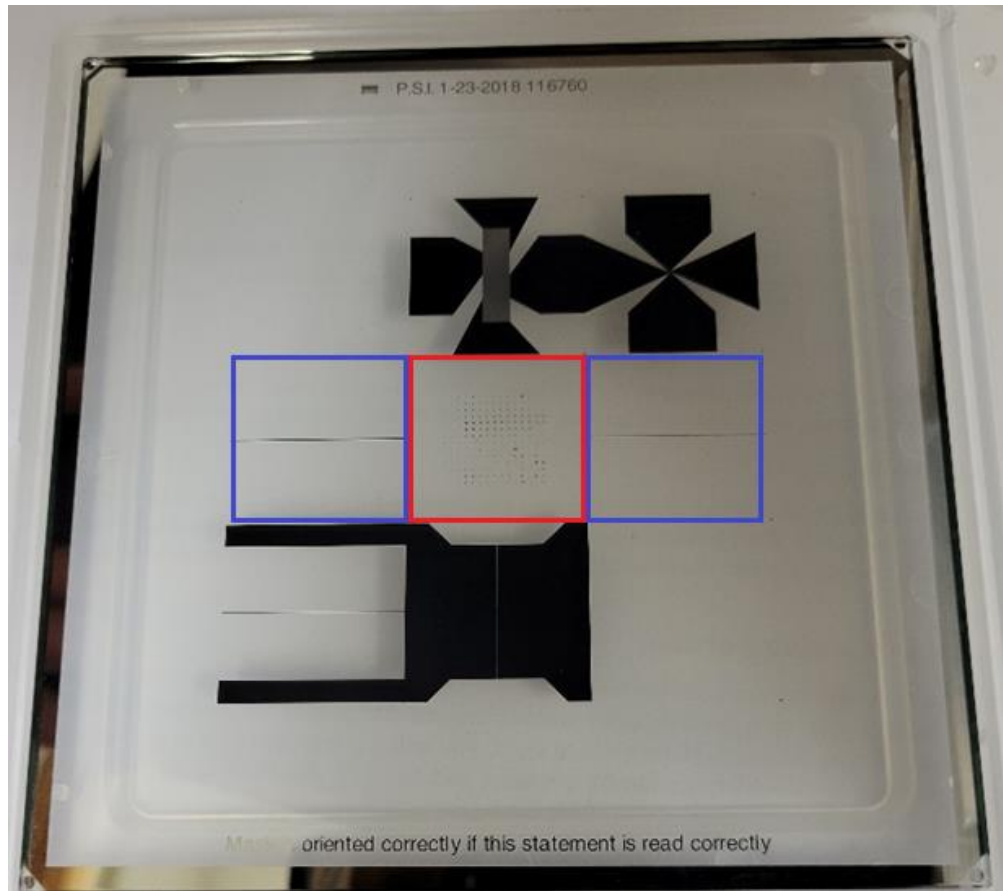


Figure 6.6: Actual picture of the photoresist mask. In the center red box, nearly undetectable with the naked eye, are a series of Corral Traps. The blue boxes to the sides are used for the 175 μm and 75 μm channels, respectively.

The other structures on the mask are irrelevant for this thesis.

The absolute best method of UV-exposure is therefore to have perfectly collimated light: perfectly parallel light that evenly exposes the entire surface. For our experiments, we used the professional lithography aligner (Suss MicroTec Model MJB4) inside The Global Water Center in Milwaukee, an affiliate of the UWM campus.

After exposure, the monomer can be efficiently removed by using the water-based

developer sold by the manufacturer, MF-321 (Microposit MF-321 Developer, Dow Chemical) that is precisely created for speed and efficiency in this solubility. By submerging the entire slide into a small bath of developer, the monomers easily dissolve while leaving behind the long-chain polymers as a still-rigid structure.

6.4 Metal Deposition Chamber

Upon removal of the polymer, the slides are immediately placed within a custom-built slide holder, built by engineering staff member Mike Condon at UWM. This slide holder, milled out of aluminum, can then be placed directly into our lab's custom-built metal deposition chamber. By decreasing the pressure inside the chamber, the vapor point of a metal will be dramatically reduced. Pushing a strong current through a tungsten wire acting as a cup causes the wire cup to heat to 900-1400 °C, vaporizing the target metal.

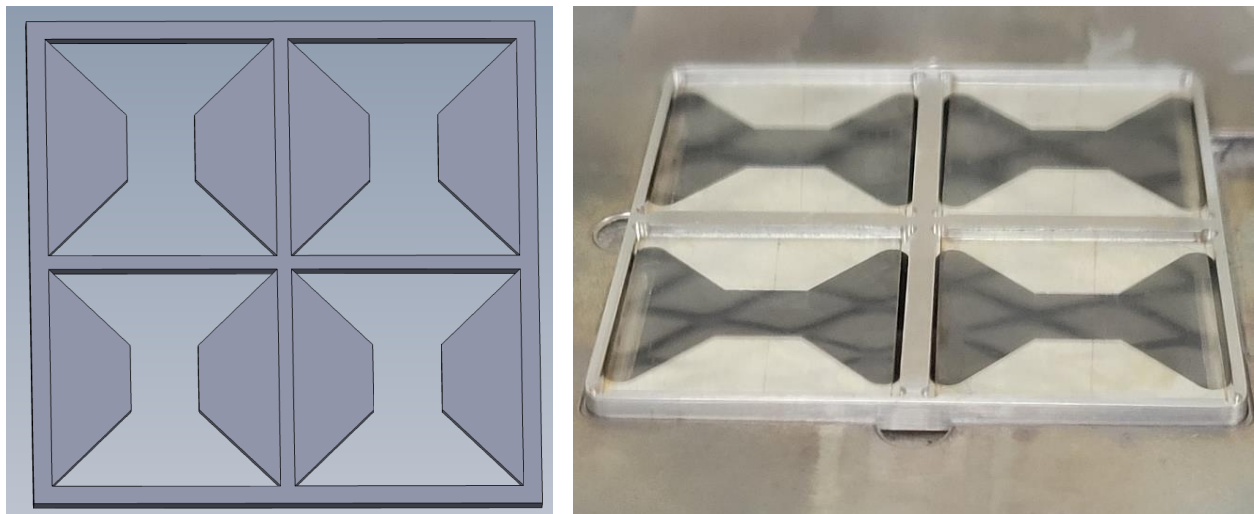


Figure 6.7: Solidworks schematic (**left**) and real image (**right**) of the custom slide holder. Each slot is 25.5 x 25.5 mm. The corners have been rounded off in the final product for ease-of-use. Real image shows the holder slotted into the evaporation chamber, with the work-surface pointed down towards the metal source.

In a vacuum, the liquid metal is then able to eject atoms radially from the source, coating the surroundings with an approximately even layer of metal. By positioning the slides directly above the source, this ensures that only atomized-metal coats the surface; if the slides are placed below, it will catch any bulkier and heavier slags of oxidized metal ejected off, causing an uneven and flawed surface.

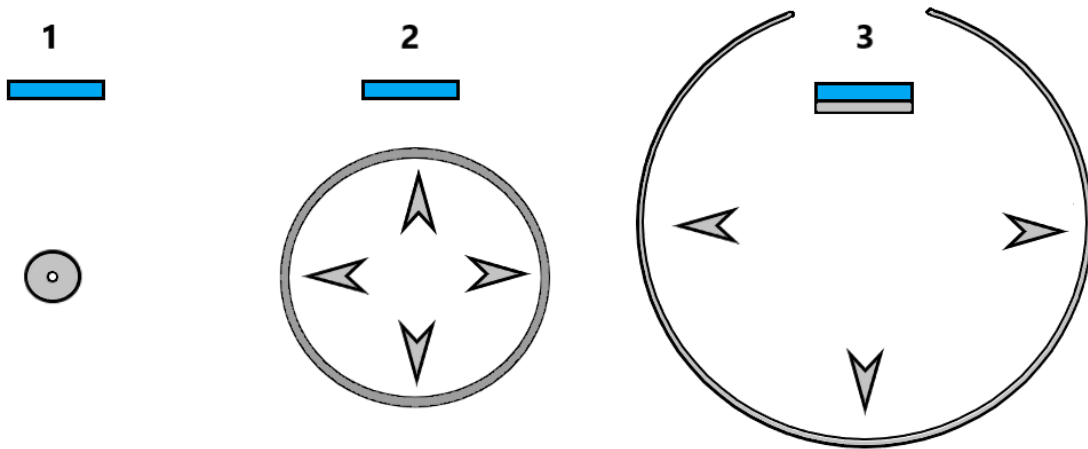


Figure 6.8: Metal evaporation at three different time points (1, 2, 3) As the metal vapor expands (grey, with arrows depicting the direction of expansion), the effective coverage thickness decreases. By placing a glass coverslip (blue) at a specific distance, a specific thickness of metal is deposited.

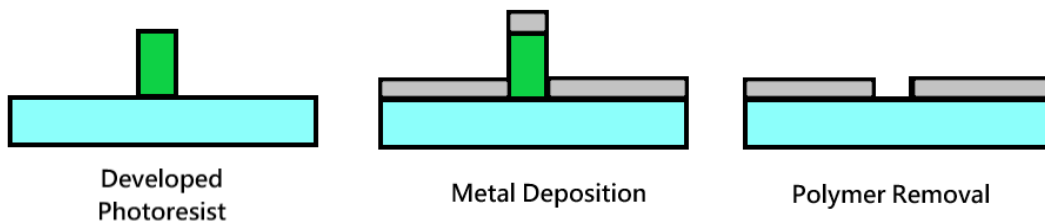


Figure 6.9: Metal lithography: positive photoresist (green) structure blocks metal deposited onto a glass sample.

To obtain a repeatable, reliable, and accurate measurement for the thickness of the metal layer, we assembled an evaporation chamber using a rough pump (Emerson Model C83CXGZZ-4786), a custom-made diffusion pump using glassware created by UWM glassblower Neil

Korfhage, metal piping, fittings, and connectors (A&N Corporation, model C4100-OF25), the chamber itself (TNBX Ultek P-E DI Pump), and an attached glass dome (Pyrex No. 6886).

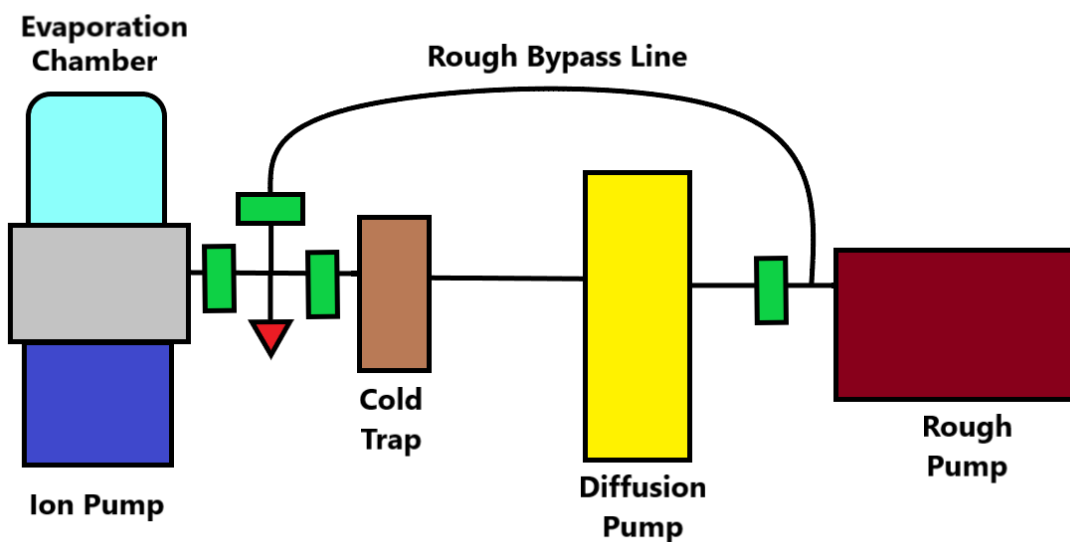
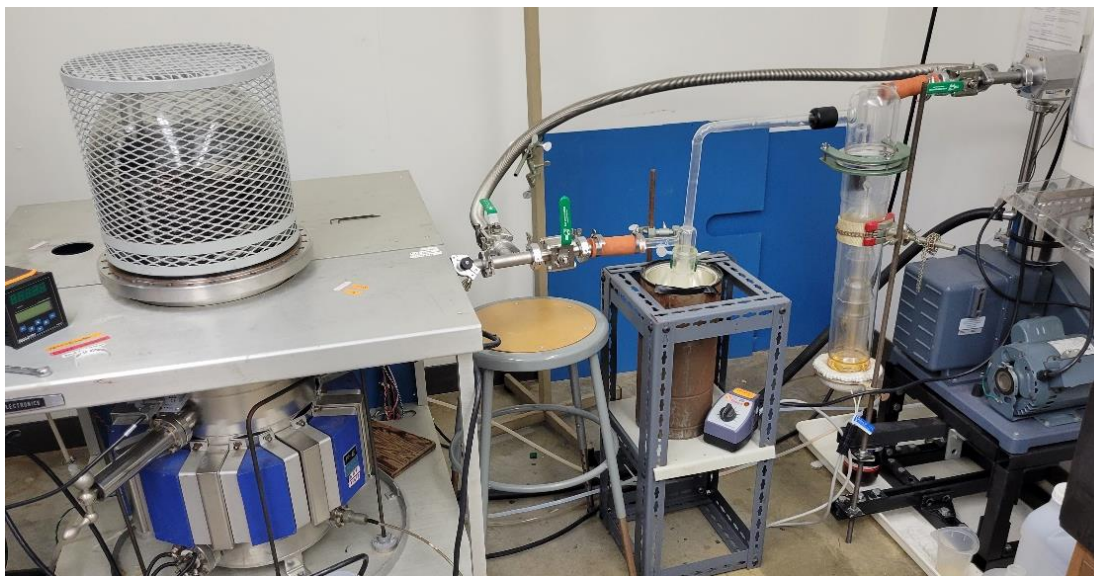


Figure 6.10: (Top) Picture of the metal evaporation chamber with attached pumps. (Bottom) A simplified schematic of the chamber's setup. The green boxes are gate valves to control which pump is drawing vacuum at any given moment, while the red arrow is the location of the atmospheric bleed valve.

The vacuum chamber houses a quartz crystal monitor that measures exact metal deposition rates, allowing for Ångstrom level accuracy, with an attached power source (TDK-Lambda) and a current monitor (Sigma Instruments, SQC-222 CoDeposition Controller) that allows for custom programs that can automatically evaporate metal to a specified thickness using a pre-loaded alumina coated tungsten wire basket (Ted Pella Inc, Style 2, #84-22) with an appropriate amount of Nichrome pellets (Ted Pella Nichrome, #29-2824). Specific care, however, should be taken as to not overload the cup: the greater the mass of metal, the more heat is required to fully melt and heat the target metal, which would invariably damage the tungsten filament. If the degradation is severe enough, to the point of breakage, it renders the whole cup and its contents worthless.

In addition, this cup has the advantage in its shape. Whereas a thin filament would eject material in all directions, and therefore dramatically increase the amount of wasted material, the cup only ejects atoms upwards towards the target substrate. This increases efficiency and reduces the amount of metal required to get a set thickness. Lastly, the distance from source-to-substrate helps to reduce the effects of the penumbra to manageable levels.

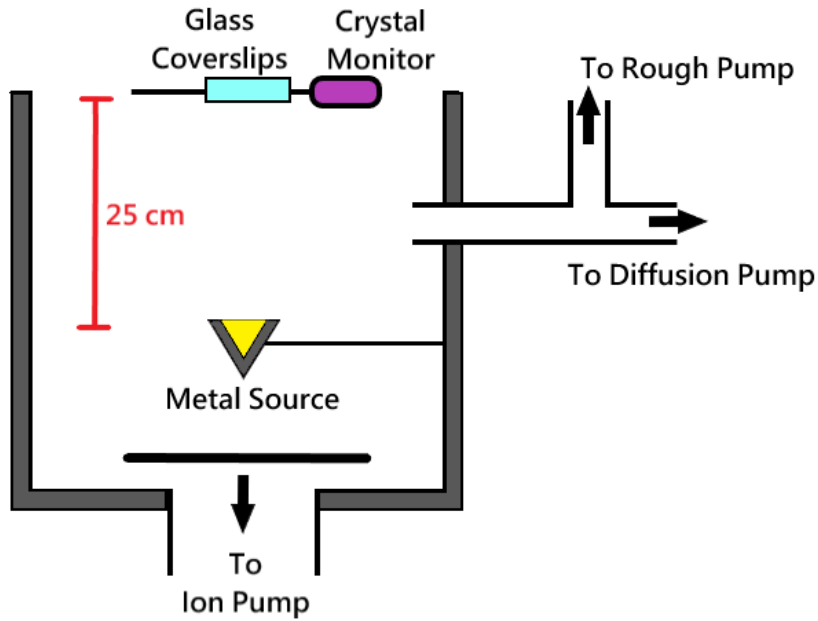


Figure 6.11: Simplified schematic of the Woehl Group Chamber. The metal source (yellow) is housed within an aluminum oxide cup, which directs metal vapor towards the coverslips (blue) above.

The final step after evaporation is also one of the most crucial steps: time. Immediately after evaporation, the metal source is still going to be hundreds of degrees Celsius, and thus if quickly exposed to air the chromium in the Nichrome source will unerringly react with atmospheric oxygen. While not immediately dangerous, if one doesn't foolishly try to touch it, the bigger issue is that the chromium oxide layer will have a dramatic effect on future experiments: the oxidation layer acts a shell on the surface of the metal, keeping the rest of the metal in its liquid form. This leads to uneven coating and worsening results over time. Even a small amount of chromium oxide with each evaporation will be detrimental, as the impurities will continue to concentrate over time. It is vital that the source be allowed to fully cool down to room temperature while still under vacuum, but thankfully during this time the samples are also protected from the dust and debris of normal atmosphere.

6.4.1 Removal of Patterned Photoresist

After removal from the metal chamber, the slides are immediately washed with Polymer Remover PG (Microchem Remover PG, G050200) and sonicated for 2 minutes. More aggressive sonication can cause metal flaking, which could ruin the device if flaked in an inopportune location, but the light sonication does ensure that the metal that was evaporated onto the polymer is shaken loose and appropriately removed, so it is not advised to ignore this step. This remover solution will quickly dissolve the polymer structures, leaving behind cavities in the metal surface.

A successive rinse in isopropanol ensures that no polymer remains behind, as any structure left behind would be multiple orders of magnitude larger than both the channel and the particles, as well as protecting the slides from dust as we move to the next step.

6.5 Attachment of Top Coverslip

As the metal evaporator cools a set of top coverslips, smaller 18x18 mm glass slides (VWR micro-cover glass, #48368-040), are AMII cleaned. Then both the metalized slides and the top coverslips are dried using the previously discussed technique of air-blasting with nitrogen gas. The top coverslip is then placed over the channel created in the metalized slide and a 65 g stainless steel weight is placed on top of the assembly. This weight helps ensure that the two slides are set as close as possible, which will be important for later. Once set and weighted, then UV glue (Norland Optical Adhesive #81) is added to two edges of the top coverslip to fasten it securely to the metalized surface.

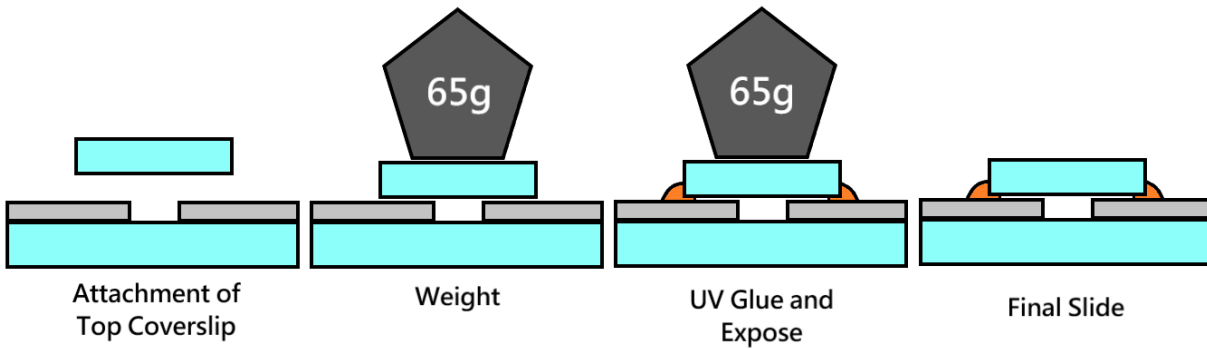


Figure 6.12: Top coverslip attachment steps. 1) A clean glass coverslip is placed on top of the metalized slides. 2) A 65 g stainless steel weight is added to press the two slides together. 3) UV Glue is added to two sides of the slide (not covering the channel) and exposed to UV light. 4) After weight removal, the microfluidic device is complete.

Unlike previously, collimated UV-light is not essential. Instead, any amount of light can be used in any direction. Thus, a series of UV blacklights are used to illuminate the entire glue surface for 60 seconds to ensure complete hardening and rigidity.

The top coverslip is multifunctional. Firstly, it ensures that the microfluidic device is rigid in its dimensions and won't be influenced by fluctuating heights from introducing fluids. Secondly, the top coverslip protects the area-of-interest from particulate matter and ensures that the experimental setup is as sanitized as possible. Once this step is completed, the slides are now fully assembled and stored for later use.

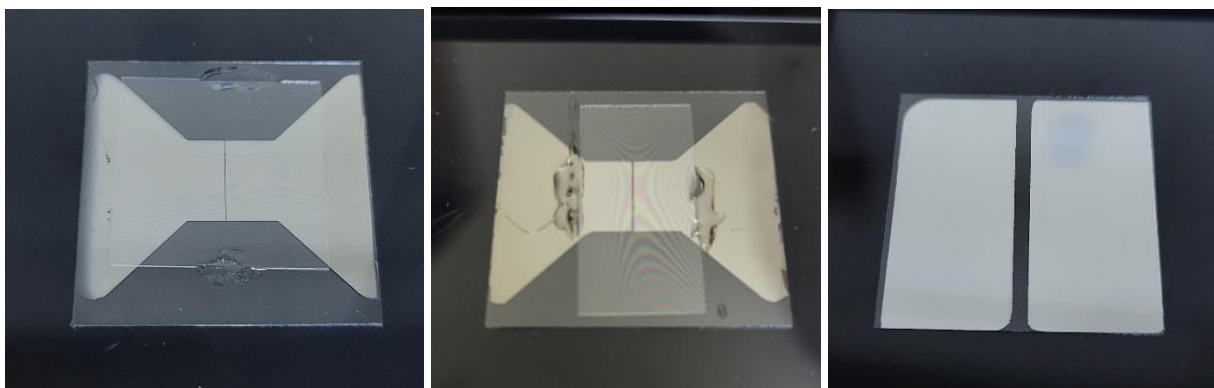


Figure 6.13: (left) Assembled Microfluidic Device, with attached 18x18 mm top coverslip. (center) Alternative model that uses a 10x20 mm top coverslip. (right) The older “wide” channel model, made using an aluminum mask instead of photolithography, with a 1.5 mm electrode separation and without its attached top coverslip.

6.6 Fluorescent Nanoparticle Solution Preparation

As a generalized procedure, sodium hydroxide was prepared in large bulk via a very standard manner: to prepare 1.000 L of solution, 39.997 grams of solid sodium hydroxide (Sigma-Aldrich 211465) is mixed with ultra-pure water (18 M Ω resistance) inside of a volumetric flask. The ultra-pure water is purified using a water purification system (Sartorius Arium Model 611) and used immediately to ensure no carbon dioxide contamination. This results in a base stock solution of 1 M solution (pH 13), which can then be diluted in a 1:1000 ratio with ultrapure water to obtain 0.001 M sodium hydroxide (pH 10). Once completed, a small sample is taken and measured with a benchtop pH meter (VWR symphony SB80PC) as added verification.

This standardized solution is then used for all dilutions: a manufacturer stock solution of target particles is sonicated for 10 minutes, using the same sonicator previously mentioned, and then diluted with the stock sodium hydroxide solution in successive 1:10 or 1:100 ratios

using calibrated pipets of varying sizes, 1-10 μL , 10-100 μL , and 100-1000 μL (Transferpette, Model S), mixed and stored within 1.00 mL sealed containers (Weaton Science 1 mL vials) to reduce carbon dioxide contamination. The final concentrations are listed as 1:10^X based off the dilutions used to obtain that result.

For example, a stock sample diluted with 3 successive dilutions of 1:100 and 1 dilution of 1:10 would be listed as 1:10⁷. This example is summarized in the graphic below. Calculating the “true” concentration would simply require knowing the concentration of the stock solution, which varies largely between the differing bead sizes.

As a group, the primary solution used in our various experiments are all differing forms of a suspension of polystyrene microbeads functionalized with carboxy groups. Work done by my predecessors was carried out with 1.5 μm diameter microbeads (Phosphorex polystyrene #138), diluted with pH 10 sodium hydroxide solution. In a basic solution, these carboxy groups deprotonate and become negatively charged, allowing for interactions with AC/DC electronic potential fields.

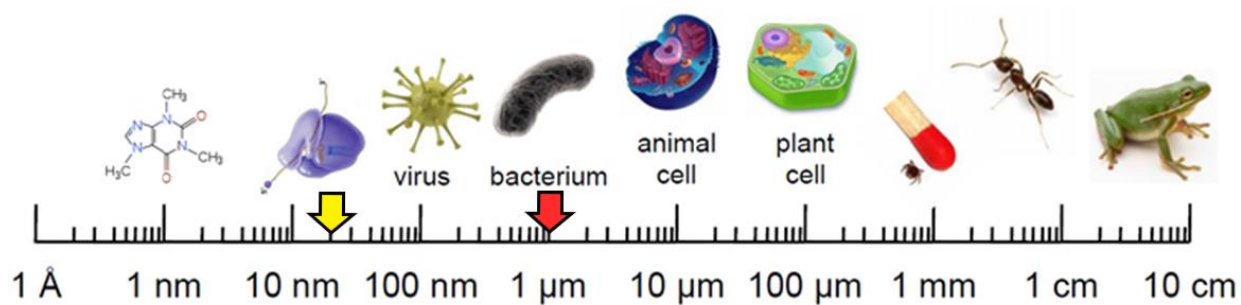


Figure 6.14: Logarithmic scale from 1 Angstrom to 10 cm, with depictions at specific intervals, such as a virus at ~100 nm. Two arrows have been added for the ~20 nm nanoparticles (yellow) and ~1.5 μm particles (red)

For the research done in this dissertation, unfortunately, 1.5 μm diameter particles are not sufficient to resolve the electric double layer, which has size constraints due to the length of the Debye layer. Instead, ~ 20 nm carboxy-modified fluorescent polystyrene nanoparticles (FluoSpheres, yellow-green, 505/515 F8787) were used, 100x smaller, to add nanometer-level detail to the exact movements of nanoparticles interacting to form the EDL. This adds yet another factor to consider: the nanoparticles are so small that they are difficult to view via brightfield optical microscopes because the scattering of light presents too much background noise, as discussed previously in Chapter 4. Thus, in addition to the carboxy groups, they were also internally functionalized with fluorescent (FL) tags with an excitation wavelength of 505 nm, enabling the nanoparticle to emit light as opposed to simply scattering light, allowing for us to have greater detectability of the particle when compared to brightfield microscopy.

These nanoparticles, according to the manufacturer, are about 2% by weight and about 27 nm in diameter. Assuming they're perfectly spherical and the density is roughly 1.0 g/cm^3 , then this would end up as roughly 3 μM . The nanoparticles were prepared in the same generalized procedure described above to obtain a $1:10^6$ dilution, which results in a roughly 3 picomolar concentration. Seeing as this number is based on numerous assumptions with few (if any) significant figures, this number should not be taken as at all accurate, but at least gives a rough estimate for the concentration.

To prepare for analysis, the solution is shaken vigorously and sonicated again for 5 minutes. This is then taken to our laser microscopy lab along with the prepared microfluidic devices.

6.7 Microfluidic Device Set-up

The microfluidic devices are attached onto a non-conductive sample-holder platform specific for our microscope. Copper wires, attached to the power source, are threaded into metal clamps on the sides of the sample-holder platform and a small piece of conductive carbon tape (Nisshin NEM Tape) is attached to the metal slides to both ensure conductivity and to act as a small cushion to prevent cracking of the device. The clamps are then tightened, which connects the power source to the electrodes through the carbon tape adhesive.

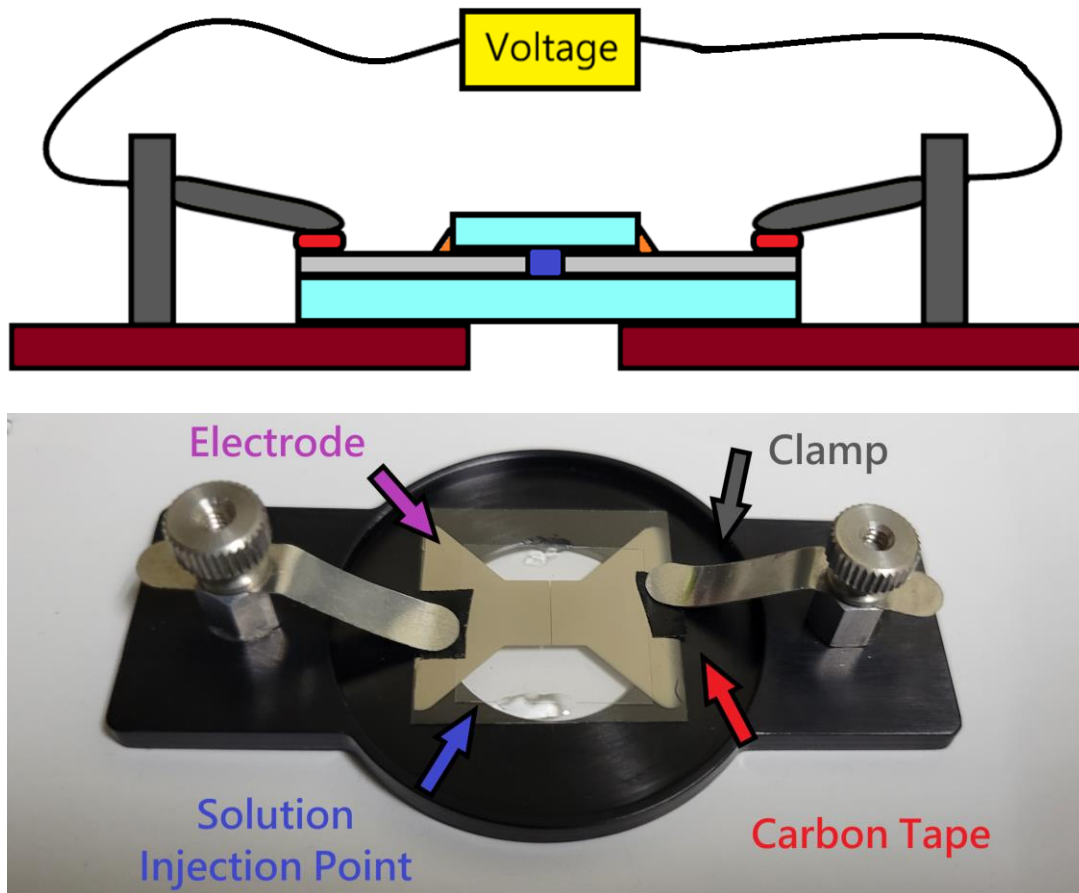


Figure 6.15: (top) Side view of the non-conductive sample-holder (dark red) with a glass microfluidic device (light blue) and metal (light grey). The metal posts (dark grey) are attached to the surface via carbon tape (red) and connected to the voltage source via copper wires. (bottom) A real image of the platform, without attached copper wires, with highlights for the clamp, carbon tape, and solution injection point (blue).

After attaching the microfluidic device to the sample-holder platform, the 1 mL vial of fluorescent nanoparticle solution is given one final vigorous shake and 1.000 μL of solution is drawn with a calibrated pipet (Transferpette Model S, 1-10 μL) and injected into the microfluidic device via capillary action. The thin space between the top coverslip and the electrodes, if created correctly, will rapidly draw the solution without any effort. If capillary action is not sufficient, a very light amount of pressure on the edge of the top coverslip using the pipet tip will help wet the surface and draw the rest of the solution in.

The space created between the electrode surface and the top coverslip is also a very useful way of quickly determining how close the two surfaces are. Using very basic geometry, if the entire 1.000 μL solution is in an 18x18 mm cavity, the height of the solution would be about 3.0 μm . Thus, if the solution is fully drawn in and any amount of solution visibly remains outside the sample cell, it can be safely assumed that the height of the channel is in the micron range, or even sub-micron, depending on the amount of fluid remaining. If the microfluidic device requires more than 1.000 μL to fill, then the height would be greater than 3.0 μm and thus outside the parameters of the experiment. Attempts have been made to accurately measure the channel height, but the results were inconclusive at best.

Once the solution has been injected, the device is quickly sealed along the edges with Vaseline (Vaseline 100% Pure Petroleum Jelly). At such small volumes, water can quickly evaporate from the microfluidic device, anecdotally observed on the order of a few minutes, and thus any experiment that isn't sealed would be incredibly time-sensitive and practically worthless: evaporation effects would cause such massive lateral movement that Brownian motion would be unobservable. Thus, by sealing the edges with non-soluble Vaseline, the

solution can avoid evaporation effects.

The sample-holder platform is then placed into the microscope and locked in place with another set of adjustable clamps, specifically avoiding the clamps used for the electrodes to prevent shorting the circuit.

6.8 Excitation Laser Intensity and Stabilization

The nanoparticles, in order to fluoresce, must be illuminated with a specific excitation wavelength, at or lower than 505 nm, to activate the fluorescence emission. To achieve this, an Argon laser (Spectra-Physics Stabilite 2017-AR) is used to provide a consistent beam at a wavelength of 514 nm and with a final output reading of 500-1000 μW .

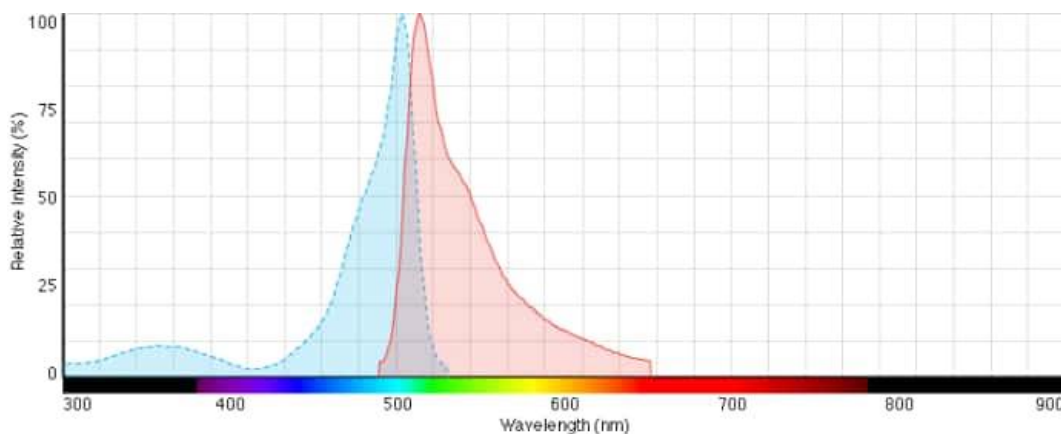


Figure 6.16: Absorbance (blue) and Emission (red) bands for the 20 nm polystyrene fluorospheres, as provided by ThermoFisher³. Absorbance peak is roughly 505 nm, and peak emission is roughly 515 nm.

The output from the laser is passed through a series of neutral density filters (Chroma) to bring the power down to a non-destructive level. To prevent vibrations from the laser emitter interfering with experiments, the laser is stationed on a floating table using air-cushioned stabilizers (Newport 12000 Laminar Flow Isolator) and the beam is transferred over to the

microscope table using a 3-axis optical fiber injection mount (Newport UST Series 561) with a focusing objective lens (Leica 439) and a single mode fiber (FiberTech Optica QSMJ-3A3A).

By maximizing the output of this fiber optic cable through careful adjustments of each axis, we can ensure optimal laser injection into the fiber. It is then passed through an intensity stabilizer (Brockton Electro-Optics Laser), which reduces the maximum power output, but provides a stable beam without randomized fluctuations in power.

After the noise eater, the beam passes through a linear polarizer and a Fresnel rhombus to create circularly polarized light before finally entering the back of the microscope. The laser then passes through an excitation filter (Chroma) that blocks all but a very specific wavelength of light; the argon laser emits mostly 514 nm light, but this is just the maximum peak. It is important to keep in mind that perfect mirrors do not exist, and thus none of the mirrors (Casix CAG0201) or neutral density filters can perfectly transmit the laser and minor errors will always compound. Additionally, if other wavelengths of light enter the fiber optic cable, then the stray light and minor fluorescing impurities within the fiber will add noise to the fluorescent signal.

After the excitation filter is a dichroic mirror (literally: “two colors”) that will reflect the incoming laser light but allow other light to pass through it. This then enters the optical objective, which then transmits light onto the sample.

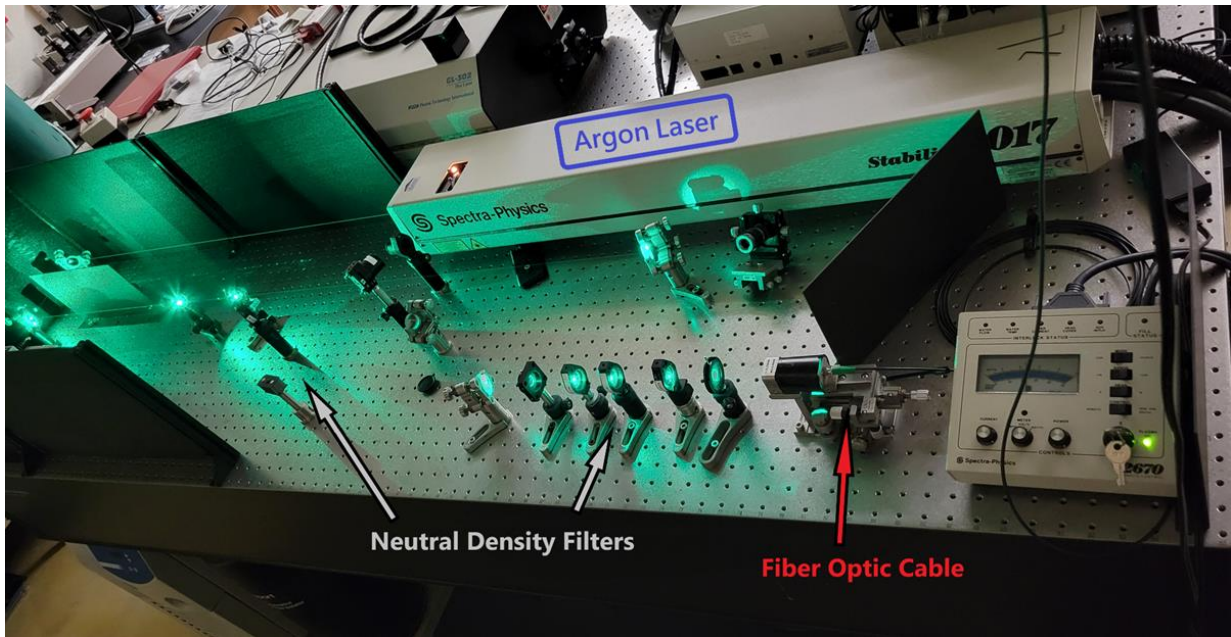
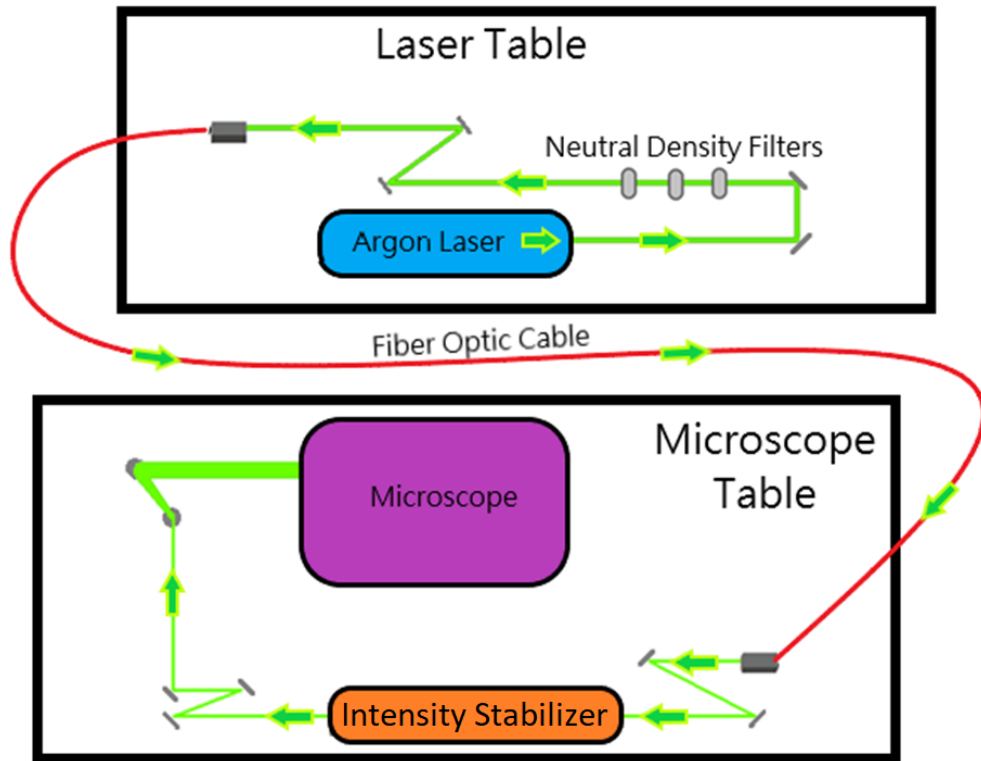


Figure 6.17 (top): The Argon Laser emits a beam that passes through several neutral density filters before entering a fiber optic cable, transferring to the microscope table, and passing through an intensity stabilizer before entering the microscope. **(bottom)** A real image of the laser table. The intensity of the beam can be seen diminishing across the neutral density filters.

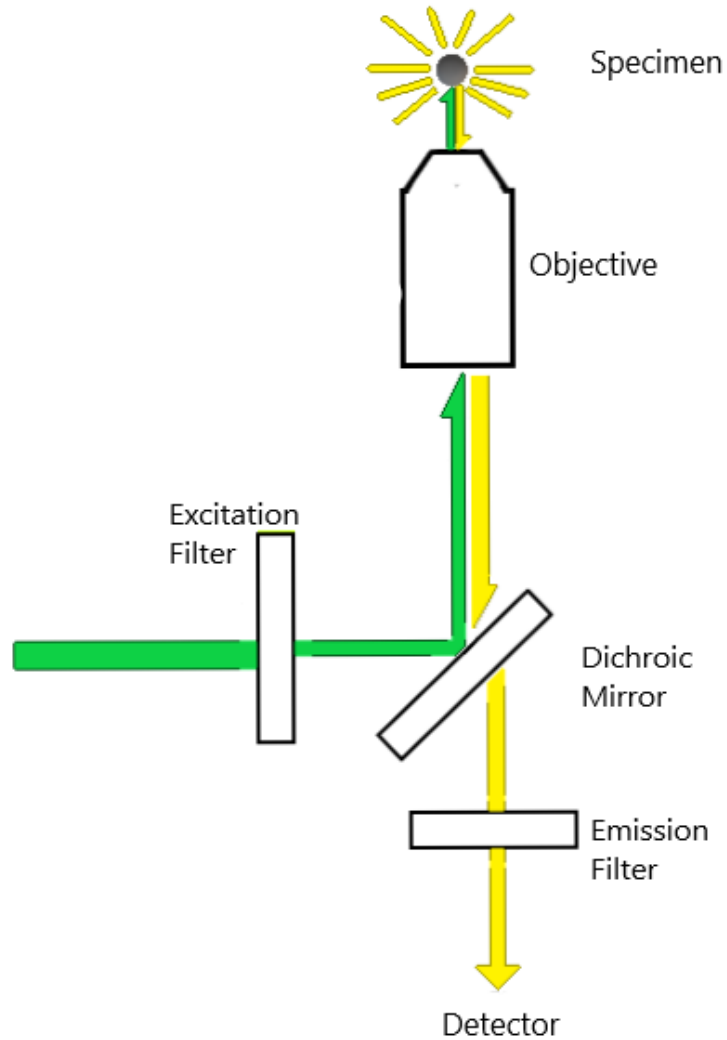


Figure 6.18– Side view of the inside of the microscope. The incoming laser light (green) passes through the excitation filter, reflects off of the dichroic mirror, passes through the objective, and interacts with the sample specimen (grey). This then fluoresces (yellow), and some of the signal re-enters the objective, passes through the dichroic mirror and emission filter, before reaching the detector.

A fluorescing sample emits light in all directions; most of this signal is lost as it emits away from the objective, but some of the fluorescent light does re-enter the objective. This fluorescent signal will then pass through the dichroic mirror and an emission filter, which blocks any other ambient light, and finally reaches the detector.

6.9 Brightfield and Fluorescent Microscopy

The microscope (Zeiss Axiovert 200M), the most crucial instrument, is rather straightforward: using simple bright-field microscopy or fluorescence microscopy and observing through the ocular lens or an attached camera, a sample can be viewed using either a 10x objective (Achromat 10x/0.25 #44-00-30), 40x objective (Zeiss EC Plan Neofluar 40/0.75) or a 100x immersion oil objective (Zeiss Alpha Plan-Fluor 100x/1.45 Oil). Unless otherwise stated, experiments were done using the 40x objective.

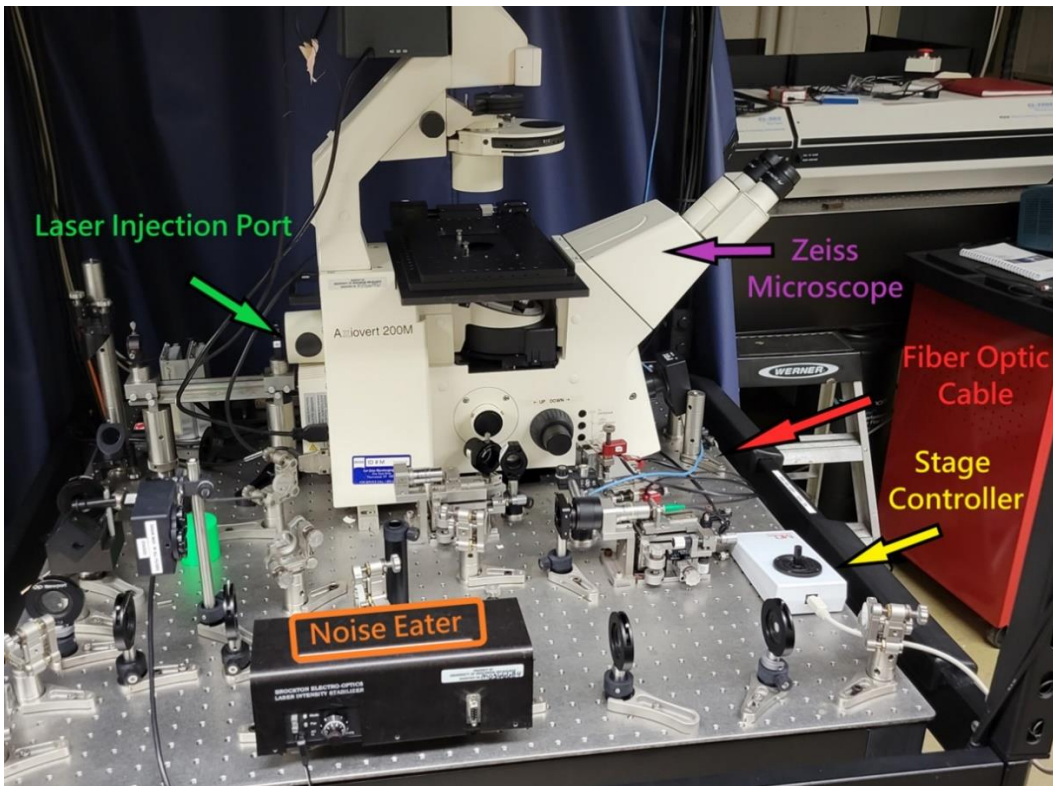


Figure 6.19: Real image of the microscope table, with noise eater in the foreground and the Zeiss microscope in the background. Laser light enters through the back of the microscope.

The sample's electrodes can be viewed via brightfield microscopy with a built-in halogen lamp, but as previously discussed, light-based microscopy is insufficient for viewing the

nanoparticles. Viewing the sample and focusing on the electrode's edge allows for finding the correct focusing parameters of the objective, and a toggle allows for switching between binocular viewing and an Electron-Multiplying Charge Coupling Device (EMCCD) camera (Photometrics Cascade II 512) installed into the base of the microscope. The EMCCD camera then sends the information directly to the computer (Dell) for viewing and recording.

Another toggle function allows for the 514 nm laser light to illuminate the sample, as well as capturing the fluorescent light emitted by the sample. Due to the setup of the microscope, the laser light is both transmitted through and collected into the objective lens set below the sample. Due to this, as well as the required focusing distance of the objective, this limits the type of samples allowed to be viewed with both the 100x and 40x objectives, as mentioned at the start of this chapter.

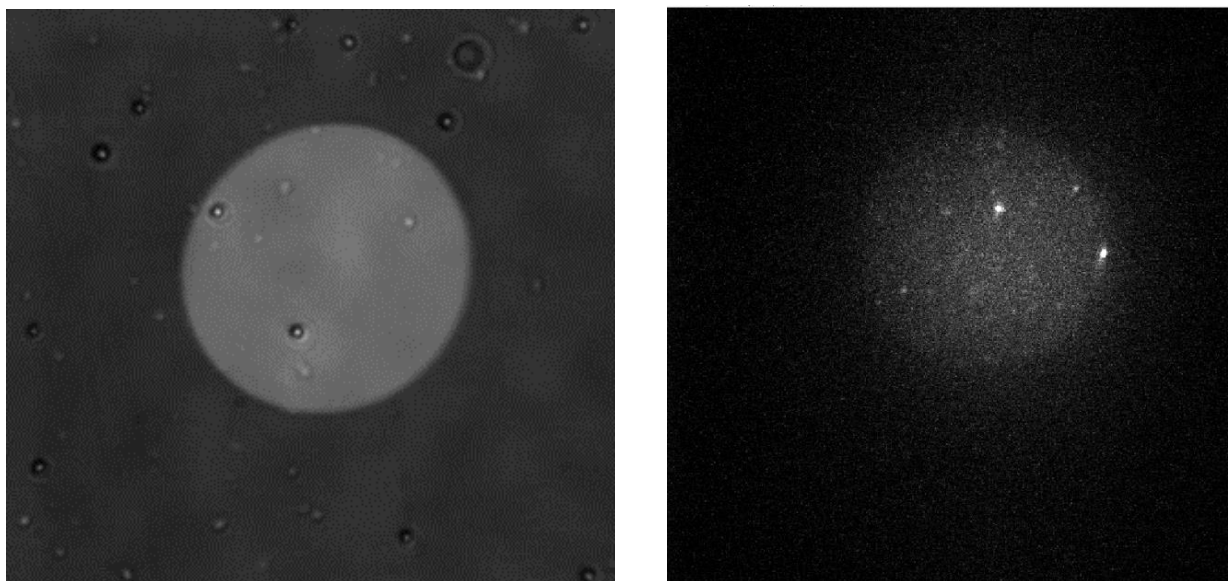


Figure 6.20: (left) Brightfield and **(right)** FL camera images of two different corral traps, 50 μm in diameter. In brightfield, the metal blocks some of the light and the trap is brighter in the unmetallized region. In the FL image, the metal doesn't fluoresce, but light from fluorescing particles can be seen in the unmetallized region. The particles in the brightfield image are 1.5 μm , while the nanoparticles in the FL image are 20 nm.

All functions of the microscope are controlled on the computer using a custom LabView (Version 2016) program, which allows for stage x-and-y-axis movements, objective z-axis movement, voltage control via an external power source, visualization of the camera output, electron multiplication for the EMCCD camera, and camera frame recording.

The voltage applied to the electrodes is controlled via the external power source (BK Precision 9123A DC Power Supply) and is used during most of the experiments. It is capable of a wide range of voltages, up to 30 V, but most commonly the voltages used are on the order of 100 to 1000 mV. The source is integrated into the LabView program, and when making changes to the voltage, LabView automatically tags the exact timestamp, even between camera frames, and includes the data in all recordings made.

The recordings are created as a series of frames in TIF files, which are then analyzed using the ImageJ/FIJI programs for particle tracking. The coordinates from particle tracking are then exported to Excel for further analysis.

- (1) *Suppressing the coffee-stain effect*. Universiteit Twente.
<https://www.utwente.nl/en/news/2020/7/688864/suppressing-the-coffee-stain-effect> (accessed 2022-10-17).
- (2) Shipley-DOW. Microposit S1800 Series Photo Resists.
- (3) *FluoSpheres™ Carboxylate-Modified Microspheres*.
<https://www.thermofisher.com/order/catalog/product/F8787> (accessed 2022-10-20).
Reprinted with permission.

Chapter 7

Troubleshooting and Initial Results

7.1 Chapter Overview

This chapter is dedicated to detailing the various analytical tools used to characterize the results shown later in Chapter 8, as well as the obstacles encountered in the process of creating a viable and reliable microfluidic sample cell. These obstacles have already been accounted for and integrated into Chapter 6: Methods, but I believe it to be a necessary chapter to highlight that the results obtained were accomplished via a non-stop iterative process. This chapter also functions as a way of being realistic about the limitations of the microfluidic cell, as well as providing an area to discuss the physical characteristics of the cell.

7.2 The Penumbra Problem

Referenced several times so far, one of the unavoidable aspects of any metal evaporation chamber setup is that there is going to be a penumbra applied to the metal. As one of my committee members quipped: “unless the source is out on the moons of Jupiter, it’s going to be a problem.” A penumbra is an inevitability due to finite-sized sources, as opposed to infinitesimally small point sources, and is best explained via a common example: sunlight casting shadows onto the ground. Thankfully, as the sources used in both evaporation chambers are roughly spherical, the mathematics provided is transitive between the two cases.

The shadow of a large building cast by the sun is not perfectly crisp; this is because right between total shadow and total illumination is a middle ground, where the part of the sun partially illuminates. In much the same way, for any metal evaporation chamber there will be a section of area where the polymerized photoresist acts as a large structure, and thus casts a “shadow” where the metal source still partially illuminates. The Sun, at a distance of 94.49

million miles and a diameter of 0.86 million miles, is mathematically comparable to a theoretical evaporation chamber, with a distance of 25.0 cm, as having a metal source of 2.30 mm (a rather accurate estimation to my own chamber, with a metal source of 2-5 mm depending on the amount of metal in the cup). This effect is summarized below, assuming a worst-case scenario of a 4 mm source:

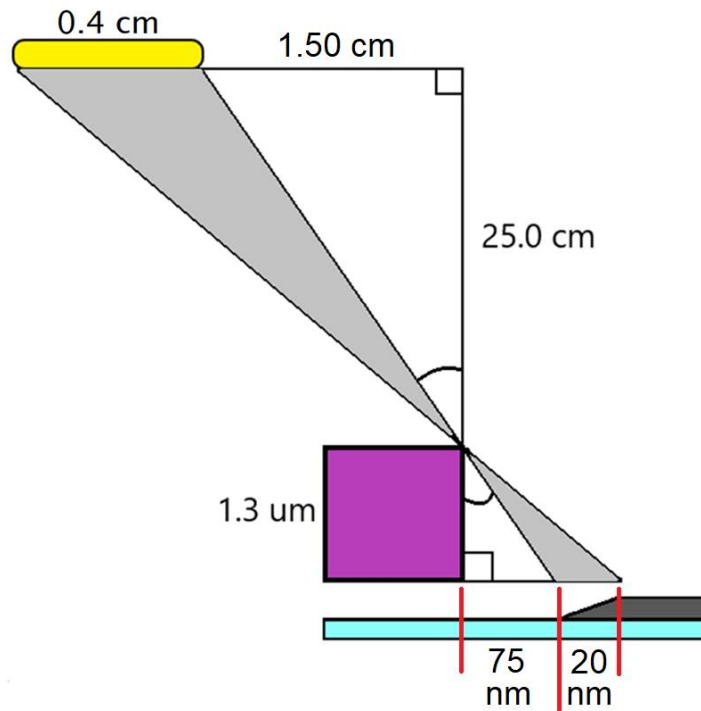


Figure 7.1: Simplified diagram showing a metal source (yellow) ejecting metal vapor (light grey) towards a glass sample (light blue). The photoresist (purple) partially obscures the vapor, leading to an unexposed gap between the polymer and metal (75 nm), a gradient deposition region (20 nm) and a full deposition layer (dark grey)

Both the length of the penumbra and the distance between the penumbra and the polymer edge can be calculated using simple geometry ratios of similar triangles based on the dimensions of our evaporation chamber: the penumbra gradient length is 20 nm, and the polymer-to-penumbra distance is 75 nm. Considering that the channel itself can be either 1000,

175, or 75 μm , this is far less than the rounding error.

The second component of the penumbra is the thickness gradient. While it might be easy to write it off as a line from 100% illumination to 0% illumination over the length, it is still necessary to verify, albeit with some assumptions. Our first assumption is that each part of the source has the same intensity and that it is only the percentage area visible by the source that determines the illumination. For the sun, this is roughly true, but for our metal source this can vary wildly: uneven heating or a thin metal-oxide film blocking evaporation from a specific section can cause the source to not be a flat value. Our second assumption is that the source is analogous to a perfect circle. For the Sun, this is certainly a very good approximation, but for the metal source in an aluminum-oxide cup, it is far less approximate. With these in issues mind, we can at least make an ideal-case estimation, presented below:

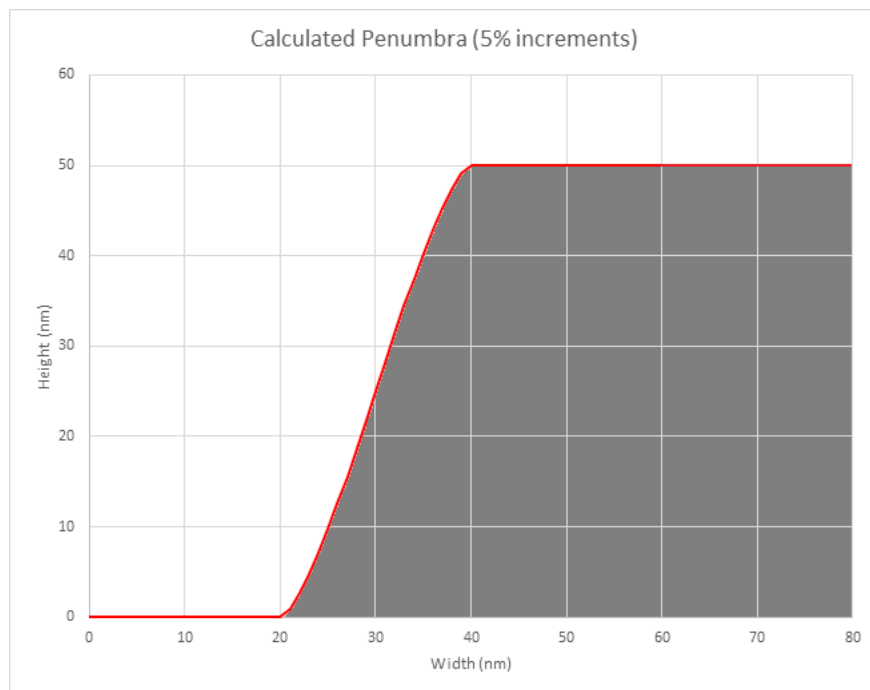


Figure 7.2: Sideview of a 20 nm penumbra at 5% increments of the source's diameter. Assuming the source to be a circle, this can be calculated as the growing area exposed by a circle's chord as a function of diameter.

The resulting curve is remarkably flat. For our purposes in future COMSOL calculations, we used the approximation of a linear slope filleted at both ends.

7.3 EDL Estimates via COMSOL calculations

Previously discussed in Chapter 2, COMSOL is a Multiphysics program that is great for analyzing a stable stationary electrostatic potential according to a specific geometry. The calculations shown here were exclusively done in the Electrostatics Module with a Stationary Study. As a refresher, we found that the electrostatic potential between parallel plates decreases linearly across the gap between them. By using a top-down view of our microfluidic cell, we can create an approximation of the electrostatic potential field between the plates. This model assumes an idealized static and stationary potential difference.

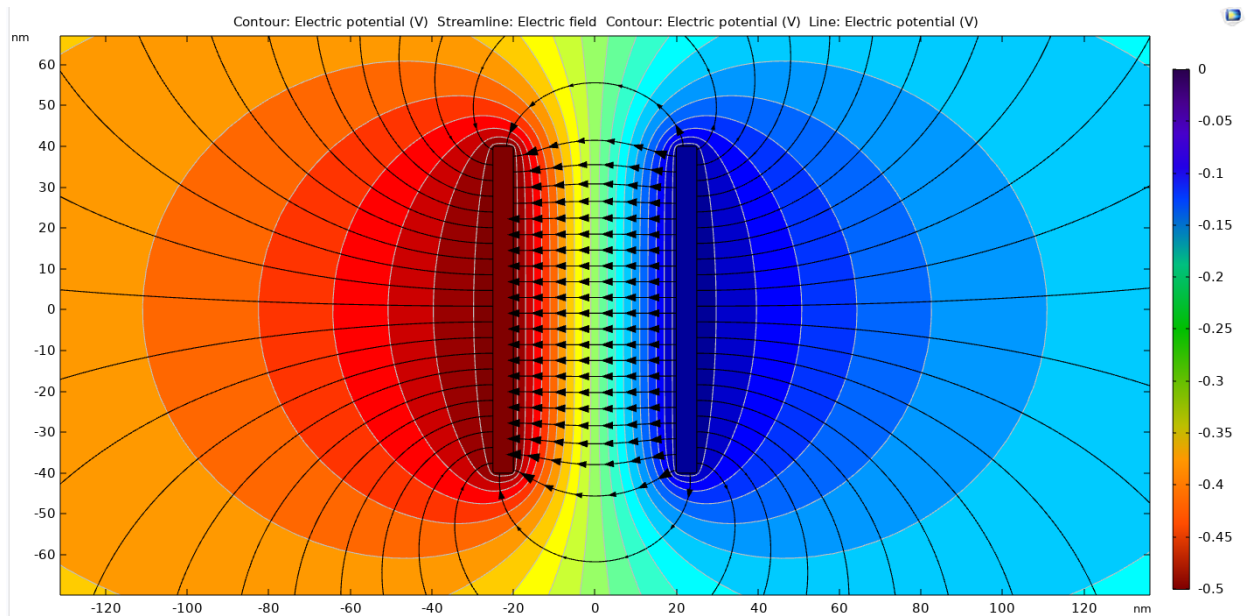


Figure 7.3: Electrostatic potential between two parallel plates, previously shown in Chapter 2, with an arbitrary 0.500 V potential, and the positive electrode on the right and the negative electrode on the left.

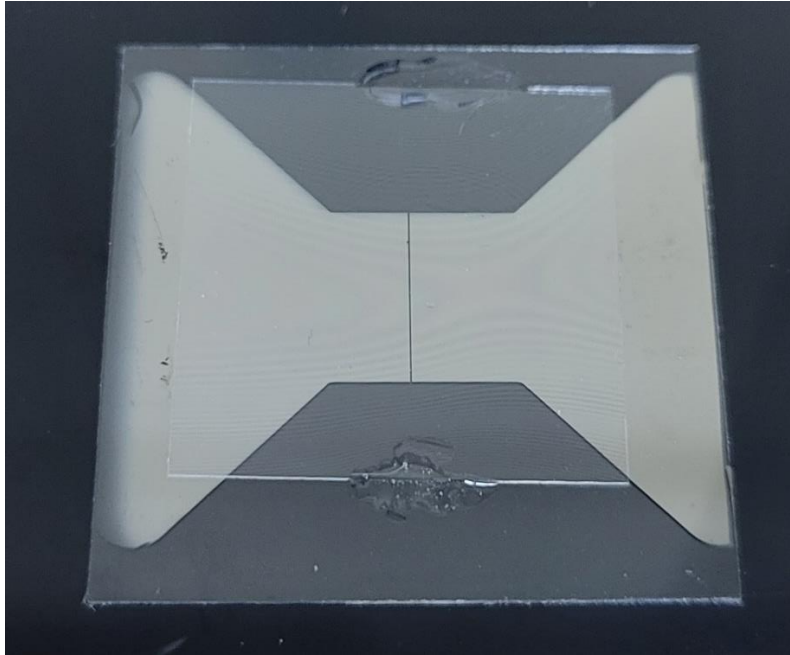


Figure 7.4: Real image of a microfluidic cell, with a thin 75 μm channel between the two electrodes.

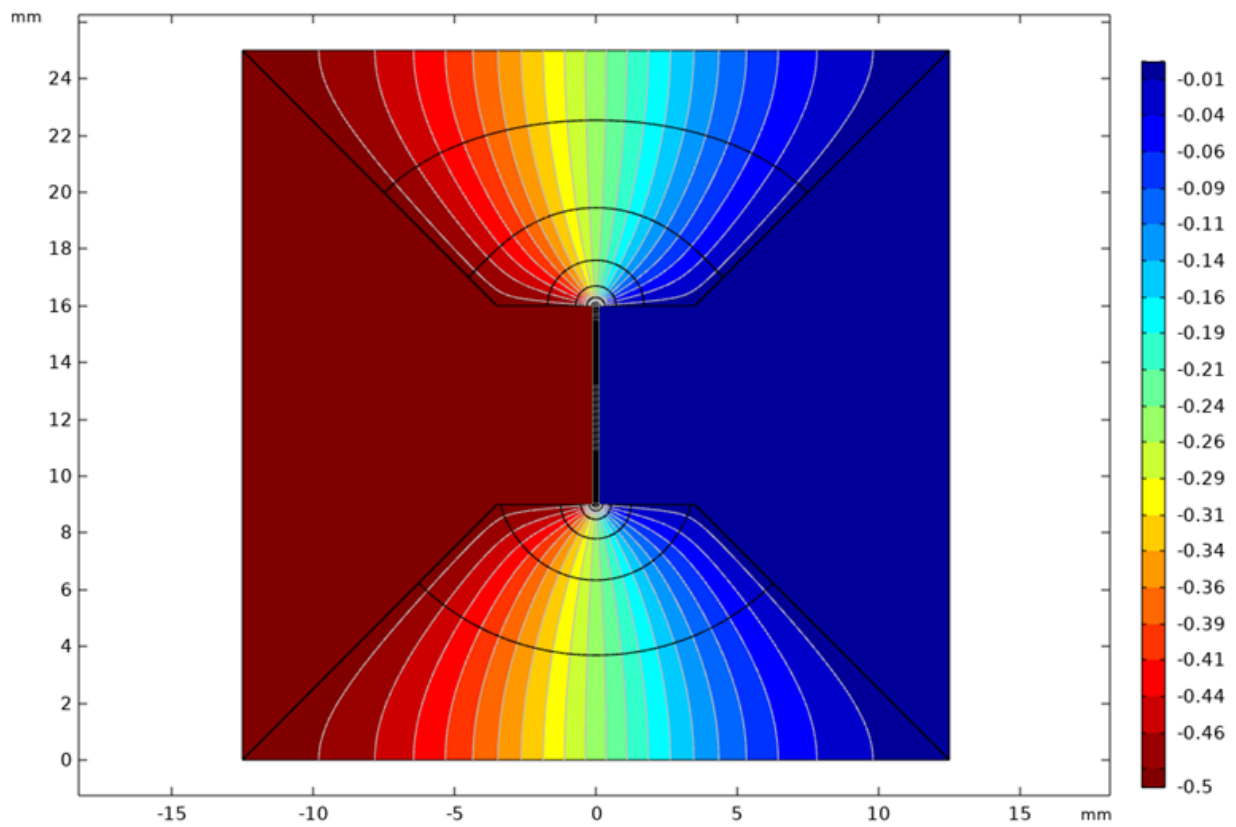


Figure 7.5: 2D COMSOL simulation of the electrostatic potential for a microfluidic cell with a 175 μm channel, with an arbitrary 0.500 V potential, and the negative electrode on the left and positive on the right.

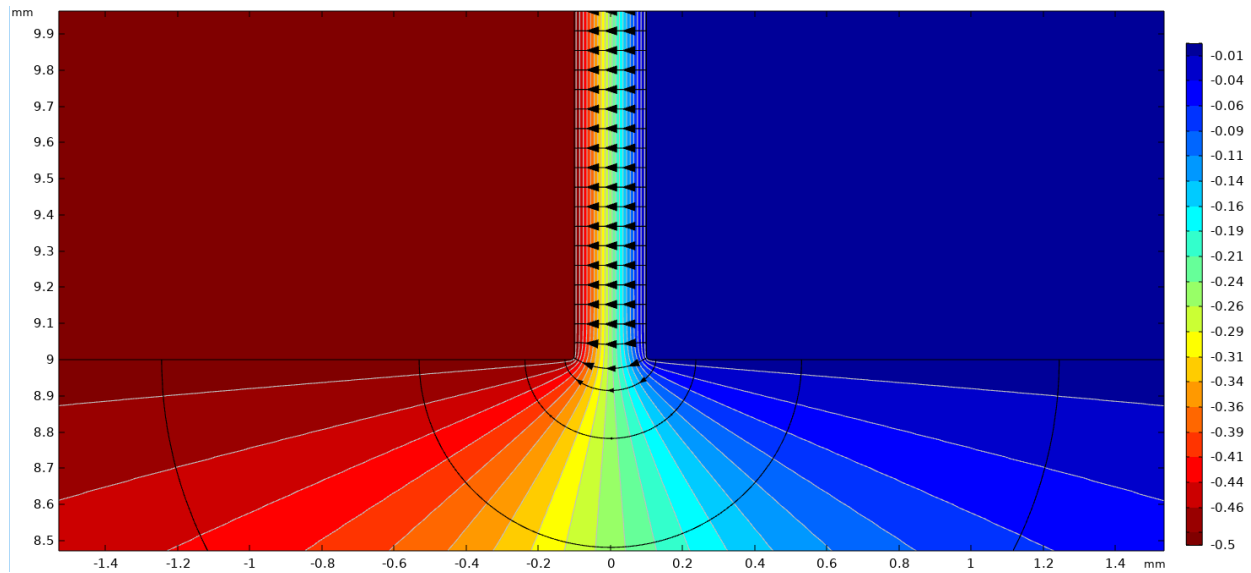


Figure 7.6: Enhanced view of the 175 μm channel shown in Figure 7.5 highlighting that the field is strongest between the electrodes, as evidenced by the dramatic increase of field line density within the channel.

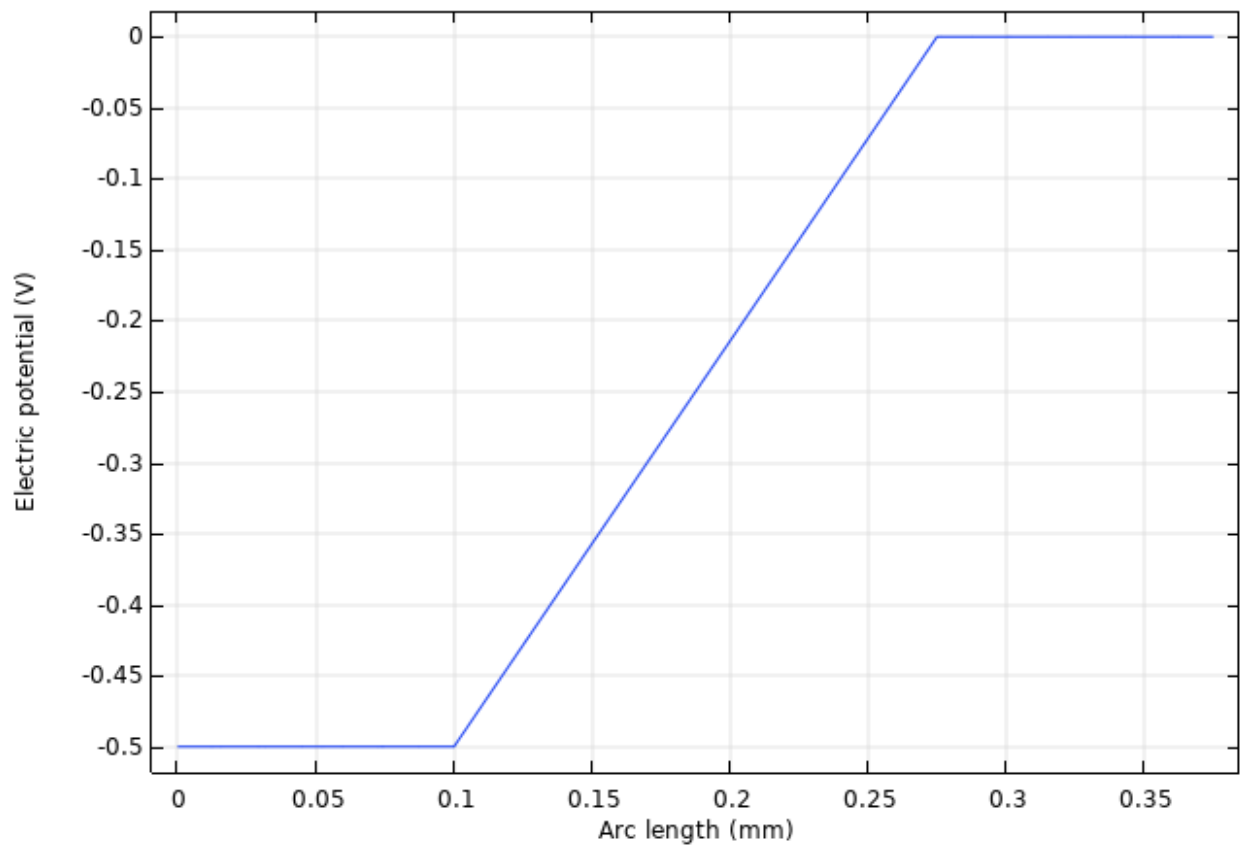


Figure 7.7: 1D line graph of the electric potential across a 175 μm channel, showing it as a linear function.

For the uninitiated (or those who skipped Chapter 2), this COMSOL simulation implies that the electric potential decreases linearly across the channel at a singular smooth rate. This static model, however, makes a few critical assumptions: it assumes that the channel between the two plates is perfectly sealed, it is a flat 2-dimensional shape (which completely ignores the influence of a penumbra), and that the aqueous medium between them does not contain a charge and does not change. While one solution is certainly to increase this analysis to 3 dimensions, for our system at least this is inadvisable due to the rather heavy computational load required and the low return on investment. Instead, shifting to a 2-dimensional cross-sectional view allows for us to analyze the potential decrease while considering both the penumbra and the solution's height.

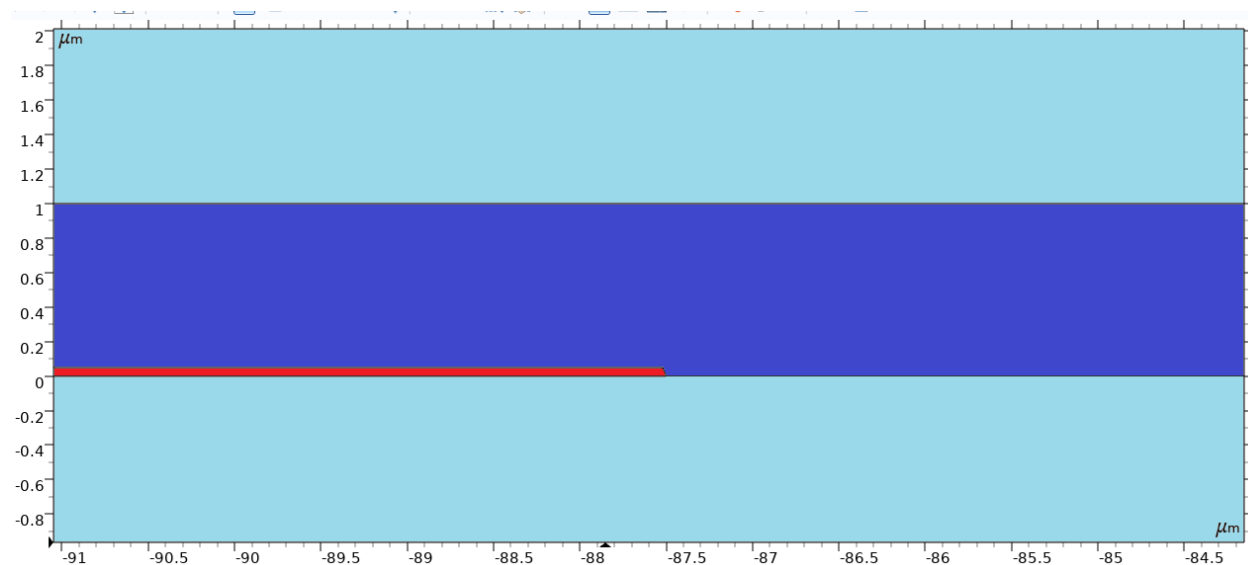


Figure 7.8: Side view of a zoomed in section of the COMSOL model, showing the glass (light blue), aqueous solution layer (dark blue) and the negative electrode on the left side (red). Both electrodes are 50 nm high and have 20 nm gradient penumbras, and the solution height is set to 1.00 μm . Displaying the entire proportional model for the electrodes is not feasible, but there is a similarly mirrored positive electrode 175 μm to the right.

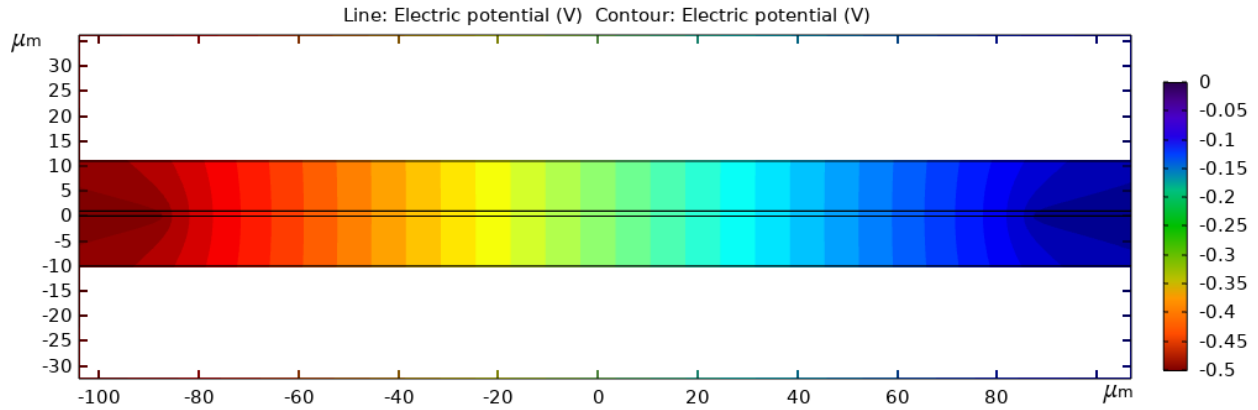


Figure 7.9: 2D COMSOL simulation of the side-view of a 175 μm channel that has a 20 nm metal penumbra. While the solution layer can be barely seen between the two glass slides, the 0.500 V electrodes are too small to be seen at this magnification; their positions can be discerned at the dark red and dark blue sections on either extreme.

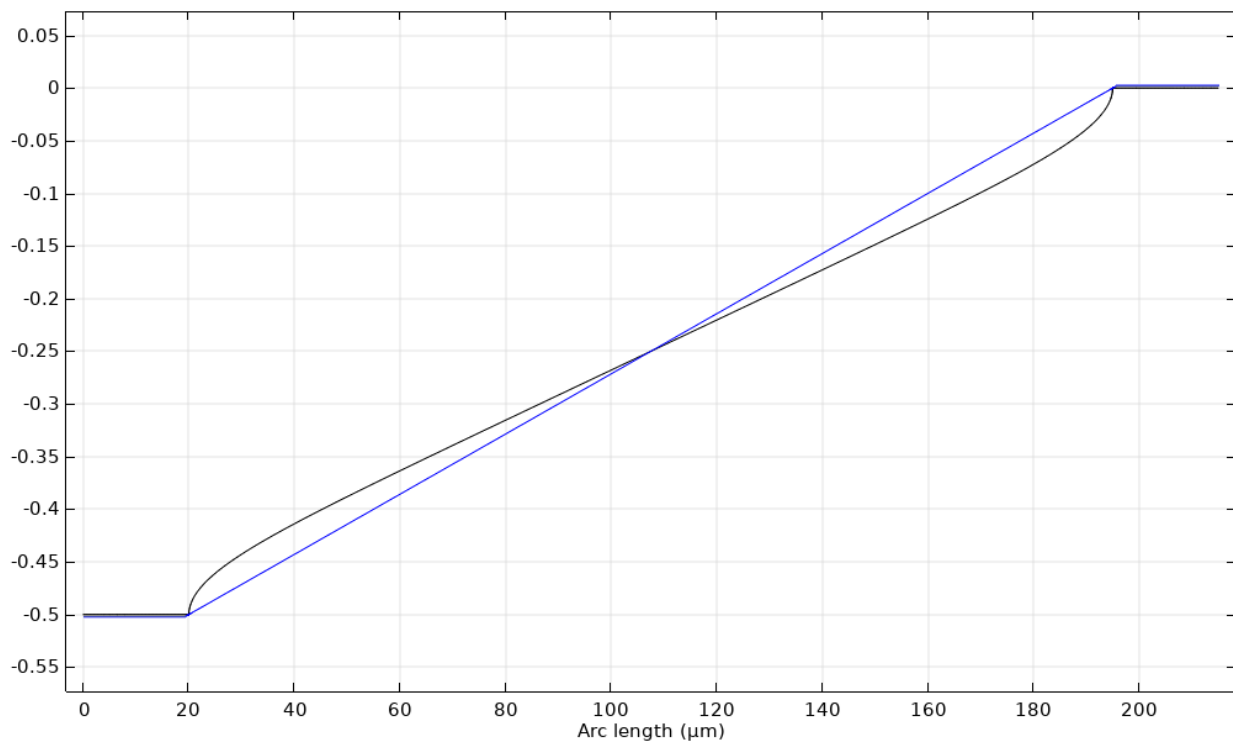


Figure 7.10: 1D line graph of the electric potential, both with a penumbra (black) and without (blue). The black line is calculated from Figure 7.9, while the blue line is from Figure 7.7.

As seen in Figure 7.9, with the electrodes being so much smaller in scale than the rest of the channel when viewed from the side, it was necessary to provide a zoomed-in view for the electrodes to show their position and their penumbra slant. The electric potential in Figure 7.10, at least visually, appears to be very similar to the previous top-down visualization, but by using a 1D line graph, the penumbra's effect is far more prevalent. As seen with the penumbra's black curve, the non-vertical electrode faces mean that the electric field has a slightly sharper potential change in the first $\sim 10 \mu\text{m}$ of the solution, before returning to a relatively flat slope ($\sim 2.40 \text{ mV}/\mu\text{m}$) for the majority of the channel. Compared to the ideal case of the blue line ($2.85 \text{ mV}/\mu\text{m}$), it is not an overly dramatic effect, but it would mean that there are additional effects to consider when a particle approaches the electrode.

This naturally brings us to the third model that fixes the final assumption made previously: the presence of an electrolyte solution and sufficient time has passed to establish electric double layers around both electrodes. In COMSOL, this was done by including the following parameters: a bulk ion concentration of $1\text{E-}4 \text{ M}$, an ion valency of 1 (assuming symmetry for NaOH), a permittivity of water of 80.1, and a calculated Debye length of 30.47 nm.

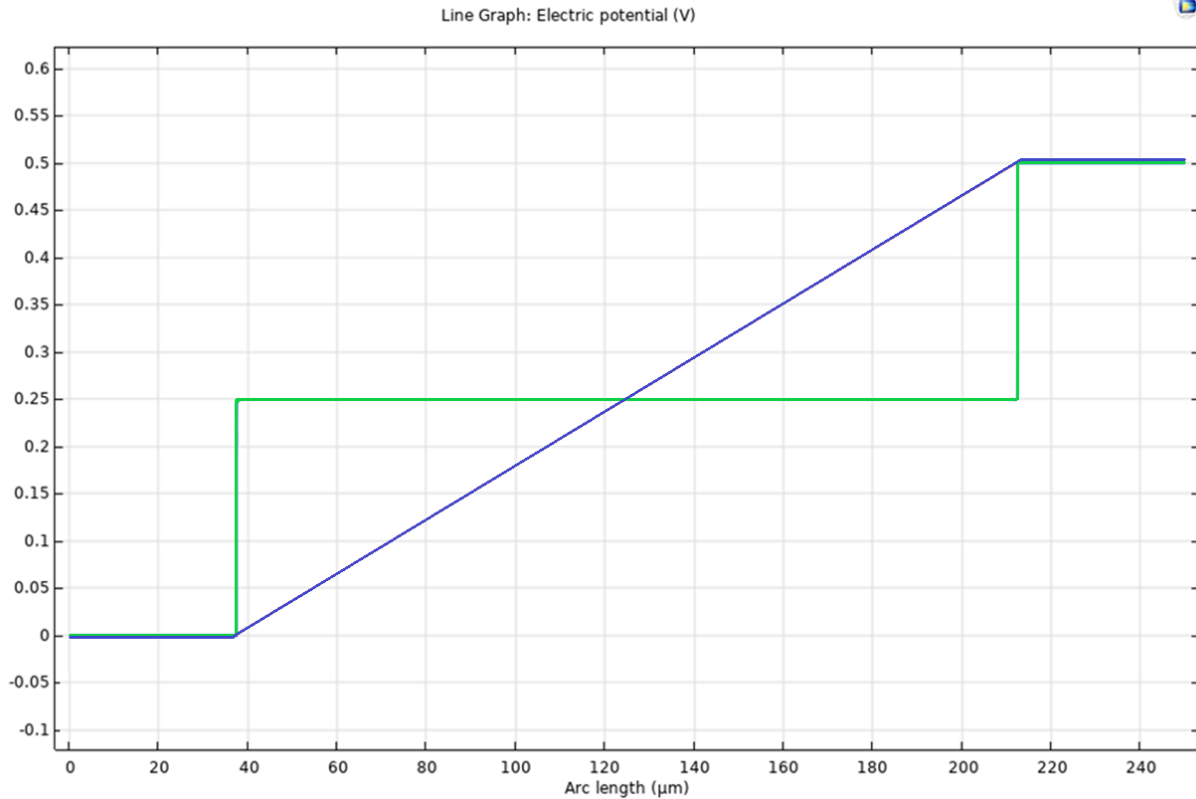


Figure 7.11: 1D plot of the electric potential across a 175 μm channel filled with pOH 4 NaOH ionic solution.

The green line highlights the rapid change in potential between the electrodes according to conventional EDL theory, while the blue line is again a reference for the electrostatic potential without a solution.

To accomplish this, we add a bulk ion concentration of 1.0×10^{-4} M to match the pOH 4 NaOH ion concentration and an estimated Debye length of 30.4 nm calculated in Chapter 2. This model follows the theories discussed previously and suggests that at an equilibrium position the electric field drops to zero after 300 nm, just a few Debye lengths. Figure 7.11 also gives us the two possible extremes and any experimental results must be somewhere between the green and blue lines.

7.4 Simulated Brownian and Data Bootstrapping from Lag Times

On the macro-scale, finding the particle trajectories for a system only requires an accounting of all the physical forces acting upon the system and solving the resulting differential equations. As a brief example: gravity accelerates an object at $g = 9.8 \frac{m}{s^2}$, the equation for distance fallen is $d_f = \frac{1}{2}gt^2$ and so after a set time of $t = 3$ seconds the ball has fallen $d_f = \frac{1}{2} \left(9.8 \frac{m}{s^2}\right) (3s)^2 = 44.1$ meters. A direct solution to an elementary problem.

Unfortunately for microscopic solutions, the ever-present chaotic Brownian motion means that such a simplified view is not feasible.

So, before we even begin to delve into the movements of a suspended particle in a microfluidic system, it is first necessary to find a way to account for a stochastic process. As Brownian motion is a fully stochastic process, we can create any number of examples by using a normalized random-number generator. For our purposes, I used Matlab's "randn" function to create a list of 10,000 random values representing a one-dimensional random walk, ranging from 3.5 to -3.5, and then plotted the cumulative sum after each step to create a series of 1-dimensional position vs. time graphs. Comparing these to the idealized Einstein-Smoluchowski equation, $\lambda_x = \sqrt{2Dt}$, it is quite clear that none of these are anywhere close a perfect match:

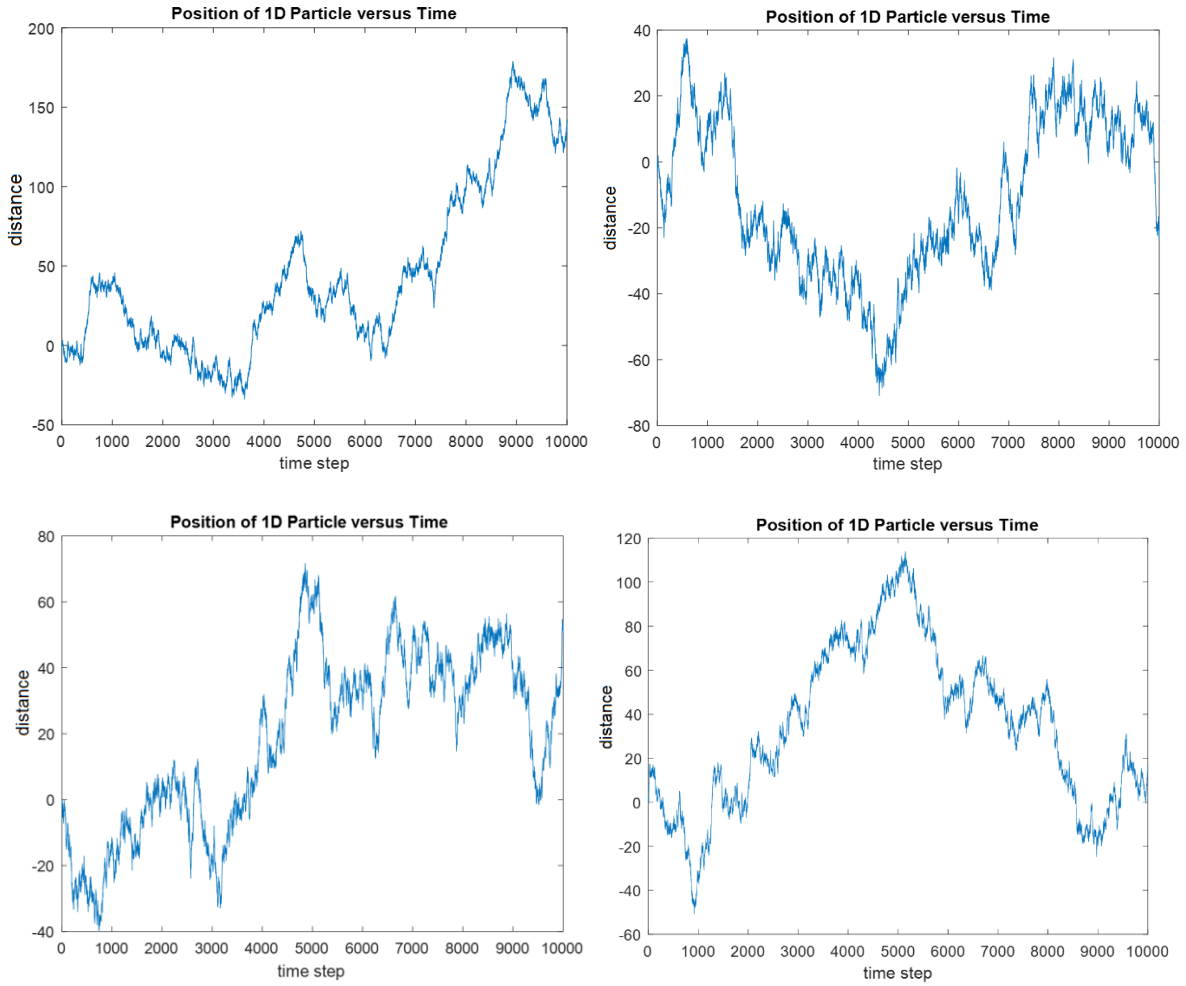


Figure 7.12: Four simulated 1D particles undergoing Brownian motion using normalized random displacements

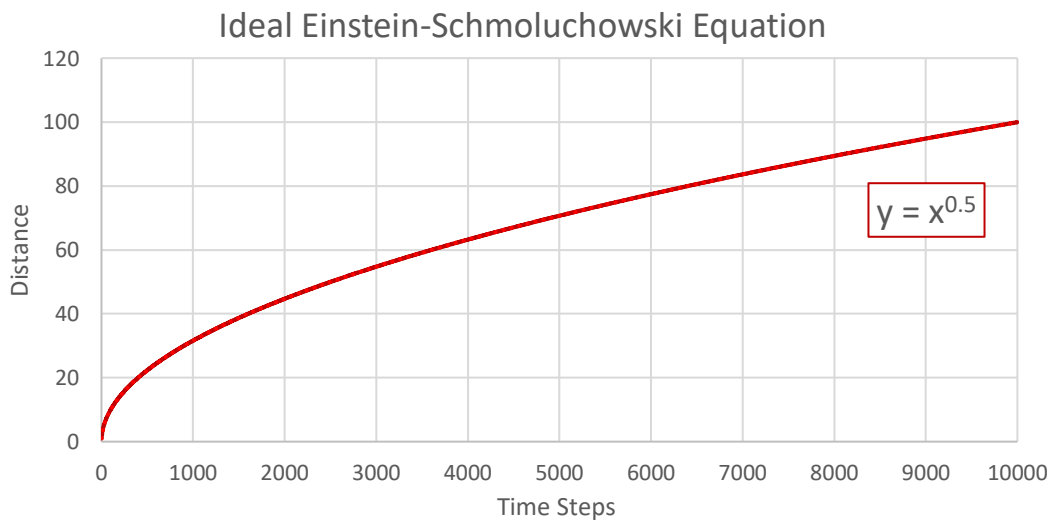


Figure 7.13: The ideal result of the Einstein-Smoluchowski equation, where $\lambda_x = \sqrt{2D} * \sqrt{t}$

It is unfortunately not possible to find a rough estimation of the diffusion coefficient based entirely on any single plot's stitched movements; it is just too chaotic. Thankfully, there is a function of stochastic processes that is extremely valuable to us: combining two or more stochastic steps creates yet another stochastic step. This gives two different ways to analyze a series of points: individually, where each step only considers the previous position, and cumulatively, where all future positions consider the first point as the origin.

The best option, however, is combining these two into "lag-time"¹ where the number of frames between each step increases: a lag-time of 1 would correspond to passing from Step 1 to Step 2, Step 2 to Step 3, etc. A lag-time of 2 would skip one step between each set of values: Step 1 to Step 3, Step 2 to Step 4. Thus, for a simple four step process, there exists six stochastic steps: [1-2, 2-3, 3-4], [1-3, 2-4], and [1-4]. Expanding this to a 10-step process results in 45 individual stochastic steps, and a 10,000-step process expands to 49,995,000 stochastic steps. This allows a relatively small number of data points to be greatly increased.

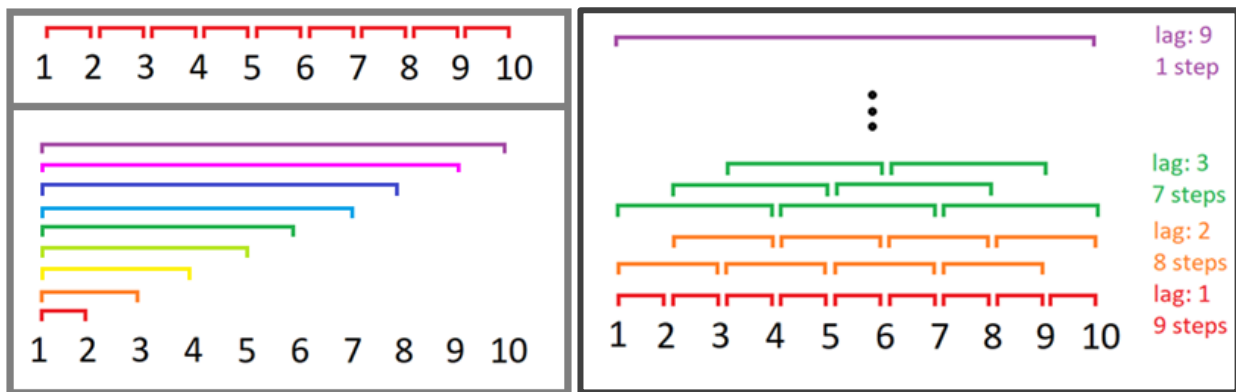


Figure 7.14 (top left): a series of 9 individual steps from 10 points, **(bottom left):** a series of 9 cumulative steps from a single origin position. **(right):** the combination of both series into lag-steps, resulting in 45 stochastic steps.

Lag-steps 4 to 8 have been skipped for simplicity.

Using this process on our previous randomly generated 10,000 values (to a ludicrous amount of nearly 50 million step values) unfortunately tends to cause an overflow error. Instead, we're going to reduce this to a bit more of a manageable 1000 values and 499,500 individual steps. Each lag-time's values are then averaged into a single distance value using a Root-Mean-Square (RMS) function and these RMS distance values are then plotted against their lag-time. In Excel, the function `"=(SQRT(SUMSQ(range)/COUNTA(range)))"` is able to do find each lag-time's value in one concise step.

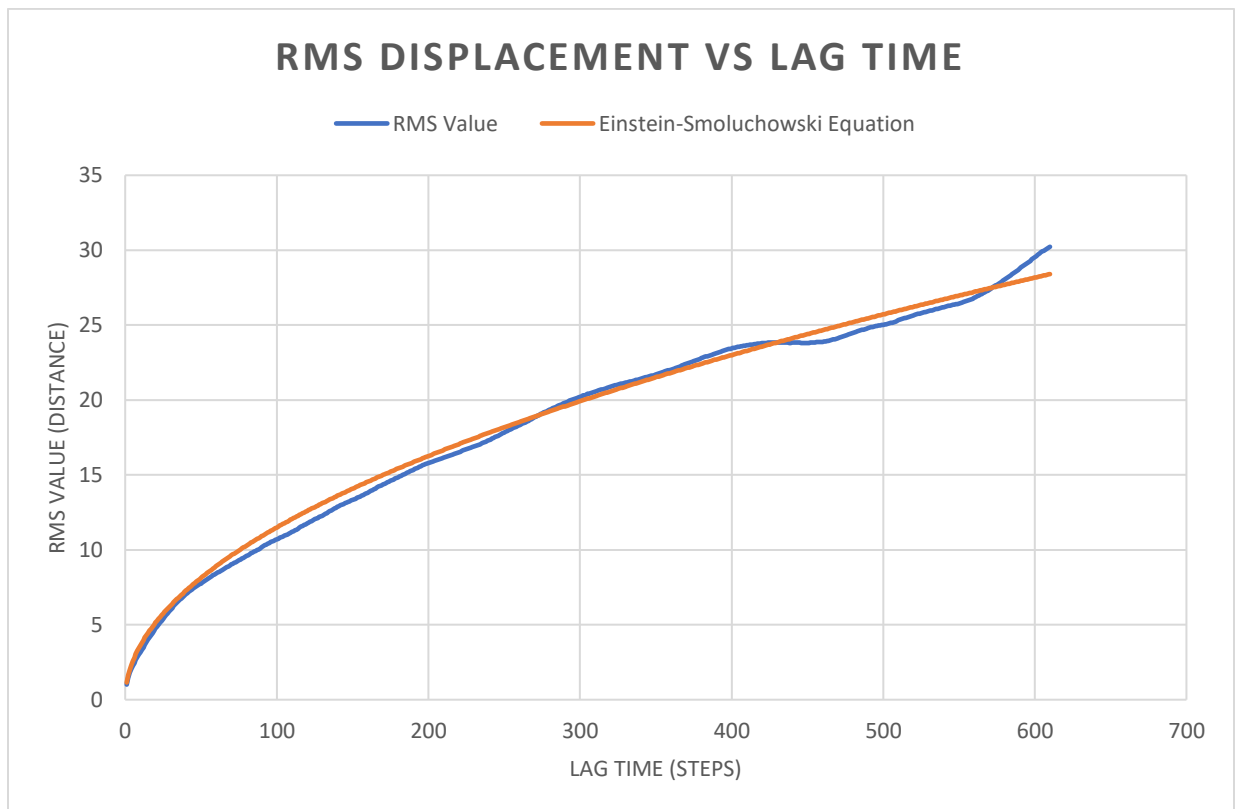


Figure 7.15: Comparison of the Einstein-Smoluchowski Equation (orange) and the RMS values of Simulated Brownian motion (blue). This represents 84% of all values, despite being only 60% of the possible lag-times.

In Figure 7.15, it is important to note two key ideas: first, the strong correlation of the RMS values to the Einstein-Smoluchowski Equations estimate of $x \propto \sqrt{t}$. This correlation occurs

because while small individual steps are stochastic the average value is not. When there are enough values, a high variance will still find the true RMS value. Secondly, while 1000 data points has up to 999 lag-times, only 600 lag-times are shown. This is because as the lag times get larger and larger, the amount of data points within each set decreases: while a lag-time of 1 has 999 data points, a lag-time of 999 only has 1 data point. As the lag-time increases, the accuracy dramatically decreases, and the high variance of values becomes increasingly detrimental. So, we have prioritized that there are sufficient data points within each lag-time and are less focused on finding the maximum lag-time.

We will expand upon these calculations in Chapter 8 when we start discussing using 2-dimensional values to find the effect of the electrostatic field on actual particles to find their ballistic component. For the rest of this chapter, however, it is sufficient to have just an understanding of how Brownian RMS values relate to the Einstein-Smoluchowski equation.

7.5 Hardware and Software Calibration for Particle Viewing

The microscope/camera setup used has two main parts that require calibration to view a nanoscale fluorescent particle: the input laser and the EMCCD Camera. This subchapter will briefly discuss the conditions and calibrations for each of these.

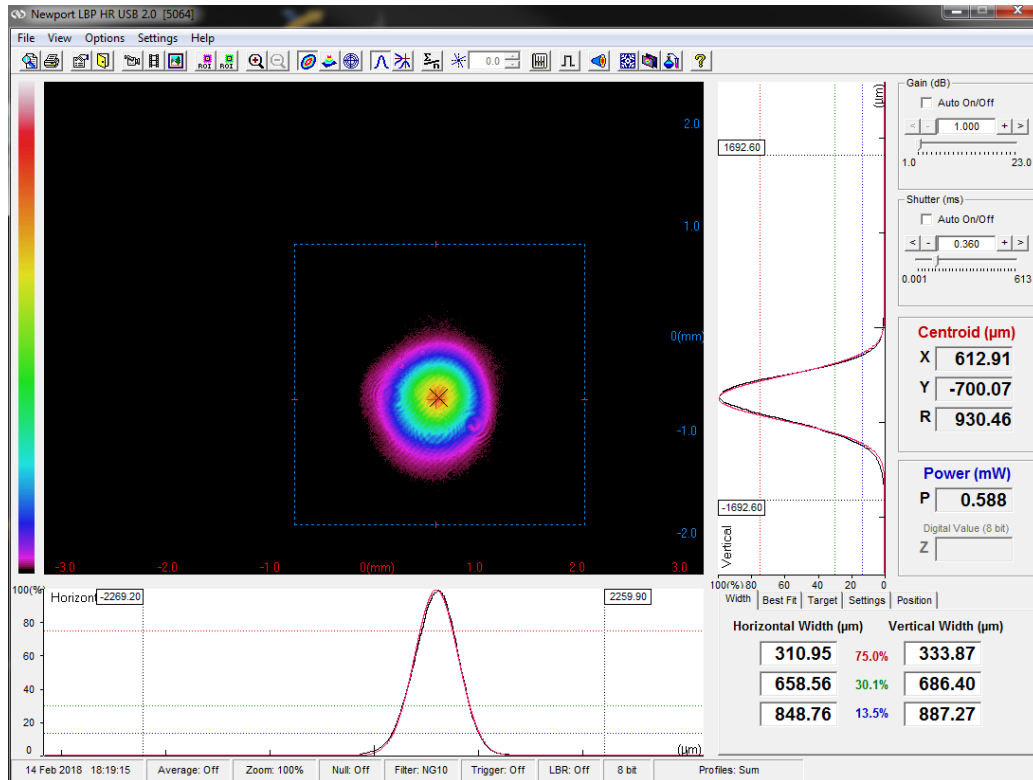


Figure 7.16: Newport LBP HR program window showing the symmetry and Gaussian fit of the 514 nm laser.

Firstly, the 514 nm argon laser is analyzed using a Newport Laser Beam Profiler (LBP) camera, which measures and shows that our laser has great beam symmetry between its vertical and horizontal widths, with only about a 4.5% error in circularity, and fits well to an expected Gaussian function. This is achieved by meticulously adjusting and cleaning all optics in the optical train leading into the entry port of the microscope, shown previously in Chapter 6.

Secondly, the EMCCD camera combined with a 40x optical objective must be properly calibrated to determine the pixel-to-micron ratio. To achieve this, a small 1.00 mm ruler with 10-micron level markers was used and fitted to the camera's view-window. With a 514 x 514 pixel window it is a simple process to estimate this ratio, but using the calibration tool of the ImageJ or FIJI programs can give better and more accurate results.

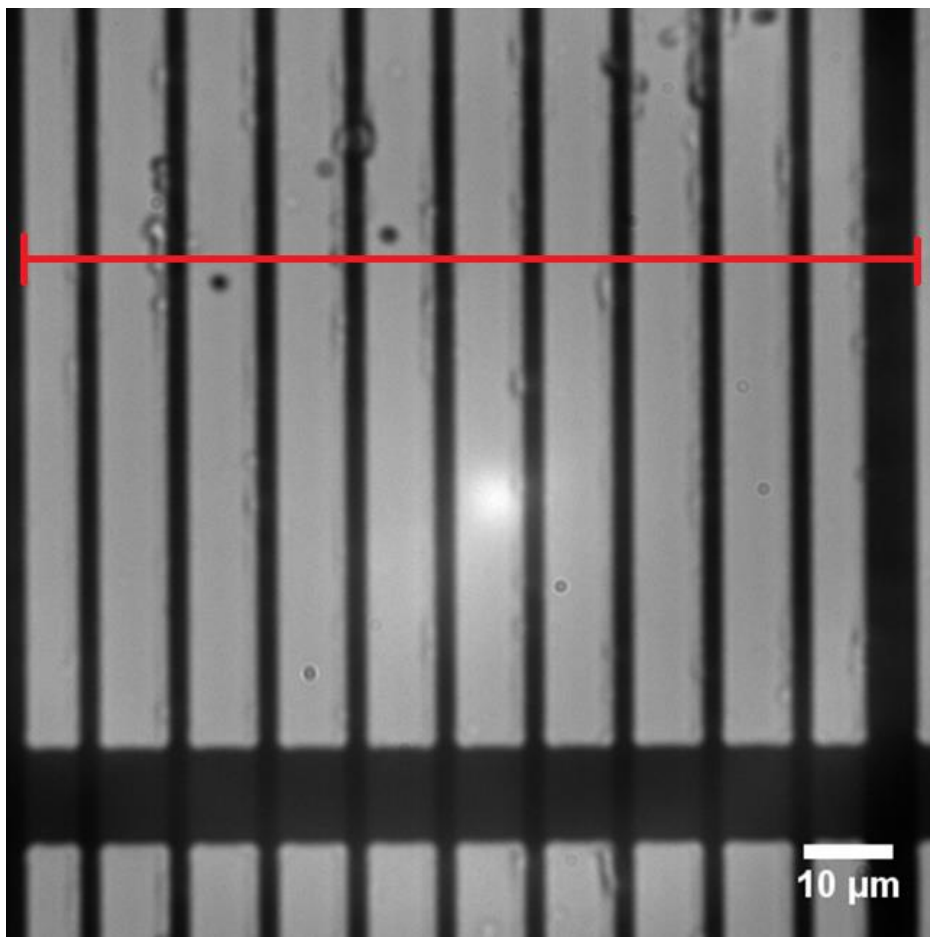


Figure 7.17: Viewing window of a micrometer ruler used for calibration at 40x magnification via brightfield illumination. The red line indicates 100 μm . The window is 514x514 pixels and has dimensions of 104x104 μm .

This calibration is applied throughout the rest of this dissertation: there are proper calibration bars in the bottom right of each image, and proper pixel-to-micron ratios have been applied to the data.

7.6 Solution Refinement and Edge Sealing

When dealing with incredibly dilute solutions, it becomes rather cumbersome to reference amounts of fluorescent in terms of molar concentrations: precise and exact picomolar

concentrations of fluorescent nanoparticles are difficult to achieve when the starting stock concentration is labelled as “about 2% solids³” (roughly 3 μM .)

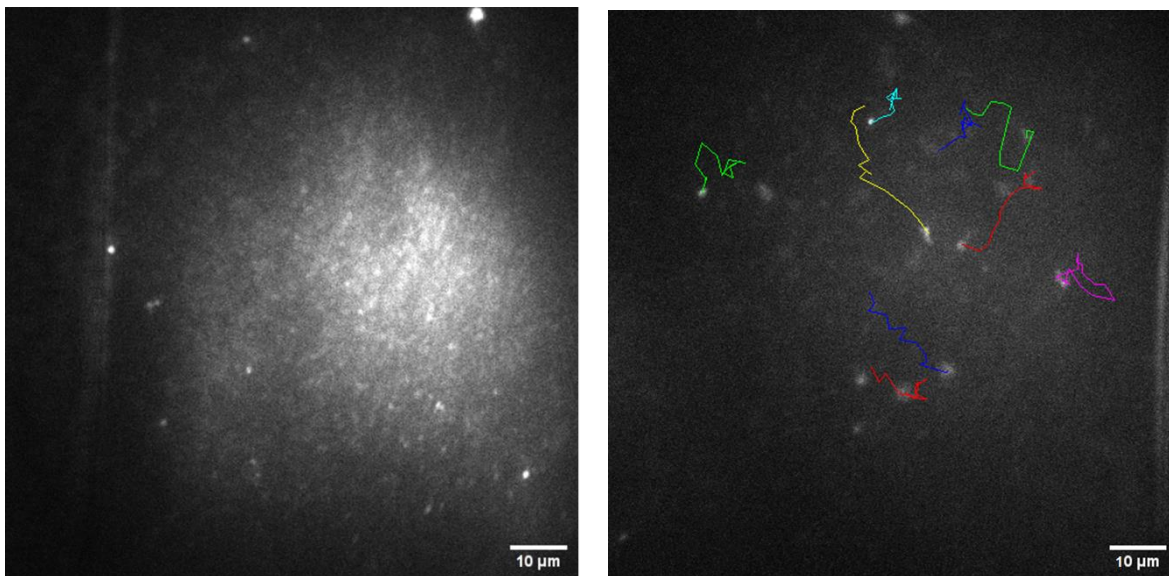


Figure 7.18 (Left): Ultrahigh concentration of fluorescent particles, roughly 100 nM.

(Right): a more dilute set of particles, with some particle trajectories, at roughly 100 pM.

At higher concentrations, as seen in Figure 7.18 (left), keeping track of a single particle is impossible for anything above 100 nM, and particles are difficult to keep resolved and distinct at anything above 100 pM. For particle tracking, an ideal concentration would be ~ 1 -10 particles in any given viewing window. Using a concentration of about 1 pM appears to give satisfactory results, but even with careful dilution using μL -level accurate pipets there is a high variance in solution results: any small changes in concentration results in a significant difference at the end. Thankfully, a sample solution can be quickly assessed by observing it in any flawed microfluidic cells that are unfit for actual experimentation.

Of course, once an ideal concentration batch is found, there are additional challenges: solution injection must be carefully done without compromising the integrity of the

nanoparticles or microfluidic cell. By means of anecdotal trials, allowing the solution to non-forcibly siphon into the electrode space via capillary action gives the best results. This is easily done by placing a 1.0 μL drop of solution along the edge of the cell. Gentle tapping of the top coverslip can help speed up the process by acting like a miniature bellows, but this requires a practiced hand: too forceful and the polystyrene nanoparticles will become impacted and immobile against the glass surfaces.

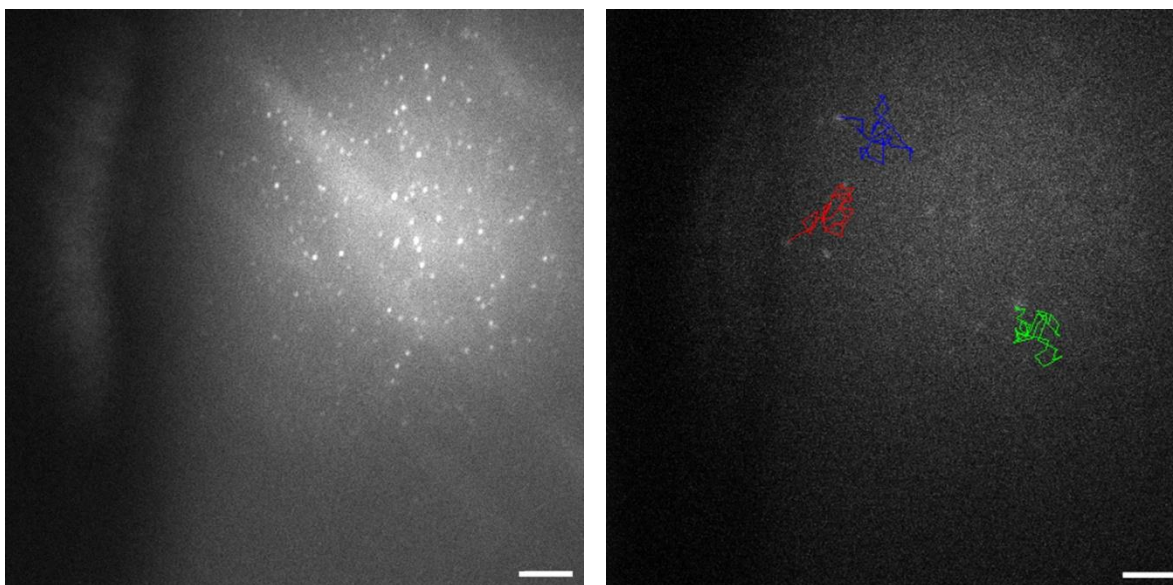


Figure 7.19 (Left): polystyrene particles immobilized and impacted onto glass. The particles appear much more in-focus and vibrant because they are immobile. **(Right):** particle-tracking lines of three different particles undergoing Brownian motion. Scalebars: 10 μm .

The last effect of the solution that must be controlled is evaporation of the solvent. As the amount of solution is only 1.0 μL , it tends to evaporate very quickly when exposed to ambient atmosphere. After being injected into the microfluidic cell, the minor and subtle differences of the glass cell's edges mean that one side of the cell will inevitably evaporate faster than the others, creating directional flow of solution towards that area. Additionally, evaporation will

gradually increase the concentration of both nanoparticles and sodium hydroxide solutes, leading to anomalous electrostatic interactions and solution viscosities.

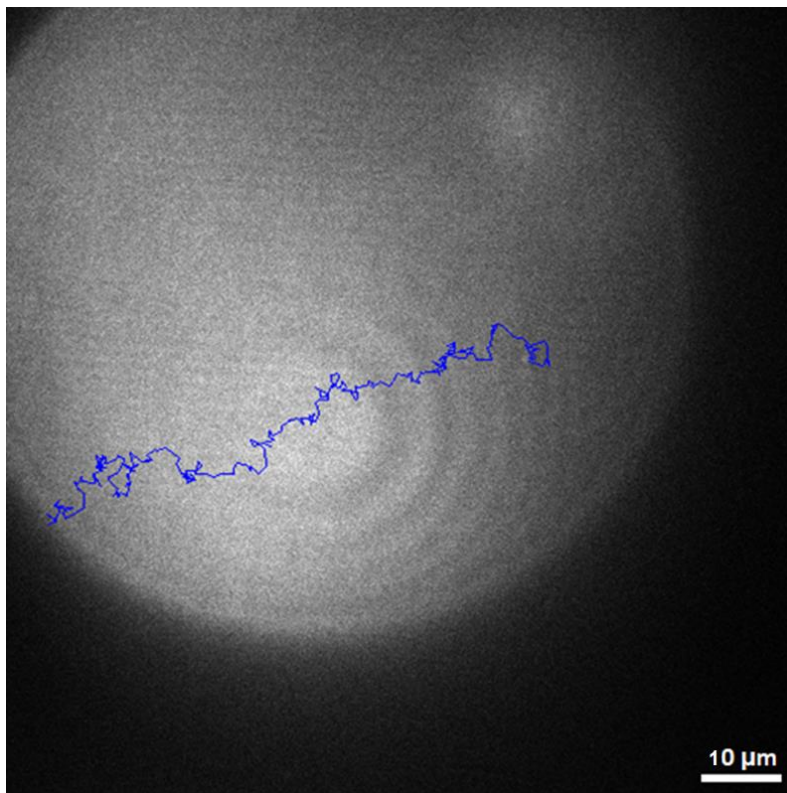


Figure 7.20: A 20 nm diameter fluorescent particle undergoing both Brownian motion and directional flow. The Brownian motion can be seen as the small chaotic movements, while the flow is a large additive factor that gives the particle a preferential direction from left-to-right. The path shown is $\sim 1.35 \mu\text{m}$ over 30.994 s.

This solution flow can vary from a subtle effect to a much stronger effect, but in either case it completely dominates any subtle Brownian movement or electrostatic effects we are seeking to analyze. While there are many methods to prevent solvent evaporation, the simplest method is sealing the sides and locking the solution inside. For our purposes, we used plain Vaseline petroleum jelly to great effect: the timeframe to stably analyze samples increased from a few minutes to hours and reduced direction flow to a complete stand-still, as seen

previously in Figure 7.19 (right) as well in the following figure, showing a single particle undergoing stochastic Brownian motion.

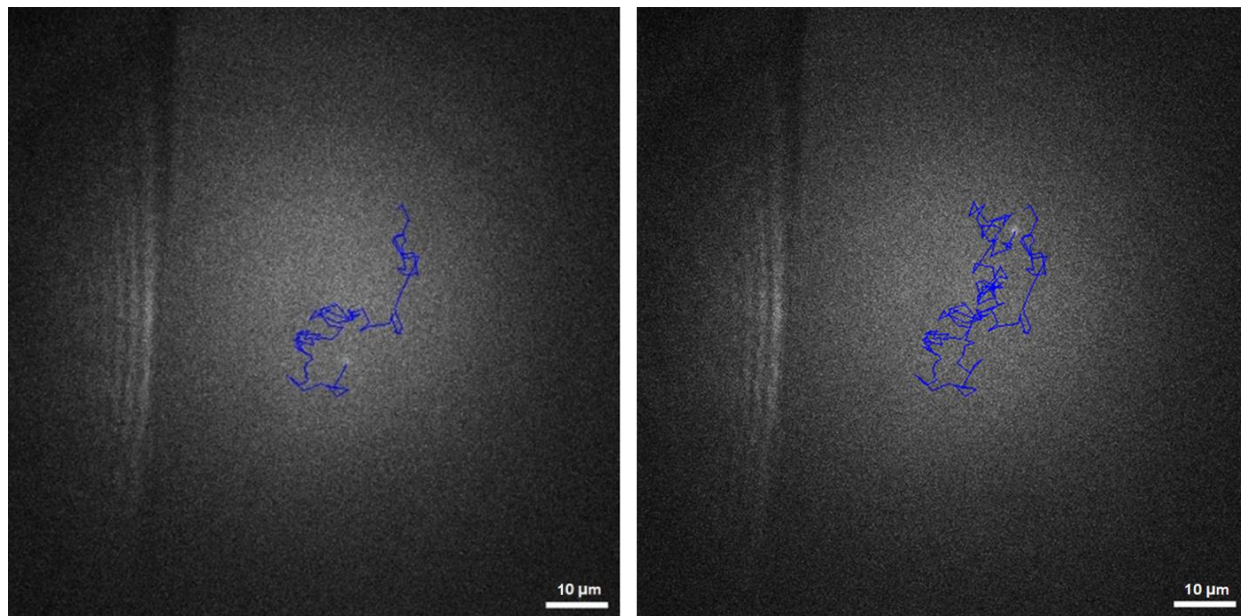


Figure 7.21: Trajectories of a Brownian 20 nm FL nanoparticle at two times: 38.731 s (**left**) and 74.079 s (**right**).

7.7 Z-Direction: Solution Height Importance

In our calculations, we assume that the Brownian motion observed is only 2-dimensional, but this is obviously a gross approximation. In truth, as seen in Figure 7.8, our sample has a variable and a relatively large solution height: initial tests using the methodology for our corral trapping experiments had a controlled 10 μm solution height, which is 200x larger than a 50 nm metal electrode and 500x larger than a 20 nm diameter particle. Very quickly it became apparent that such a massive solution height was inadvisable: a nanoparticle's fluorescent image varies with height and if the particle moves too far outside of the focal plane it is undetectable, and therefore the goal became to minimize the solution height as much as possible.

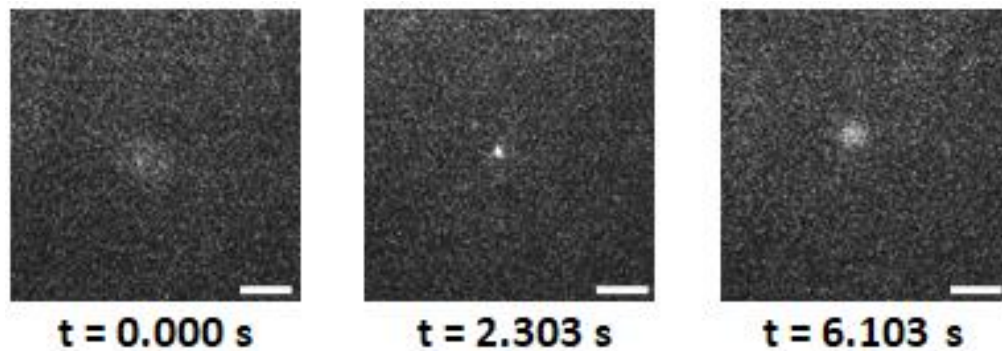


Figure 7.22: Zoomed-in fluorescent images of a nanoparticle as it diffuses vertically at selected positions: **(left)** above the focal plane, **(middle)** in focus, and **(right)** below the focal plane. Scalebars: 10 μm .

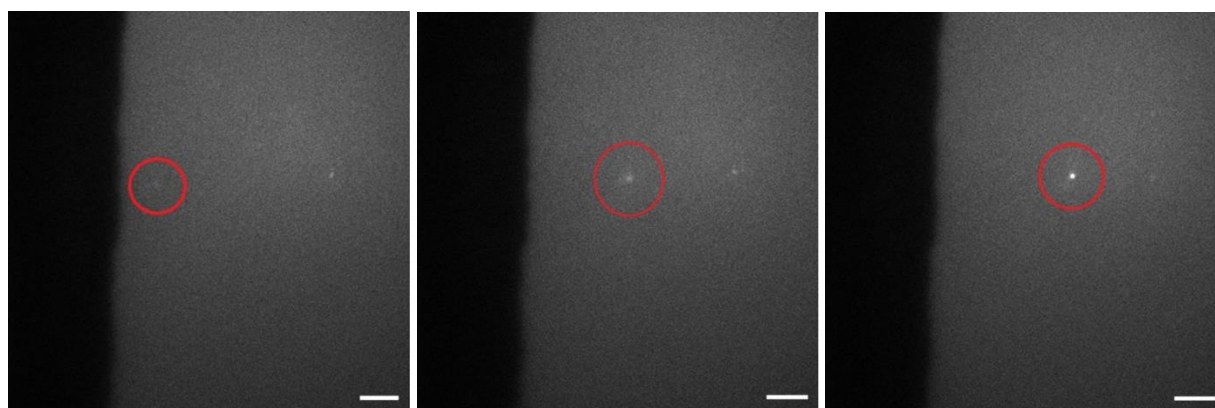


Figure 7.23: Frames of a fluorescent nanoparticle (red) emerging from behind the electrode (black bar on the left) and moving down into focus. The solution space above the electrode is too large in this case. Scalebars: 10 μm .

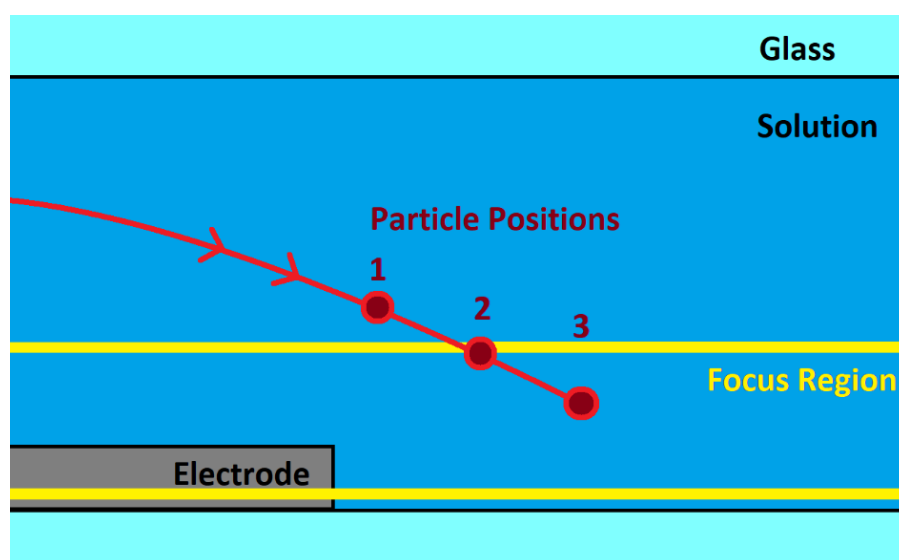


Figure 7.24: Simplified side-view depiction of the particle's trajectory in Figure 7.23.

While there are numerous ways to decrease the channel height, each with varying efficiency, the simplest and fastest method was to slightly alter the attachment procedure of the top coverslip. By gently placing a small stainless-steel weight onto the top coverslip, it presses the two slides together without causing any worry of cracking the glass. Then, using a UV-curing glue, the top coverslip is attached to the electrodes while under this weighted stress and locked into position. The metal weights are then removed, and the height is at a sub-micrometer level.

Each microfluidic cell is slightly different when it comes to the exact height, but slides can be eliminated for being too large using a quick volume conversion. Since $1.00 \mu\text{L}$ is $10^9 \mu\text{m}^3$ and each top coverslip is $18 \times 18 \text{ mm}$, if $1.00 \mu\text{L}$ perfectly fills this space, then the height must be at maximum $3.0 \mu\text{m}$. If more than $1.0 \mu\text{L}$ is required, it is rejected and thrown out. By anecdotal evidence this appears to be a satisfactory to keep fluorescent particles within the focus region.

7.8 Voltage Assessment and Electrode Issues

The final hurdle for ensuring consistent reliable results is finding the right potential: too low and nothing happens, too high and the system falls apart. Applying too many volts will even cause the electrolysis of water, completely breaking the microfluidic cell. To test the specific bounds of the sample cells, a series of scout experiments was thus conducted to test the extreme bounds of the system.

Firstly, a standard solution ($\sim 10 \text{ pM}$) of nanoparticles was subjected to a DC potential tuned to 5.00 V to see how quickly particles would react to such a strong field, their maximum speed, as well as whether a strong electrolysis reaction would occur under normal conditions. The

results of this were barely caught on video: a particle reacted so incredibly strongly that it is viewed for just two frames, resulting in an incredible speed of $\sim 580 \mu\text{m/s}$. To put it mildly: that's too fast (and the solution quickly undergoes electrolysis).

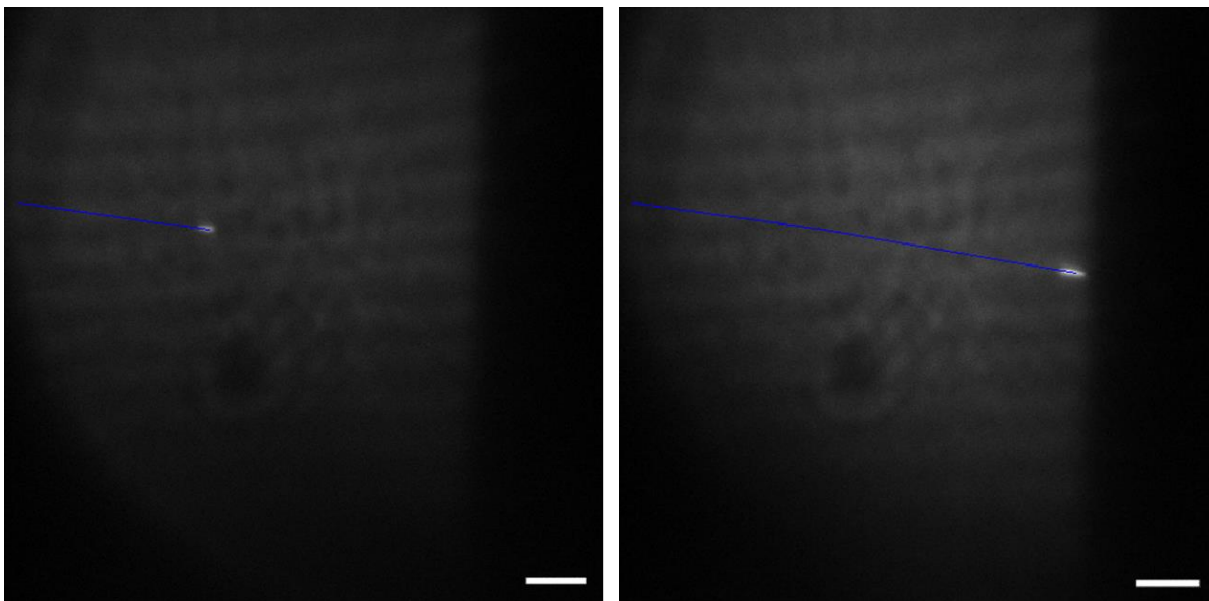


Figure 7.25: two frames of a 20 nm FL particle after the application of 5.000 V across a 250 μm channel. The second frame is only 0.1495 seconds later. Scalebars: 10 μm

The second voltage scouting experiment we'll discuss is that of what happens after the electrode is turned off: EDL theory only considers what occurs along the electrode after the system has reached an equilibrium, whereas our interest is in the area of ambiguity between fully disperse and homogenous solution at time zero and the build up of a double layer equilibrium. This will often necessitate turning the electrode on-and-off to analyze the same system at different conditions, and thus it is important to understand the conditions once the potential is removed.

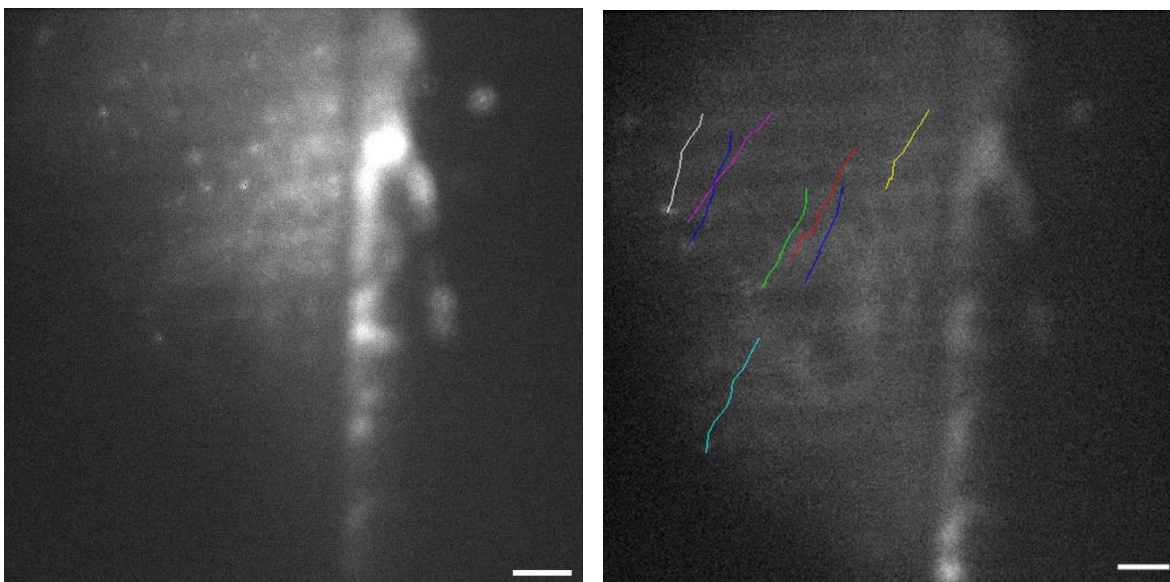


Figure 7.26: Two frames of an electrode (right side of image) after voltage has been turned off on an electrode that has nanoparticles clustered on it. Scalebars: 10 μm

As seen in Figure 7.26, if there is a significant concentration of particles adhered to the electrode, then once the electrode is turned off, the particles will dislodge and disperse away. But as these particles can themselves cause additional force effects as they migrate, they create their own microcurrents of solution. The particles dispersing are unidirectional and of nearly the exact same magnitude, suggesting that the particles are being affected by the same directional flow component. As these flow effects are an added complexity factor, this reinforces the need for keeping nanoparticle concentrations as low as possible.

The last scouting experiment was seeing whether a slightly lower voltage, 2.000 V, but a higher concentration (~ 10 nM) would cause the solution to saturate the electrode and see how far the potential voltage “reaches” into the bulk solution.

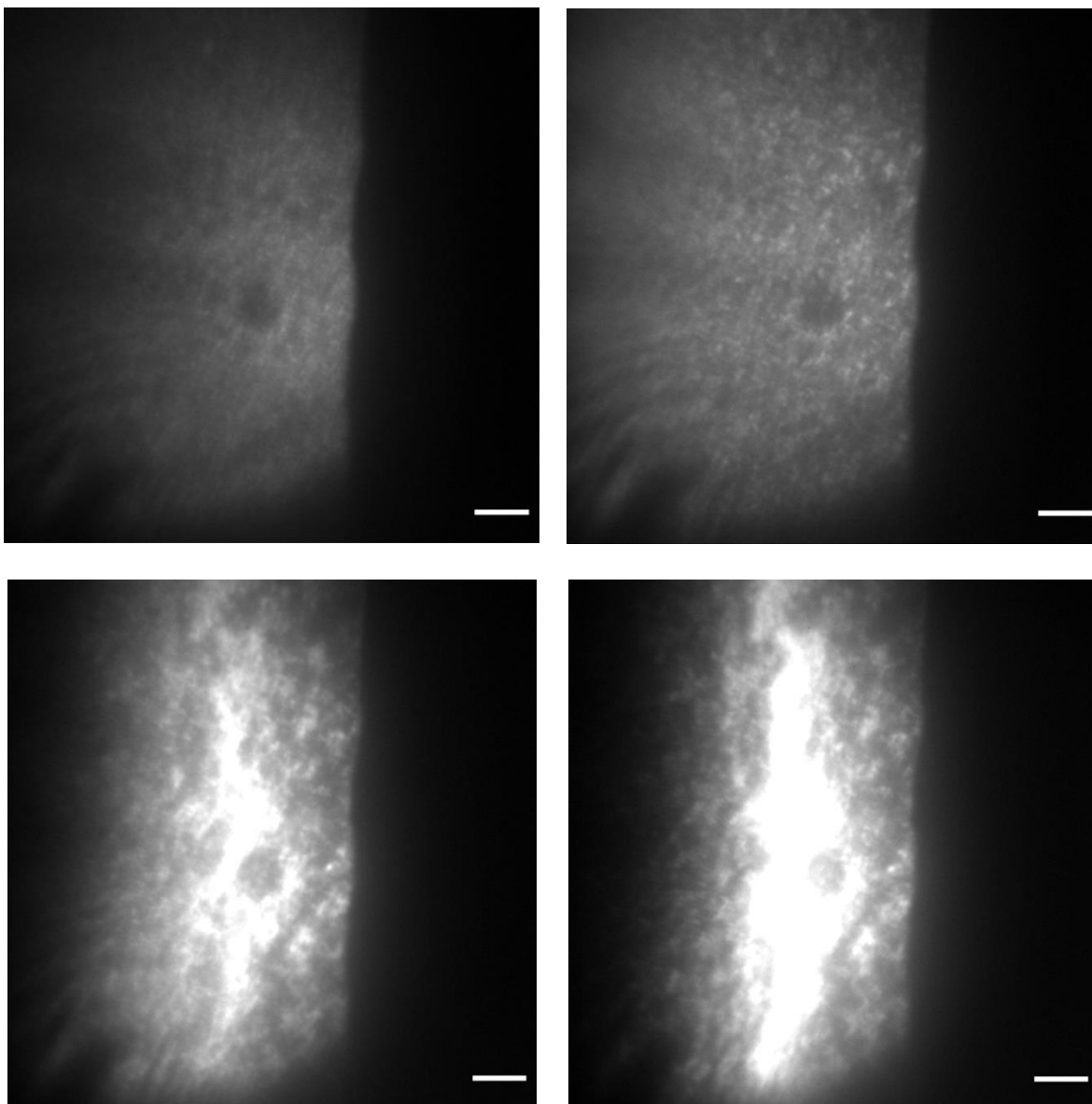


Figure 7.27: Time lapse of nanoparticles aggregating along an electrode after the application of 2.000 V. The increasing brightness is due to the increasing concentration of fluorescent particles. The times, in order, starting at the top left: **(a)** 0.00 s **(b)** 6.47 s **(c)** 13.08 s **(d)** 19.70 s. Scalebars: 10 μm

As seen in Figure 7.27, the results were rather dramatic: over the course of 20+ seconds the nanoparticles rapidly depleted from the bulk solution and formed a massive particle aggregate along the electrode, several hundred micrometers in depth, where they were quickly

immobilized into what appeared to be a thick gel-like structure, leaving the bulk completely devoid of fluorescent particles. This structure could possibly be analogous to the Stern Plane from EDL theory, just far more massive in scale. The overlapping signals of billions of nanoparticles further stresses the need for dilute solutions using far reduced voltages.

With these extreme parameters better understood, we can now move away from troubleshooting the double electrode microfluidic cells, and head towards our true goal and our next chapter: direct observation and analysis of nanoparticles and separating the stochastic Brownian force from the ballistic force of the electric double layer.

- (1) Michalet, X. Mean Square Displacement Analysis of Single-Particle Trajectories with Localization Error: Brownian Motion in Isotropic Medium. *Phys Rev E Stat Nonlin Soft Matter Phys* **2010**, *82* (4 Pt 1), 041914.
- (2) Udad, X. S. Controlling and Manipulating Microscopic Particles in Solution By Using Various Electric Field Geometries, 2019.
- (3) *FluoSpheres™ Carboxylate-Modified Microspheres*. <https://www.thermofisher.com/order/catalog/product/F8787> (accessed 2022-10-20).

Chapter 8

Potential Reduction and EDL Establishment Results

8.1 Chapter Overview

This chapter focuses on the data that is the result of an optimal microfluidic double electrode cell. First, we will start with characterizing simple Brownian motion and comparing the experimental diffusion values to theory, before then moving on to applying an electrostatic potential and extracting the ballistic component from the displacement data. We'll then transition from there to include multi-particle attraction and Brownian agreement, and then extrapolate the effective voltage, which will be expanded upon in Chapter 9.

8.2 Brownian Motion and Calculated Diffusion Coefficient

As discussed earlier, theorized in Chapter 1 and simulated in Chapter 7, a particle undergoing Brownian motion displays a characteristic displacement as a function of the square root of time: $\lambda_x = \sqrt{2Dt}$. While not immediately obvious for a particular particle displacing over time, the function emerges by taking the RMS deviation of a collective set of lag-times.

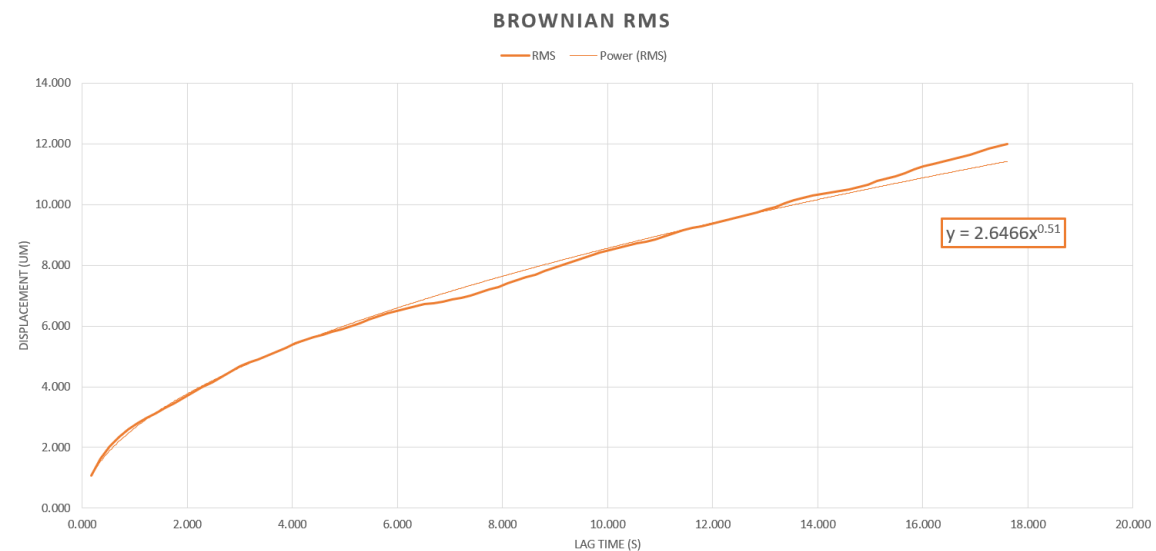


Figure 8.1: RMS deviation vs increasing lag time for a 20 nm FL particle undergoing Brownian motion. The exponential value was calculated using a power law fit function.

Extracting the diffusion coefficient out of a $t^{1/2}$ function is rather complicated: Brownian motion ($f(x) = (2Dt)^\alpha$), can be ideal ($\alpha = 0.50$), sub-diffuse ($\alpha < 0.5$), or super-diffuse ($\alpha > 0.5$) depending on whether an external condition helps or hinders the particle's movement, and the value seen in Figure 8.1, $\alpha = 0.51$, indicates that the particle is remarkably close to "ideal" Brownian. This is not always the case, however, and it can be difficult to find a good approximation with large magnitude stochastic scenarios. While affixing the value of α to be exactly 0.50 is certainly possible, it masks any sub-or-super-diffuse behavior. Instead of worrying about such intricacies, it is far easier to instead take the mean-square value of diffusion, or MSD, because this is a much cleaner function, $\langle x^2 \rangle = 2Dt$, where the slope of the line is equal to twice the diffusion coefficient. If movement is either sub-or-super diffuse, the line will not be linear.

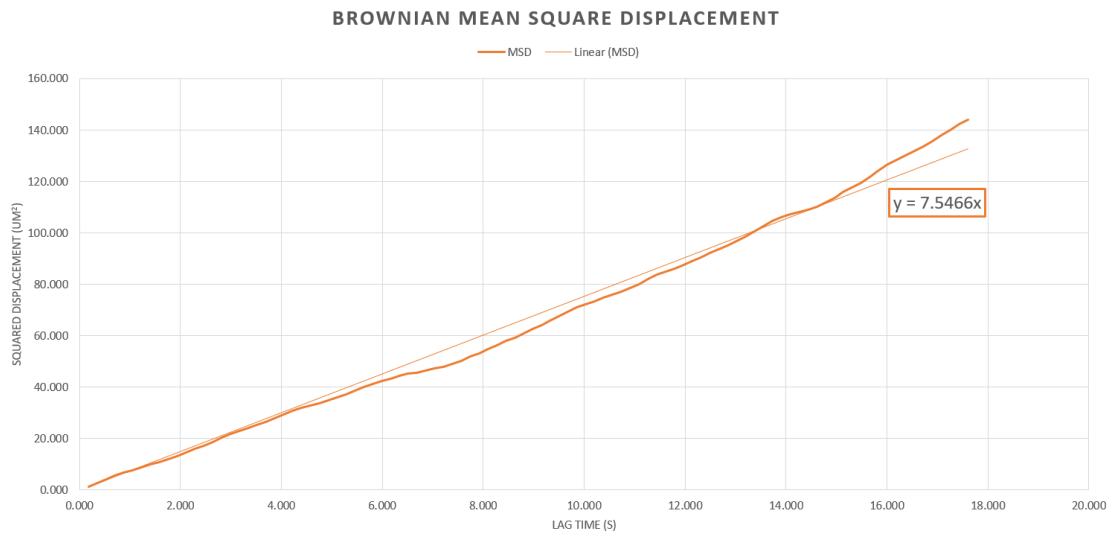


Figure 8.2: Linear MSD plot of the experiment seen in Figure 8.1. The slope is twice the diffusion coefficient, D .

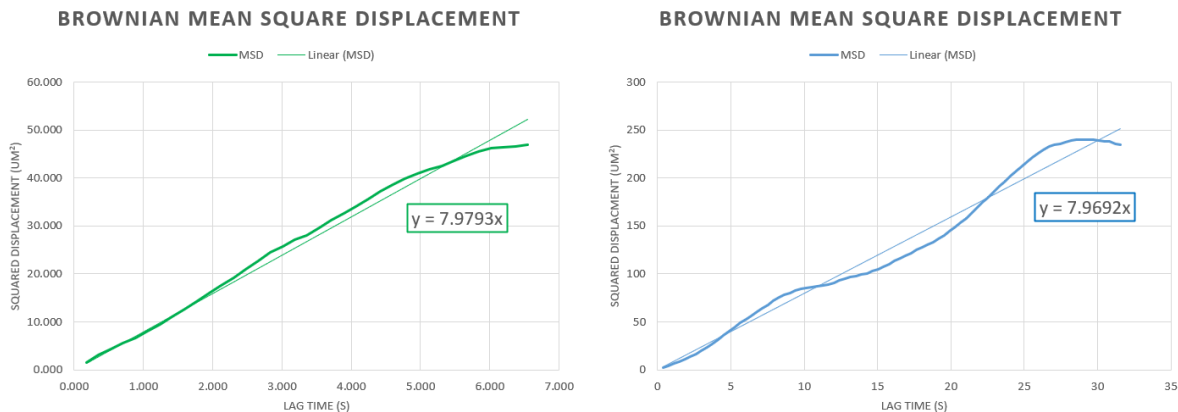


Figure 8.3: Two more MSD plots of additional experiments on different samples of 20 nm FL nanoparticles, taken months apart using different microfluidic cells, with values in the same approximate range.

Taking this estimation, as well as many more from other experiments, we can find that our 20 nm fluorescently tagged polystyrene nanoparticles will have a diffusion coefficient of roughly $3.9 \mu\text{m}^2/\text{s}$. By referring to Equation 1.8, we can calculate an effective particle radius:

$$D = \frac{RT}{N_A} \frac{1}{6\pi\eta a} \quad (1.8)$$

$$a = \frac{RT}{DN_A 6\pi\eta} \quad (8.1)$$

Using an R value of $8.314 \text{ m}^3 \text{ Pa K}^{-1} \text{ mol}^{-1}$, a temperature of 293 K, and assuming the viscosity of a 10^{-4} M sodium hydroxide solution being roughly similar to water at 1.00 mPa s, we can then find that the effective radius of our “20 nm diameter” nanoparticles (manufacturer radius estimate: 14 nm) comes out to around 50 nm.

At first glance, this might seem rather alarming, as it implies that the radius is off by a factor of four, but it is important to remember that this is an effective particle radius which includes not only the particle, but the solvation shell and any counterions that make up its own EDL around the particle. Essentially: the effective radius of the nanoparticle is going beyond just the

physical structure of the nanoparticle by incorporating rigid and semi-rigid layers of solvent and counter-ions attracted to the carboxy groups, creating a larger dynamic radius as it moves through solution.

Considering that in Chapter 2 we found that the Debye length for a pH 10 sodium hydroxide solution was 30 nm, the combination of a 14 nm radius particle with a 30 nm “solvation shell” comes remarkably close to the calculated value of 50 nm (although this is not to suggest that the Debye length is equivalent to the size of the solvation shell). However, the calculation of the diffusion coefficient is not the end goal of this research.

8.2.1 Simulated Ballistic Component Extraction

Much like in Chapter 7.4, before we even begin to incorporate mathematical functions into experimental results it is first necessary to create a theoretical framework via simulated results. To achieve this, we only need to introduce an additive factor to the stochastic Brownian motion’s perturbations.

Taking the same values found earlier, we can now add a secondary effect: a small directional value added to every step. Using very large values (anything greater than the standard deviation) becomes a trivial solution as the Brownian motion component fades from importance and becomes nothing more than noise: a difference of +/- 1.0 $\mu\text{m/s}$ means little when the ballistic component is a massive 1000 $\mu\text{m/s}$. When small directional components are used (for example something as small as 10% of the standard deviation) then the ballistic component is not as immediately recognizable and requires a bit more effort.

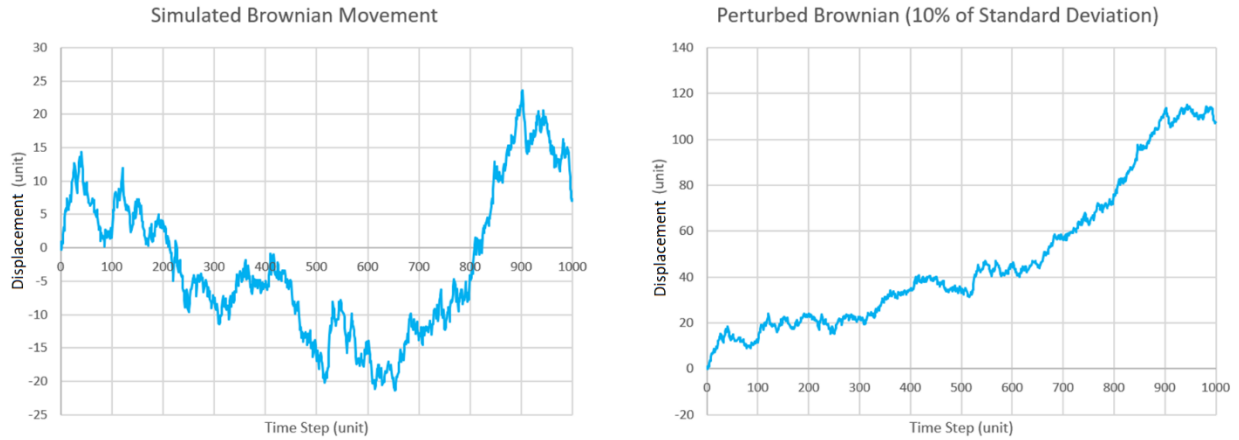


Figure 8.4 (left): Simulated trajectory of a particle undergoing Brownian motion from Chapter 7. **(right):** the same simulated values with an added perturbation of +0.1000 units, or 10% of the standard deviation.

In Figure 8.4, the Perturbed Brownian graph shows many of the same Brownian hallmarks as the Simulated Brownian Movement, but with a slight overriding direction layered on top. An experimental example would be something akin to Figure 7.17, where a particle undergoing Brownian motion also had a single directional ballistic flow. The rough estimated value of the ballistic component can be found by taking the start-and-end points of a particle and performing a simple distance/time calculation, but this only works on smaller scales and the error is quite large: Figure 8.4 (right) is certainly not a perfectly straight line, and on any small timescale there are several cut-backs in the opposite direction of the additive as well as regions where the Brownian component is noticeably larger.

This perturbed data set can then have the same data boot-strapping method done as in Chapter 7.4 to create a Ballistic-Brownian MSD value $\langle \Delta x_{\text{Perturbed}}^2(t) \rangle$, and then subtract the purely Brownian MSD value $\langle \Delta x_{\text{Brown}}^2(t) \rangle$ found previously to find the MSD ballistic component $\langle V(t)^2 \rangle$, or the RMS component $V_{\text{RMS}}(t)$:

$$\langle(\Delta x)_{\text{Perturbed}}^2(t)\rangle = 2nDt + \langle V(t)^2 \rangle \quad (1.22)$$

$$\langle(\Delta x)_{\text{Brown}}^2(t)\rangle = 2nDt \quad (1.19)$$

$$\langle(\Delta x)_{\text{Perturbed}}^2(t)\rangle - \langle(\Delta x)_{\text{Brown}}^2(t)\rangle = (2nDt + \langle V(t)^2 \rangle) - 2nDt = \langle V(t)^2 \rangle \quad (8.2)$$

$$\sqrt{\langle(\Delta x)_{\text{Perturbed}}^2(t)\rangle - \langle(\Delta x)_{\text{Brown}}^2(t)\rangle} = V_{\text{RMS}}(t) \quad (8.3)$$

Thus, by subtracting the MSD of Brownian motion from the MSD of ballistically perturbed Brownian motion, we can find the Root of the “MSD subtraction” (R-MSD subtraction) deviation value of just the ballistic component:

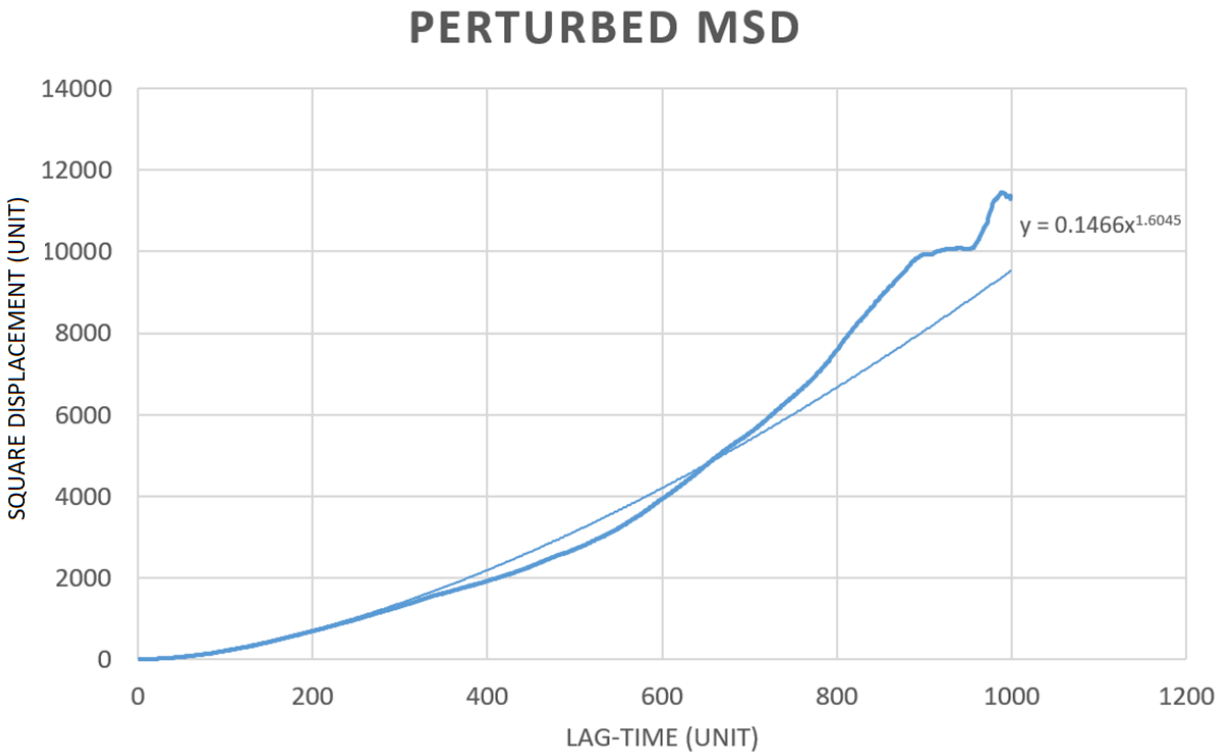


Figure 8.5: Mean-Square Displacement vs Lag-time. Comparatively, a pure Brownian function should be linear.

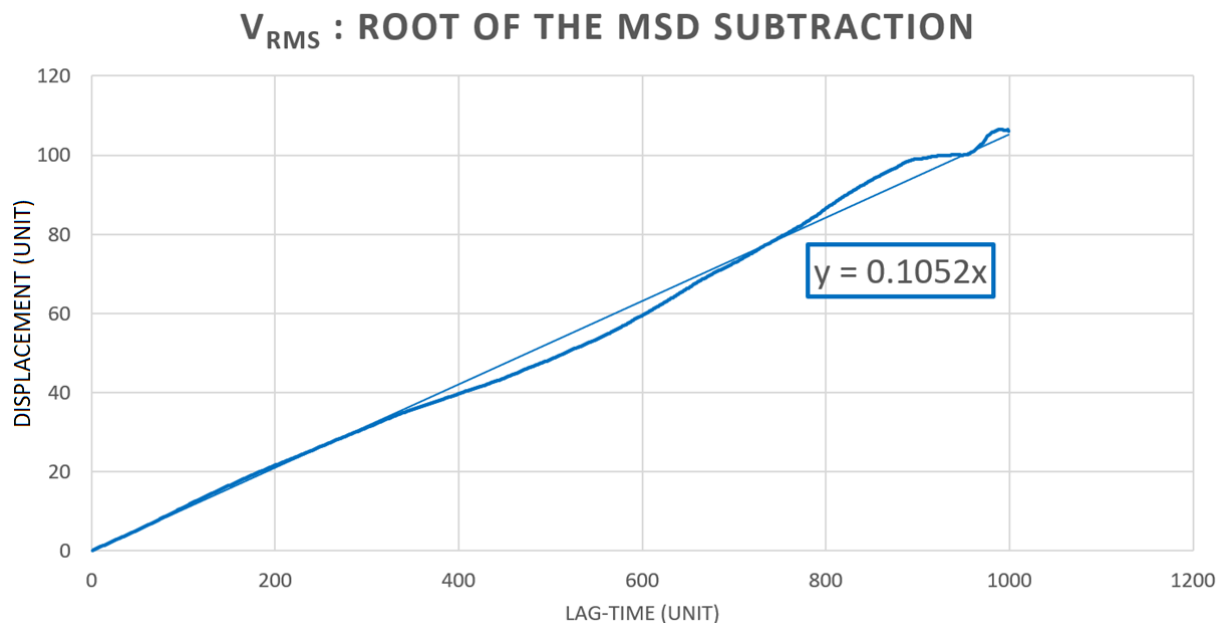


Figure 8.6: The calculated ballistic component V_{RMS} , found by subtracting the values in Figure 8.5 by the MSD from Figure 8.4, and taking the square root of the result, or R-MSD subtraction. The actual perturbation was +0.1000 units (10% of the standard deviation) which matches the slope of $|0.1052|$ units with a 5% error.

This system is of course an ideal case: the simulated Brownian values are known, and we are just adding the ballistic component onto the raw data. When it comes to real experimental values, we will not have this opportunity to pre-emptively know the magnitude of Brownian motion or its “true” value.

Thankfully, the microfluidic cell is structured in a very specific way to eliminate as much uncertainty as possible by using two distinct and independent axes: perpendicular to and parallel with the electrode. The perpendicular axis x_{axis} will have both ballistic and Brownian components, while the parallel axis y_{axis} will be unaffected by the field and thus be purely Brownian. By the means of this simulated example, we now have a verified pathway to extract and calculate the ballistic component of an experimental set of values: subtracting $\langle \Delta y_{axis}^2(t) \rangle$

from $\langle \Delta x_{axis}^2(t) \rangle$, and taking the square root, to find V_{RMS} for a given particle.

$$\text{Y-axis (Brownian)} \quad \langle \Delta y_{axis}^2(t) \rangle = 2Dt \quad (8.4)$$

$$\text{X-axis (Perturbed)} \quad \langle \Delta x_{axis}^2(t) \rangle = 2Dt + \langle V(t)^2 \rangle \quad (8.5)$$

$$\text{Ballistic Component} \quad \sqrt{\langle \Delta x_{axis}^2(t) \rangle - \langle \Delta y_{axis}^2(t) \rangle} \approx V_{RMS}(t) \quad (8.6)$$

8.2.2 X-and-Y Axis Brownian Similarity

Naturally, an immediate concern is whether $\langle \Delta y_{axis}^2(t) \rangle$ and $\langle \Delta x_{axis}^2(t) \rangle$ are truly comparable. Theoretically, it makes perfect sense, but for the sake of verification we'll go through a brief example. Often, multiple particles are observed undergoing Brownian motion in a given sample and their movements, while stochastic, are roughly of the same magnitude. We can use one such example to illustrate the similarity of not only the x-and-y axes, but also agreement between different particles within the same solution.

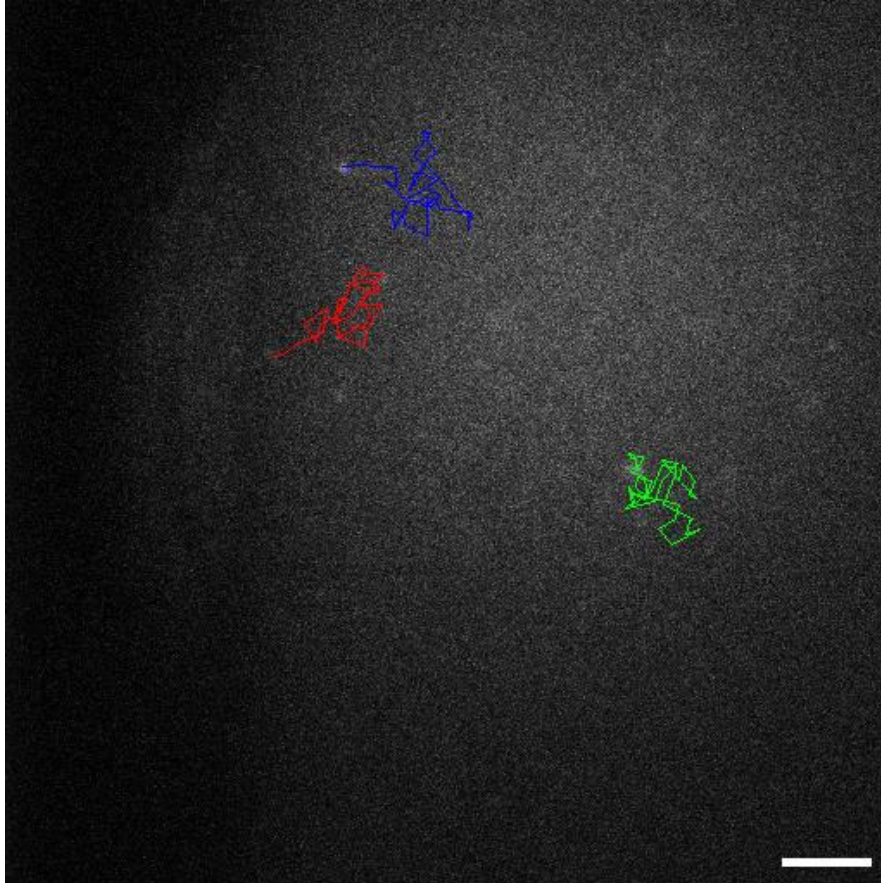
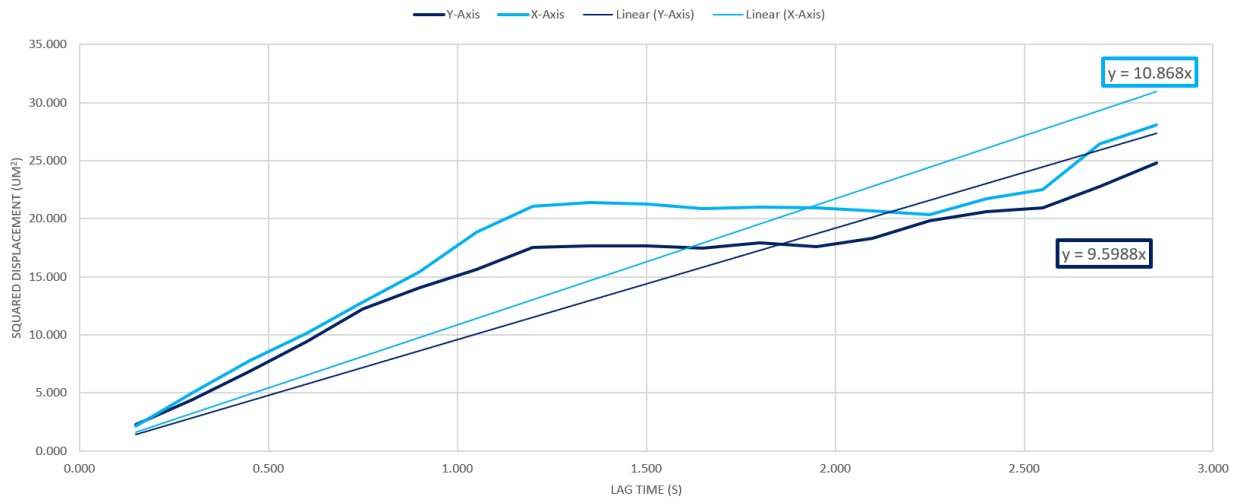


Figure 8.7: Trajectories of three 20 nm FL particles undergoing pure Brownian motion. The scale bar is 10 μm .

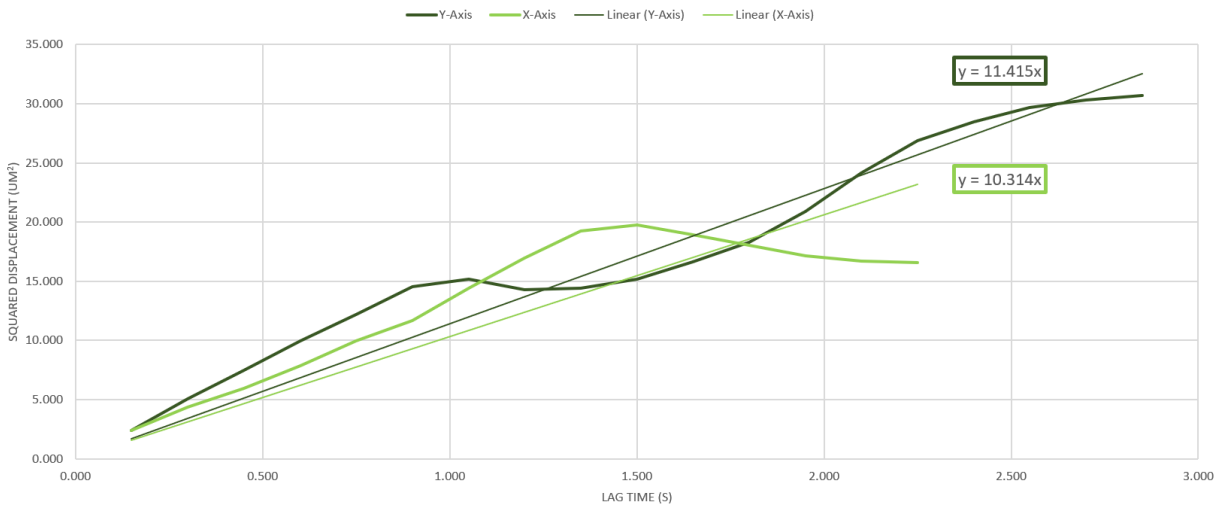
These three particles have their own unique movement profiles, without any unidirectional flow mechanics or overriding factors. If the x-axis movements are independent from y-axis movements, then each of these particles should result in roughly similar diffusion coefficients for both axes. As a brief reminder, the stochastic nature of Brownian motion means that on short time scales they won't be perfectly equivalent, but there shouldn't be a wild deviation.

Figure 8.8 (next page): The X-axis and Y-axis mean square displacements of the three freely diffusing particles (blue, green, red) shown in Figure 8.5. The slopes were calculated using the bootstrapped MSD method shown in Chapter 7. The darker color in each graph depicts the Y-axis, while the lighter color is the X-axis.

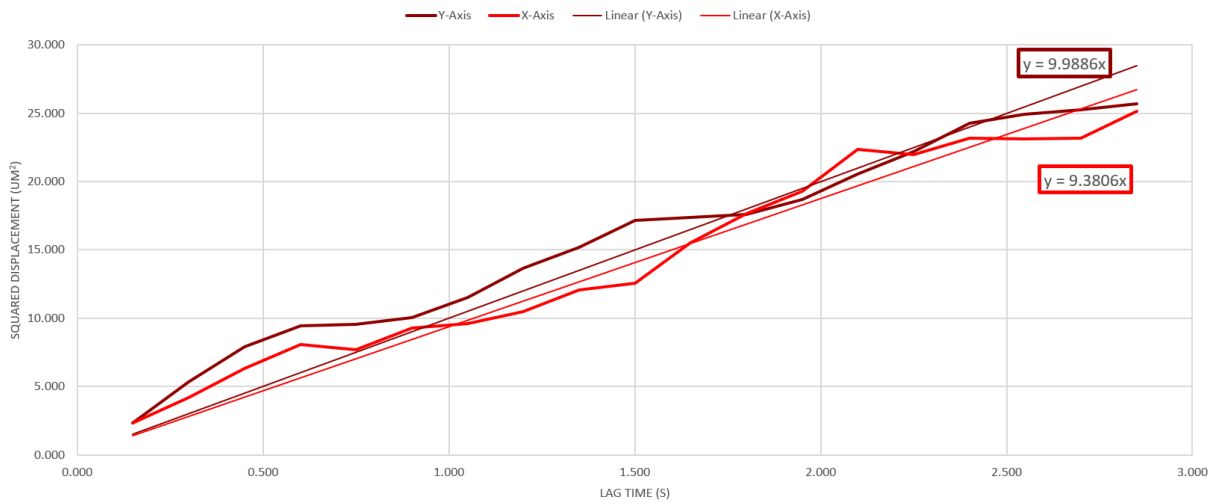
BLUE PARTICLE MSD



GREEN PARTICLE MSD



RED PARTICLE MSD



These slopes, while not perfect, show strong agreement between the x-and-y axes, and a good agreement between the different particles. The microscopic differences in effective radius between each particle, the randomized nature of Brownian motion, and the shorter timescale of this data set are the most probably causes for any slight variation in the diffusion coefficients, but it should still be clear that the x-and-y axes are determined by the same diffusion coefficient for each particle.

	Diffusion coefficient ($\mu\text{m}^2/\text{s}$)			Effective Radius
	X-Axis	Y-Axis	Average	
Blue	5.434	4.800	5.117	41.7 nm
Green	5.157	5.708	5.432	39.3 nm
Red	4.690	4.994	4.842	44.1 nm

Table 8.1: Calculated diffusion coefficients, for the particles shown in Figure 8.5, as well as their average. The values are then used to find an approximate particle radius, using Equation 8.1

8.3 Single-Direction Ballistic Component

There are three primary regions where the magnitude of the ballistic component compared to Brownian: much greater, on the same order of magnitude, and much smaller. As demonstrated in Chapter 8.2.1, a ballistic component that is at least $\sim 10\%$ of the standard deviation of Brownian motion can be directly observed, but anything below this threshold becomes indistinguishable to Brownian's ever-present randomness, and the stochastic nature of Brownian motion places a hard lower bound. (For the purposes of this dissertation, we won't go through the countless examples of this region: seeing nothing happen gets very boring very quickly.)

For ballistic components greater than Brownian, the opposite holds true: Brownian motion becomes so insignificant that it is hardly worth calculating: if a particle is moving at $500 \mu\text{m/s}$, Brownian deviation of $\pm 2 \mu\text{m/s}$ will hardly make a difference. In the following experiment, as a particle is observed undergoing stochastic Brownian motion, a voltage is applied to initiate the formation of the EDL. In this extreme case, the particle immediately moves towards the oppositely charged electrode before impacting it, becoming immobilized. We can still calculate the V_{RMS} value, but it can be just as easily calculated by taking the slope of the line:

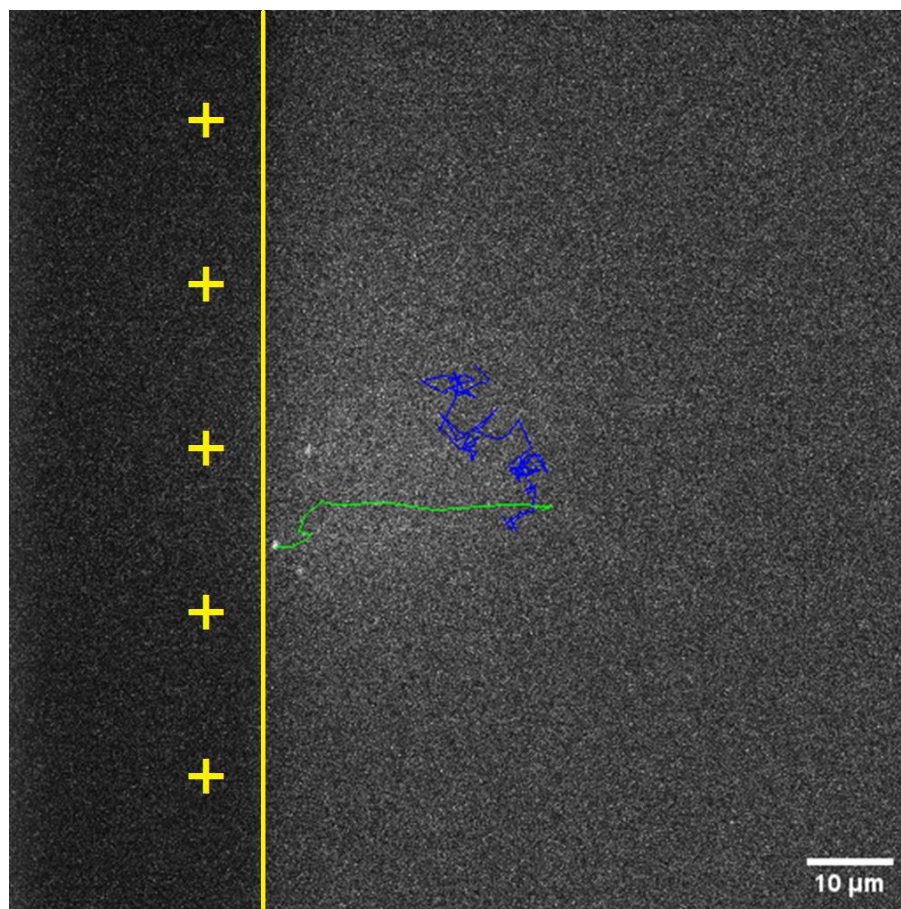
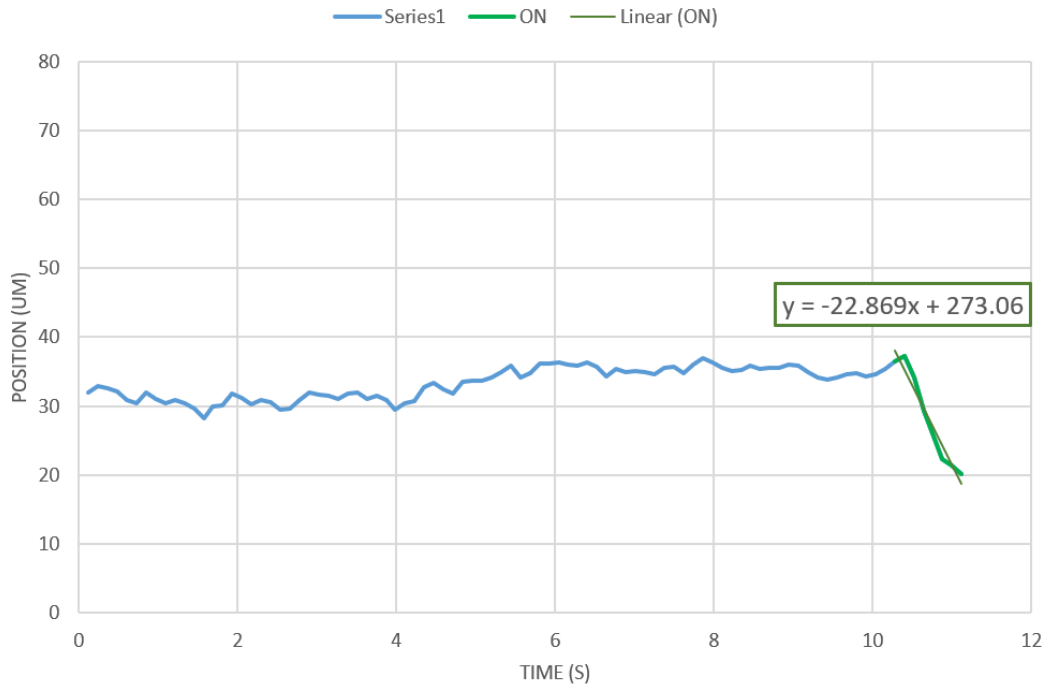


Figure 8.9: Particle Tracking showing the difference between Brownian (blue) and Ballistic (green) movements. The electrode and charge (yellow) have been added for emphasis. The particle moves towards the electrode after an application of 5.00 V. The channel between the electrodes is $1500 \mu\text{m}$ wide.

PARTICLE X-AXIS MOVEMENT



BALLISTIC COMPONENT

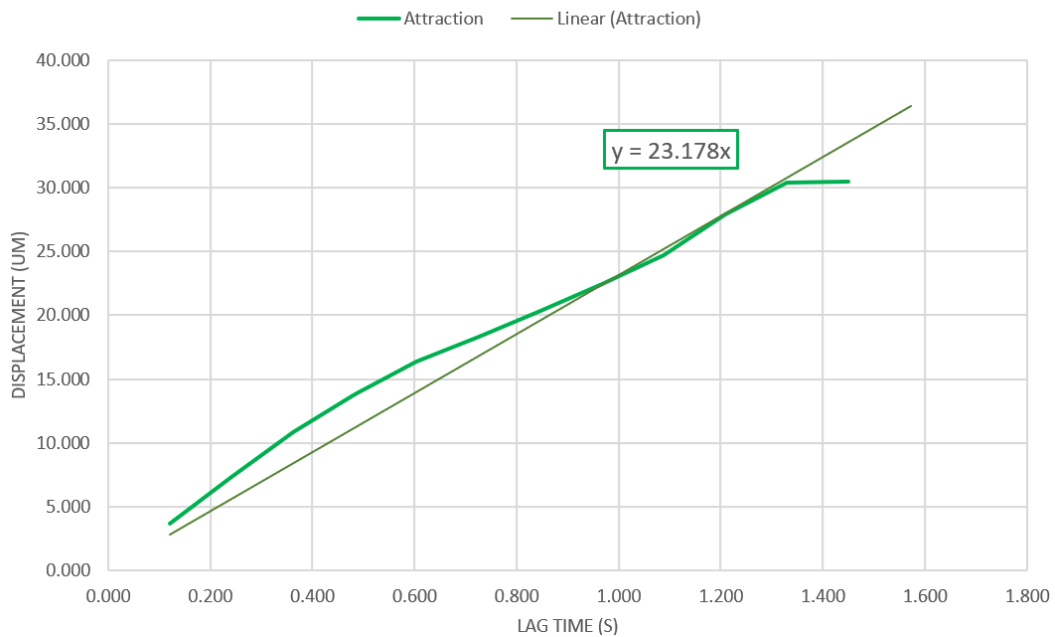


Figure 8.10 (top): The X-axis movements of the particle shown in Figure 8.9, with the voltage turning on represented as the change in color from blue to green. The slope of $22.87 \mu\text{m/s}$ is calculated via Excel's linear fit function. **(bottom):** The ballistic component using the R-MSD subtraction method, calculated to be $23.19 \mu\text{m/s}$.

The third region, where Brownian and ballistic motion are similar in magnitude, is a transitory section between the two extremes, which is why the calculation of V_{RMS} via R-MSD subtraction becomes necessary: the Brownian randomness becomes significantly larger, and the particle's trajectory becomes unavoidably erratic.

To highlight this transition, we're going to consider two examples, shown in Figures 8.11a and 8.11b. In both cases, the distance between the electrodes is $175\ \mu\text{m}$, the applied electrostatic potential is $0.3000\ \text{V}$, and both use negatively charged $20\ \text{nm}$ FL particles at the same concentration. The only difference between these two cases appears to be that Figure 8.11a has a smaller Brownian motion magnitude. This discrepancy could come from several factors, including a difference in temperature, viscosity (due to slightly higher/lower sodium hydroxide concentration), and different solution heights leading to glass-solution interactions.

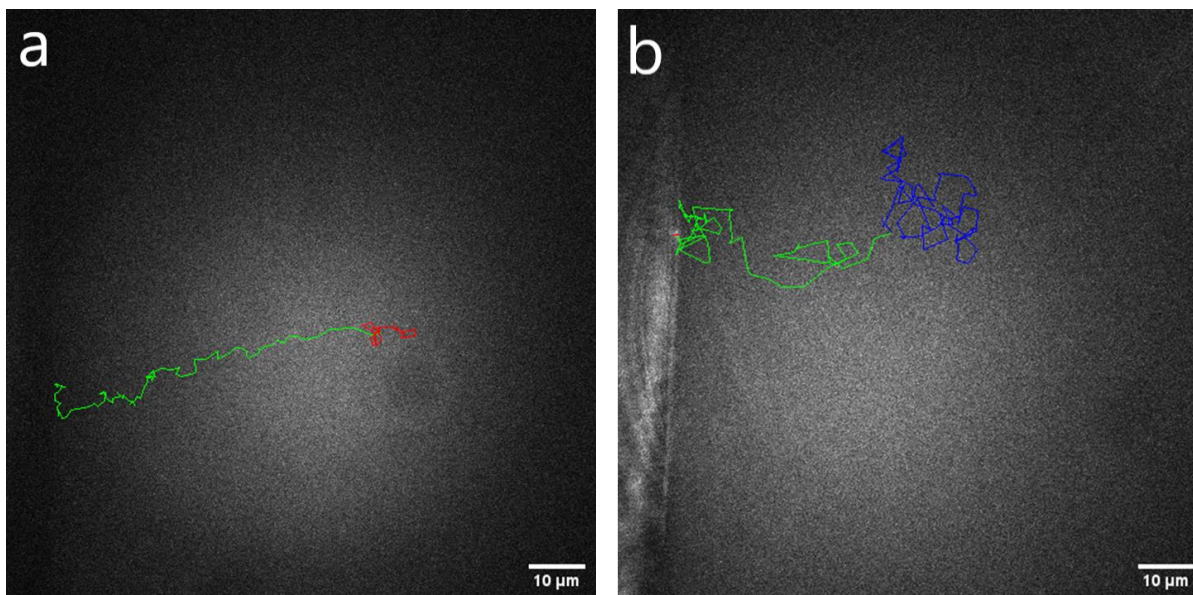


Figure 8.11: Two different particle trajectories of negatively charged $20\ \text{nm}$ FL particles. The red (**left, a**) and blue (**right, b**) lines represent the movement of the particles without any applied potential on the electrodes. Green lines in both represent the movement after the application of $0.30\ \text{V}$, with the positive electrode depicted on the left. In both cases, the electrode distance is $175\ \mu\text{m}$.

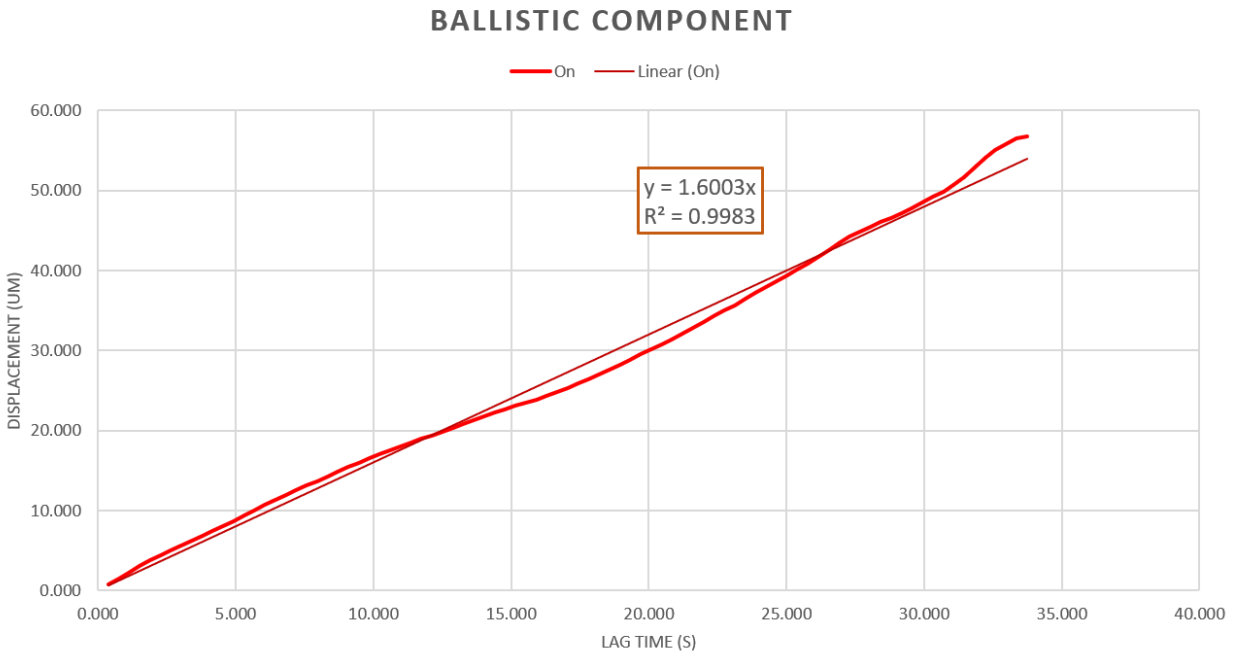
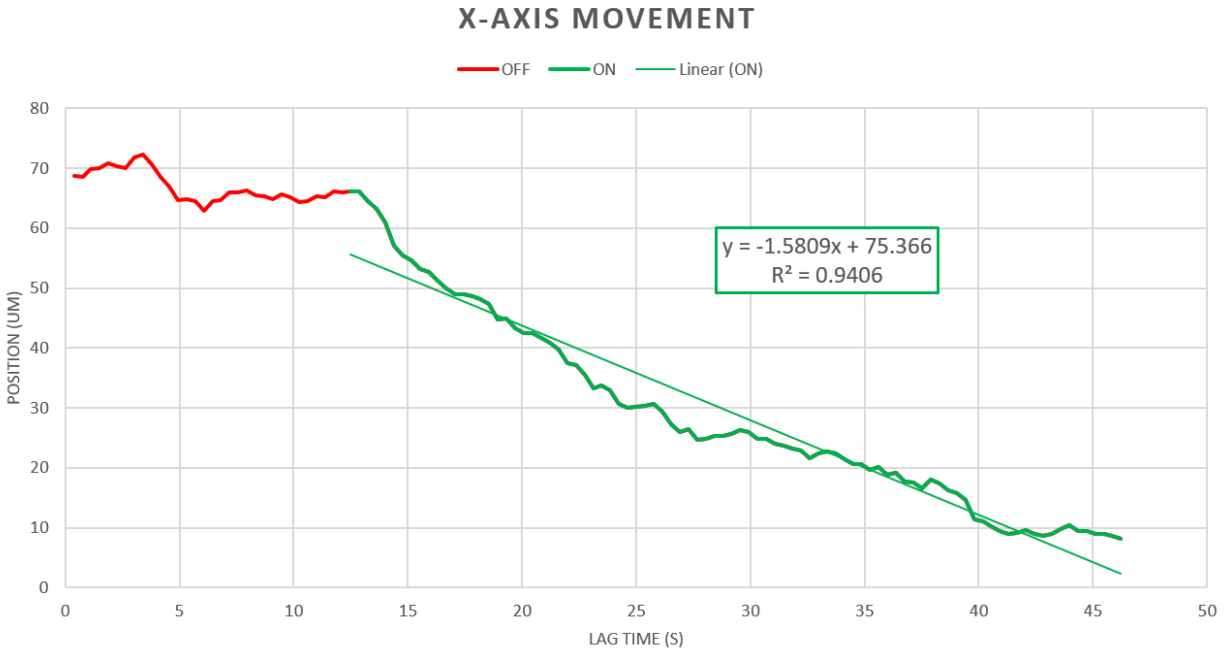


Figure 8.12 (top): Plots of X-axis movement vs time and **(bottom)** RMS displacement vs lag time of the particle shown in Figure 8.11a, along with their R^2 values. The ballistic component was calculated using the R-MSD subtraction method. The slopes and R^2 values were calculated using Excel’s fit function, with the ballistic component resulting in 1.581 and 1.600 $\mu\text{m/s}$ with R^2 values of 0.941 and 0.998 respectively.

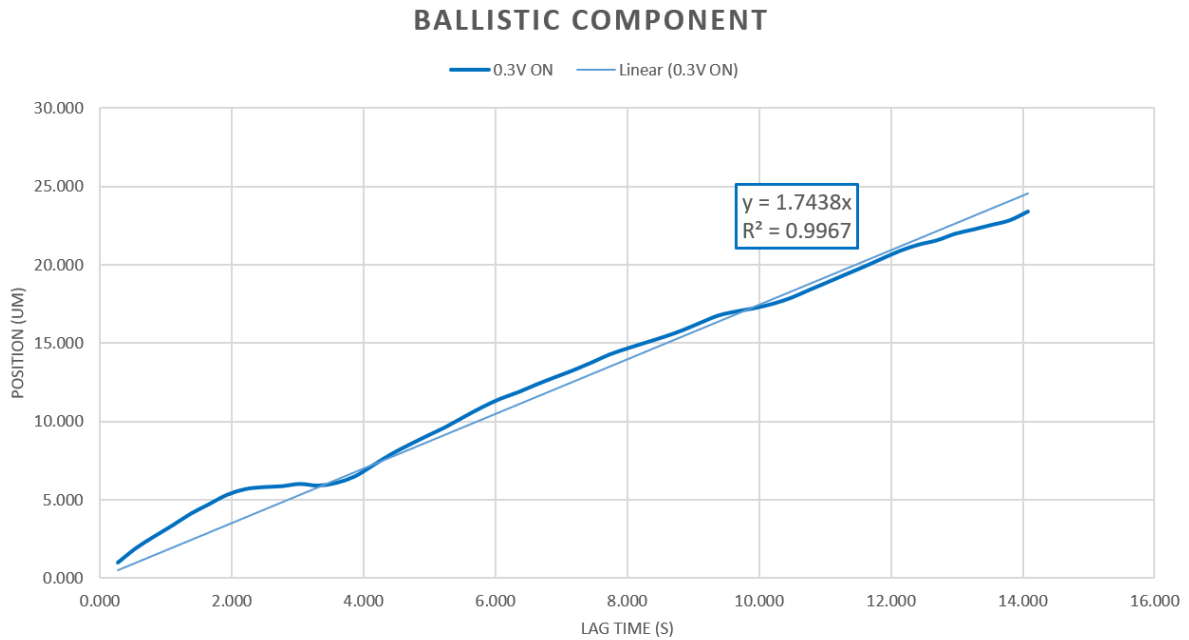
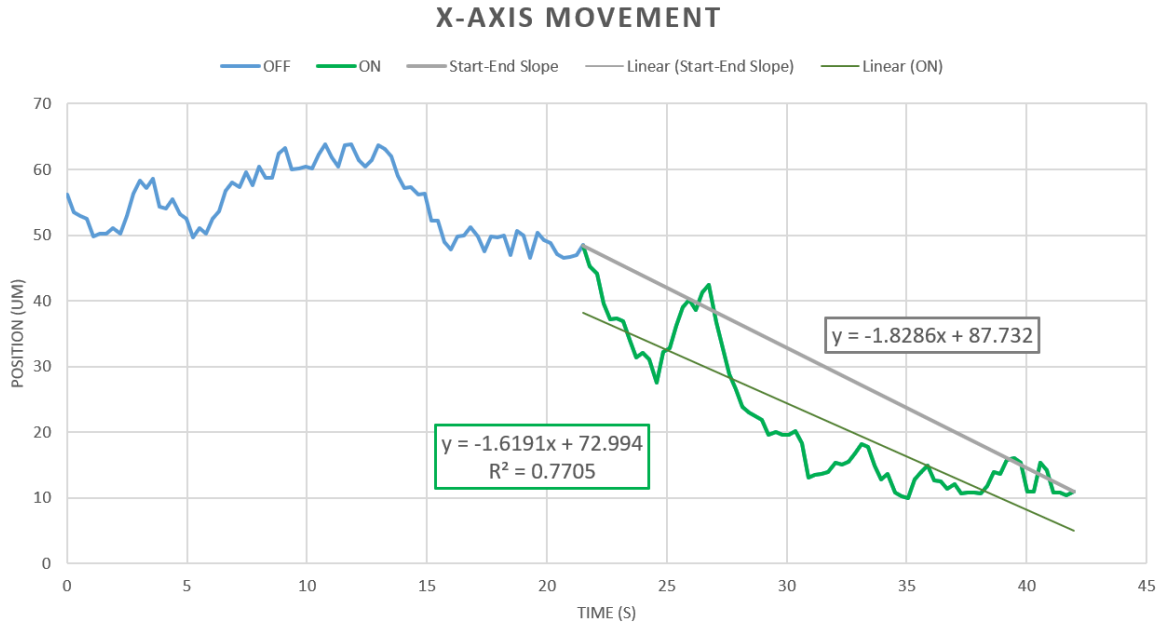


Figure 8.13 (top): Plots of X-axis movement vs time graph **(bottom)** RMS displacement vs lag time of the particle shown in Figure 8.11b, along with their R^2 values calculated using Excel’s fit function. The ballistic component is calculated via root of the R-MSD subtraction method. The grey line is a start-to-end slope to show the overall change in position over time. The ballistic components are 1.619 and 1.7438 $\mu\text{m/s}$ with R^2 values of 0.771 and .997 respectively. The start-to-end slope is 1.829 $\mu\text{m/s}$ but has no R^2 value because it is only two data points.

The first case, shown in Figure 8.11a, is right on the cusp of the transitory period. With a relatively low diffusion and Brownian magnitude, the sudden application of electrostatic potential creates a linear movement towards the electrode with minimal fluctuations. This is reflected in Figure 8.12, where both slopes (time-based movement and R-MSD subtraction) are in close agreement and with high coefficient of determination values, R^2 . (The R^2 value describes how well the slope fits the raw data, on a scale of 0.000 to 1.000, with high numbers indicating high agreement.) In a case such as this, the rigorous R-MSD subtraction method might not be completely necessary, but it does carry a slight increase in R^2 as well as the nearly 100-fold increase in boot-strapped raw data points, as described in Chapter 7.4.

The second case, shown in Figure 8.11b, is instead a case where the R-MSD subtraction method is necessary. With a higher variability in Brownian motion magnitude, massive fluctuations can be seen not only in the x-axis, but in larger movements along the y-axis. This fluctuation causes the movement after application of the electric voltage in Figure 8.13 (top) to be quite random with an R^2 value of 0.771 and a slope of 1.619 $\mu\text{m/s}$. For the sake of an additional viewpoint, a start-to-end line was included (shown in grey). It represents the absolute displacement between when the electrode is turned on and when the particle reaches the electrode, at an average speed of 1.829 $\mu\text{m/s}$. These lines, however, do not account for how the larger Brownian motions might have influenced the overall speed. The stochastic deviations are just too large to obtain a single reliable value using traditional methods, giving two values that are off by about 12%.

In dramatic contrast, the R-MSD subtraction method reduces the more extreme and erratic movements and filters out the Brownian deviations to provide a much smoother line with a slim

R² fit of 0.997, much better than the previous 0.771, and a slope of 1.744 $\mu\text{m}/\text{s}$. This consistent and reproducible method, while certainly more time consuming, is a far superior method in calculating the effective ballistic motion induced by an electrostatic potential.

8.4 Multi-particle Analysis

Similar to Chapter 8.2.2 when it came to agreement between the X-and-Y axes, another concern that naturally arises is that of the ballistic component induced by the electric field; two similar particles being affected by the same force should behave similarly. If the particles react to the induced field differently, then the framework would be unreliable.

To illustrate that the calculated ballistic component is comparable between particles, we can consider the following case in which two particles are freely diffusing for 11 seconds before an electrostatic potential is applied to the electrodes:

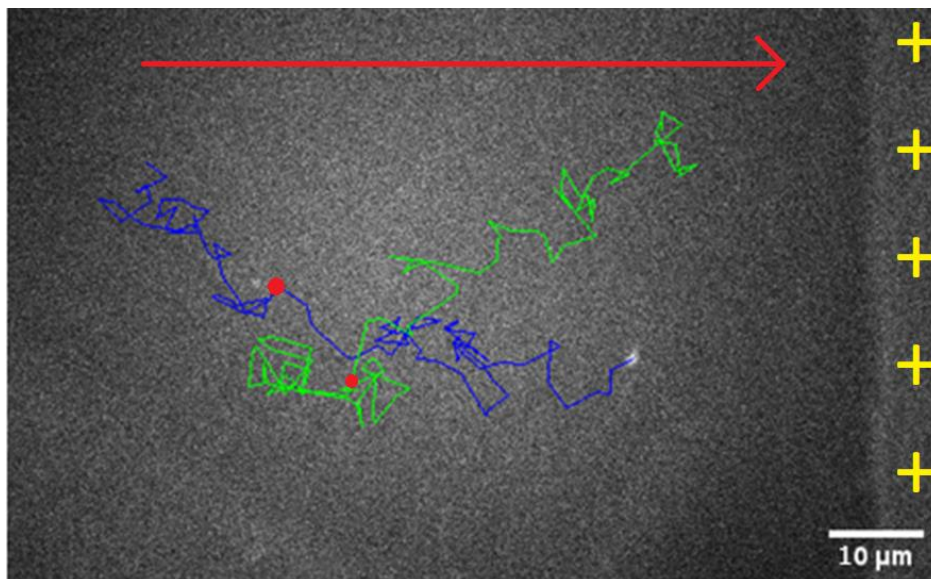


Figure 8.14: Trajectories of two negatively charged 20 nm FL particles (blue and green), over 25 seconds. Both particles started freely diffusing until a 0.300V potential is applied, indicated on each with a red dot with a red arrow in the direction of attraction towards the positive electrode (yellow +). The electrode distance is 175 μm .

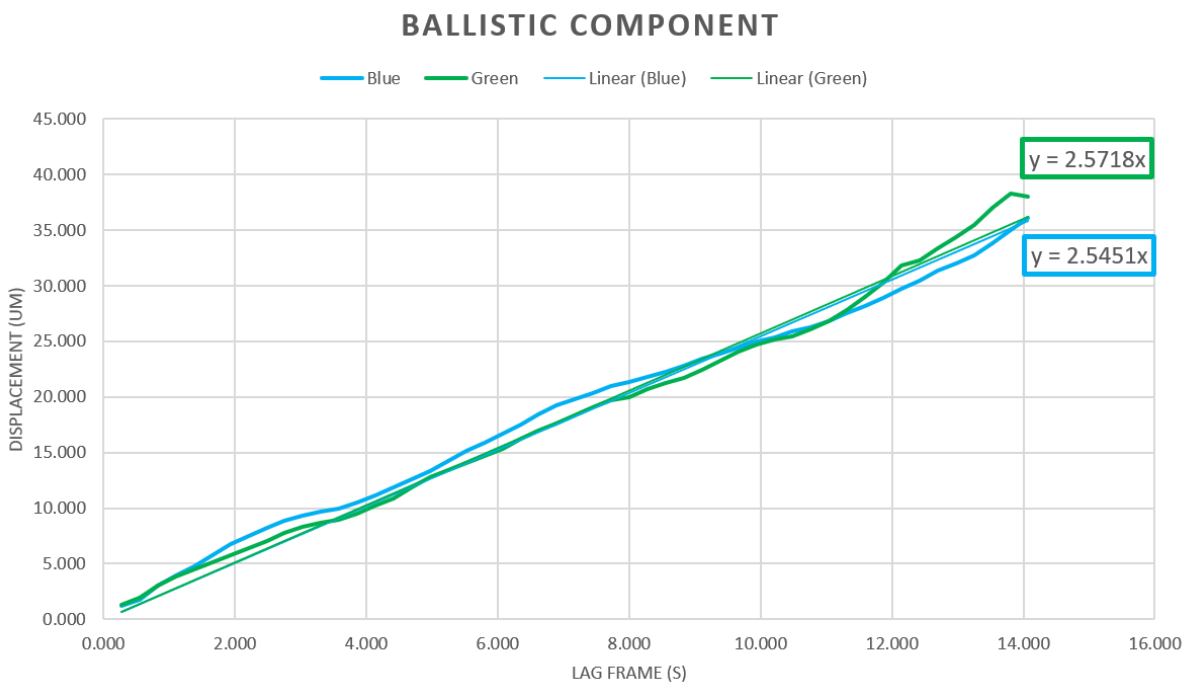
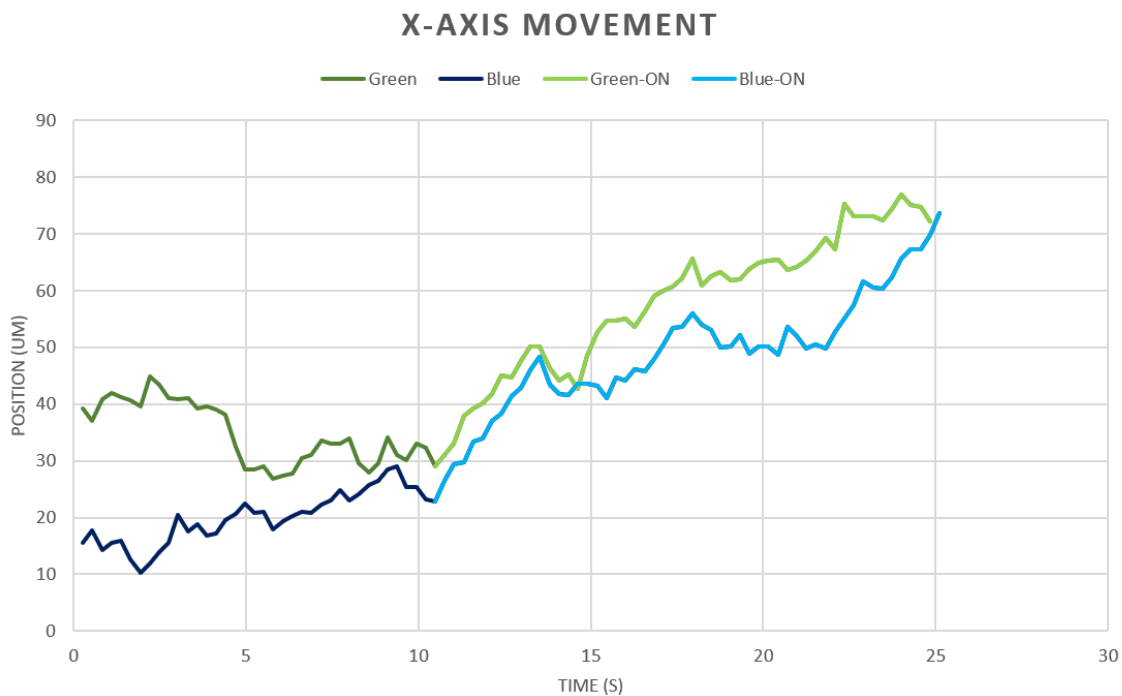


Figure 8.15 (top): X-axis movements of the two particles shown in Figure 8.12. The darker green and blue lines signify when there was no electrostatic potential, while the lighter colors signify when the 0.300 V was applied.

(bottom): Ballistic values for the two particles calculated using R-MSD subtraction.

As seen in Figures 8.14 and 8.15, the two particles are affected similarly after application of the electrostatic potential: the green particle moved at 2.572 $\mu\text{m/s}$, while the blue particle moved at 2.545 $\mu\text{m/s}$, which is a difference of just 1.05%. Just by looking at the particle trajectories in Figure 8.14, this dramatic correlation is not immediately obvious, and if one were to only use the X-Axis trajectories, the overlaid effects of Brownian motion cause the particles' movements to be too chaotic to be considered equivalent. This reinforces both the case that the applied ballistic force is uniform between particles as well as further validates the R-MSD subtraction method's ability to extract the Brownian component and isolate the ballistic component.

8.5 Effective Voltage Calculations

Now that we have validated the framework and methodology, we can now use these calculated values to find out how the EDL is affecting the electrostatic potential between the two electrode plates. To accomplish this, we will first consider Stokes' law, where the drag force F_D is a function of viscosity of the liquid η , the radius of the particle a , and the terminal velocity of the particle v_t :

$$F_D = 6\pi\eta a * v_t \quad (8.7)$$

We can briefly consider a negative particle moving through the medium towards a positive electrode as comparable to finding the force on an object falling through air towards the ground at its terminal velocity. Thus, we can find the ballistic component by using the terminal velocity of the particle as it moves through the solution. To find the terminal velocity, we would need to find the attractive force F_A of the electrode.

We can combine Equation 2.3 with the definition of a charge as the number of charges per particle with the principle elementary charge, and the electric field between two plane-parallel electrodes as being equal to the voltage applied V_q divided by their distance d :

$$\mathbf{F}_A = q\mathbf{E} \quad (2.3)$$

$$\mathbf{E} = \frac{V_q}{d} \quad (8.8)$$

$$q = ze_0 \quad (8.9)$$

$$\mathbf{F}_A = q\mathbf{E} = \frac{V_q q}{d} = \frac{V_q ze_0}{d} \quad (8.10)$$

Because the only forces acting on the particle are the attractive force and the drag force, we can find a direct relationship between the terminal velocity of the particle, the effective voltage V_{eff} , and the effective electric field, E_{eff}

$$\mathbf{F}_D = \mathbf{F}_A \quad (8.11)$$

$$6\pi\eta a * v = \frac{V_q ze_0}{d} \quad (8.12)$$

$$V_{\text{eff}} = d \frac{6\pi\eta a}{ze_0} * v_t \quad (8.13)$$

$$E_{\text{eff}} = \frac{V_{\text{eff}}}{d} = \frac{6\pi\eta a}{ze_0} * v_t \quad (8.14)$$

Assuming the particles are of similar size and charge, doubling the electric field will double the terminal velocity of the particle. This is seen in Figure 8.16, where two particles were subjected to two different voltages, 0.500 V and 1.000 V, which is an increase of the electric field by a factor of 2. This resulted in an increase of the ballistic component from 2.0301 $\mu\text{m/s}$ to 3.9485 $\mu\text{m/s}$, an increase by a factor of 1.945 (very close to what was expected). The slight decrease in ballistic speed may be due to several factors, including small differences in the

particles or solution, but the overall concept holds true.

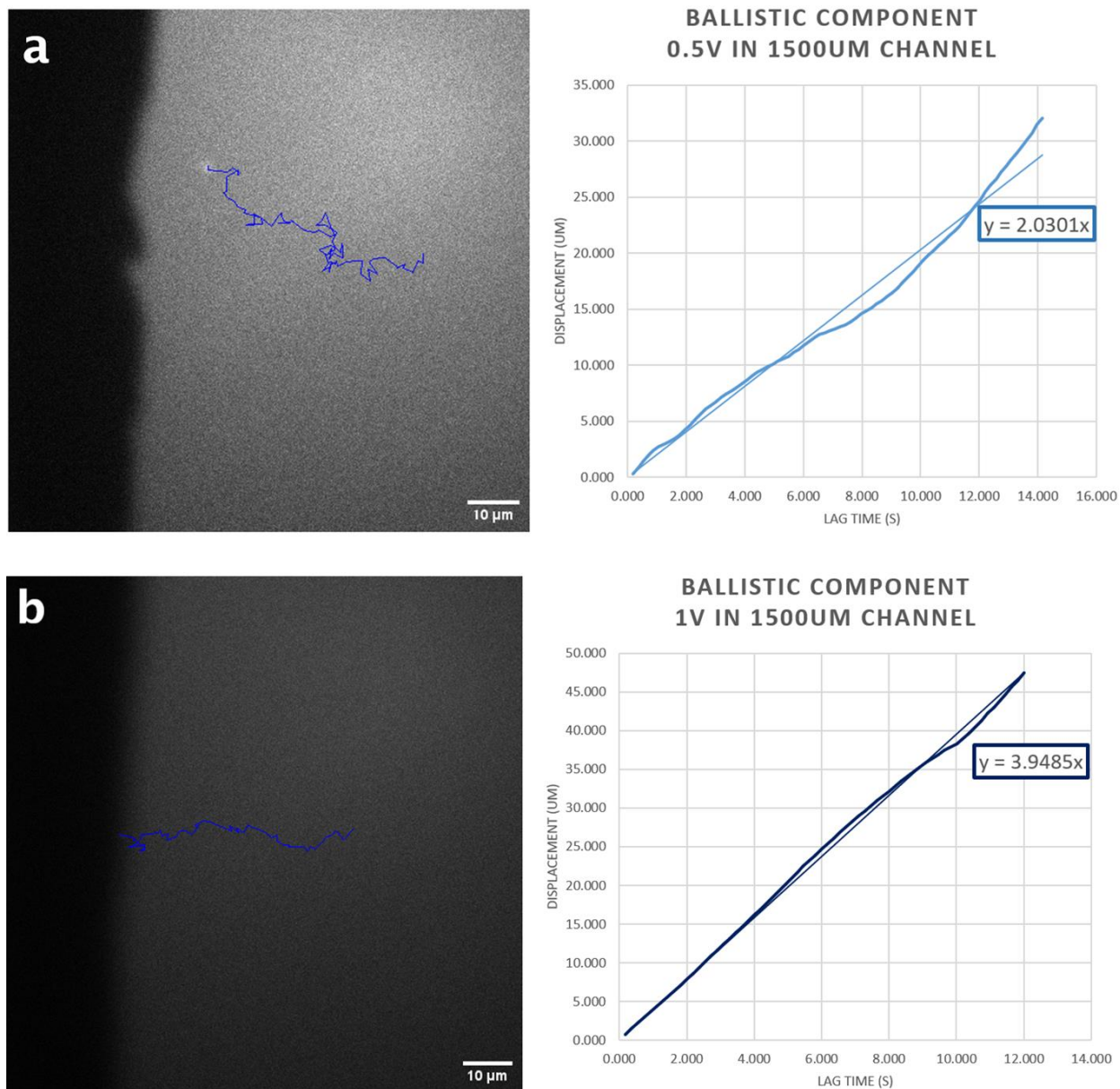


Figure 8.16: Particle trajectories (left) and calculated ballistic components (right) of two 20 nm FL particles (**a, b**) from different microfluidic cells with a 1500 µm electrode distance. The only alteration was that (a) used a potential of 0.500V and (b) used 1.000V (resulting in an electric field of 333 V/m and 667 V/m, respectively).

By using the same value for viscosity in the Brownian calculations done in Chapter 8.2, including using the effective particle radius of 50 nm as obtained from the diffusion coefficient,

and using the manufacturer’s assumed concentration of charges as roughly 1000 per particle, we can calculate the effective electric field felt by the particles as determined by the ballistic terminal velocity.

This gives a rather startling result: an applied 333 V/m electric field is reduced to an effective field of 12.6 V/m, while a 667 V/m field is reduced to 24.6 V/m. These values are much lower than the applied electric field, but a more curious discovery is when we consider how much the effective value has decreased from the original value: they have been reduced by roughly the same percentages, 96.21% and 96.31% respectively.

$$\%Reduct = \left(1 - \frac{V_{eff}}{V_0}\right) = \left(1 - \frac{E_{eff}}{E_0}\right) \quad (8.15)$$

We can apply this same calculation retroactively to the previous results in this chapter, as seen in the table below. Two different but consistent patterns emerge: the 1500 μm electrodes have a reduction of around 96.0%, while the 175 μm electrodes have a 99.1% or 99.4% reduction.

Figure	8.10	8.16	8.16	8.12	8.13	8.15	8.15
d (μm)	1500	1500	1500	175	175	175	175
v_t (μm/s)	23.178	2.0301	3.9485	1.6003	1.7438	2.5718	2.5451
V_0 (mV)	5000	500	1000	300	300	300	300
V_{eff} (mV)	216.4	19.0	36.9	1.65	1.80	2.65	2.62
E_0 (V/m)	3333	333	667	1714	1714	1714	1714
E_{Eff} (V/m)	144	12.6	24.6	9.43	10.3	15.1	15.0
%Reduct	95.7%	96.2%	96.3%	99.4%	99.4%	99.1%	99.1%

Table 8.2: Collection of data from different figures presented throughout the chapter. The green section accounts for the 1500 μm separated electrodes, and the blue accounts for the 175 μm electrodes. Equations 8.13, 8.14, and 8.15 were used for the effective voltage, effective electric field, and the reduction percentage.

This begins our first curiosity: according to the proposed theoretical values shown in Figure 7.8, there should be a near complete reduction of the electrostatic potential after just a few Debye lengths at 30.3 nm each. Yet in these experimental results there is still a significant percentage of the initial voltage that affects the suspended charged particles in the channel.

This phenomenon, as well as many others, will be discussed in more detail in Chapter 9. Additional examples of calculated terminal velocities and effective voltages for both electrode setups have been provided in the following Supplemental section. These are included to reinforce the topic, not act as new information and will not be discussed in depth.

8.6 Supplemental Examples

Below is a summary of the supplemental examples shown in this subchapter. Comparing these values to those shown in Table 8.2 will highlight a consistent trend.

Figure	8.17	8.18	8.18	8.19	8.20	8.21	8.22	8.22	8.23	8.23	8.23
d (μm)	1500	1500	1500	175	175	175	175	175	75	75	75
v_t ($\mu\text{m/s}$)	1.352	4.211	2.828	2.538	2.334	1.654	2.595	2.440	1.773	1.244	0.930
V_o (mV)	500	1000	1000	300	300	200	300	300	200	200	200
V_{eff} (mV)	12.6	39.3	26.4	2.61	2.40	1.70	2.67	2.51	0.78	0.55	0.41
E_o (V/m)	333	667	667	1710	1710	1140	1710	1710	2670	2670	2670
E_{eff} (V/m)	8.40	26.2	17.6	14.9	13.7	9.71	15.3	14.3	10.4	7.33	5.47
%Reduct	97.5	96.1	97.4	99.1	99.2	99.2	99.1	99.2	99.6	99.7	99.8
	%	%	%	%	%	%	%	%	%	%	%

Table 8.3: Summary of the Supplemental Figures, separated by color to signify different electrode distances: 1500 μm (green), 175 μm (blue), and 75 μm (orange). The voltages are represented as mV for clarity, the electric field is highlighted as and the %Reduct was calculated using Equation 8.14.

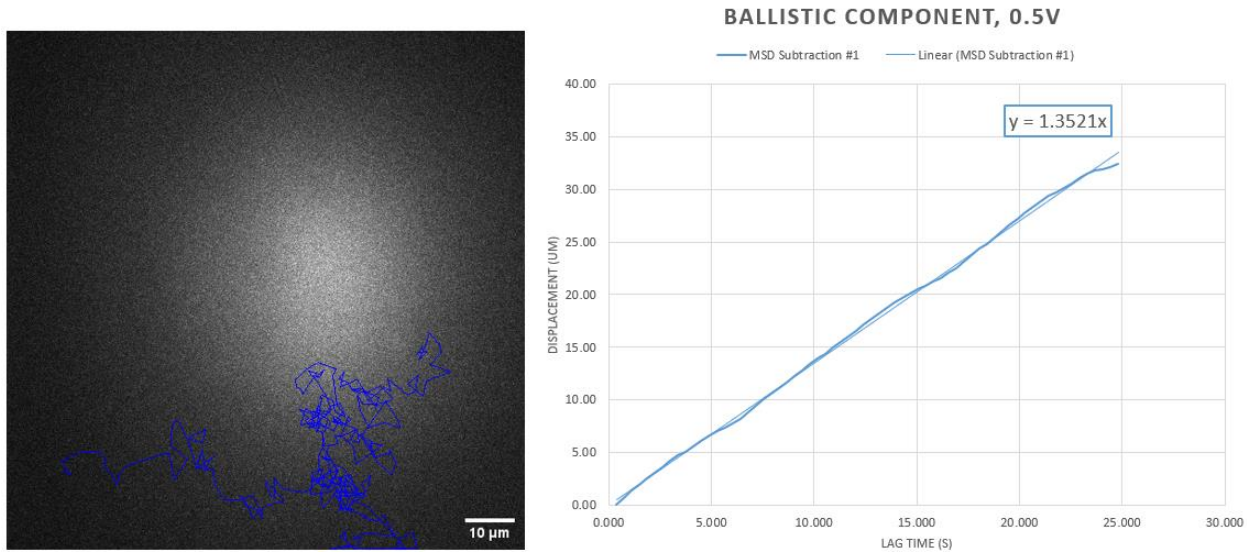


Figure 8.17: Particle Tracking (left) and ballistic component (right) of a 20 nm FL particle. The electrodes are 1500 μm apart, and the applied potential was 0.500 V, with the positive electrode shown on the left.

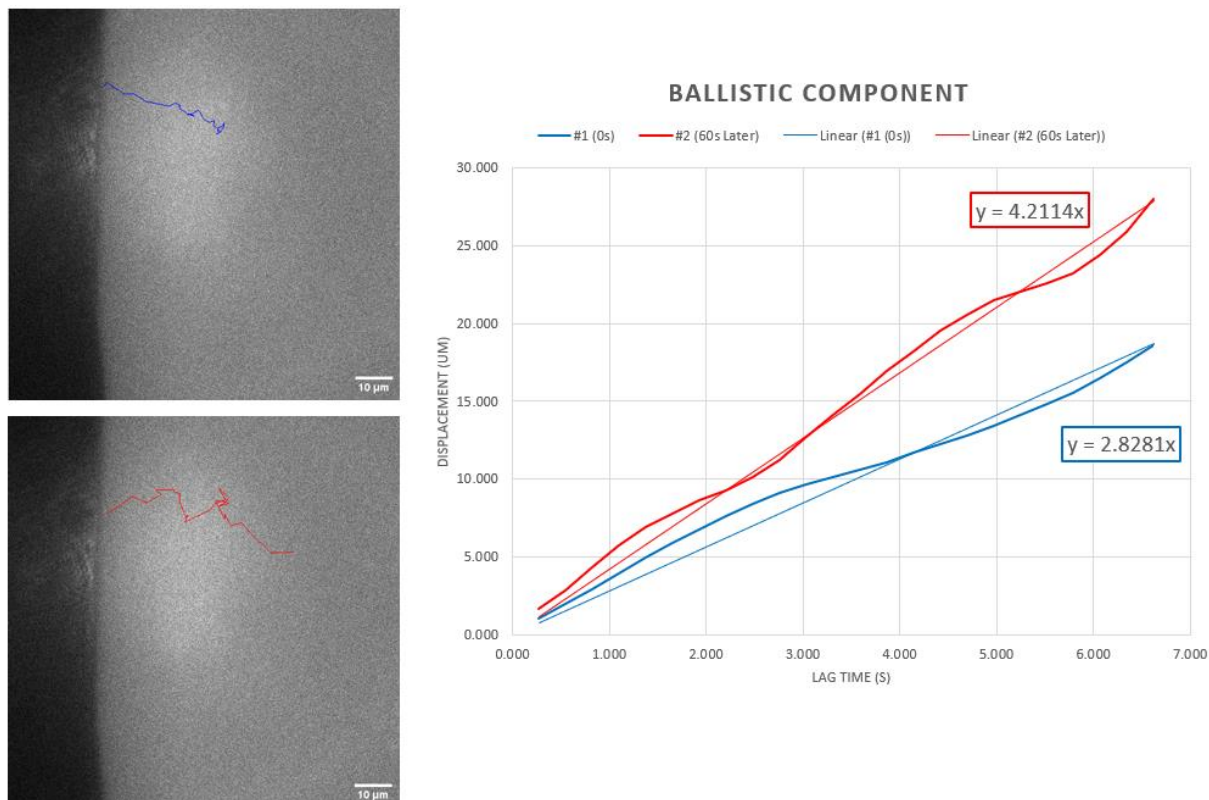


Figure 8.18: Particle Tracking of two particles (left) and their ballistic components (right). Both are 20 nm FL particles. The 1st particle (top, in blue) was visible immediately as the potential was applied, while the 2nd particle (bottom, in red) appeared 60.1 seconds later. The electrodes are 1500 μm apart with 1.000 V applied potential.

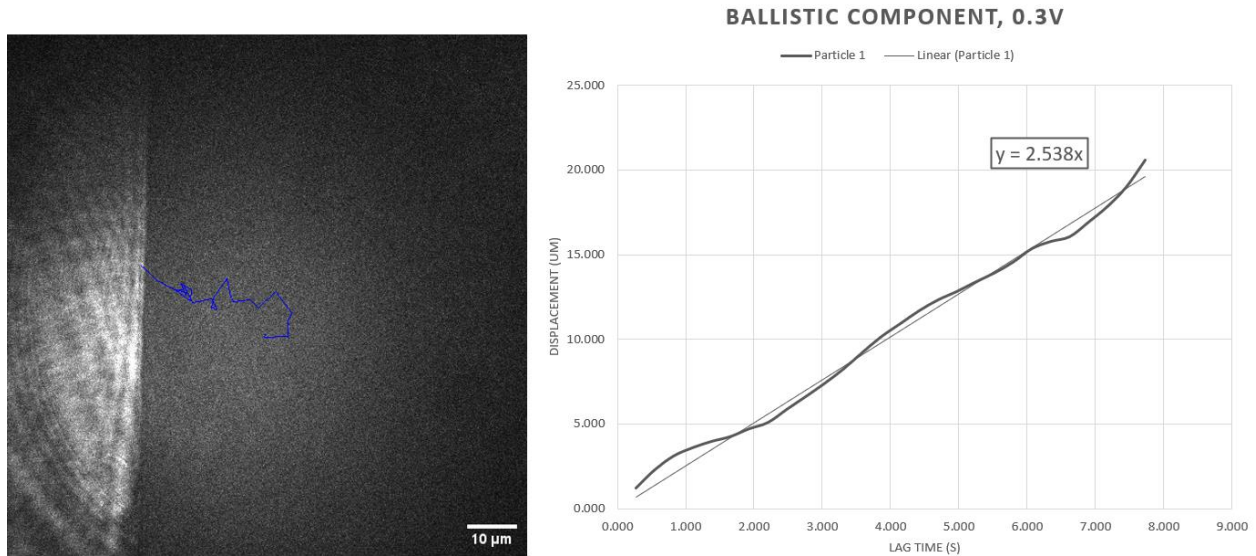


Figure 8.19: Particle Tracking (left) and ballistic component (right) of a 20 nm FL particle. These electrodes, with the positive shown on the left of the image, are 175 μm apart, and the applied potential was 0.300 V.

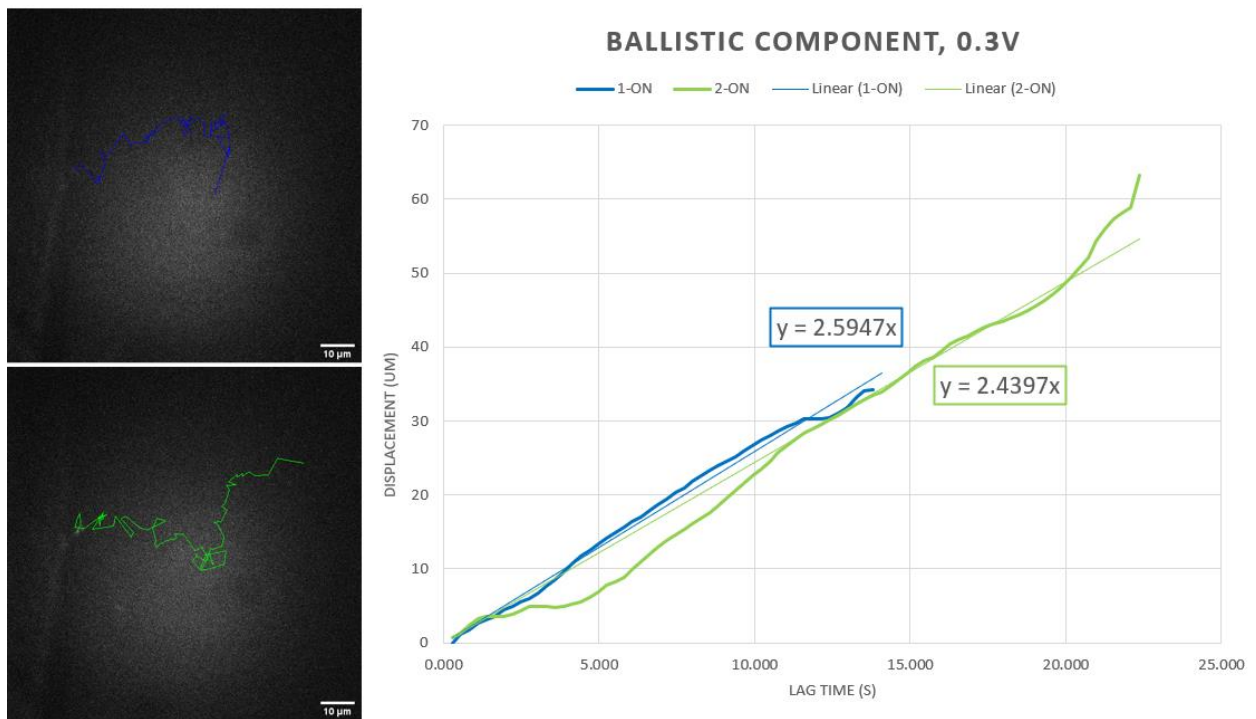


Figure 8.20: Particle Tracking of two particles (left) and their ballistic components (right). Both are 20 nm FL particles. The 1st particle (top, in blue) was visible immediately as the potential was applied, while the 2nd particle (bottom, in green) appeared immediately after (19.6 second after application). The electrodes are 175 μm apart.

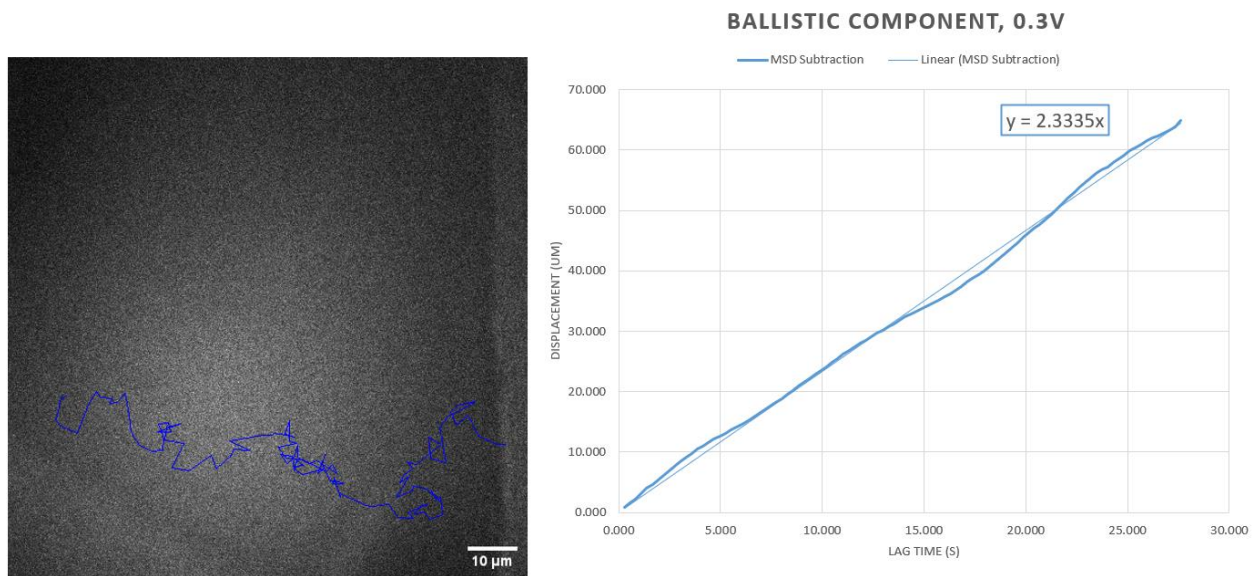


Figure 8.21: Particle Tracking (left) and ballistic component (right) of a 20 nm FL particle. The electrodes, with the positive shown on the right of the image, are 175 μm apart, and the applied potential was 0.300 V.

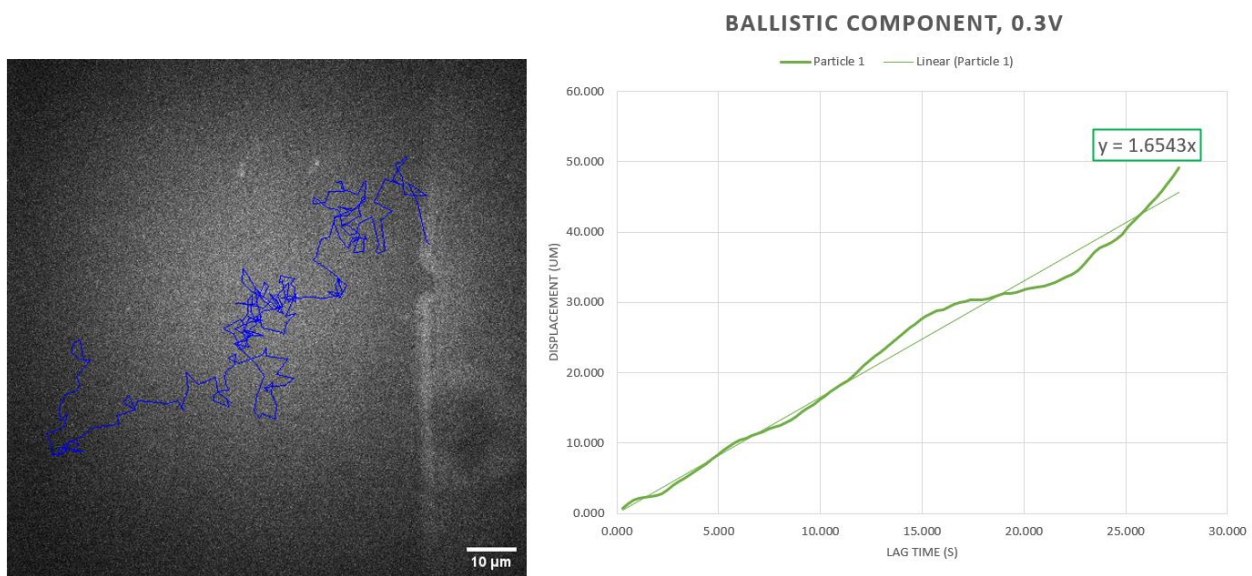


Figure 8.22: Particle Tracking (left) and ballistic component (right) of a 20 nm FL particle. The electrodes, with the positive shown on the right of the image, are 175 μm apart, and the applied potential was 0.300 V.

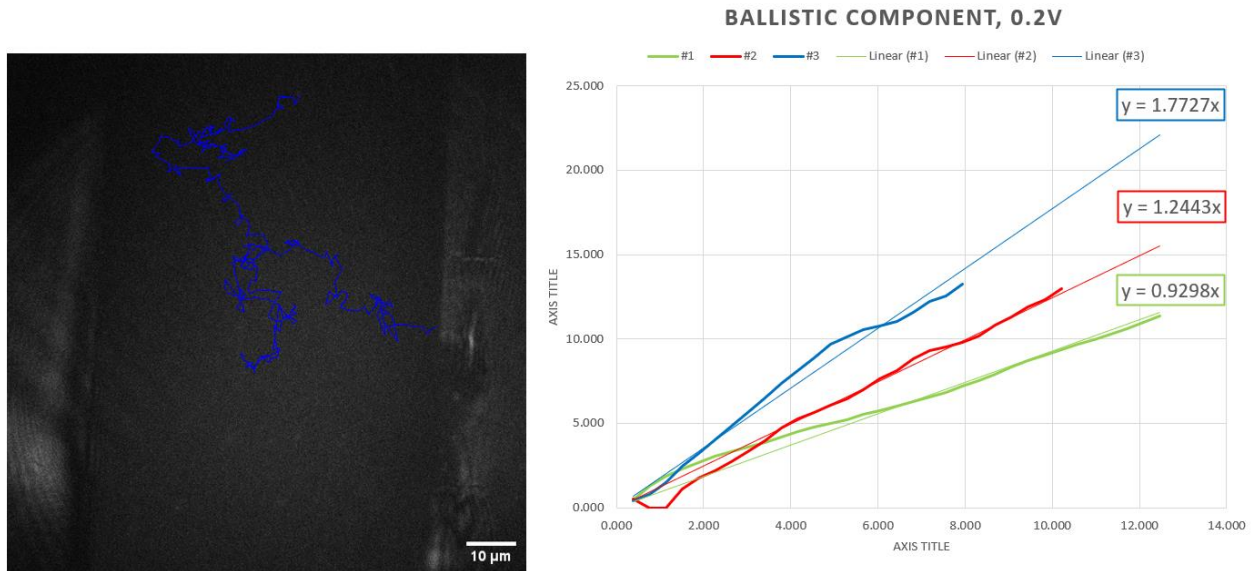


Figure 8.23: Particle Tracking (left) and ballistic component (right) of a single 20 nm FL particle. The electrodes are now 75 μm apart, and the applied potential was 0.200 V. Both electrodes are visible, on the left and right, and the 0.2 V applied potential was toggled between them for varying times: green (45.36 seconds), red (9.83 seconds) and blue (8.316 seconds). The particle tracking shows the entire path for simplicity.

Chapter 9

The Rebound Effect and Future Goals

9.1 Chapter Overview

This chapter is dedicated to exploring the unexpected occurrences during experiments in the 75 μm and 175 μm channels, as well as providing some supportive hypotheses to explain them. We will begin with a brief overview of the electric field's time-dependent decay before returning to our curious results from Chapter 8. After that will be an exploration of what occurs when the applied voltage is turned off as the charged particle attempts to return to Brownian motion, with an extended focus on what we colloquially refer to as the "rebound effect." We'll then suggest some possible explanations before discussing future endeavors and some preliminary experimental results that delve deeper into the establishment of and departure from the equilibrium position of the electric double layer.

9.2 EDL Establishment Time

As noted in Table 8.2 and the supplemental Table 8.3, there is a clear relationship between the applied voltage and the particle's speed; when the applied voltage is reduced by half, the particle's velocity was reduced by half. However, by using this velocity to calculate the effective potential via Stoke's Law, the effective values would not be anywhere close to the applied values. For a 1500 μm channel, the effective voltage was somewhat consistent reduction of ~96.0% of the applied voltage. For the 175 μm channel, it was ~99.2% of the applied voltage.

One of the biggest similarities between the previous chapters' examples is that the particles were analyzed just before the potential was applied, and for anywhere from 10 to 40 seconds afterwards. Naturally, a concern is that there was not sufficient time for the EDL to establish, which is indeed where the subtle differences between the experimental values emerge.

There is some inconsistency in exactly what occurs on longer timescales. According to most conventional theories¹⁻⁷, the EDL charging time for a pH 10 NaOH solution should be on the order of tens or hundreds of milliseconds. Certainly, there is a very rapid reduction in the effective voltage over time, and the nanoparticles do not behave as if they are being affected by the full applied potential: after an initial jolt, the nanoparticles settle towards a roughly consistent velocity. However, *charging time* is not the same as *completion time*: charge time is how long it takes a capacitor to charge $1 - \frac{1}{e^5} = 99.32\%$ of its supply^{8,9}, which means that the EDL has not *completely* established after this time; instead, the EDL's reduction of the applied potential would slowly continue trending towards 100% depletion until it becomes effectively undetectable. In fact, many of the examples were below the 99.3% charge time threshold.

(As a quick aside, note the similarity between charge time and the discussion of Debye length in Chapter 2.8: after 5 Debye lengths, the potential should be reduced by 99.3%.)

Thus, in the interests of exploring more of just how long it takes for the EDL to fully reach an equilibrium state, we must consider the change in velocity for particles within the channel. For our first case, Figure 9.1 and Table 9.1, we have a single electrode attracting multiple particles over the course of 65 seconds. The camera was positioned to capture incoming particles from out of frame, with one particle within the frame at the time of application of 0.300 V. The potential was applied for 1 minute, with the speeds of the particles indicating the effective voltage.

The first two particles, tracked as green and blue, were closest to the electrode and had a slightly higher velocity than the later particles, Red and Teal. Red and Teal both have very similar velocities, despite being measured at 30-60 seconds after the application of the 0.300 V

potential. This indicates that the decreasing field does have a time-dependence, but at a much slower rate than is suggested by contemporary theory, before plateauing significantly.

One minor but important concern is that the second particle, in green, was faster than the first particle, in blue. This could have been due to several factors, including a smaller effective radius or higher concentration of negative surface charges.

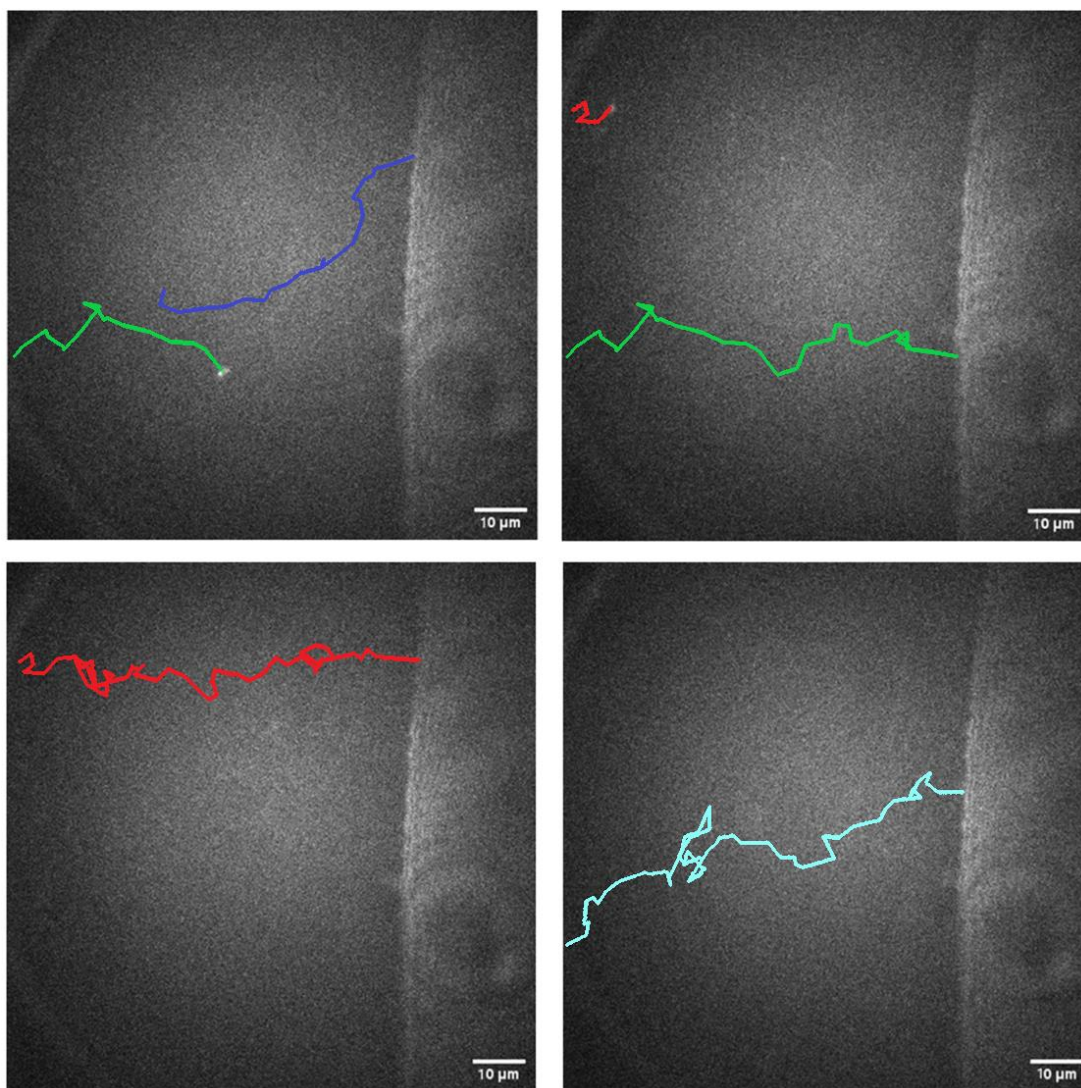


Figure 9.1: Particle trajectories of four different particles, shown in order of appearance, in a 175 μm channel. Blue was present at the application of 0.300 V, with Green appearing 1.68 s later. Red appears at 10.38 s, and Teal appears at 35.90 s. The total time shown here is 52.75 seconds.

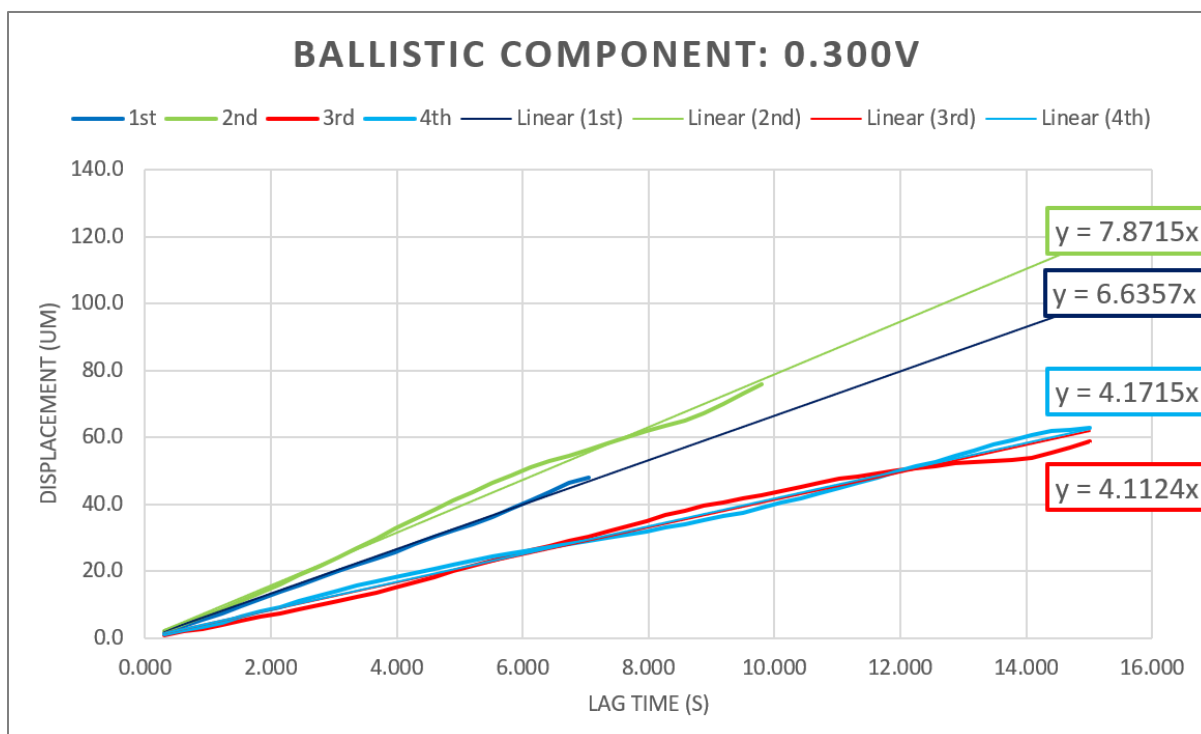


Figure 9.2: Particle velocities calculated via R-MSD subtraction, with each color corresponding to the particle tracking color shown in Figure 9.1.

Particle:	Blue	Green	Red	Teal
<i>Start time (s)</i>	00:00	01:68	10:38	35:90
<i>End time (s)</i>	07:20	12:04	27:04	52:75
v_t (um/s)	6.636	7.872	4.172	4.112
V_{eff} (mV)	4.10	4.86	2.58	2.54
<i>%Reduct</i>	98.63%	98.38%	99.14%	99.15%

Table 9.1: Summation of Figure 9.2. The start and end time, with 0:00 being the time point when 0.300 V were applied, are the times for which the nanoparticles are within frame and have their speed calculated. The velocities are from Figure 9.2, and both V_{eff} and %Reduct were calculated via equation discussed in Chapter 8. The electrode distance was 175 µm and the particle radii were calculated to be ~30 nm.

To assuage the issue of particles having slightly different particle radii and surface charges, a second experiment was done with the exact opposite idea: moving the camera to specific stationary positions to follow a single particle. A particle was chosen that was immediately next to the soon-to-be negative electrode. After a 0.300 V potential was applied, the particle was then attracted across the entire 175 μm channel towards the positive electrode. The camera was moved between three total viewing positions (negative electrode, bulk solution, and positive electrode), and the velocities were separately calculated for each position.

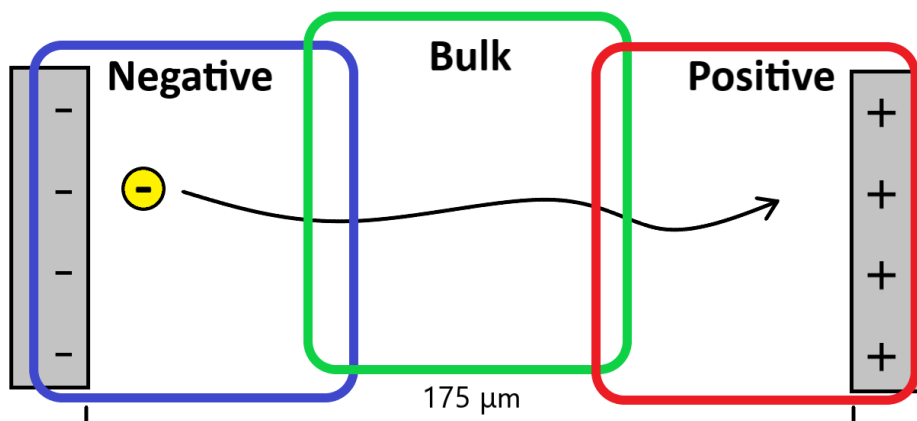


Figure 9.3: Simplified view of the camera positions of the 20 nm nanoparticle (yellow) as it travelled 175 μm from the negative electrode (left, blue), through the bulk (center, green) to the positive electrode (right, red). The applied potential was 0.300 V.

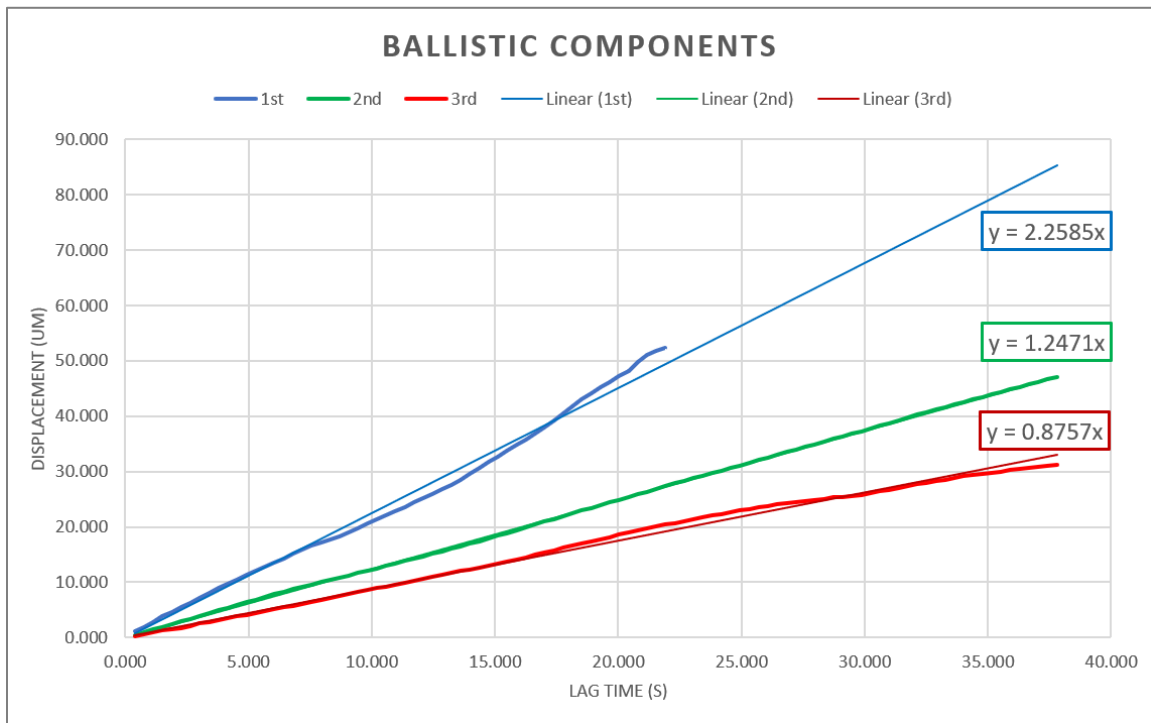
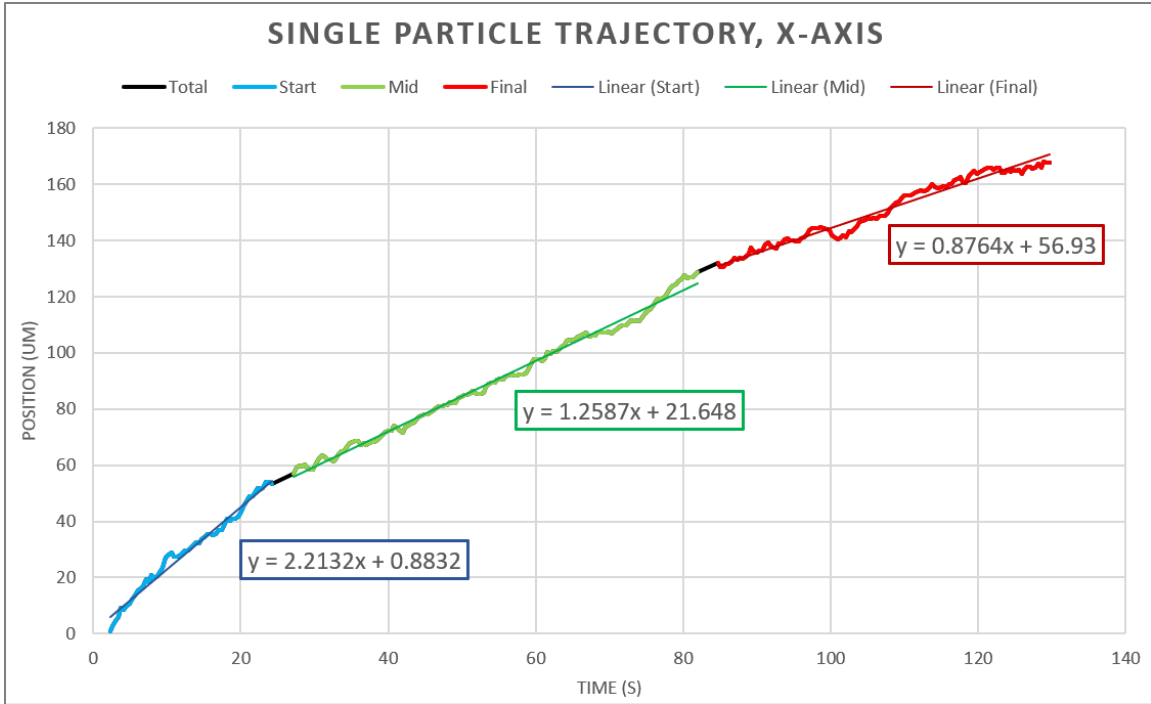


Figure 9.4: (top) X-axis position vs time graph of the particle, with the colors corresponding to the camera positions shown in Figure 9.3. The shorter black lines on the trajectory are the camera reposition times, about 3 seconds. **(bottom)** Ballistic component velocities for the three camera positions using R-MSD subtraction.

Position	Negative	Bulk	Positive
<i>Start time (s)</i>	02:27	27:88	85:98
<i>End time (s)</i>	24:66	83:16	131:75
v_t (um/s)	2.259	1.247	0.876
$V_{effective}$ (mV)	2.33	1.28	0.90
<i>%Reduction</i>	98.84%	99.36%	99.55%

Table 9.2: Summation of Figure 9.4, for a 20 nm FL nanoparticle travelling through a 175 μm channel with a solution viscosity of 1.5 mPa-s after an applied 300 mV potential. The start and end times represent the exact times the particle was visible within each camera position, with roughly 3 second transitions between each.

The results of this single-particle focus reveal an interesting phenomenon: the particle's ballistic velocity appears to be dominated by a time-dependence, while a possible position-dependence is either insignificant or insufficient to isolate. The constant rate of speed makes it appear that the electric field is constant throughout, although there might be significant increases very close to the electrodes. This effective potential, however, does decrease slowly over time, even on a scale of over 130 seconds, with the charge time threshold being passed at some point before 80 seconds. A decaying effective potential yields a decaying particle velocity, which can be seen in Figure 9.5 below. The plot was constructed using a rolling 100 frames, where the slope is considered as the average velocity from the previous 100 x-axis movements, with the resulting graph showing a clear decay function:

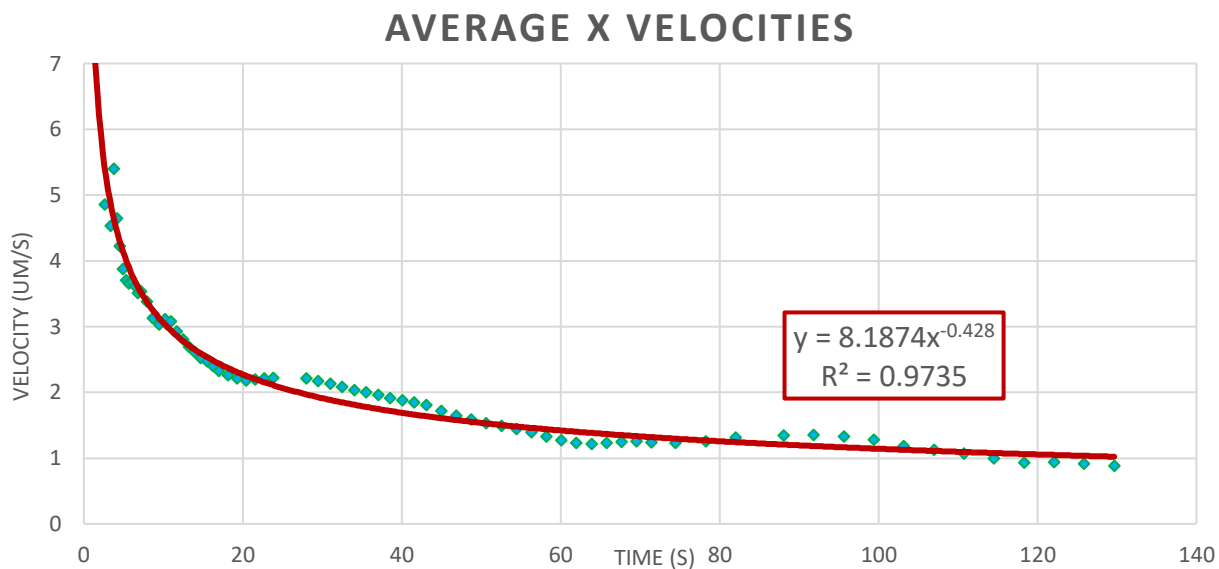


Figure 9.5: 100-frame average velocities of the nanoparticle shown in Figure 9.4. The later velocities were given less weight to increase the accuracy of the power-fit function for the earlier velocities.

The duration of this decay is rather difficult to track using the methods presented in this dissertation: with low concentration of particles, the overall presence of fluorescing nanoparticles decreases over time, eventually resulting in large periods of time without any fluorescing particles being present. As an anecdotal case, one experiment was attempted with a stationary camera over a 1500 µm channel for an hour using a 0.500 V potential, with the last fluorescing nanoparticle being seen at the ~30-minute mark, still under the apparent effect of an electrostatic field.

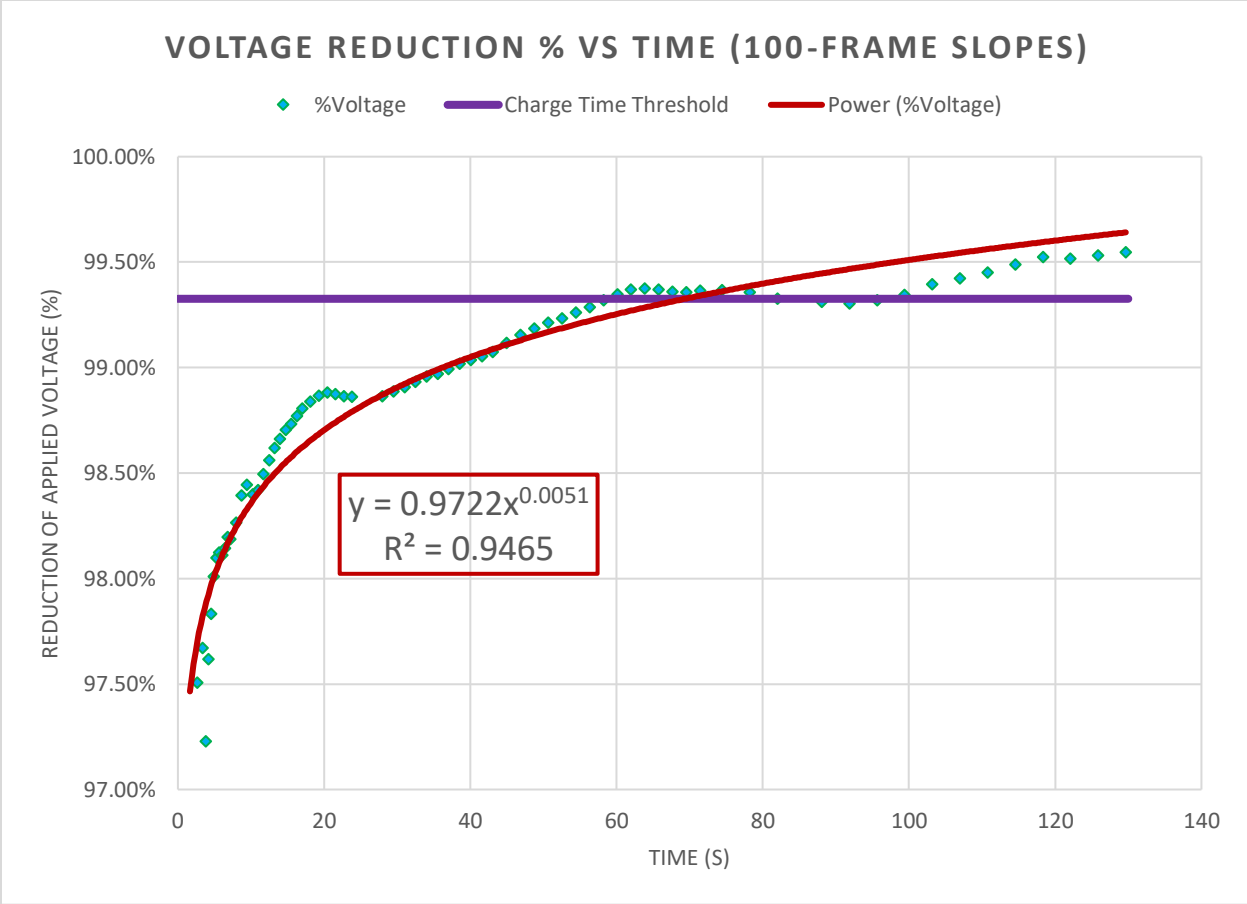


Figure 9.6: Velocities from Figure 9.5 converted into %Reduct of the applied voltage of 300 mV. The purple line represents the charge time definition of 99.32% reduction, here shown to waver between 60 to 100 seconds.

Attempting to solve this issue by increasing the concentration of particles then encounters the issues presented in Chapter 7: if the concentration is too large, nanoparticles will begin to coagulate and cluster along the electrode, creating physical barriers that introduce flow dynamics to the solution. Secondly, as the potential decays below a certain threshold, the particle enters the region where the Brownian motion factor begins to dominate. On longer timescales, the effective potential could be extractable, but with a limited observation window this would be impractical to obtain. Thus, at present, it was not determined experimentally how long it takes for the electrostatic potential to fully reach equilibrium. The only conclusive

statement these methods can provide is that the charge time is far longer than the theoretical timescale of a few seconds and is instead in the order of minutes.

9.3 Rebound Effect

Having analyzed what occurs after the initiation of an applied potential, as well as discovering that the decay function of the effective voltage was magnitudes longer than initially anticipated, the next question we sought to answer was what would happen after the potential was turned off: would there be a noticeable halt to the nanoparticle's trajectory as soon as the potential was cut?

What instead occurred was something wholly unexpected: the nanoparticle immediately reversed course, heading in the opposite direction as it had been moving just moments prior. This effect is independent of which direction the field is applied; the nanoparticle consistently moves counter to the applied field as soon as the field disperses. If the nanoparticle is being attracted by the field towards the positive electrode, it will suddenly be repulsed from that same electrode when the voltage is turned off. However, this effect is short-lived; in most cases, it lasts only about 3-5 seconds before the nanoparticle returns to a purely Brownian motion pattern.

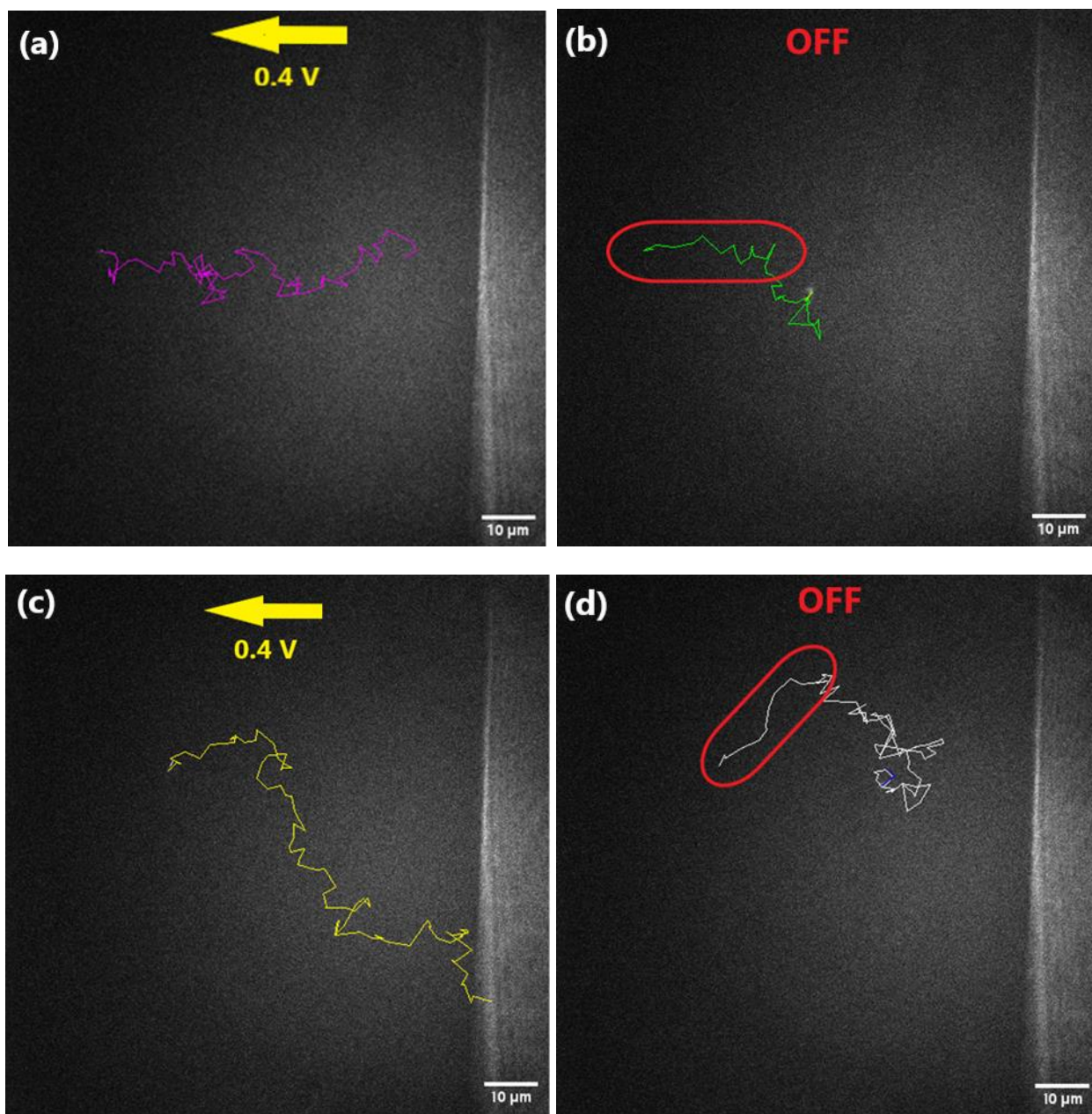


Figure 9.7: Two sets (a-b and c-d) of a nanoparticle's trajectories as it is influenced by a 0.400 V potential (a, c) and the rebound of the particle immediately after the potential is set to 0.000 V (b, d). Red circles have been added as emphasis to the rebounding effect.

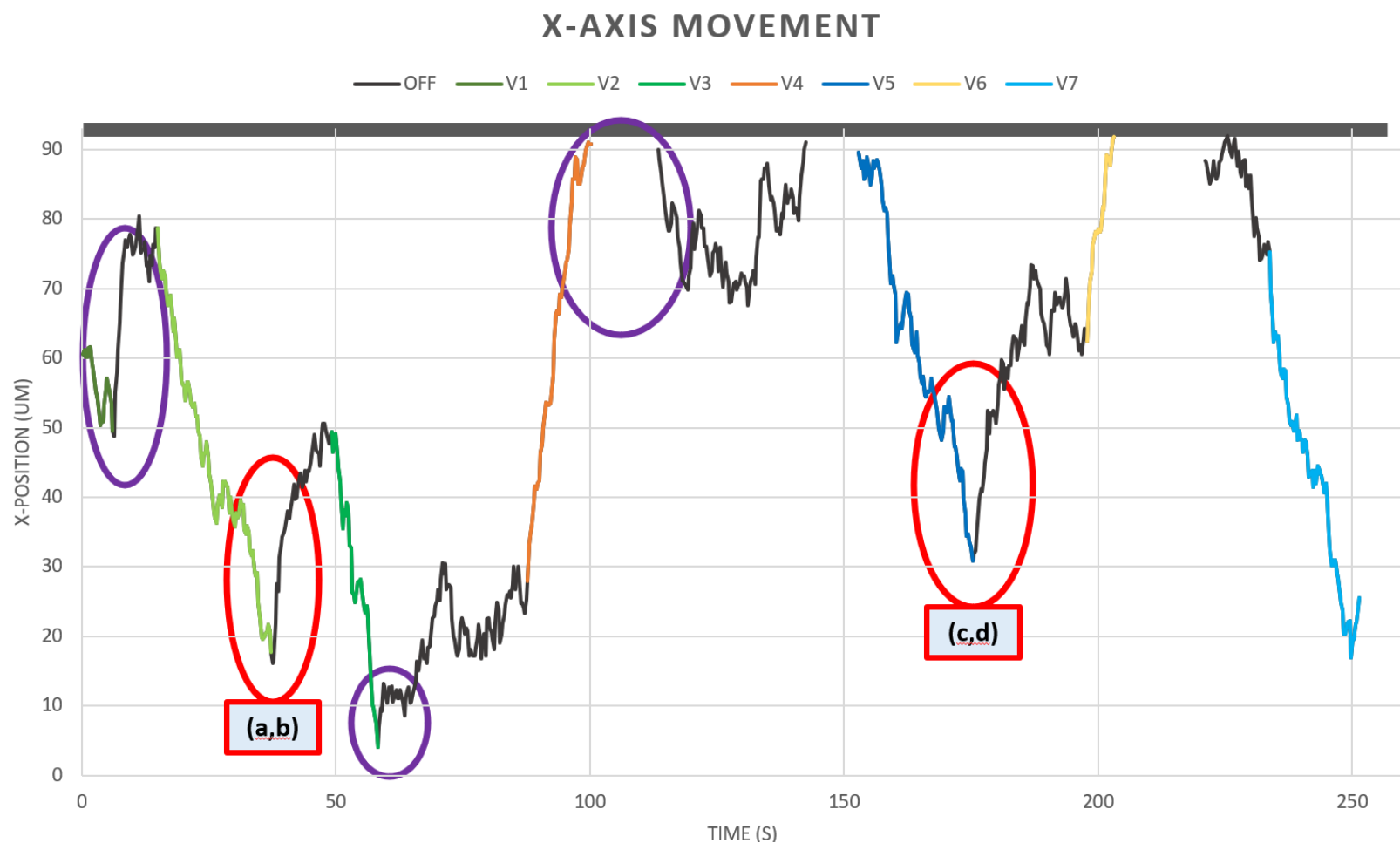


Figure 9.8: The full x-axis movements of the nanoparticle shown in Figure 9.7, with red boxes showing the exact cases. The top of the graph indicates the electrode (grey bar). The cool-colored lines (green/blue) indicate particle positions when a negative potential is applied to the electrode, and warm-colors (yellow/orange) indicate when a positive potential is applied. Any black line represents the potential being turned off. Highlighted regions (red/purple circles) show the apparent Rebound Effect. All potentials shown here are 400 mV

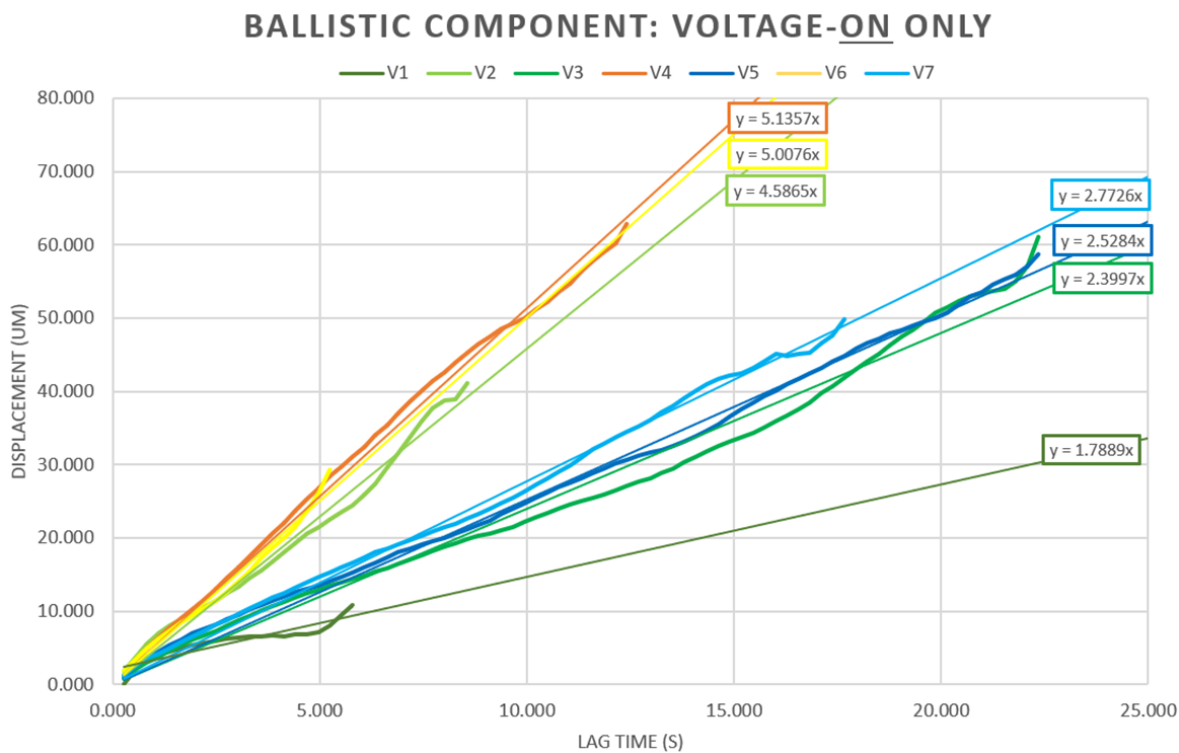


Figure 9.9: Ballistic components of the particle, with the colors matching the appropriate times where the potential was applied in Figure 9.8. The dominating factor for ballistic component magnitude appears to be length-of-time, matching the expectation from the decaying %Reduction from Figure 9.6. The apparent outlier, V1 at 1.7889 $\mu\text{m/s}$, had potential applied for an additional ~ 30 seconds, and is actually in-line with the expectation.

These rebounding movements rapidly decay in proportion to the amount of time that the field was applied. A short-time application of potential of only 1-5 seconds has a visibly shorter Rebound Effect than one in which the field has been applied for 10-30 seconds, although the exact length does vary between experiments. Another complicating factor is that while there is some decay function, stochastic Brownian motion quickly dominates after a few seconds: the short time scale of response means that eliminating the Brownian factor using MSD subtraction is not viable. We can see several of these same behaviors in another experiment under similar circumstances (175 μm electrode distance with a switching series of 300 mV potentials):

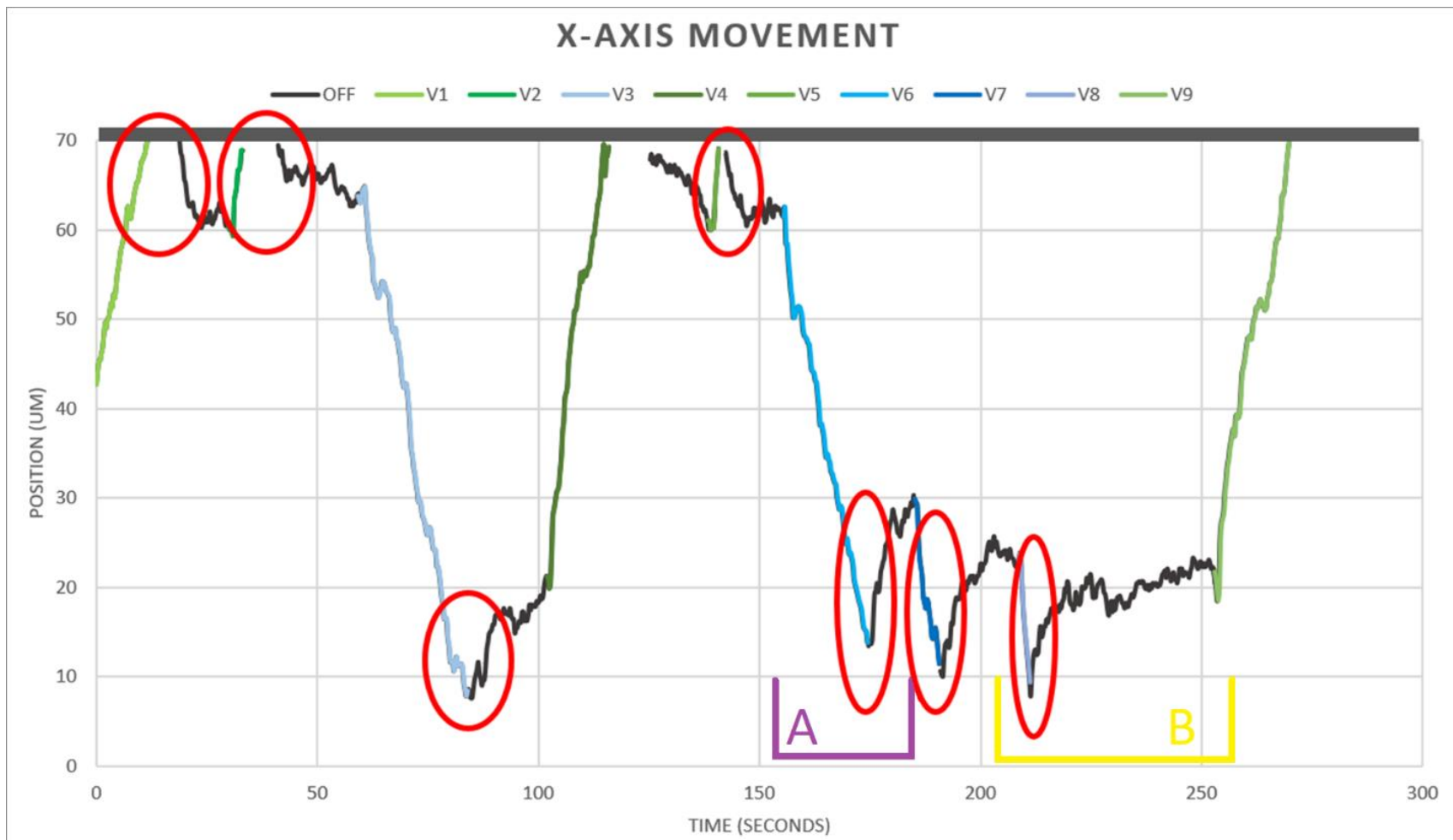


Figure 9.10: The total x-axis movements of a 20 nm FL nanoparticle in a 175 µm channel, all with 300 mV applied potentials. The dark grey bar at the top of the graph indicates the rough position of the electrode. Green lines indicate a positive (attractive) potential on the electrode, while blue indicates a negative (repulsive) potential. Black lines indicate the voltage is turned off and observed rebound effects (red circles) occur immediately as the voltage is switched off.

Two highlighted sections (A/purple and B/yellow) are presented in Figure 9.11.

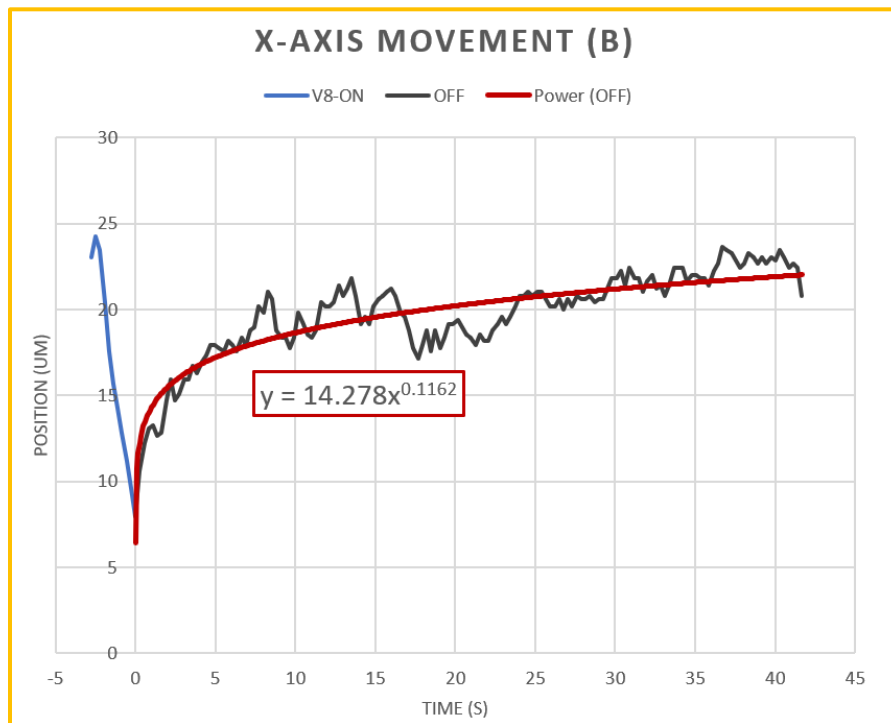
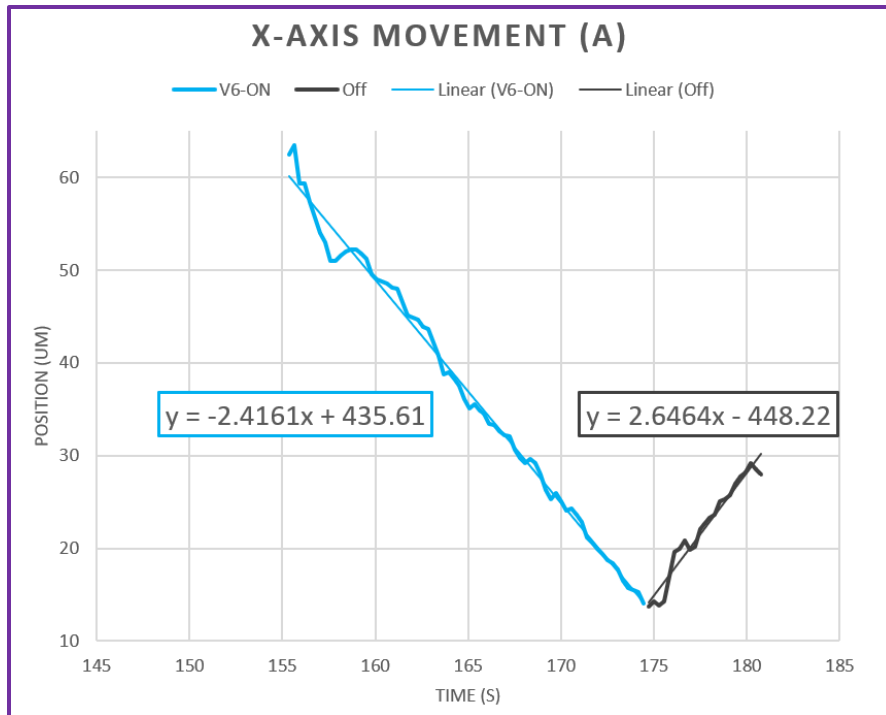


Figure 9.11: Highlighted sections from Figure 9.10. **(top, A)** The rebound velocity is on a short timescale and of a similar magnitude to the ballistic component. **(bottom, B)** The rebound effect does have a characteristic decay function, lasting for at least 5-10 seconds, as it returns to pure stochastic Brownian.

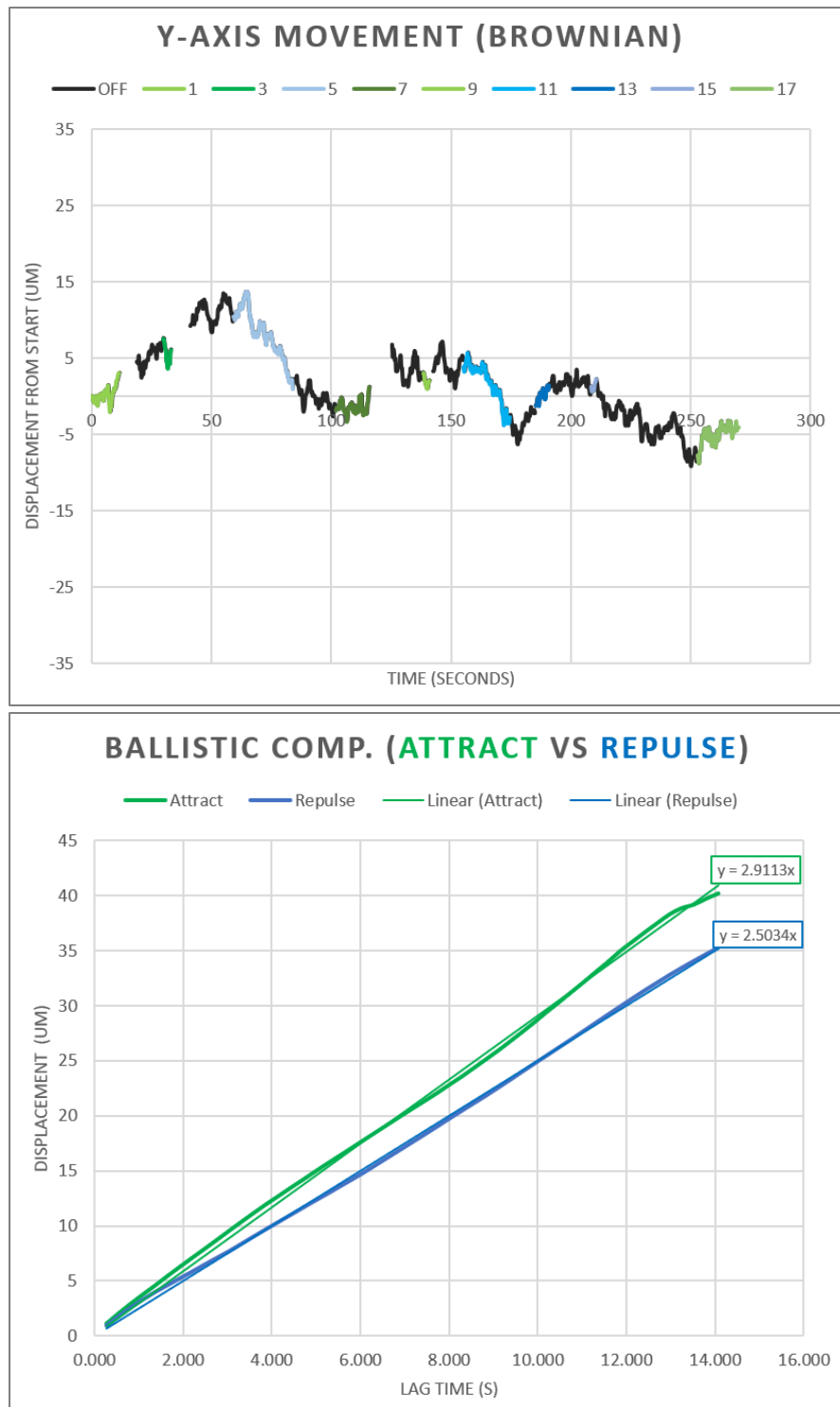


Figure 9.12 (top): Y-Axis Brownian movements set to the same scale as Figure 9.10, for comparison to highlight “normal” Brownian motion. **(bottom):** Averaged R-MSD subtracted ballistic components of all the attractive (green) and repulsive (blue) applications. This is to highlight the similar ballistic velocities between the two directions, with attraction being slightly stronger.

Again, the rebounding effect reliably occurs as soon as the potential is cut, always in the opposite direction of the electric field's directional push. The rebound effect is temporary, starting with a mirrored ballistic component, Figure 9.11.A, before rapidly decaying down to the characteristic Brownian motion of a null field, Figure 9.11.B. The magnitude of Brownian motion can be seen in the Y-Axis movements of Figure 9.12, which is comparable to the Brownian sections when the field has been turned off (black) in Figure 9.10.

In addition, this effect appears to have an inverse relationship with electrode distance: the 1500 μm channels have little-to-no noticeable rebound effect, while the 175 μm and 75 μm channels have consistently repeatable rebounds that are strongly prominent and independent of electrode proximity or field direction.

9.4 The Effects of Increasing Viscosity

To get a complete picture of the establishment of the electric double layer, namely the decaying field function and an exploration of the rebound effect, reconsider Equation 8.13:

$$V_q = \frac{6\pi\eta ad}{ze_0} * v_t \quad (8.13)$$

The alterable variables are electrode distance d , potential V_q , particle radius a , number of charges z , and solution viscosity η . Having previously explored altering both distance and applied potential (and considering that particle radius and surface charges are difficult to alter independently) the only remaining independent variable that can be easily altered is viscosity. Utilizing glycerol, a highly viscous polar chemical that is fully miscible in water, we can reliably increase the viscosity without dramatically altering any of the other variables.

A series of solutions were made by adding glycerol to the normal pH 10 solution of 20 nm FL

nanoparticles to create an array of glycerol-water mixtures. Utilizing a viscosity calculator¹⁰⁻¹² the following viscosities were calculated: 0% glycerol (1.00 mPa s), 10% glycerol (1.38 mPa s) and 25% glycerol (2.41 mPa s). The increased viscosity will also lower the magnitude of the diffusion coefficient in a similar manner according to Equation 1.8:

$$D = \frac{RT}{N_A} \frac{1}{6\pi\eta a} \quad (1.8)$$

These two effects, a slowed terminal particle velocity and a minimized diffusion coefficient, results in the particle being observed for a longer time with a more consistent overall speed; increased viscosity improves the signal-to-noise ratio across the board. This can be seen in the following two examples, one with a 10% solution in a 175 μm channel and one with a 25% glycerol solution in a 75 μm channel.

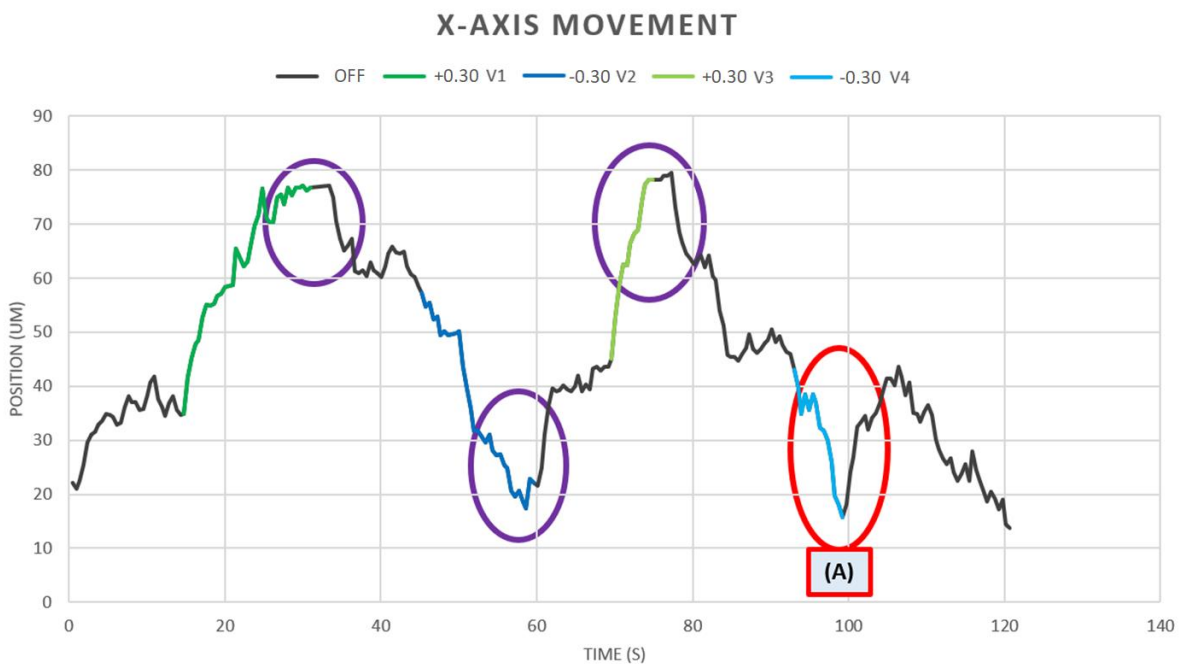


Figure 9.13: X-Axis movements of a 20 nm FL nanoparticle in a 175 μm channel and 10% glycerol solution. The particle was attracted towards (green) and repulsed from (blue) the electrode with a 300 mV potential. The purple circles highlight rebounding effects. The ballistic component and red highlighted area are presented in Figure 9.14.

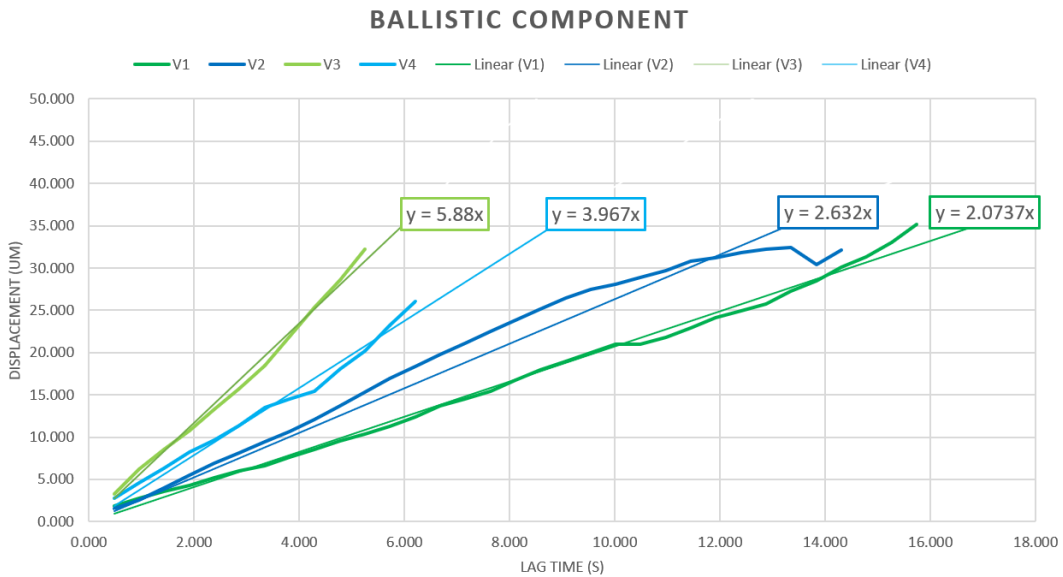
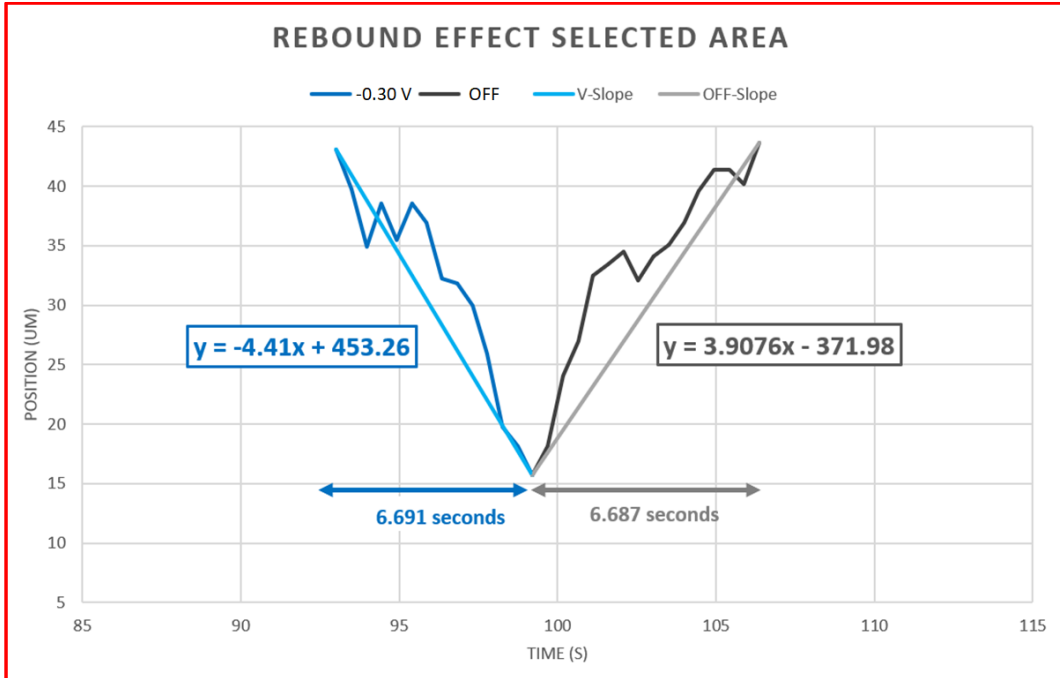


Figure 9.14 (top, red): A highlighted section from Figure 9.13. The applied potential's terminal velocity and the resulting rebound effect have a similar slope, even after a relatively short application time of just 6.69 seconds.

(bottom) The ballistic components, from Figure 9.13, appear to be a function of time: the longer time intervals of applied potential result in a lowered average terminal velocity. This matches the results seen in Figure 9.6, suggesting an underlying characteristic decay function.

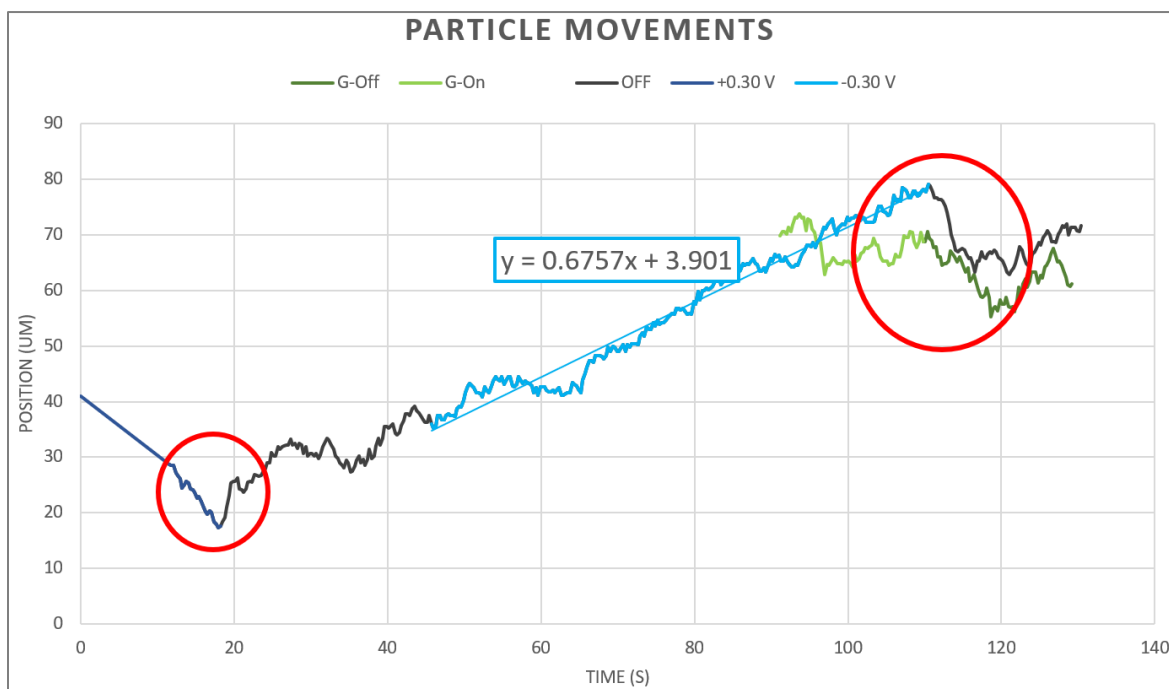
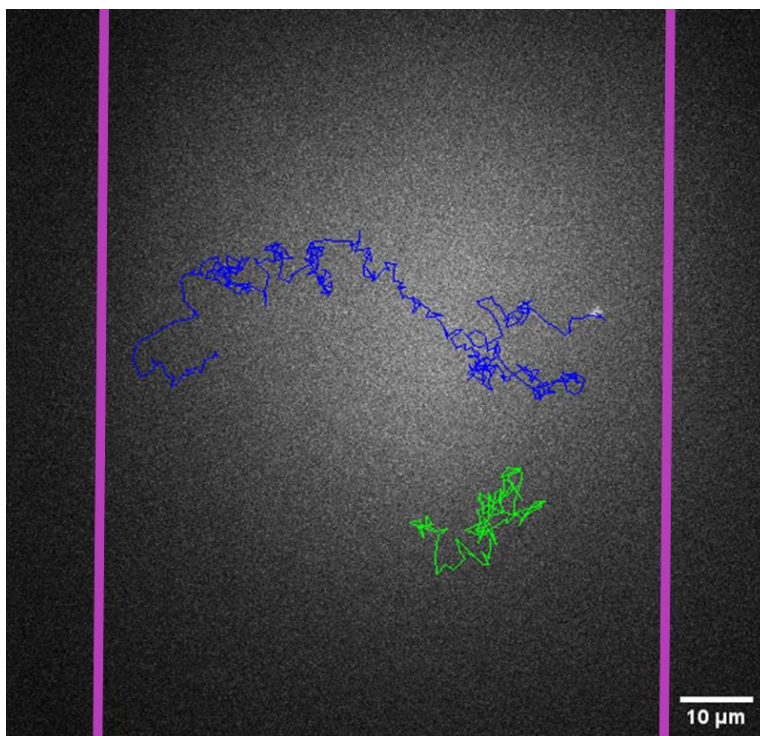


Figure 9.15 (top): The trajectories of two 20 nm FL nanoparticles (blue and green) in a 25% glycerol solution with the opposing electrodes (purple lines) 75 μm apart, with an applied potential of 300 mV in both cases. **(bottom)** The movements of the two particles, with highlighted rebounding effects (red). The position at 0.00s is an estimate because the tracking video had to be quickly realigned at the start, but all other points are accurate.

Using the Brownian MSD slope from the Y-axis components from Figure 9.15, the diffusion coefficient D was calculated to be $1.5 \mu\text{m}^2/\text{s}$. By comparing the diffusion coefficient for a sample without glycerol to its viscosity, previously calculated in Chapter 8.2 to be $3.9 \mu\text{m}^2/\text{s}$ with a viscosity of 1.00 mPa s , this would correlate to a viscosity of 2.60 mPa s . As the theoretical value of a 25% glycerol solution was found to be 2.41 mPa s , this correlates reasonably well, with some minimal error occurring naturally from variability in effective nanoparticle radius, NaOH interactions, and the roughly approximated temperature.

Although it is partially visible in all previous examples, there is another rebounding phenomenon readily visible for the blue particle in Figure 9.15 (bottom): there is some correlation between the length of time the electric potential is applied and the length of the resulting rebound effect. (Important note: due to the currently unknown length of the rebounding effect, we will only be considering the immediate linear rebound effect, and momentarily discounting the decay function discussed in Figure 9.11.) The first 0.30 V potential was applied for 17.94 seconds, and the rebound is a movement of $8.77 \mu\text{m}$ over 2.50 seconds. The second 0.30 V potential was applied for 64.73 seconds, and the rebound is $15.92 \mu\text{m}$ over 6.11 seconds. Momentarily taking the rebound as a linear function (it's not; see Figure 9.11), this suggests that a 4-fold increase in potential application time results in a doubling in rebound time and distance. Due to the greatly increased viscosity for Figure 9.15, these distances are considerably smaller than those seen in Figures 9.8, 9.10, and 9.13, although bizarrely the length of the rebound effects are still comparable between each example despite the change in viscosity. Clearly, more work is required to pull out the true underlying relationship.

As one final example, another 25% glycerol sample was prepared and the potential was

varied for two different times to see if there was a correlation between longer charge times and the resulting rebound, which can be seen in Figure 9.16 below. The first 300 mV potential was applied for 112.39 seconds, which resulted in a 17.35 μm rebound over 5.56 s, seen in the red circle. The second potential, again 300 mV, was applied for 43.37 seconds, which resulted in a rebound of 8.98 μm over 4.73s. According to these results, there is again a correlation between increased charge time and the strength of the rebound, but in this case the difference is largely for total-distance travelled, with less impact on the length of time (although there is still some correlation between these as well).

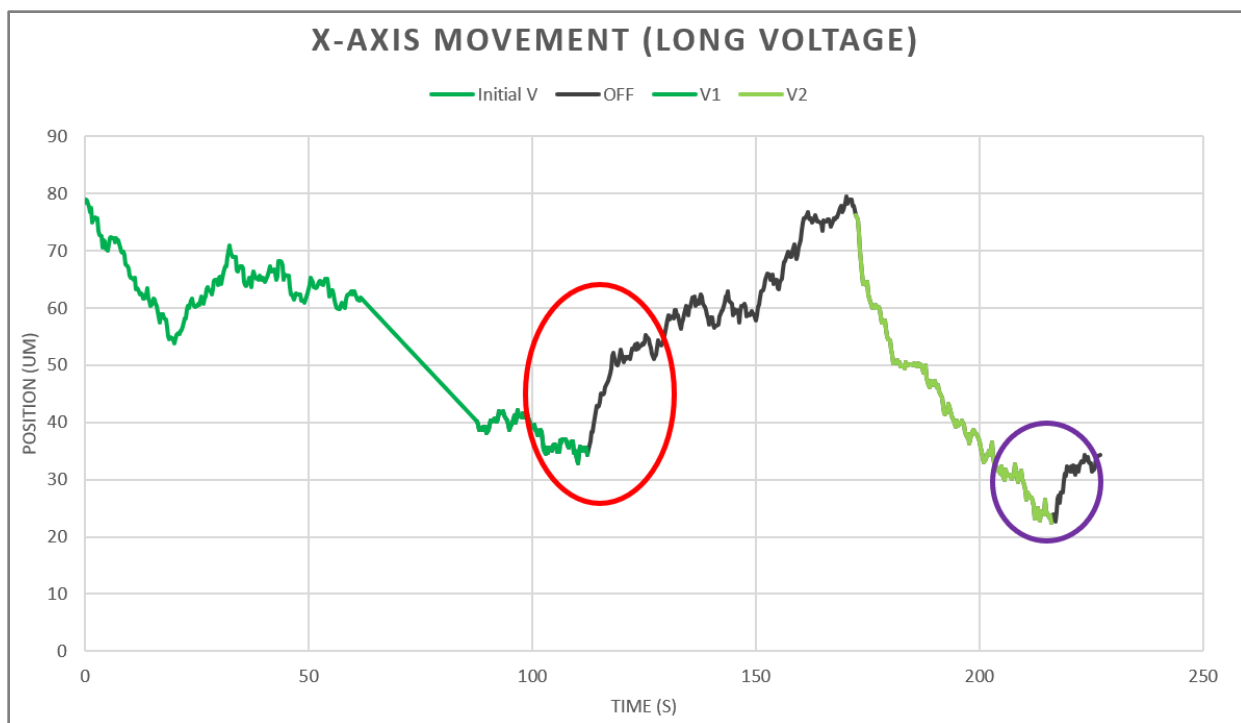


Figure 9.16: The X-axis movements of a 20 nm nanoparticle in pH 10 NaOH and 25% glycerol within a 75 μm channel, with two highlighted rebounding effects. The red circle highlights the rebound after 112.4 seconds of an applied 300 mV, while the purple circle highlights the rebound after 300 mV was applied for 43.4 seconds. The linear segment in the first voltage application is the result of readjustment of the camera during recording, stitched together and estimated for clarity on charging time. It has no effect on the resulting rebound.

The only conclusive statement these results can provide is that there is a repeatable rebounding response upon the removal of an applied potential, with some correlation between the charge time length and the magnitude of the response. The specifics are unfortunately unclear, although there is clearly a wealth of information to be gained with further research.

9.5 Hypotheses and Future Goals

This subchapter's purpose is to propose a plausible explanation of these strange results. These initial hypotheses are made to serve as a starting point for the next investigator on the path towards understanding. When possible, I've included some suggestions for future experiments that could delve further into the phenomena seen here, and to quote Einstein¹³: "it is hoped that some enquirer may succeed shortly in solving the problem suggested here."

The first key hypothesis is that of difference between applied voltage and effective voltage. As discussed in Figure 7.8, there are two extremes: the electrostatic potential with and without an established Electric Double Layer. What Figure 9.6 suggests is that there is a transition period between these extremes at time scales much longer than initially thought, and that the potential undergoes a measurable time-dependent decay function. The length of time that this decay tapers off is unknown, but the data suggests that the full charge time of 99% of the applied potential is much larger than initially assumed, in some cases taking more than a minute, while the last remaining percent is still effective in inducing an attraction velocity for many more minutes afterwards. This is summarized in Figures 9.17 and 9.18, with emphasis on the non-equilibrium status of the observed potential, as seen by the slow reduction of the potential and the particle's resulting terminal velocity.

CAPACITOR, EDL, AND EXPERIMENTAL

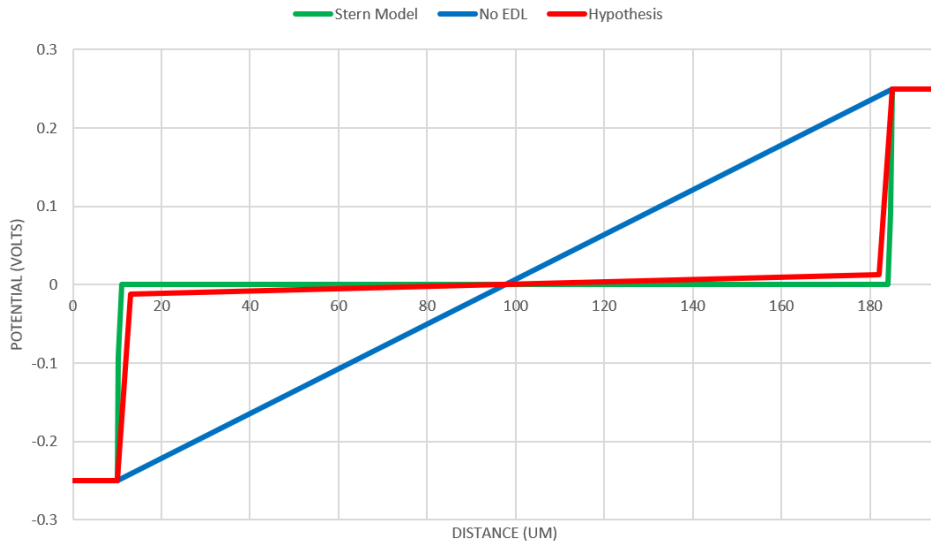


Figure 9.17: Hypothetical 1D graphs of the electric potential across a 175 μm channel with pH 10 NaOH solution: with Stern Model EDL (green), without an EDL or in a vacuum (blue), and the observed experimental hypothesis (red). The experimental hypothesis is a reduction of less than 99% of the applied potential.

EQUILIBRIUM ESTABLISHMENT TIME

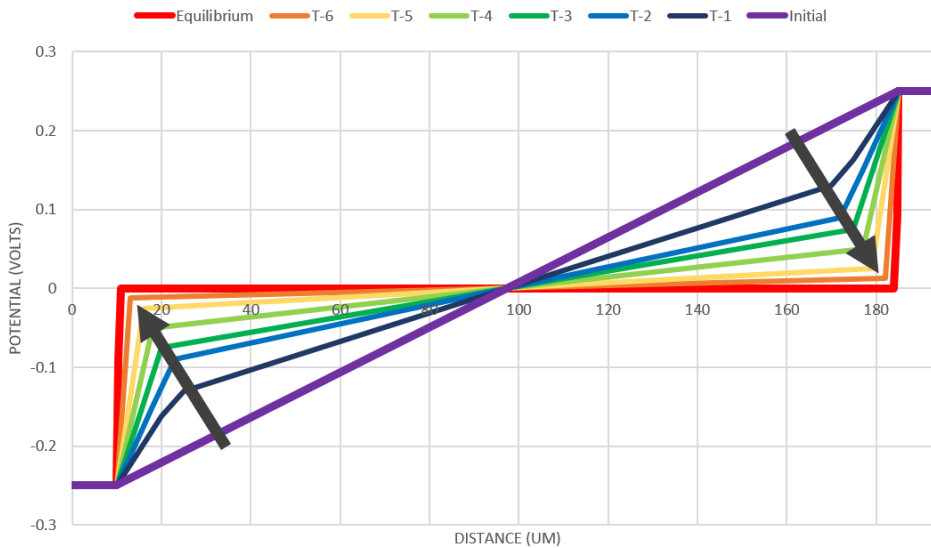


Figure 9.18: Hypothetical 1D line graphs of the electric potential across a 175 μm channel with pH 10 NaOH solution. The purple line represents the potential at time = 0, while the red line represents the potential at equilibrium according to the Stern model, with the rest of the colors as a change-over-time spectrum. The black arrow represents the direction of change over some unknown time scale. (The exact values are pure conjecture).

The second hypothesis about the potential reduction concerns the solution's non-uniform conditions and resulting electroosmotic flow. Importantly, this specifically concerns the positive sodium ions and their interactions with the glass surface, and not the negative nanoparticles. The hydroxide ions in solution will react with the -OH groups present on all glass surfaces as silanol groups, Si-OH. The hydroxide ions will deprotonate the silanol, acting like a weak acid and leaving behind Si-O⁻, and the sodium ions in solution will then be attracted to the negative glass surface. This greatly depletes the free sodium ions in solution, creating an EDL along the glass surface.

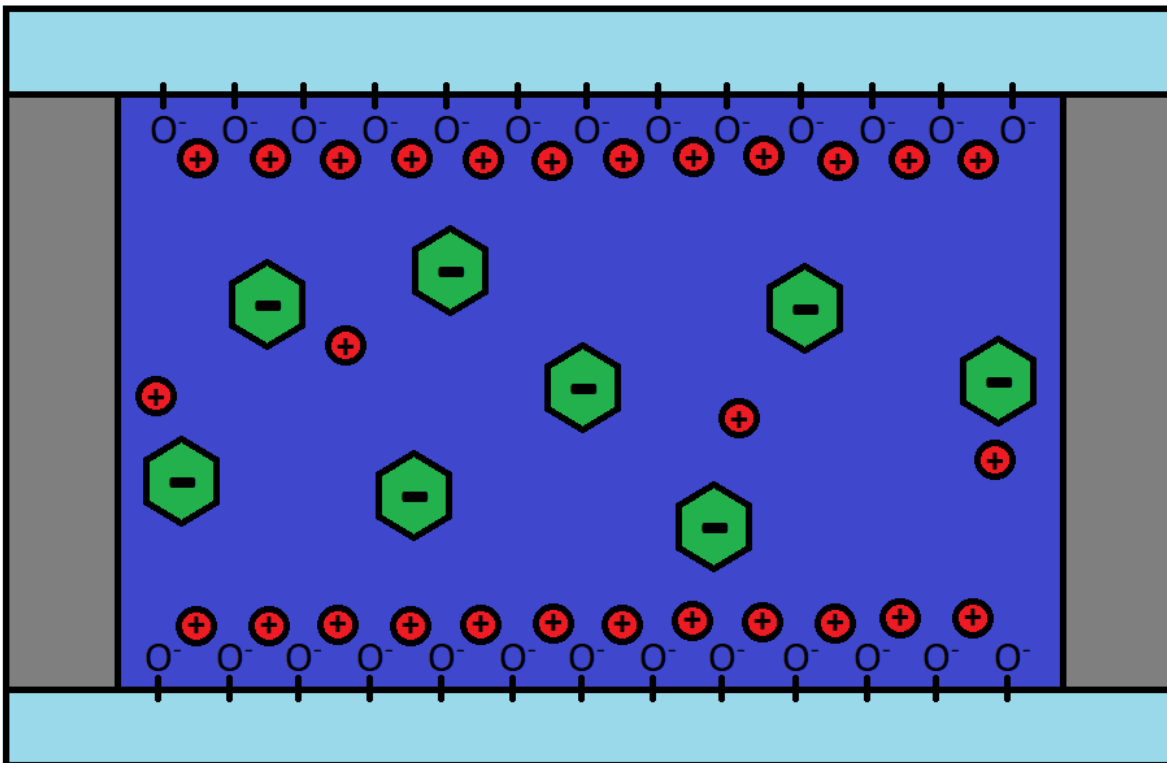


Figure 9.19: Side-view of an idealized microfluidic cell, with electrodes (grey), glass (light blue), solution (dark blue), sodium ions (red) and negatively charged 20 nm FL particles (green). Along the glass surface are several deprotonated silanol groups, depicted as an O⁻. The glass surface attracts sodium ions, creating an EDL, while leaving the solution with far fewer bulk sodium ions.

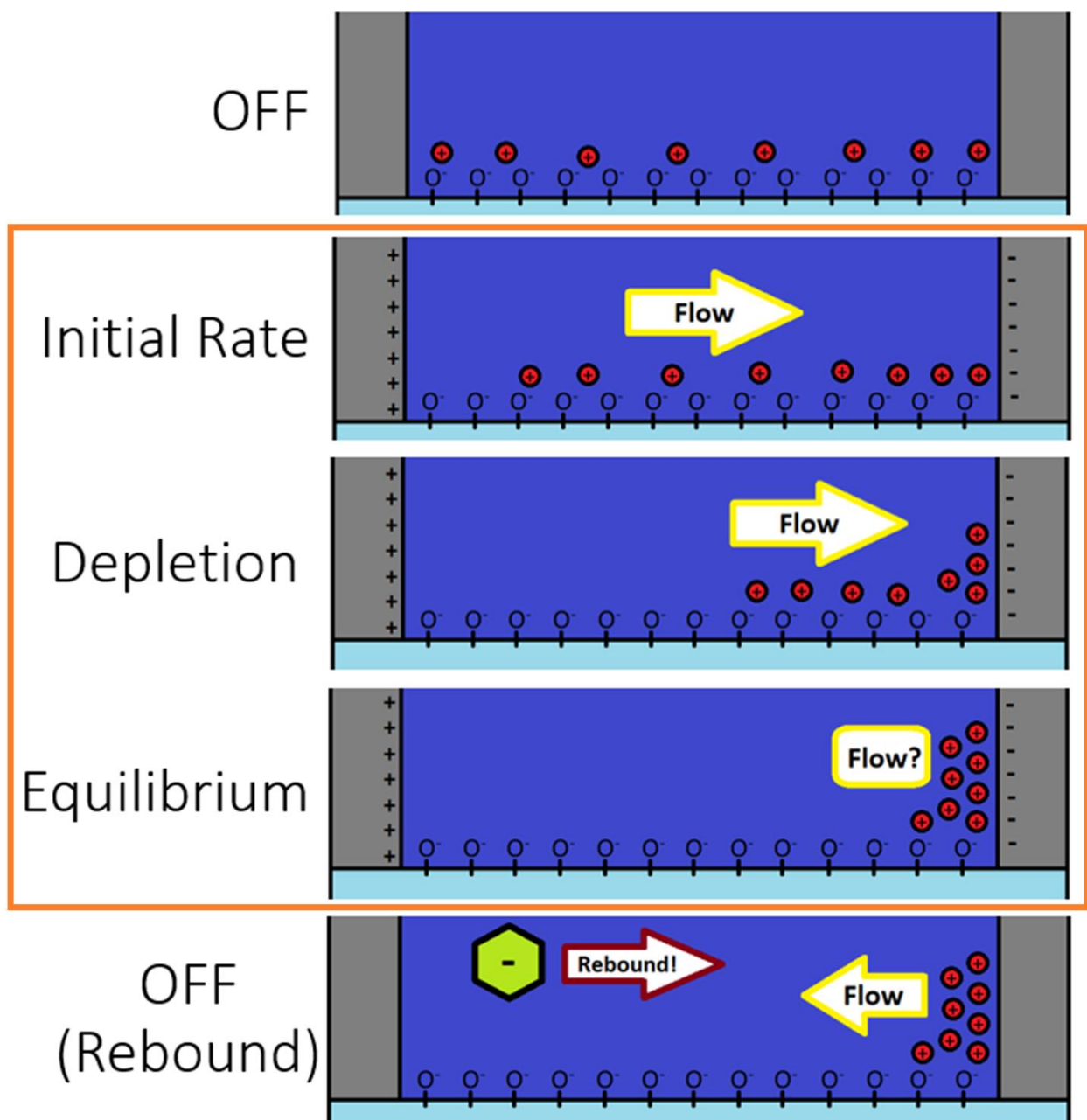


Figure 9.20: A simplified view of positive sodium ions (red circles) inducing electroosmotic flow within the electrode channel at five different times of an applied electric potential (orange box): electrode off, initial rate at the moment the electric field is activated, depletion of sodium ions from the glass surface, and the cessation of electroosmotic flow. The fifth image depicts when the electric field is deactivated: the sodium ions induce a directional flow that is antithetical to the observed rebound effect of the nanoparticle (green, negatively charged).

Under the influence of a strong electric field, however, the sodium ions will be drawn along the surface of the glass towards the negative electrode, “dragging” the water with it and inducing a hydrodynamic flow to the solution. Electroosmotic flow was not included in previous calculations for several reasons, primarily because there is a time-dependence on the electroosmotic flow: as the sodium ions are depleted from the glass surface, the electroosmotic flow decreases to zero. To maintain a constant flow rate, there would have to be a constant replenishment of counter-ions, otherwise there are no remaining ions present to continue.

The second reason it was not included is due to the nature of the microfluidic cell: the cell is rigid and static with no inlets or outlets. If the electroosmotic flow were considered constant, this would imply that there is a continual migration of solution towards one electrode, which would create a nonsensical situation of having a far greater amount of solution in one half of the channel. This would necessitate some manner of circular convection currents to return the incoming water back to the bulk, much like an oceanic rip-current functions to return water to the ocean after it crashes against a beach. This becomes an increasingly complex system that is difficult to meaningfully analyze. Also, as the electroosmotic flow moves in the opposite direction to the negative nanoparticle, this would correspond to greater resistance to the ballistic component. As this results in a higher effective potential, this would mean the reduction is actually *over-estimated*, and that the decay rate is slower than initially assumed!

The main focus of the electroosmotic flow hypothesis instead deals with the depletion of the positive ions from the solution. Assuming that a large portion of the sodium ions will be attracted and partially adhered to the glass instead of moving towards the negative electrode, the resulting EDL along the negative electrode would contain significantly fewer counterions

and cause the resulting effective potential would be far stronger than expected. Assuming a worst-case scenario that the solution is completely devoid of ionic salts, this would result in longer Debye lengths and longer equilibrium charge times for the electric double layer.

While electroosmosis is an effect that does occur in the microfluidic cell and does have an influence on the terminal velocity of the nanoparticles, it requires much more work to integrate into the work presented in this dissertation. Slight variability in pH should have a negligible effect on the nanoparticle's overall charge as the pK for carboxylate groups (pKa of ~5 or lower)¹⁴ is less than of silanol on glass (pK of ~7.5)¹⁵ and thus the nanoparticles will be fully deprotonated before the glass. As such, the time-dependence of the electroosmotic flow might be calculated by doing a series of experiments with larger pH values: increasing the concentration of sodium hydroxide increases the strength and duration of electroosmotic flow. The inclusion of electroosmotic flow, or the provisions to discount it entirely, would provide a more complete picture of the finite system presented here.

Crucially, however, the electroosmotic effect does not explain the "Rebound Effect" as the returning sodium ions would induce a flow in the opposite direction to the observed nanoparticle's rebound. There must be yet another factor that causes this unexpected result.

The current hypothesis for the rebound effect is that of battery-like behavior: as electrons are added to the electrode, migrating counter-ions enhance the electric charge, which increases the self-capacitance of the electrodes, which in turn increases the amount of charge that can be added to the electrode. As a cyclic process, this effectively allows for specifically adsorbed ions to function like a miniature battery and increases the total charge density allowed when compared to vacuum.

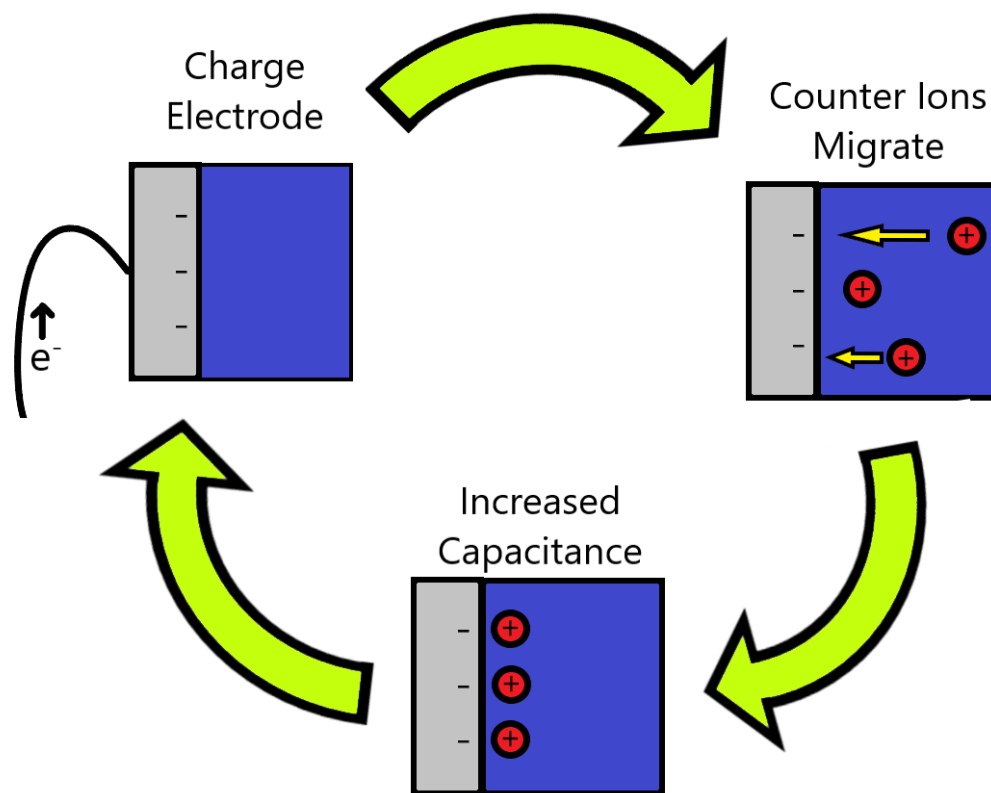


Figure 9.21: A simplified view of the hypothetical cyclic electrode charging mechanism. The negative electrode (grey) receives electrons from the power source, which causes counter-ions (red) to migrate and form the EDL, which then increases the capacitance of the electrode, allowing for more charge to build.

When the potential is then turned off, adsorbed ions do not immediately dissipate, but instead gradually desorb, detach, and diffuse over time. However, the electrode charge does dissipate quickly, resulting in a large coverage of counterions on both electrodes that now induce an electric field that is of the same magnitude as the imposed field, but in the opposite direction. This counter-field induces a ballistic motion onto the charged nanoparticles in the direction opposite to their previous direction, suddenly changing direction as a strong rebound. As the counterions on the electrode dissipate, the counter potential quickly drops to zero, and the particles return to pure Brownian motion.

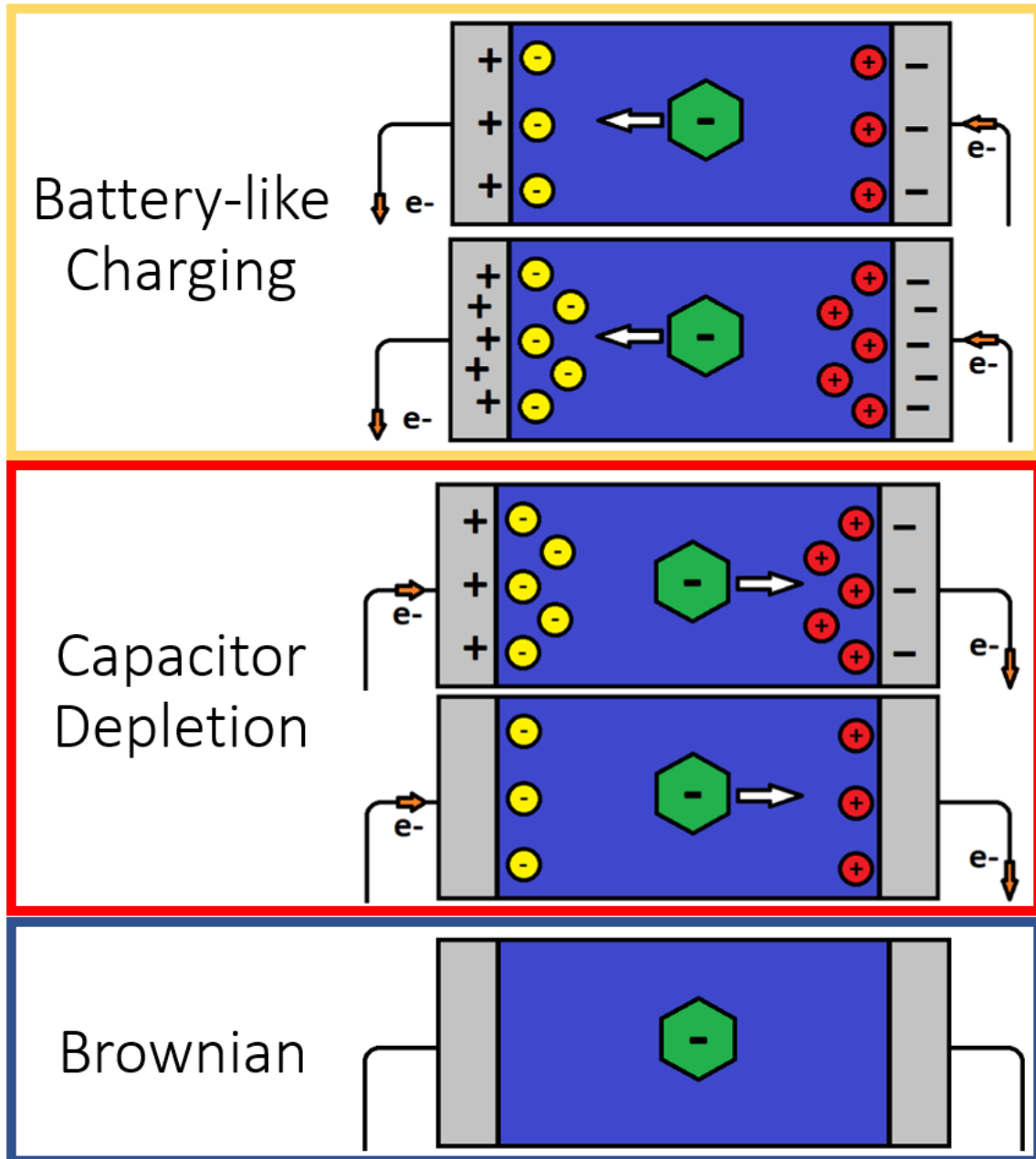


Figure 9.22: An idealized microfluidic cell, with electrodes (grey), solution (blue), sodium and hydronium ions (red), hydroxide ions (yellow), and negatively charged 20 nm FL particles (green). In the Battery-like Charging, the electrons flow onto the negative electrode, which accumulates more positive ions over time and allows for more electrons to be added. In Capacitor Depletion, the electrons rapidly flow onto the positive plate, but the counter-ions slowly dissipate. Once the counter-ions fully diffuse, the nanoparticle returns to pure Brownian motion. A white arrow shows the experimentally observed movement of the nanoparticle, including the rebound effect.

The hypothesis in Figure 9.21 explains the observed relationship between electrode charging time and the resulting rebounding effect: longer charge times result in a greater concentration of adsorbed ions in the electric double layer, which would then require more time to discharge and thus creates a longer lasting reversed field.

The hypothesis presented in Figure 9.22 is consistent with both the observed longer required charge time of the EDL, as well as the observed movements of the rebounding effect: counter-ions introduce a time-dependent delay as the capacitor shifts into battery-like behavior, while the slow dissipation of counter-ions from electrodes induces a counter field that pushes the negatively charged nanoparticle in the direction of electron migration. This also explains why a higher viscosity solution results in longer rebounding effects: the reduced mobility of the counter-ions lengthens the time it takes to diffuse from the capacitor.

Transitioning away from a parallel plate capacitor model and treating the electrodes as pseudo-capacitors could provide more insight into the exact processes occurring in these finite systems. Additional instrumentation to measure real-time current and capacitance while under direct particle observation would confirm or deny these hypotheses. Another future experiment could be conducted by changing the parameters of the nanoparticles themselves: changing the particle's radius without altering the total net charge would provide insight into particle response speed and Brownian considerations, using neutral particles could confirm whether this is purely an electric field effect or an electroosmotic solution flow effect, and using positively-charged particles of similar dimensions could confirm whether this effect is uniform regardless of charge. As these further experiments move into the realm of repeating nearly all the previous experiments shown here, which would surely take many more years of research, it

is unfortunately here that I must end this dissertation with an unsatiated hunger for knowledge.

It is my sincere hope that this is a sufficient starting point for the next researcher to unravel the answer that has eluded me for years. I look forward to your work.

9.6 Conclusions

This dissertation delves below the visible threshold of standard illumination-based microscopy, into the largely unexplored nanoscale level of non-equilibrium particle movements in microfluidics by using fluorescent emissions of 20 nm diameter nanoparticles. By utilizing a lag-time based approach to single particle tracking, the Brownian-based diffusion of these nanoparticles was extracted and compared to expected values. By using a rigid 2-dimensional microfluidic cell, with the application of an electric potential in only one axis, this allows for dynamic analysis of a single particle by simultaneously calculating the Brownian diffusion along the y-axis and the ballistic component of the electric field along the x-axis by using mean-square-displacement subtraction. The resultant lag-time based ballistic components showed a reliable and repeatable percentage reduction of the applied potential to be higher than expected, while the time-dependent decay function of the potential took place over far longer timescales than had previously been estimated. Along with the unexpected result of an apparent rebound-like effect, these observations strongly indicate that there is more to explore on the nanoscale-level of particle microfluidics, with some preliminary hypotheses and future experiments proposed to give possible explanations and guidance.

- (1) Morrow, R.; McKenzie, D. R. The Time-Dependent Development of Electric Double-Layers in Pure Water at Metal Electrodes: The Effect of an Applied Voltage on the Local pH. *Proceedings of the Royal Society A: Mathematical, Physical and Engineering Sciences* **2012**, 468 (2137), 18–34. <https://doi.org/10.1098/rspa.2011.0323>.
- (2) Morrow, R.; McKenzie, D. R.; Bilek, M. M. M. The Time-Dependent Development of Electric Double-Layers in Saline Solutions. *J. Phys. D: Appl. Phys.* **2006**, 39 (5), 937–943. <https://doi.org/10.1088/0022-3727/39/5/007>.
- (3) Wu, J. Understanding the Electric Double-Layer Structure, Capacitance, and Charging Dynamics. *Chem. Rev.* **2022**, 122 (12), 10821–10859. <https://doi.org/10.1021/acs.chemrev.2c00097>.
- (4) *Intrinsic limitations of impedance measurements in determining electric double layer capacitances | Elsevier Enhanced Reader.* <https://doi.org/10.1016/j.electacta.2011.12.051>.
- (5) Mei, B.-A.; Munteshari, O.; Lau, J.; Dunn, B.; Pilon, L. Physical Interpretations of Nyquist Plots for EDLC Electrodes and Devices. *J. Phys. Chem. C* **2018**, 122 (1), 194–206. <https://doi.org/10.1021/acs.jpcc.7b10582>.
- (6) Kilic, M. S.; Bazant, M. Z.; Ajdari, A. Steric Effects in the Dynamics of Electrolytes at Large Applied Voltages. II. Modified Poisson-Nernst-Planck Equations. *Phys. Rev. E* **2007**, 75 (2), 021503. <https://doi.org/10.1103/PhysRevE.75.021503>.
- (7) Tivony, R.; Safran, S.; Pincus, P.; Silbert, G.; Klein, J. Charging Dynamics of an Individual Nanopore. *Nat Commun* **2018**, 9, 4203. <https://doi.org/10.1038/s41467-018-06364-1>.
- (8) Evans, P. *Capacitor Charge Time Calculation*. The Engineering Mindset. <https://theengineeringmindset.com/capacitor-charge-time-calculation/> (accessed 2023-04-07).
- (9) Storr, W. *RC Charging Circuit Tutorial & RC Time Constant*. Basic Electronics Tutorials. https://www.electronics-tutorials.ws/rc/rc_1.html (accessed 2023-04-07).
- (10) *Calculate density and viscosity of glycerol/water mixtures.* http://www.met.reading.ac.uk/~sws04cdw/viscosity_calc.html (accessed 2023-02-08).
- (11) Volk, A.; Kähler, C. J. Density Model for Aqueous Glycerol Solutions. *Exp Fluids* **2018**, 59 (5), 75. <https://doi.org/10.1007/s00348-018-2527-y>.
- (12) Cheng, N.-S. Formula for the Viscosity of a Glycerol–Water Mixture. *Ind. Eng. Chem. Res.* **2008**, 47 (9), 3285–3288. <https://doi.org/10.1021/ie071349z>.
- (13) Einstein, A. Investigations on the Theory of the Brownian Movement. 11.
- (14) Haslak, Z. P.; Zareb, S.; Dogan, I.; Aviyente, V.; Monard, G. Using Atomic Charges to Describe the p K_a of Carboxylic Acids. *J. Chem. Inf. Model.* **2021**, 61 (6), 2733–2743. <https://doi.org/10.1021/acs.jcim.1c00059>.
- (15) Behrens, S. H.; Grier, D. G. The Charge of Glass and Silica Surfaces. *The Journal of Chemical Physics* **2001**, 115 (14), 6716–6721. <https://doi.org/10.1063/1.1404988>.

Curriculum Vitae

Quintus S. Owen

Curriculum Vitae: Quintus S. Owen

EDUCATION & TRAINING

PhD Program in Chemistry – University of Wisconsin-Milwaukee, Dept. of Chemistry and Biochemistry
Defense Date: May 4th, 2023

Bachelor of Science in Chemistry, Minors in Physics and Psychology – Wake Forest University
August 2007 to May 2012

PRESENTATIONS AND PUBLICATIONS

“Immobilization and Isolation: Electrostatic Corral Trapping of ssDNA”

Poster presented at UWM Research Symposium – May 2014

“Counteracting Brownian Motion: Optical Tweezers and the ABEL Trap”

Presented at UWM Research Seminar – April 2015

“Efficient Cleaning Methodology for the Removal of Superfluous Material on Polystyrene Microspheres”

Poster presented at UWM Research Symposium -- April 2015

“Towards a Super-Resolution of Map of the Electric Double Layers”

Poster presented at UWM Research Symposium -- April 2018

“A Super-Resolution Map of Non-Equilibrium Electric Double Layers”

Poster presented at UWM Research Symposium – May 2019

Winner: Keith Hall Award for Excellence in Graduate Research – 1st place poster

Poster presented at ACS Great Lakes Conference – May 2019

“A Model for Finite Non-Equilibrium Electrolyte Solutions”

Poster presented at COMSOL Conference Boston -- October 2019

“Infrared Spectroscopic Measurements of the Structure of Organic Thin-Films; Furfural on Pd(111) and Au(111) surfaces” by R. Bavisotto, N. Hopper, A. Boscoboinik, **Q. Owen**, and W. Tysoe

Paper in CrystEngComm – June 2021

“DC Corral Trapping of Single Nanoparticles and Macroparticles in Solution” by C. Carlson, X. Udad, **Q. Owen**, A. Patel, W. Chang, and J. Woehl.

Paper in Journal of Chemical Physics – April 2022

“Utilizing Fluorescent Nanoscale Particles to Create a Map of the Electric Double Layer” by **Q. Owen**

Doctoral Dissertation, University of Wisconsin-Milwaukee, Expected December 2022

SKILLS AND EXPERIENCE

Nanotechnology/Nanolithography
High Vacuum Chambers
Fluorescence Microscopy
Scanning Electron Microscopy
COMSOL modelling program

Photolithography
Chemical Vapor Deposition
Confocal Microscopy
Optical Systems
Lab Safety Officer

PROFESSIONAL WORK EXPERIENCE

GRADUATE RESEARCH ASSISTANT

University of Wisconsin-Milwaukee, Milwaukee, WI • August 2013 to Present

TEACHING ASSISTANT

University of Wisconsin-Milwaukee, Milwaukee, WI • August 2013 to Present

- *Chemistry 100: Chemical Science*
- *Chemistry 101: Chemical Science for Nurses*
- *Chemistry 102: General Chemistry I*
- *Chemistry 104: General Chemistry II*
- *Chemistry 561: Physical Chemistry I*
- *Chemistry 562: Physical Chemistry II*

UNIVERSITY TUTOR & PRIVATE TUTOR – CHEMISTRY

University of Wisconsin-Milwaukee, Milwaukee, WI • August 2013 to Present

HONORS AND AWARDS

Teaching Assistant of the Year Award, Chemistry – May 2020

Keith Hall Award for Excellence in Graduate Research, 1st place poster – April 2019

Graduate Student Travel Award – October 2019

University of Wisconsin-Milwaukee Chancellor's Award – Fall 2013 to Spring 2018

UWM Student Success Award – May 2014

NON-ACADEMIC VOLUNTEER WORK

Extra Life Children's Charity Events, 8th Note Coffeehouse – 2013 to Present

Senior Staff Member and Event Planner, Deeplight LARP – 2018 to Present